4.11 Effects on Radiation-Induced Segregation in Fine Grain Stainless Steel

F. Kano*, Y. Tsuchiya*, N. Saito*, A. Naito** and I. Ioka**
Toshiba Corporation*
Department of Materials Science, JAERI**

1.Introduction

The recent mechanistic consideration on irradiation induced stress corrosion cracking (IASCC) has focused on the role of grain boundary segregation. The depletion of chromium at grain boundary due to irradiation is considered to be the most important factor because stress corrosion cracking susceptibility of thermally sensitized stainless steels is determined by the degree of chromium depletion at grain boundary[1]. Depletion of chromium at grain boundaries in stainless steels has been implicated as a contributing cause for component stress corrosion cracking in Light Water Reactor (LWR). The chromium depletion caused by irradiation, radiation induced segregation (RIS), is in contrast to enrichment caused by thermal processing of alloys.

We investigated the irradiation characteristic of the fine grain stainless.

2.Experimental

The specimens were commercial SUS304L (similar to Type 304) stainless steel's sheets (100X50X1mm thickness). All the specimens were heat treated, followed by water-cooling.

The 3mm diameter TEM disks were irradiated with 12MeV Ni^{3+} ions at 573K. The dose was 1 dpa at 1 μm depth from the surface. The damage peak depth and Ni ion range peak depth were over 3 μm. It is known by analysis that at 1 μm -depth the influence of an irradiation nickel ion can be removed by TRIM calculation. After irradiation, the specimen surface was removed by electropolishing to 1 μm and back-thinned for perforation in $HClO_4$ + CH_3COOH solution.

Microstructural observation and compositional analysis across grain boundary were conducted using a FE-TEM (TOPCON EM-002BF, 200kV) with an EDS analyzer. The probe electron beam size for the analysis was 0.4nm on the specimen.

3.Results

The Cr profile of usual grain stainless steels, about 70 micron, having no segregation due to the perfect thermal heat treatment measured by EDS across the grain boundary after 1.3dpa irradiation are shown in Fig.1. The Cr profile of 12micron fine grain size after 1.3dpa irradiation measured by EDS across the grain boundary are shown in Fig.2. Cr profile of 7micron fine grain size after 1.3dpa irradiation measured by EDS across the grain

boundary are shown in Fig.3. No Precipitates were observed in grain and at grain boundary before and after irradiation in all specimens.

Cr depletion at grain boundary after irradiation in all specimens is shown. But Cr depletion at grain boundary tends to be restrained with decreasing the grain size.

4.Summery

We had succeeded to manufacture 304L stainless steels with 7micron grain size by cold work and thermal heat treatment. If grain size is smaller, it may be restrained Cr depletion more at grain boundary after irradiation. However the effect may be saturated. It is suggested that there is a proper size of grain to restrain the Cr depletion after irradiation. Because we think that the full length of grain boundary in a finer grain get longer, and therefore a probability of point defect extinction per unit length of grain boundary decreased.

We hope the proper grain stainless steel is useful for SCC.

References

1)S.M.Bruemmer, E.P.Simonen, P.M.Scott, P.L.Andresen, G.S.Was, J.L.Nelson, J.of Nuclear Materials 274(1999)299-314.

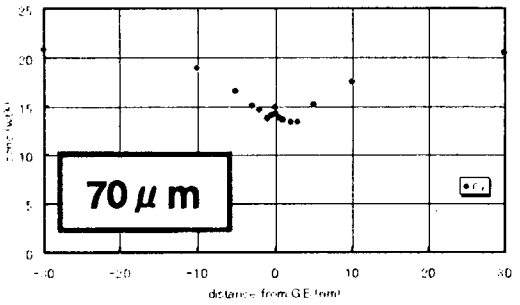

Fig.1 Cr grain boundary segregation in 70micron stainless steel after irradiation.

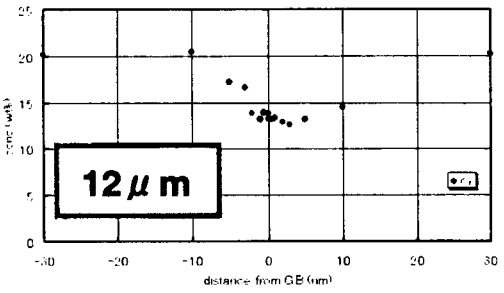

Fig.2 Cr grain boundary segregation in 12micron stainless steel after irradiation.

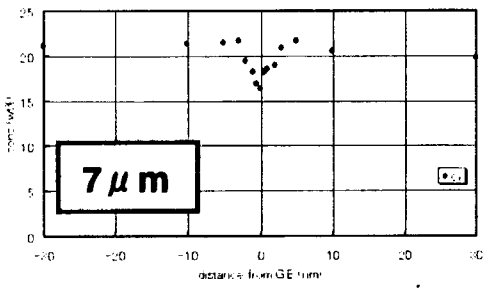

Fig.3 Cr grain boundary segregation in 7micron stainless steel after irradiation.

4.12 In-situ TEM Observation of Defect Clusters and their Fast Diffusion in Copper and Gold under Ion Irradiations

Hiroaki Abe, Tadayasu Tadokoro * and Naoto Sekimura*

Research Center for Nuclear Science and Technology, University of Tokyo, Shirakata Shirane 2-22, Tokai, Naka, Ibaraki 319-1188, Japan
Department of Quantum Engineering and Systems Science, University of Tokyo, Hongo 7-3-1, Bunkyo, Tokyo 113-8656, Japan *

1. Introduction

Irradiation with ions and neutrons produces bunches of atomic displacements in materials, so-called displacement cascades. Recent studies with molecular dynamics (MD) simulations predicted punching of tiny interstitial-type dislocation loops at the periphery of displacement cascade regions in iron and copper. Their activation energies of diffusion were estimated less than 0.1 eV, even smaller than that of single interstitial atoms. Conventional post-irradiation observations with transmission electron microscopy (TEM) are less valid, and no clear evidence has been derived yet. This is because the mobile defects may be active only under irradiation. The purpose of this study is to report first experimental evidence of such highly-mobile defect clusters by in-situ TEM observations under ion irradiation and to clarify the defect-impurity interactions.

2. Experimental procedure

Well-annealed copper and gold disks were electrochemically perforated to achieve electron-transparent thin foils. Irradiation was performed with 100 keV C^+ ions and a current of 2.5 x 10^{13} C/cm^{2}s, or 240 keV Cu^+ ions and 5.1 x 10^{11} Cu/cm^{2}s at temperatures ranging from 573 K to 823 K. Taking into account the irradiation geometry, in which the angle between the ion beam and the sample normal is 30 degrees, projected ranges from the sample surface were estimated by TRIM calculations as 115 and 57 nm for carbon and copper ions, respectively. Since the thickness of the observed regions was typically 50 - 70 nm, roughly 81 - 89 % and 31 - 58 % of incoming carbon and copper ions penetrate the sample, respectively. Microstructural evolution was observed mainly with the weak-beam dark-field technique (**n** = [001], **g** = 200, **g**(4-6**g**)). The image was videotaped without image processors so as to achieve the maximal time resolution.

3. Results and discussion

Tiny defect clusters (less than 10 nm in size) were formed by ion irradiation, whose accumulation rate correlated with irradiation time as shown in figure 1. Majority of them were vacancy- type

clusters including stacking fault tetrahedra. Continuous irradiation annihilated them with lifetime ranging from 0.1 to 3 s, which depends on ion species. In case of copper irradiations we detected the interstitial type which has short lifetime and its annealing behavior is different from the vacancy-type. Some of them transform into highly-mobile clusters only under irradiation, which are presumably sessile-to-glissile transition of interstitial dislocation loops. The clusters occasionally disappeared when they absorb enough vacancies with the typical lifetime of several to tens of thirtieth seconds.

TRIM calculations indicated roughly 20 % or less of irradiated ions remained in the samples. As increasing ion fluence, we observed decrease in evolution rate of defect clusters, longer lifetime of the clusters, and lower mobility of glissile loops. Unless carbon is one of interstitial-type impurities in copper, it substitute or strongly-bonded with vacancies resulting retardation of diffusion of vacancies and even mobile clusters. This behavior strongly related to the carbon onion nucleation.

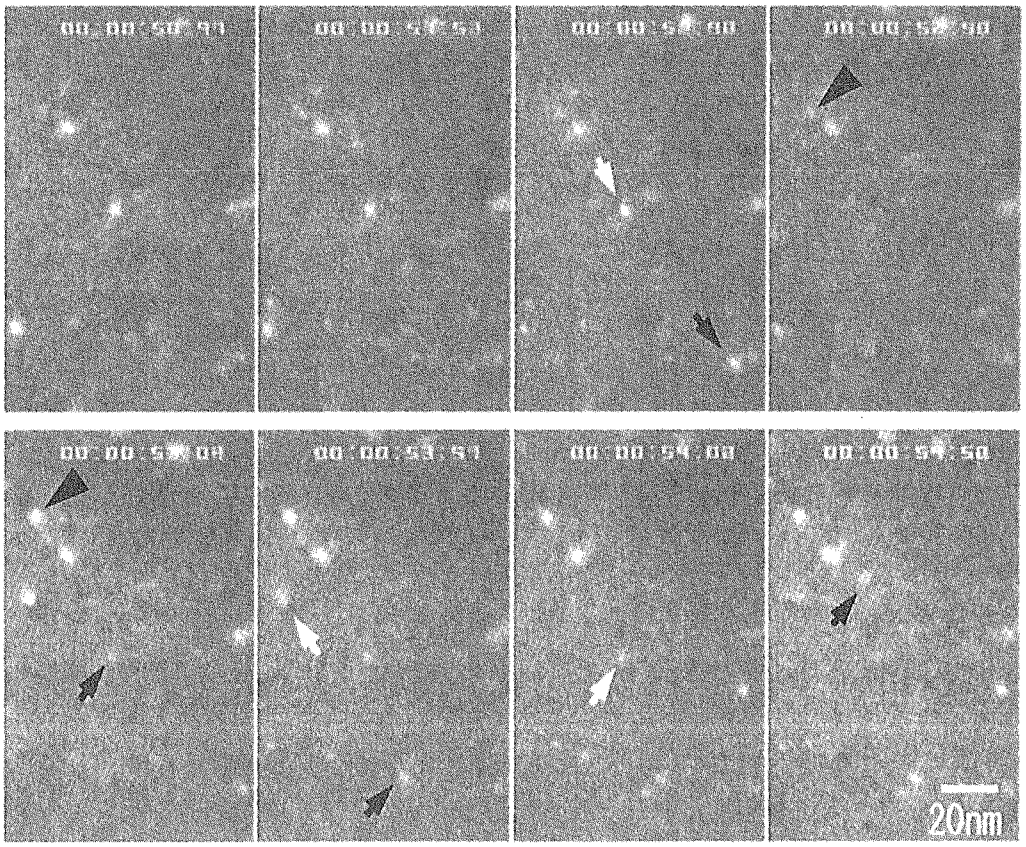

Figure 1. Microstructural evolution in copper irradiated with 100-keV C^+ ions at 573 K. The sequence is captured from videotapes whose time resolution is 1/30 s. The black and white arrows show formation and annihilation of defect clusters, respectively, while the black large arrow show motion of defect clusters.

4.13 *In-situ* Observation of Growth Processes of Titanium Nitride Thin Films by Implantation of Nitrogen Ions

Y. Kasukabe*, Y. Fujino* and S. Yamamoto**
International Student Center / Department of Electronic Engineering, Tohoku University*
Department of Material Development, JAERI**

1.Introduction

Titanium nitrides show metallic, covalent and also ionic properties, which make them interesting from both points of view of fundamental research and technical applications. Their fascinating physical properties are naturally related to the electronic structure. It is well known that the valence d orbitals of titanium (Ti) are more contracted than valence s- and p-orbitals, and split in energy by the bonding interaction with the ligand atoms, nitrogen (N) ones. The bonding interaction gives rise to transformations of the Ti sublattice, and to covalent properties. Because of the covalent properties, the nitrides of Ti are technologically important, for example, as corrosion-resistant coatings on cutting tools and diffusion barriers in silicon microcircuits.[1,2] It has also been revealed that properties of epitaxially-grown TiN films are superior to those of polycrystalline ones. Thus, much interest has been focused on the epitaxial films. Recently, it was reported in the light of *ex-situ* experiments that NaCl-type TiN films were epitaxially grown by the N-implantation into deposited Ti films.[3] However, the nitriding process of epitaxial Ti films, especially of the heated films, by N-implantation has not been sufficiently understood.

The purpose of this work is first to throw light on changes of the crystallographic and electronic structures of heated Ti films by N-implantation, using *in-situ* transmission electron microscopy (TEM) and electron energy loss spectroscopy (EELS), and then to discuss the epitaxial growth mechanism of TiN films.

2.Experimental

Detailed descriptions of the preparation of evaporated-Ti films were presented in the earlier paper.[3] The 100-nm-thick Ti films were deposited by an electron-beam heating method in an ultra-high vacuum onto thermally cleaned NaCl substrates held at room temperature (RT). The ultimate pressure in the working chamber was less than 4×10^{-9} Torr. The Ti films separated from NaCl substrates were heated up to 350℃ at the heating rate of 2℃/min in the 400 kV analytical and high resolution TEM combined with ion accelerators at JAERI-Takasaki.[4] The implantations of N_2^+ ions with 62 keV into the deposited Ti films held at 350℃ were performed in the TEM. The pressure in the TEM specimen chamber was below $1\text{-}2\times10^{-7}$ Torr. According to the Monte Carlo simulation using the TRIM85 code, the projected range of N_2^+ with 62 keV was 55 nm, and thus most of the implanted ions are thought to be retained inside the Ti films. The N- concentrations in Ti films were able to be estimated from the implantation dose measured by a Faraday cage. The maximum dose in this experiment was 5.40×10^{17} ions/cm^2, which corresponded to the N/Ti ratio of 0.954 (the average atomic concentration of N in the Ti film).

3.Results and discussion

Titanium films grown on NaCl (001) surfaces at RT consisted mainly of (03・5)- and ($\bar{2}$1 ・ 0)-oriented hcp-Ti (lattice constants: a=0.296 nm, c=0.471 nm) and (110)-oriented

CaF_2-type TiH_x ($x \cong 1.5$; lattice constant: a=0.441 nm). The growth mechanism of both hcp-Ti and TiH_x agrees with the results of previous paper[3]: Ti films evaporated on NaCl substrates spontaneously absorbed hydrogen (H) from the interior of the NaCl, and then TiH_x grew partially in addition to hcp-Ti. The orientation relationships between the hcp-Ti and the NaCl substrate are (03·5)Ti //(001)NaCl and $[2\bar{1}\cdot 0]$Ti // $[\bar{1}\,10]$ NaCl:
(03·5)-oriented hcp-Ti, and $(\bar{2}1\cdot 0)$Ti// (001)NaCl and [00·1]Ti//[100] NaCl:
$(\bar{2}1\cdot 0)$-oriented hcp-Ti. Judging from the electron diffraction (ED) intensity, the growth of the (03·5)-oriented hcp-Ti is preferred to that of $(\bar{2}1\cdot 0)$-oriented one. On the other hand, the orientation relationship between the TiH_x and NaCl is (110)TiH_x//(001)NaCl and [001]TiH_x// [110]NaCl: (110)-oriented TiH_x.

The deposited Ti film was heated up to 350°C. Figure 1 shows the variation of the lattice expansions of hcp-Ti, TiH_x, with the temperature of films. The lattice expansion is defined as $100(a_T - a_0)/a_0$, where a_0 is a lattice constant of a crystallite in unimplanted films held at RT, and a_T is that in heated films held at a temperature T. There is no noticeable change in ED patterns up to 100 °C. The lattice constant of TiH_x decreases gradually with the rise of temperature from 100°C to 300°C. Furthermore, the ED intensity of TiH_x also decreases with the rise of temperature and there is no ED from TiH_x at 350°C. These results mean that H atoms which constitute TiH_x escape from it with heating films, and are completely dissociated at 350°C. The H-dissociated unstable fcc-Ti sublattice is transformed into hcp-Ti. On the other hand, there is no noticeable change of lattice constants of hcp-Ti up to 350°C.

Nitrogen ions were implanted into the Ti films, which consist of only hcp-Ti, held at 350°C. In the N-implanted Ti film (N/Ti=0.954), there coexisted NaCl-type TiN_y (lattice constants: a=0.424 nm) and a small amount of hcp-Ti (lattice constants: a=0.296 nm, c=0.485 nm). Since reflections of TiN_y, observed up to N/Ti=0.269, were weak and diffuse, lattice constants of TiN_y could be evaluated with $N/Ti \geq 0.381$. The orientation relationships between hcp-Ti and NaCl are the same as those in unimplanted Ti films. Crystallites of TiN_y are formed in the two orientations; (001)-oriented TiN_y: (001) TiN_y //(001)NaCl and [100] TiN_y //[100]NaCl, and (110)-oriented TiN_y: (110)TiN_y//(001)NaCl and [001]TiN_y //[110]NaCl. Figure 2 shows the variation of the lattice expansions of hcp-Ti, TiN_y, with increasing N-dose. The lattice expansion is defined as $100(a_N - a_0)/a_0$, where a_0 is a lattice constant of a crystallite in unimplanted films held at RT, and a_N is a lattice constant of a

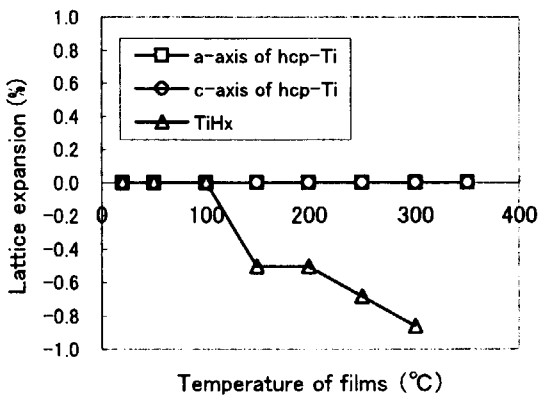

Fig. 1 Variation of lattice expansion with temperature of films

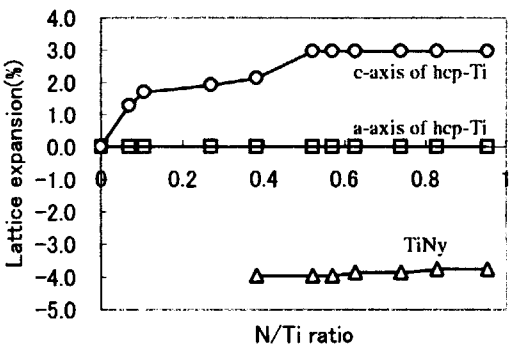

Fig. 2 Variation of lattice expansion with N/Ti ratio.

crystallite in N-implanted films. Since the Ti sublattice of both TiH_x and TiN_y is a fcc lattice, the lattice constant of TiH_x in unimplanted films at RT is taken as a_0 in order to evaluate the lattice expansion of TiN_y. The lattice constant of c-axis of hcp-Ti increases with N-dose. This means that the hcp-Ti lattice is expanded by the occupation of O-sites by N atoms. Therefore, strain due to this lattice expansion can be considered as one of the driving forces for the hcp-fcc transformation of Ti sublattices. On the other hand, the slight increase in the lattice constants of TiN_y with $N/Ti \geq 0.381$ is attributed to the increase in the N concentration of TiN_y. Most of hcp-Ti crystallites in unimplanted Ti films were
(03・5)-oriented hcp-Ti and the formation of (001)-oriented TiN_y was preferred to that of (110)-oriented one. Therefore, it can be considered that (001)-oriented and (110)-oriented TiN_y are epitaxially formed by the transformation of (03・5)-oriented and $(\bar{2}1 \cdot 0)$-oriented hcp-Ti, respectively.

In-situ observation of EELS during heating Ti films elucidated that the variation of the energy of loss peak due to excitation of plasma oscillation of the areas where TiH_x grew in the as-deposited Ti film was different from that of the areas where hcp-Ti grew. Figure. 3 shows the variation of energies of the loss peaks with the temperature of films. The energy loss of ~17.0 eV for hcp-Ti at RT was found to agree well with the theoretical value of ~17.6 eV calculated, assuming that 3d and 4s electrons are all free. For TiH_x at RT in Fig. 3, the energy loss peak of ~19.5 eV is due to excitation of plasma oscillation involving electrons in the valence band consisting of bonding states formed by Ti 3d and H 1s orbitals. The higher loss energy for TiH_x than for hcp-Ti can be considered to reflect the existence of additional valence electrons from H. The loss peak for TiH_x in Fig. 3 shifts to lower loss energy with increasing temperatures of films. This means that the electron density in the valence band consisting of Ti 3d and H 1s bonding states decreases with increasing temperatures of films, due to the release of H from the TiH_x. On the other hand, the loss peaks due to plasmon excitation for the implantation of N into hcp-Ti at 350℃ gradually shifted to higher loss energy with increasing in N-dose. This means that the electron density in the hybridised N2p/Ti3d valence band increased with the dose of N: The number of N atoms bonding to Ti atoms increased with the dose of N. It can be considered that the increase in the electron density of the hybridised band leads to the reinforcement of hardness of TiN_y.

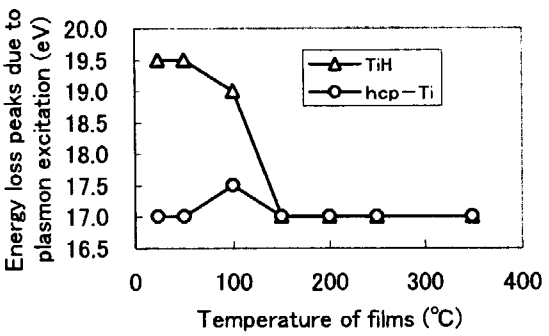

Fig. 3 Variation of the energy of loss peak due to excitation of plasmon with temperature of films.

References

1) G. S. Chen, J. J. Guo, C. K. Lin, Chen-Sheng Hsu, L. C. Yang, and J. S. Fang, J. Vac. Sci. & Technol. **A20** (2002) 479.
2) J. E. Sundgren, Thin Solid Films **128** (1895) 21.
3) Y. Kasukabe, N. Saito, M. Suzuki, Y. Yamada, Y. Fujino, S. Nagata, M. Kishimoto, and S. Yamaguchi, J. Vac. Sci. & Technol. **A16** (1998) 482.
4) H. Abe, H. Naramoto, K. Hojou, and S. Furuno, The TEM-Accelerators Facility at JAERI-Takasaki and its Application to Materials Science, JAERI-Research **96-047** (1996) 1.

4.14 Preparation of Metal-doped TiO_2 Films by Pulsed Laser Deposition

S. Yamamoto*, A. Miyashita*, Y. Choi*, T. Umebayashi*, S. Tanaka* and H. Naramoto**

Department of Material Development, JAERI*

Advanced Science Research Center, JAERI**

1. Introduction

Titanium dioxide (TiO_2) doped with several kinds of transition metals has been studied for improving photocatalysis or modification of optical, electrical and magnetic properties using ion implantation and several deposition techniques. Especially in anatase TiO_2 films, the influence of metal doping on the photocatalytic properties has not been clarified because anatase has been difficult to realize the metastable phase. Therefore the synthesis of high quality metal-doped epitaxial TiO_2 films has been required for the reliable characterization of photocatalytic properties. In the present study, we explore the preparation conditions of epitaxial anatase and rutile TiO_2 films doped with Cr, Nb, Ta and W by pulsed laser deposition (PLD). The annealing effect on the crystal quality, concentration of doped metal and orientation relationships have been studied using Rutherford backscattering spectroscopy (RBS) with channeling and X-ray diffraction.

2. Experimental

Epitaxial TiO_2 films were grown on $SrTiO_3$ (001) and α-Al_2O_3 (0001) substrates by PLD using a KrF excimer laser (wavelength: 248 nm, repetitionrate: 10 Hz). The laser beam was incident on a single crystal TiO_2 (rutile) and a metal target, alternately. Oxygen gas was flowed into a growth chamber through a mass flow meter to achieve the pressure about 4.7 Pa. The temperature of substrates during the deposition was 500°C. RBS/channeling analysis using a 3 MV single-stage-accelerator at JAERI/Takasaki was employed to characterize the epitaxial films. The analyzing 2.0 MeV $^4He^+$ ions were incident and backscattered particles were detected at 165° scattering angle.

3. Results and discussion

The epitaxial anatase TiO_2 (001) films were obtained on $SrTiO_3$ (001) substrates. Also the epitaxial rutile TiO_2 (001) films were grown on α-Al_2O_3 (0001) substrates. In order to study the stability of anatase TiO_2 (001) films for post-deposition annealing treatment, the transformation temperature from anatase to rutile structure was evaluated. Deposited anatase TiO_2 (001) films on $SrTiO_3$ (001) substrates were annealed between 800°C and 1100°C in air for 1h. Figure 1 shows the X-ray diffraction patterns from the anatase TiO_2 (001) films on the $SrTiO_3$ (001) substrate, (a) annealed at 1000°C in air for 1h and (b) annealed at 1100°C in air for 1h, respectively. XRD analyses show no transformation to rutile structure up to 1000 °C. After annealing at 1100°C, the changing from the anatase TiO_2 (001) to the (110)-oriented rutile is observed. In general, the anatase-rutile transformation has been observed between 700°C and 900°C for polycrystalline films mixed with anatase and rutile phases. In this result shows the higher transformation temperature from anatase to

rutile structure. The thermal stability of high quality anatase TiO_2 (001) films is probably affected the substrates with small lattice mismatch.

Figure 2 illustrates the 2.0 MeV $^4He^+$ RBS spectra from the W doped anatase and rutile TiO_2 films on the $SrTiO_3$(001) and the α-Al_2O_3 (0001) substrates. These films were simultaneously deposited at 500°C up to 150 nm thick. The growth of anatase TiO_2(001) and rutile TiO_2(100) films were confirmed by XRD analysis. The concentration of W is estimated to be 0.4 at. % from RBS. In Fig. 2 (a), the huge reduction of Ti (1.37 MeV ~ 1.45 MeV) and W components of the TiO_2 film in the aligned spectrum compared with the random one suggests the doped W atoms incorporate into the substitutional sites in the anantase TiO_2 lattice. In Fig. 2 (b), the respective minimum yields in the TiO_2 <100> aligned spectrum is 2.9 % for Ti and 2.8 % for W components, which suggests that doped W atoms are incorporated into the substitutional sites in the rutile TiO_2 lattice almost completely. The similar results were obtained in Cr-, Nb- and Ta-doped anantase TiO_2 (001) and rutile TiO_2 (100) films with a doping level up to 1.5 at. %. RBS/channeling analysis reveals that Cr-, Nb- and Ta-doped atoms are incorporated substitutionally into the anatae and rutile TiO_2 lattice sites.

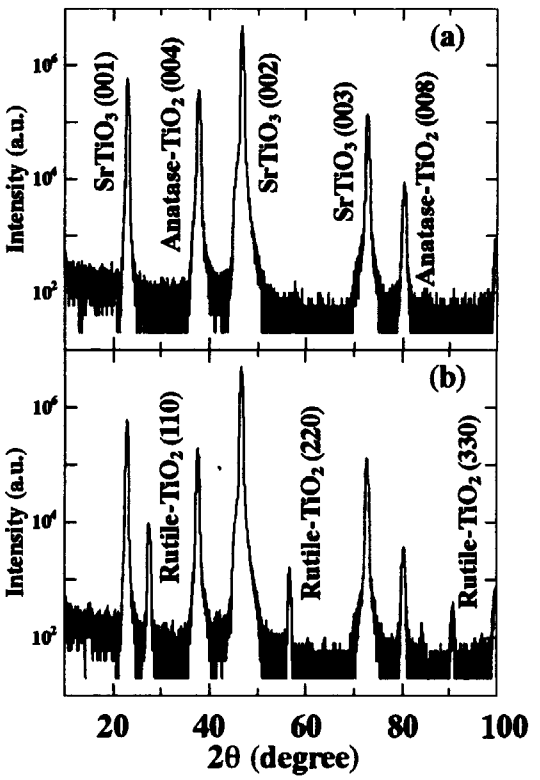

Fig. 1 X-ray diffraction patterns for anatase TiO_2 (001) films on the $SrTiO_3$ (001) substrate annealed at different temperatures (a) 1000°C and (b) 1100°C in air for 1h.

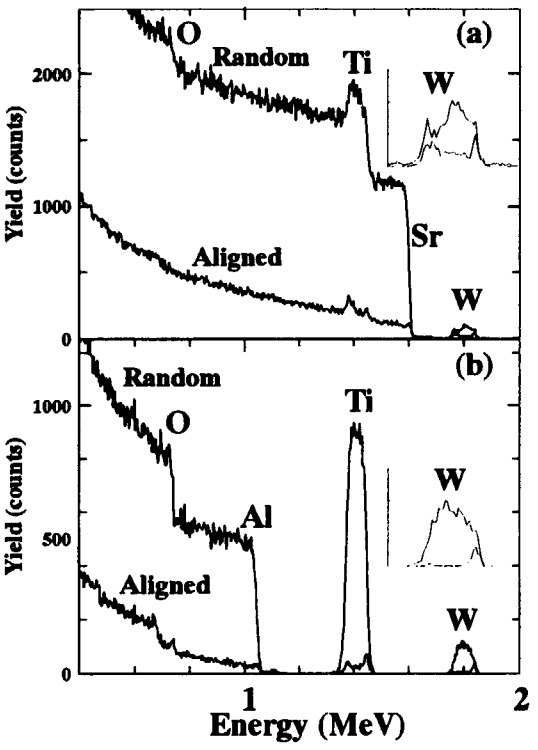

Fig. 2 2.0 MeV $^4He^+$ RBS/channeling spectra for (a) W doped anatase TiO_2(001) film on $SrTiO_3$ (001) substrate and (b) W doped rutile TiO_2 (100) film on α-Al_2O_3 (0001) substrate.

4.15 Micro-PIXE Analysis of Cobalt Sorbed by Lichen Biomass

T. Ohnuki*, F. Sakamoto**, N. Kozai***, T. Sakai****, T. Kamiya*****, M. Oikawa**** and T. Sato****

Advanced Science Research Center, JAERI*, Department of Research Reactor, JAERI**, Department of Environmental Science, JAERI***, Advanced Radiation Technology Center, JAERI****, Department of Material Development, JAERI*****

1. Introduction

The migration of radionuclides in terrestrial environment must be studied to estimate the impact of radioactive waste disposal to biosphere. Radionuclides are sorbed by inorganic and organic compounds during migration in terrestrial environment. Many researchers have studied the sorption of radionuclides by inorganic compounds. However, there is little study to examine the sorption by organic compounds in terrestrial environment. Microbial surfaces function as cation-binding sites to sorb actinides[1,2]. These suggest that sorption of radionuclides by microbes affects migration behavior of radionuclides in environment.

Lichens occur worldwide[3] and the ability for lichens to accumulate metals has led to their use in monitoring radionuclides fall-out as arising from accidents e.g. Chernobyl[4] and from nuclear weapons tests[5]. However, these studies have not identified accumulation mechanisms.

Lichens are defined as symbiotic organisms composed of mycobiont and photobiont[3]. Some lichen have lower and upper cortex and some interesting metabolites, i.e. melanin in lower cortex. This suggests that the accumulated radionuclides are localized in lichen. Distribution of radionuclides in lichen should be examined to elucidate the sorption mechanism by lichen.

Cobalt is contained in low-level radioactive wastes. We have applied the μ-PIXE technique to analyze distributions of the sorbed Co in lichen.

2. Experimental

Discs 1 cm diam., weighing *ca* 9 mg were cut from the outer margin of *Parmotrema tinctorum* (Nyl.) Hale collected near Hitachi Seaside Park, Ibaraki Prefecture, Japan. We followed the pretreatment method of lichen samples suggested by the literature[6]. Samples were air dried at 30°C prior to weighing and wetted thoroughly with deionized water immediately prior to experimental incubation to minimize osmotic concentration of Co in lichen biomass.

Moistened samples were incubated in 25 ml 0.1 M NaCl solutions containing 5.0×10^{-4} mole/l $CoCl_2$ solution for up to 96 hours at pH values from 3 to 5 by addition of concentrated NaOH and HCl solutions. The ionic strength of the Co solution was adjusted to 0.1 M with NaCl. Sorption experiments were performed at room temperature. At predetermined time interval, a 1 ml supernatant was sampled and the Co concentration was measured by ICP-AES. Solution pH was measured by a TOA HM-30S pH meter with a combined electrode of TOA GS-5015C.

The washed lichen samples were air dried in sterile polypropylene centrifuge tubes

overnight, followed by desiccation in an oven at ca. 30 °C for 2 hours. Samples were cut to obtain thin section by edge of razor. Elemental distributions in thin section samples were examined using in-air μ-PIXE technique. A proton beam with the energy of 2.6 MeV from the single-ended machine was used for in-air μ-PIXE analysis developed at TIARA facility in Japan Atomic Energy Research Institute[7]. The beam spot was approximately 1 μm in diameter. The maximum scanning area for the μ-PIXE analysis system was 740 x 850 μm^2 [8].

3. Results and discussion

Co sorption by *P. tinctorum* reached steady state within 1 day (2 replicates). This indicates that the sorption rate of Co by *P. tinctorum* is very fast. Co uptake by lichen biomass was averaged around 27 wt% and was independent of solution pH between 3 and 5. Solution pH varied during the incubation period from initial pHs of 3, 4 and 5 falling to 2.9, 3.5 and 3.6 respectively.

Sorbed Co was distributed in upper and lower cortex, in medullary and algal layers of *P. tinctorum*, evident by μ-PIXE (Fig. 1). K was distributed in almost all regions of *P. tinctorum* in the cross section (Fig. 1). Fe was not distributed in lower cortex, but in upper cortex, algal layer and medullary layer (Fig. 1). The distribution of P (Fig. 1) indicates that P was distributed in upper and lower cortex. These elemental distributions show that the distribution of Co does not correspond to those of K, Fe, and P. Note that drying and desiccation of the lichen sample probably does not cause loss of the non-volatile elements of Co, K, P, and Fe.

The PIXE image of the distribution of Co (Fig. 1) indicates that Co density differed among lower cortex, medullary layer and algal layer. Highest density in the two-dimensional distribution of Co was obtained in the lower surface. The density of Co in algal layer was lower than those in medullary layer and both surfaces indicating that the density of Co in the lichen ordered lower surface > upper surface, medullary layer > algal layer. Low density of Co in algal layer (Fig. 1) shows direct evidence that mycobiont in lichen sequesters inorganic toxic metals from photobiont.

Time dependent Co peak intensities of the PIXE spectra of the lower cortex, medullary layer and algal layer (Fig. 2) indicate that Co density in the lower cortex and medullary layer increased up to 48 hours, followed by the decrease with time. The density of Co in the algal layer increased with time in the present experimental duration. These show that Co sorbed by the upper and lower cortexes and medullary layer is retarded to be transported into algal layer.

References

1) R.J.C. McLean, D. Fortin, D.A. Brown, Can. J. Microbiol., 42 (1996) 392-400.
2) B. Volesky, Z.R. Holan, Biotechnol. Prog., 11 (1995) 235-250.
3) T. H. Nash In:. Lichen biology, ed. Nash TH pp. 136-153, (1996).
4) J. Paatero, T. Jaakkola, S. Kulmala, J. Environ. Radioactivity 38, (1998) 223-247.
5) W.G. Hansen, Health Phys. 22 (1972) 39-42.
6) J. R. Haas, E. H., Bailey, & O.W. Purvis, American Mineralogist 83(1998) 1494-1502.
7) T.Kamiya, T.Suda and R.Tanaka, Nuclear Inst. Method B 118 (1996) 447-450.
8) T. Sakai, et al., Biological Trace Element Research Vols. 71-72 (1999)77-82.

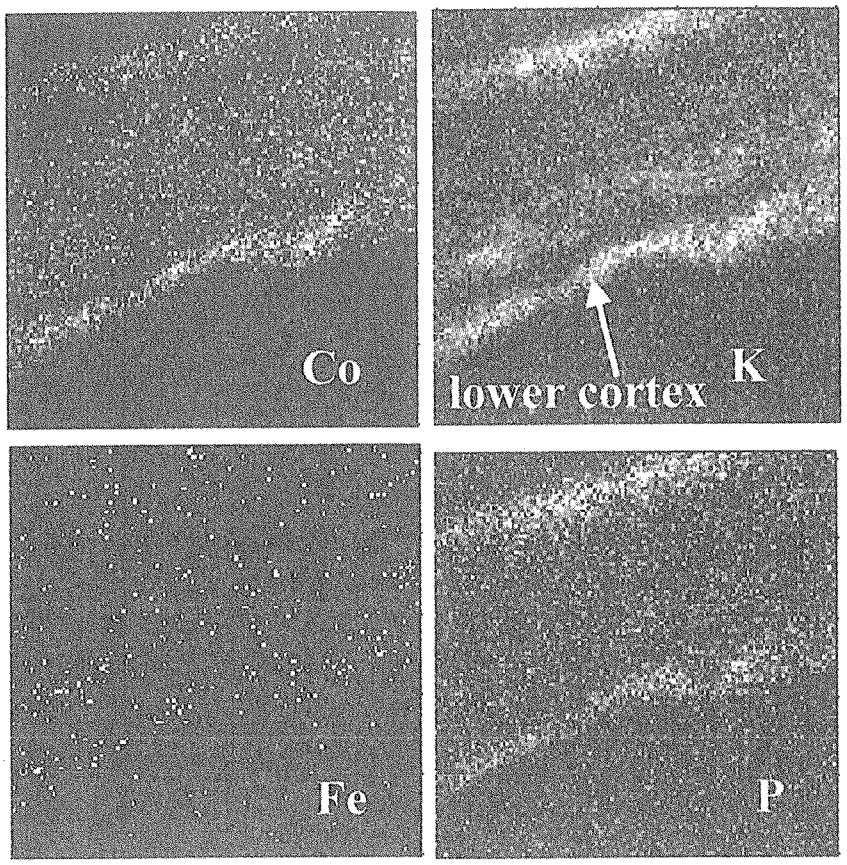

Fig. 1 PIXE images of Co, K, Fe and P distributions on the cross section of *P. tinctrum*. Brighter area shows higher elemental concentration in PIXE image. The scanning area in μ-PIXE analysis is 22x23 μm^2.

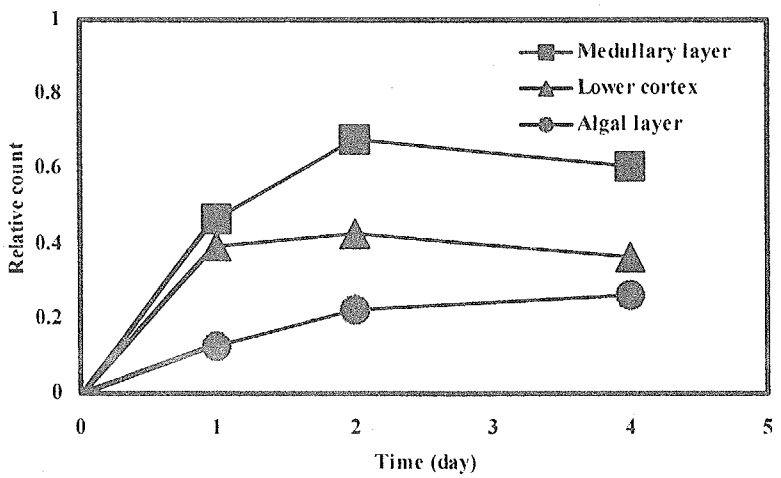

Fig. 2 Time dependent peak areas of Co in the PIXE spectra in the region of lower cortex, medullary layer and algal layer. The PIXE spectra were normalized to the peak intensity of S.

4.16 Energy spectra of electrons emitted from solids bombarded by MeV carbon clusters

H. Kudo*, W. Iwazaki*, T. Suguri*, Y. Saitoh**, S. Yamamoto***, K. Narumi****, and H. Naramoto****
Institute of Applied Physics, Univ. of Tsukuba*
Advanced Radiation Technology Center, JAERI**
Department of Material Development, JAERI***
Advanced Science Research Center, JAERI****

1. Introduction

An accelerated atom cluster induces correlated atomic impacts when it is incident on a solid target. This causes pronounced radiation effects different from those induced by impact of a single ion or a small molecule. Actually, fast cluster ions in the MeV/atom velocity range give rise to nonlinear radiation effects on solid targets with respect to the number of atoms in the cluster n. These radiation effects by fast atom clusters have been reviewed recently by Jacquet and Beyec,[1] and by Parilis.[2]

The nonlinearity has so far been reported for energy loss (stopping power), sputtering, lattice damage, secondary ion emission, and total electron emission yield. It is notable that the total electron emission yield per atom, which corresponds to the emission current, depends on n weaker than linearly. This is contrast to the radiation effects accompanying atomic displacements, i.e., sputtering and lattice damage, for which n dependence is stronger than linear. It has been accepted that the cluster-induced phenomena associated with nuclear stopping are "superlinear", while those with electronic stopping are "sublinear".

The aim of the present work is to investigate the cluster effects by energy analysis of the cluster-induced electrons. This would provide knowledge about the electronic processes in the cluster impact phenomena. Such a basic approach will also be of practical importance for future applications of fast-cluster impact to material processing, for example.

2. Experiment

The 0.5MeV/atom C_n^+ (n =1, 4, 8) beams obtained from the 3MV tandem accelerator at JAERI-Takasaki were incident on the samples of Nb evaporated on alumina substrate, highly-oriented pyrolytic graphite (HOPG) with a cleaved (0001) surface, and chemically cleaned Si(100). The secondary electrons were measured at 135° with respect to the beam direction using a 45° parallel-plate electrostatic spectrometer of the double-deflection type, as shown in Fig. 1. The electron measurements were carried out at room temperature under a pressure of ~6×10^{-6} Pa.

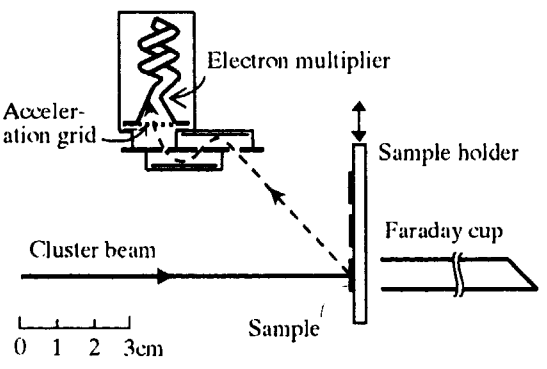

Fig. 1 Experimental setup.

The beam current has been monitored using a Faraday cup, shown in Fig. 1, while moving the sample holder away from the beam path. In most cases, the electrometer connected to the samples indicated negative values for incidence of C_8^+, indicating appreciable emission of positive ions from the bombarded surface.[3)]

The existence of contaminant atoms on the surfaces is anticipated under the present vacuum conditions. This should slightly change the transmission of outgoing electrons across the surface, but should not affect the n dependence of the electron energy spectra, which is of primary interest in the present studies.

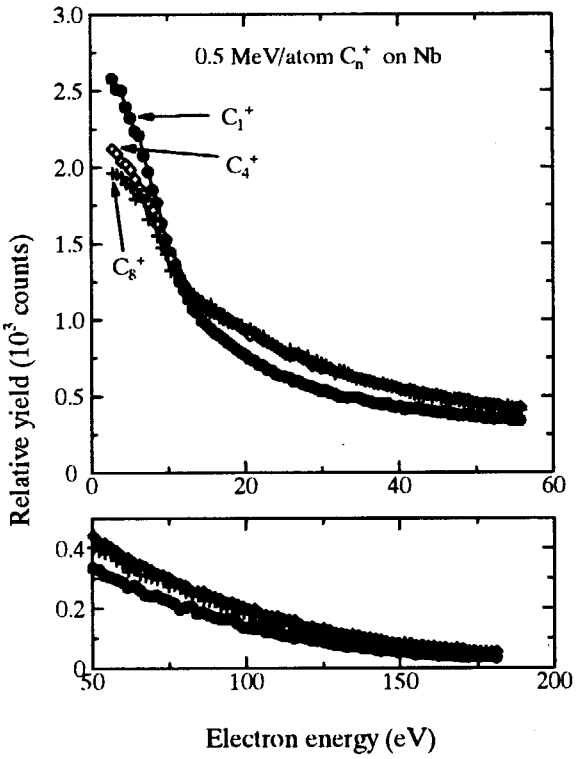

Fig. 2 Energy spectra of electrons emitted from Nb bombarded by 0.5 MeV/atom C_1^+, C_4^+, and C_8^+.

3. Results and discussion

The energy spectra of electrons presented here are raw data, i.e., the yield in the vertical axis is the number of electron signals counted. Accordingly, the spectra include no correction for the energy acceptance of the spectrometer, which is proportional to the electron energy, nor for the energy dependence of the efficiency of the electron multiplier. This is of minor importance because the measured electron yields for different experimental conditions are compared always at the same electron energy.

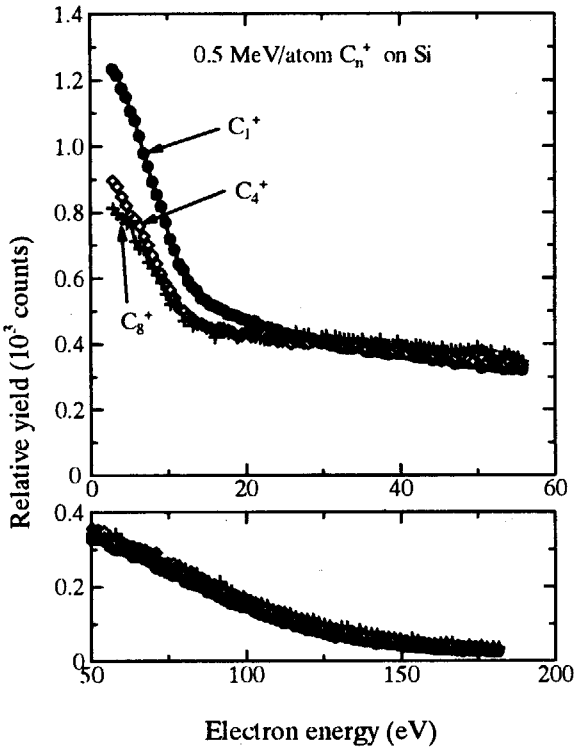

Fig. 3 Energy spectra of electrons emitted from Si bombarded by 0.5 MeV/atom C_1^+, C_4^+, and C_8^+.

Figures 2-4 show energy spectra of the cluster-induced electrons emitted from Nb, Si, and HOPG, respectively. The measured electron yields for the same number of incident C_n^+ (n =1, 4, 8) were divided by n so that the spectra per projectile C atom can be compared each other. We see from Figs. 2–4 that the electron yield for C_4^+ and C_8^+ at energies lower than ~10 eV is suppressed by a factor of ~0.8, compared with that for C_1^+. At higher energies, on the contrary, the electron yield for the cluster ions is slightly

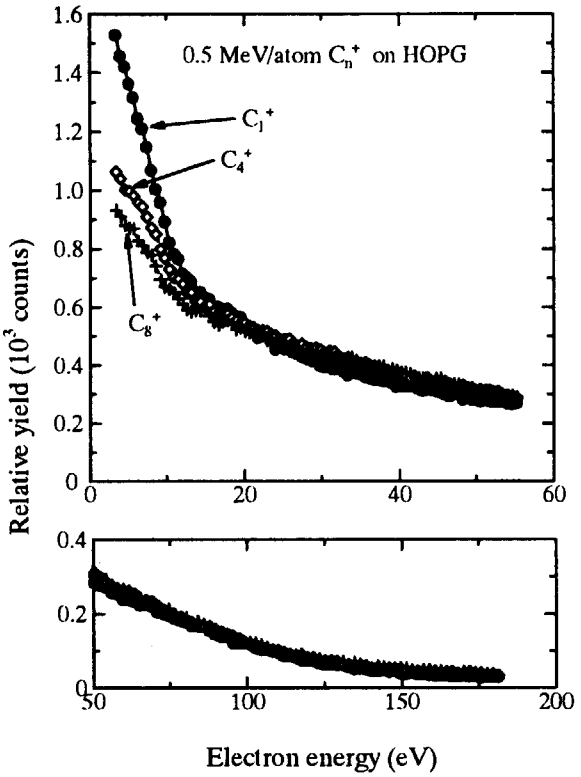

Fig. 4 Energy spectra of electrons emitted from HOPG bombarded by 0.5 MeV/atom C_1^+, C_4^+, and C_8^+.

enhanced.

The sublinear effect at energies lower than 10 eV is consistent with the reduction of the total electron yield, reported previously by the Orsay group. The sublinear behavior of the low-energy yield cannot be accounted for quantitatively in terms of the stopping powers for the cluster ions. Indeed, recent calculations by Kaneko[4] concluded only small difference (typically a factor of 0.95-0.97) between the stopping powers for C_1^+ and C_8^+ in the present velocity range.

The superlinear effect at higher electron energies has been found first in the present work. The similar effects have also been found for 1.6 MeV/atom Au_3^+ relative to the case for Au_1^+. The superlinear effect is probably due to the multi-stage scattering of the target electrons by the cluster ions, which should shift the energy distribution of the electrons that are produced by the single(-stage) scattering to the high-energy side. This process might be investigated by the binary-encounter model of ion-induced ionization of orbital electrons in a target atom,[5] which demonstrate a higher-energy transfer process to a moving electron than to an electron at rest. Detailed analysis is now under way to study the atomic process that is essentially responsible for the cluster-induced electron emission.

References

1) D. Jacquet, Y. Le Beyec, Nucl. Instrum. Methods B 193 (2002) 227.
2) E. Parilis, Nucl. Instrum. Methods B 193 (2002) 240.
3) K. Hirata, Y. Saitoh, K. Narumi, Y. Kobayashi, Appl. Phys. Lett. 81 (2002) 3669.
4) T. Kaneko, Phys. Rev. A66 (2002) 052901.
5) M. E. Rudd, Y.-K. Kim, D. H. Madison, T. J. Gay, Rev. Mod. Phys. 64 (1992) 441.

4.17 Amorphization of Carbon Materials Studied by X-ray Photoelectron Spectroscopy

K. Takahiro*, R. Ookawa*, T. Morikawa*, K. Kawatsura*, S. Yamamoto**, K. Narumi***, H. Naramoto***

Department of Chemistry and Materials Technology, Kyoto Institute of Technology*

Department of Material Development, JAERI**

Advanced Science Research Center, JAERI***

1. Introduction

Ion implantation into carbon materials, such as graphite, diamond, C_{60} and glassy carbon, results in changing their chemical and physical properties. Crystalline-to-amorphous transformation called "amorphization" causes a drastic change in their properties[1]. Amorphization is one of the most important phenomena in the fields of ion beam modification of carbons.

Raman spectroscopy is a standard tool for the structural characterization of ion-implanted carbons. In case of ion-implanted graphite, for example, the structural changes are well characterized by the broadening of two prominent lines in a Raman spectrum, including the Raman active E_{2g} line at ~1580 cm^{-1} (referred to as *G* band) and the disorder induced line at ~1355 cm^{-1} (referred to as *D* band)[2]. However, Raman spectroscopy becomes insensitive to the changes in the structure of carbons after amorphization because the Raman spectrum exhibits a broad band in the range of 900 -1800 cm^{-1} (ref. 2).

In the carbon materials, the environment around a carbon atom affects its electronic structure on core-level as well as valence band. Therefore, the examination of the electronic structure can provide information about the structure of carbons. X-ray photoelectron spectroscopy (XPS) is widely used to study the electronic structure, and can be applied to the structural characterization of carbons[3-5].

In our previous work for deuteron-irradiated C_{60} films, we found that the shape of a C 1s XPS spectrum became asymmetric as the deuteron dose increased[6]. We speculated that the asymmetry came from the growth of a graphitic layer in the amorphized C_{60} films according to the result from Raman analysis. However, the origin of the asymmetry remains unclear. In the present work, amorphization processes have been investigated by using XPS and Raman spectroscopy for various carbons, including highly oriented pyrolytic graphite (HOPG), isotropic graphite, glassy carbon (GC) and C_{60}, to clarify the origin of the asymmetry appeared on the C 1s line.

2. Experimental procedure

HOPG, manufactured by Molecular Device Tools for Nano Technology, Russia, was cleavaged with a Scotch Tape just before XPS measurements. Isotropic graphite (ISO-880U grade) was supplied from Toyo Tanso, Japan. Glassy carbon (Tokai Carbon, Japan; GC-30 grade) was mechanically polished to mirror surface with 1 μm diamond slurry on a cloth lap. C_{60} films were prepared onto Si substrates by vacuum evaporation of C_{60} powders of 99.98 % purity, manufactured by Term, USA.

XPS analysis using monochromatized Al Kα radiation was performed with JEOL 9010. XPS is sensitive to only near surface of carbons. The carbon samples were irradiated with 1 keV Ar ions produced by a sputter-etching gun, which is equipped with JEOL 9010. The XPS analysis can be done without breaking vacuum after ion irradiation.

Raman spectroscopy was applied to characterize the ion-irradiated carbons. Higher-energy irradiation is needed because the information depth in Raman analysis for carbon is approximately 100 nm. The carbon samples were also irradiated with 100 keV Ar ions using the ion implanter at TIARA so that radiation damage distributed almost uniformly at depths of 0-100 nm in the carbons.

3. Results and discussion

Figure 1 shows C 1s core-level XPS spectra for HOPG irradiated with 1 keV Ar ions at various doses. The peak position of the C 1s line shifts from 284.3 eV to 284.2 eV after irradiation. Significantly, the line width becomes larger as the irradiation dose increases. In addition, the shape of the C 1s line is found to be asymmetric.

In Fig. 2, the half width at half maximum (HWHM) values of the C 1s line for HOPG, ISO-880U, GC-30 and C_{60}/Si are plotted as a function of irradiation dose. In all kinds of samples examined, the HWHM values for the low-energy side, referred to as "HWHM-low", increases abruptly from ~0.3 eV to ~0.5 eV with irradiation at a dose of 0.05×10^{16} cm^{-2}. Above that dose, the HWHM values are almost constant (~0.5 eV) against the dose. In contrast, the HWHM values for the high-energy side, "HWHM-high", become larger gradually with the dose and reach 0.8~0.9 eV, depending on the sample, at a dose of 0.5×10^{16} cm^{-2}. The HWHM-high at 1×10^{16} cm^{-2} for HOPG and ISO-880U is approximately 0.8 eV, significantly smaller than that for GC and C_{60}/Si (~0.9 eV), indicating the difference in the amorphized structure between the former and latter samples even when irradiated up to 1×10^{16} cm^{-2}, corresponding to 3 dpa. For all the samples, the difference between the HWHM-low and HWHM-high, that is, the asymmetry of the C 1s line, increases with increasing the dose. We shall discuss evolution of the asymmetry accompanied by ion irradiation.

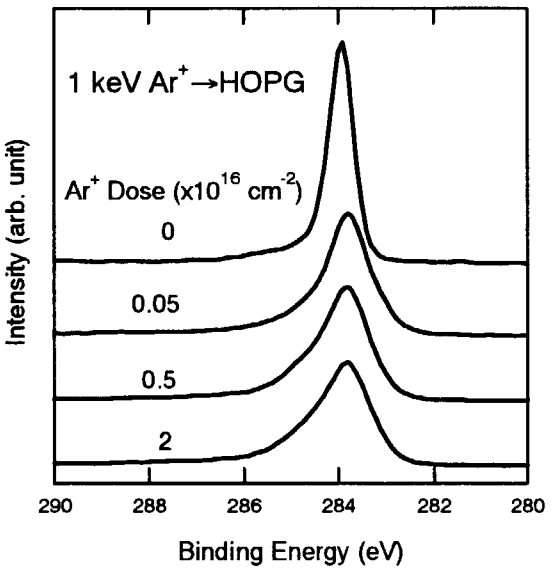

Fig. 1 C 1s XPS spectra for HOPG irradiated with 1 keV Ar ions at various doses.

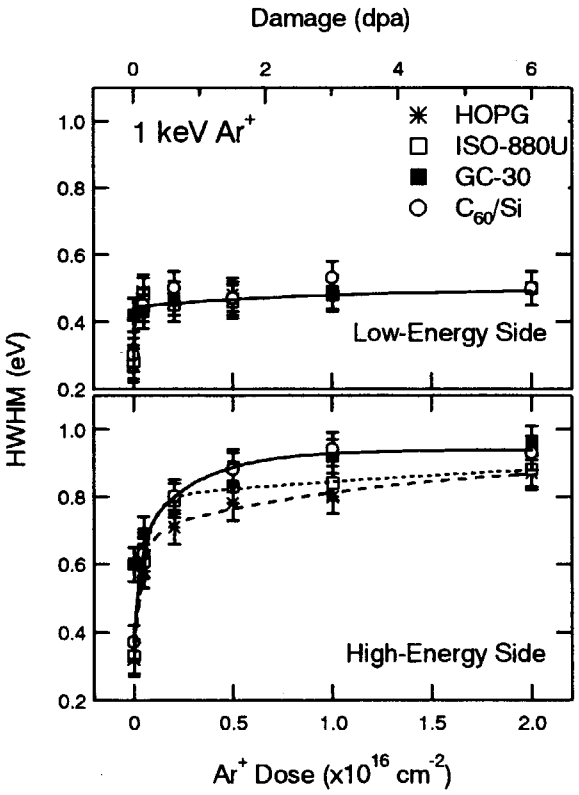

Fig. 2 HWHM values of C 1s XPS spectra for HOPG, ISO-880U, GC-30 and C_{60}/Si as a function of 1 keV Ar^+ dose and accumulated damage in the unit of dpa.

Cheung[3] pointed out that the asymmetry of the C 1s line comes from the delocalization of π-electron on a graphitic component in an amorphous carbon. Therefore, the increased asymmetry indicates the increased size of a graphitic domain. This is referred to as "size effect" hereafter. For graphitic materials, however, ion irradiation should lead to the reduction in size of a graphitic domain. Information about the size of a graphitic layer in an ion-irradiated carbon can be obtained from a Raman spectrum because the peak height ratio of the *D* band to *G* band, I_D/I_G, in the spectrum depends on the size of a graphitic layer[7,8].

Figure 3 shows irradiation dose dependence of the peak height ratio I_D/I_G in Raman spectra for HOPG and C_{60}/Si. In case of HOPG, the I_D/I_G increases as the dose increases up to 4×10^{14} cm^{-2}, corresponding to 0.25 dpa, indicating that the size of a graphitic layer becomes smaller[7,8] as has been expected. On the other hand, the I_D/I_G for C_{60}/Si decreases with the dose, suggesting the increase in size of a graphitic layer.

According to the findings by Cheung[3], the shape of the C 1s line might be related to the size effect. However, this is not the case for HOPG as described above. Thus, evolution of the asymmetry of the C 1s line shown in Fig. 2 dose not relate to the increase in the size of a graphitic layer, but relates to structural disorders, such as bond angle disorder, produced by ion irradiation. In conclusion, the origin of the asymmetry of the C 1s line for ion-irradiated carbons has not been well understood yet, but we can exclude the size effect from the origin of the asymmetry.

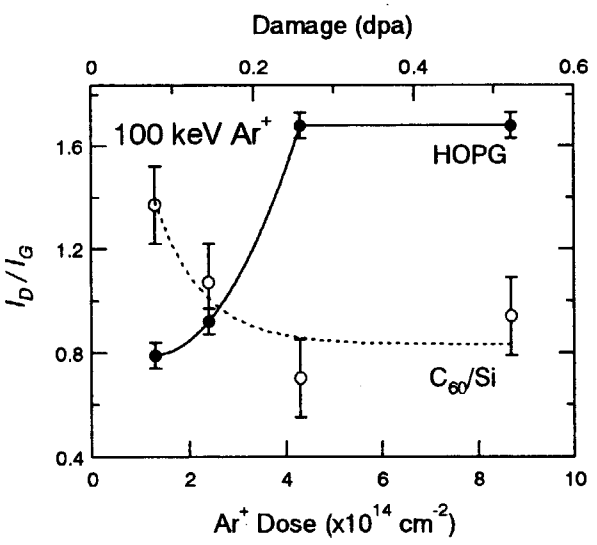

Fig. 3 Intensity ratio I_D/I_G in Raman spectra for HOPG and C_{60}/Si as a function of Ar^+ dose and accumulated damage in the unit of dpa.

References

1) M. S. Dresselhaus and R. Kalish, Ion Implantation in Diamond, Graphite and Related Materials, Springer-Verlag, Berlin (1992), and references therein.
2) B. S. Elman, M. S. Dresselhaus, G. Dresselhaus, E. W. Maby and H. Mazurek, Phys. Rev. B 24 (1981) 1027.
3) T. T. P. Cheung, J. Appl. Phys. 53 (1982) 6857.
4) M. Ramm, M. Ata, K. W. Brzezinka, T. Gross and W. Unger, Thin Solid Film 354 (1999) 106.
5) D. -Q. Yang and E. Sacher, Surf. Sci. 504 (2002) 125.
6) R. Ookawa, K. Takahiro, K. Kawatsura, F. Nishiyama, S. Yamamoto and H. Naramoto, Nucl. Instr. Meth. B 206 (2003) 175.
7) F. Tuinstra and J. L. Koening, J. Chem. Phys. 53 (1970) 1126.
8) A. C. Ferrari and J. Robertson, Phys. Rev. B 61 (2000) 14095.

4.18 Effects of Ion Irradiation on Surface Modification of Hydrogen Materials

H. Abe*, H. Uchida**, Y. Azuma***, H. Itoh****and T. Kamiya*
Department of Material Development, JAERI*
Faculty of Engineering, Tokai University**
Graduate school of Engineering, Tokai University***
Preparations Office for JAERI-JNC Integration****

1. Introduction

The effect of ion irradiation on the rate of electrochemical hydrogen absorption by Pd and Mm (misch metal)-Ni based hydrogen storage alloy, which used as a negative electrode of the nickel-metal hydride battery, was investigated. Surface modifications are crucial to improve the reactivity of hydrogen with metals because the dissociation of the H_2 molecules in the gas phase or the dissociation of the H_2O molecules in electrochemical process is the first step of the overall reaction of hydrogen absorption by metals[1]. The dissociation of the H_2 or H_2O molecule becomes markedly influenced by surface conditions of a material. It is indispensable to improve the hydrogen absorptivity in the material. Regarding the hydrogen storage in metals, it was reported that the hydrogen reaction rate depend strongly on the surface state of metals. For surface modification of materials, since low energy ion irradiation, i.e., ion implantation is known to be a quite useful method. These facts give the possibility that the hydrogen absorptivity in Pd and Mm are improved by surface modification due to ion irradiation[2, 3]. In order to examine the effects of ion irradiation on the hydrogen absorption process in Pd and Mm, we have performed proton (H^+) and argon ion (Ar^+) irradiation into the materials. Hydrogen absorption in ion irradiated Pd and Mm were also evaluated. Based on the obtained results, we discuss the correlation between ion irradiation and hydrogen absorption in Pd and Mm.

2. Experimental

The samples used in this study were Pd sheets (99.99 % purity) with a size of 15 x 15 x 0.1 mm^3 and $MmNi_{3.48}Co_{0.73}Mm_{0.45}Al_{0.34}$ (Mm = $La_{0.35}Ce_{0.65}$) pellet with a size of 13 mmϕ with a thickness 2 mm. Regarding Pd, prior to irradiation, all samples were annealed at 1173 K in a flowing pure N_2 gas (99.9998 % purity). Ion irradiation was made with Ar^+ in an acceleration energy of 350 keV, dose range from 1 x 10^{14} to 1 x 10^{17} /cm^2. In case of Mm sample, ion irradiation was made with H^+ and Ar^+ in an acceleration energy of 350 keV, dose range from 1 x 10^{14} to 1 x 10^{16} /cm^2 respectively.

Hydrogen absorption measurements were

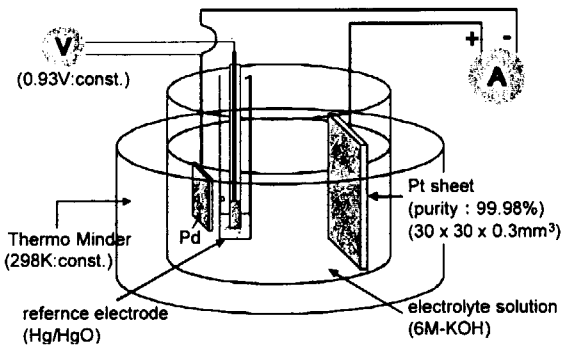

Fig. 1 An electrolytic cell with palladium/misch metal cathode apparatus

performed for the irradiated and unirradiated samples. An electrolytic cell with palladium/mische metal cathode apparatus, which is shown in Fig.1, was used to characterize hydrogen storage of the samples[4, 5]. The rate of hydrogen absorption of a sample was measured electrochemically in a 6M-KOH using an open cell as the chane of current density mA (g-alloy)$^{-1}$ at a constant voltage -0.93 V and 298 K, the H concentration absorbed by the negative electrode was calculated.

3. Results and discussion

3.1 Pd-H system

Figure 2 shows the results of hydrogen reaction rate in the non-irraidated, 350 keV argon ion irradiated Pd. Typical electrochemical hydriding curves, non-irradiated, dose range from 1 x 10^{14} to 1 x 10^{17} /cm^2 are measured at 298 K. The hydrogen reaction rate can be determined from a temporal change in the [H]/[Pd] value. The value of non-irradiated, 1 x 10^{14}, 1 x 10^{15}, 1 x 10^{16} and 1 x 10^{17} /cm^2 samples were estimated to be [H]/[Pd] = 0.0018, 0.0035, 0.0037, 0.0052 and 0.0108 respectively for the initial stage at reaction time from 0 to 350 minutes. The hydrogen reaction rate of the ion irradiated sample was higher (max. 6 times) than that of the non-irradiated one.

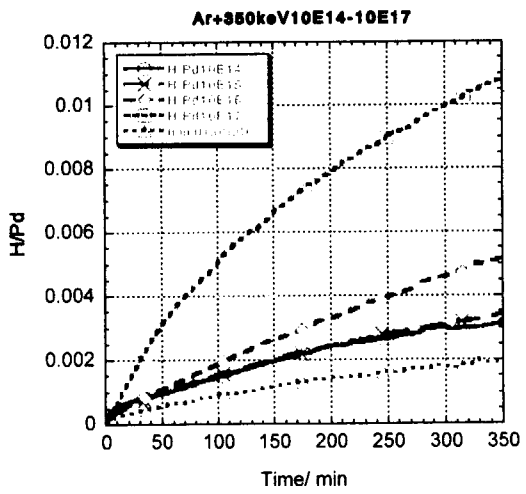

Fig.2 Change in the ratio of absorbed hydrogen atoms to Pd atoms ([H]/[Pd]) for the non-irradiated and irradiated samples.

A sample irradiated with a dose of 1 x 10^{17} /cm^2 exhibited a much higher rate than the other samples, indicating that the increase in ion dose, namely, the increase in vacancy concentration is effective to enhance of the initial rate of hydrogen absorption by Pd.

3.2 Mm-H system

Figure 3 shows the curve of the initial hydrogen absorption by Mm-Ni based alloy samples irradiated at two different dose of 1 x 10^{14} and 1 x 10^{16} /cm^2 of H^+ and Ar^+ ions.

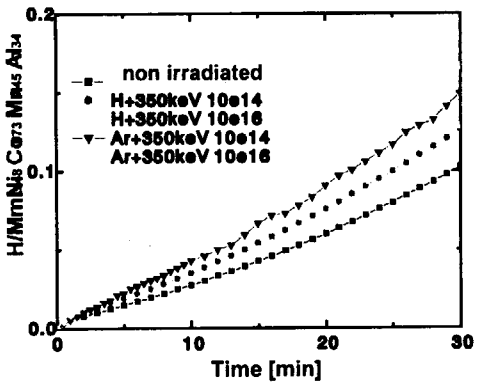

Fig.3 Change in the ratio of absorbed hydrogen atoms to Mm-Ni based alloy ([H]/[Mm]) for the non-irradiated and irradiated samples.

Compared with an unirradiated sample, the initial rate became higher (max. 1.44 times) as the ion mass increased from H^+ and Ar^+ (Table. 1.). For same ion, the rate became higher for the sample with a higher ion dose. These results are similar to those measured for the Pd samples with respect to the effects of the ion mass and the ion dose on the rate. Therefore, in this study, we assume similar

distribution of vacancy in the Mm-Ni based alloy.

Table. 1 Reaction rate of Mm-H system.

Ion	Dose /cm^2	standardized reaction rate
Non irradiated		1.00
H^+	1 x 10^{14}	1.25
H^+	1 x 10^{16}	1.26
Ar^+	1 x 10^{14}	1.50
Ar^+	1 x 10^{16}	1.70

As a result, ion irradiated Pd/Mm sample was found to induce a higher absorption rate than that of the non-irradiated one. The initial hydrogen absorption rate was also found to increase with increasing irradiation energy. These results suggest that defects introduced in Pd/Mm by ion irradiation facilitate the rate of nucleation and growth of hydride.

A further study is needed to investigate a vacancy distribution in the Mm-Ni based alloy.

References

1) H. Uchida, Int. J. Hydrogen Energy 24 (1999) p.861.
2) H. Abe, A. Uedono, H. Uchida, A. Komatsu, S. Okada and H. Itoh, Material Science Forum 363-365 (2001), p.156.
3) H. Abe, H. Uchida, Y. Azuma, A. Uedono, Z. Q. Chen, H. Itoh, Nucl. Inst. and Meth. in Phys. Res. B 206 (2003) p. 224.
4) H. Uchida, M. Sato, W. Cui, T. Tabata, M. Kumagai, H. Takano and T. Kondo, Journal of Alloys Compounds 293-295 (1999) p. 30.
5) H. Uchida, K. Yamashita, T. Tabata, H. H. Uchida, M. Iwase and Y. Katoh, Journal of Alloys Compounds 293-295 (1999) p.751.

4.19 Study of ion beam induced defects in ZnO by using slow positron Beam

Z. Q. Chen*, M. Maekawa*, S. Yamamoto**, T. Sekiguchi***, A. Kawasuso*
Advanced Science Research Center, JAERI*
Department of Material Development, JAERI**
Nanomaterials Laboratory, National Institute for Materials Science***

1. Introduction

Zinc oxide (ZnO) is a promising material for the application in the short wavelength light emitting devices[1] because of its wide band gap (3.37 eV) and large exciton binding energy (60 meV). However, There is a serious doping problem in ZnO. It is very difficult to get p-type conductivity by doping. Ion implantation is one of the methods for the selective doping in semiconductors. But the ion-implantation always causes severe damages. The defects introduced by implantation will strongly affect the performance of devices. It is therefore necessary to study the introduction and recovery of implantation induced defects. Positron annihilation is a powerful method to study vacancy defects in semiconductors because of the high sensitivity of positron to vacancies[2]. In this work, Al^+/N^+ ions were co-implanted to ZnO single crystals in order to get p-type ZnO as suggested by Yamamoto et al[3]. The implantation induced defects as well as electrical properties were studied by positron annihilation and Hall measurements.

2. Experiment

Undoped n-type ZnO single crystals with (0001) orientation were purchased from the Scientific Production Company (SPC). Prior to ion implantation, the ZnO samples were annealed at 900°C to remove any grown in defects. After that, the samples were implanted with Al^+, N^+ and Al^+/N^+, respectively. Multiple-step implantation was performed for each ion species with several energies ranging from 50 to 380 keV. The ion doses were from 10^{12} cm^{-2} to 10^{15} cm^{-2}. After implantation, the samples were annealed in nitrogen ambient for 30min from 20 to 1200°C. The implantation induced defects and their recovery after annealing were studied by the measurements of Doppler broadening of positron annihilation radiation using a variable energy (0-30 keV) slow positron beam. The S-parameter, which is defined as the ratio of the central region to the total area of the 511 keV annihilation peak, is used to characterize the defects introduced by implantation. Hall measurements were performed using the van der Pauw method.

3. Results and discussion

Figure 1 shows the representative change of S-E curves before and after ion-implantation. In all the implanted ZnO samples, the S-parameter shows increase with increasing ion dose, suggesting vacancy-type defects were introduced. The major defect species might be vacancy clusters. The defect layer thickness obtained by the analysis of the S-E curve shows

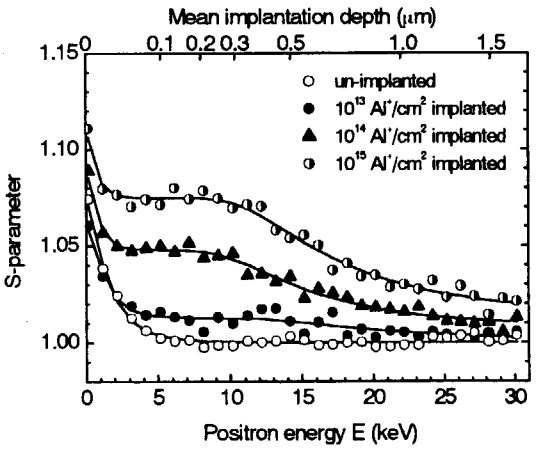

Fig.1 S-E curves measured for the ZnO before and after Al^+ implantation with different doses.

good agreement with the TRIM simulation.

Figure 2 shows the S-E curves for the Al^+-implanted ZnO after annealing. The annealing of the defects in Al^+ implanted sample shows two stages. As-shown in Fig.3, the S-parameter shows increase in the first (20-600°C) and decreases to the bulk value in the second stage (600-900°C), which might be due to the agglomeration of vacancy clusters and their recovery, respectively. The formation of positronium might be responsible for the large increase of S-parameter after annealing, which indicated the formation of large voids. This result suggests that the Al^+-implantation induces amorphization in ZnO. Further annealing above 600°C will cause the transformation of the amorphous structure to the crystalline structure through the recrystallization process. The strong n-type conductive layer after Al^+ implantation and annealing suggests that all the Al^+ ions are activated and act as donors.

The annealing of the N^+-implantation induced defects shows more complicated behavior as compared to the aluminum implantation (Fig.2). There are four annealing stages. The increase and decrease of the S-parameter in the first two stages (20-500°C and 500-800°C) might be due to the increase of vacancy cluster size and the recovery of the vacancy clusters, respectively. The increase of S-parameter again in the third stage (800-1100°C) and its recovery to the bulk state in the last stage (1100-1200°C) might be due to the formation and disappearance of nitrogen related defect complexes. The substitution of oxygen with nitrogen near the vacancies causes the increase of S-parameter. Due to the formation of vacancy-nitrogen complexes, a much higher temperature of 1200°C is needed to remove the defects in the N^+-implanted sample as compared to the Al^+-implanted one. The Hall measurements show that the nitrogen implanted layer still exhibits n-type conductivity. The possible reasons for the failure of nitrogen acting as acceptors may be due to the compensation by the residual donor type defects, such as V_O and Zn_i, or the out diffusion of nitrogen after high temperature annealing.

For the Al^+/N^+ co-implanted sample, the annealing of the defects shows similar behavior as that of N^+ implantation. This reveals that the annealing behavior in stage III and IV is related with nitrogen-defect complex. But some difference can be also seen in the third stage. The increase of S-parameter for the co-implanted sample is suppressed as compared to the N^+-implanted sample. This may indicate the formation of N+Al+N complexes, which will act as acceptors as suggested by Yamamoto et al[3]. The number of vacancy-nitrogen complexes is then reduced, so the increase of S-parameter is weakened. In this co-implanted sample, the

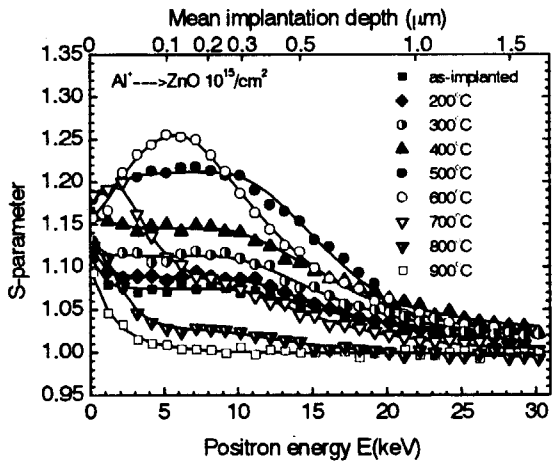

Fig.2 S-E curves measured for the Al^+-implanted ZnO after annealing at different temperatures.

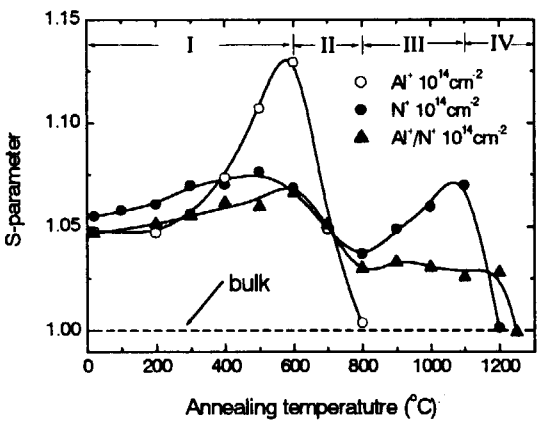

Fig.3 Annealing behavior of the S-parameter for the ZnO implanted with Al^+, N^+ and Al^+/N^+.

formation of positronium is also observed after annealing, but the intensity is much smaller than that of Al^+-implantation. The increase of S-parameter during the annealing in the first stage is also much smaller for the N^+-implanted or Al^+/N^+ co-implanted sample as compared to that of the Al^+-implanted one. This means that the nitrogen suppresses amorphization or void formation. The co-implanted ZnO layer still shows n-type conductivity from Hall measurements. We assume that even though some of the nitrogen and aluminum ions might have interaction, the N+Al+N acceptors are over compensated by the other Al^+ donors or donor-type defects like V_O or Zn_i. Suppression of these defects is then very crucial for the successful p-type doping in ZnO.

References

1) D. C. Look, Mater. Sci. Eng., B 80 (2001) 383

2) R. Krause-Rehberg and H. S. Leipner, *Positron Annihilation in Semiconductors, Defect Studies*, Springer Series in Solid-State Sciences 127 (Springer, Berlin, 1999)

3) T. Yamamoto and H. Katayama-Yoshida, Jpn. J. Appl. Phys. 38 (1999) L166

4.20 Application of micro-PIXE to Study on Sorption Behavior of Heavy Elements on Mixtures of Minerals -Improvement of Detection of Clay Minerals by A High Resolution X-ray Detector-

N. Kozai*, T. Ohnuki**, T. Sakai***, M. Oikawa***, T. Satoh***
Department of Environmental Sciences, JAERI*
Advanced Science research Center, JAERI**
Advanced Radiation Technology Center, JAERI***

1. Introduction

The purpose of this study is to understand migration behavior of heavy metals in soil environment. As results of industrial activities, toxic heavy metals have been released to and stored in the soil environment. Soil is mixture of various minerals such as clay, other silicate, iron, and phosphate minerals. We have used micro-PIXE to investigate sorption behavior of heavy metal ions on minerals in their mixtures. The spatial resolution of the micro-PIXE analyzing system developed in the TIARA facility, JAERI is less than 1 μm in diameter [1], which allows us to obtain highly sensitive two-dimensional element-mapping and is thus suited for investigating distribution of elements sorbed on a mixture of minerals.

Clay minerals play very important role on migration of heavy metal elements in soil because clay minerals are ubiquitous in soil and many of them sorb cations. Allophane, imogolite, and naturally occurring anionic clays such as hydrotalcite sorb anions. However, it was difficult to detect clay minerals by the previous micro-PIXE analyzing system in the TIARA facility. Clay minerals contain low-energy characteristic X-ray emitters Si (1.74 keV), Al (1.49 keV), Mg (1.25 keV), and Na (1.04 keV) as major elements, and it is hard for the Ge detector of the micro-PIXE analyzing system to detect those elements. Thus, mapping of clay minerals in a mixture with other minerals is difficult even when the clay minerals in the sample can been seen well by an optical microscope.

A high resolution X-ray detector was recently introduced to the micro-PIXE analyzing system in the TIARA facility. Detection of clay minerals has been greatly improved with this detector. This paper describes how detection of clay minerals has been improved.

2. Experimental

A mixture of three minerals was prepared. This contained a swelling clay mineral montmorillonite 50% by weight, a synthetic iron (III) hydroxide ferrihydrite 25%, and a synthetic calcium-phosphate mineral hydroxyapatite 25%. The montmorillonite used was natural and purchased from Kunimine Industries. The interlayer cations of this montmorillonite were exchanged with Mg^{2+} (Mg-montmorillonite) beforehand. The ferrihydrite with particle size between 25-46 μm was prepared according to the method by Schwertmann and Cornell[2]. The hydroxyapatite with a particle size of 20 μm in diameter was purchased from Bio-Rad laboratories Inc. This mixture sample is to use for study on sorption behavior of heavy elements, and the results of sorption experiments using this mixture sample will be described elsewhere. For comparison, a synthetic mica named Na-4 mica[3] with a composition of $Na_4Al_4Si_4Mg_6O_{20}F_4 \cdot H_2O$

and low impurities was also analyzed by micro-PIXE.

The mixture sample was spread on a glassy carbon plate with water and then the spatial elemental distribution of the samples was measured by micro-PIXE by a proton beam with the energy of 2.6 MeV. To detect characteristic X-rays, a high purity Ge detector with a crystal size of 100mm^2 (ORTEC IGLET-X) and a Si(Li) detector with a crystal of 30 mm^2 (PGT LS-30135) were used at the same time.

3. Results and discussion

Figure 1 shows elemental mapping of the mixture sample measured by micro-PIXE. The Ge detector was used for mapping of Fe (6.40 keV) and Ca (3.69 keV) because detection of these elements by the Ge detector was better than the Si(Li) detector. Figure 1C and 1D shows distribution of montmorillonite obtained by those two detectors. Mapping of montmorillonite was greatly improved by using the Si(Li) detector. The gross count of Si obtained by the Si(Li) detector was approximately 65 times greater than that obtained by the Ge detector. The montmorillonite contained Mg, Al, and Si, and the sum of the gross counts of Mg, Al, and Si by the Si(Li) detector was approximately 95 times greater than that of Si by the Ge detector. Figure 1C was drawn by mapping those three elements. By optical microscope observation of this sample, montmorillonite was found over the sample (Figure not shown). Figure 1C well shows such distribution of montmorillonite. However, distribution of montmorillonite obtained by the Ge detector is unclear (Fig 1E). The distributions of montmorillonite, ferrihydrite, and apatite in the mixture sample can be clearly distinguished from each other by combination use of the Ge detector and the newly installed Si(Li) detector.

In the synthetic mica the molar ratio of Al to Si is 1:1, and these elements are located in the same position in the mica structure. The Al in the synthetic mica was undetectable by the Ge detector. The detection of the Al by the Si(Li) detector was good, and the ratio of the net count of the Al and that of the Si in the synthetic mica obtained by the Si(Li) detector was 0.90 to 1. Similarly, the ratio of the net count of the Mg to that of the Si in the synthetic mica was 0.75 to 1.

Because the newly installed Si(Li) detector are very sensitive to Mg, Al, and Si, the following experiments may become possible in the TIARA facility.

1) Distinguish of Si-containing minerals: For example, clay minerals may be distinguished from silica sand by inclusion of Al. Some clay minerals may be distinguished from each other whether they contain Mg or Al.

2) Detection of hydrotalcite: Hydrotalcite is a representative anionic clay. Anionic clays contains anions in the interlayer and these anions are exchangeable with other anions. Anionic clays are rare in nature and synthetic anionic clays have been investigated on chemical, catalytic, and electronic properties and else. Hydrotalcite is undetectable by the Ge detector because it contains Mg and Al only as component metal elements.

These may bring various experimental options to related research fields.

References

1) T. Kamiya, T. Suda, R. Tanaka, Nucl. Instr. Meth. B, 118 (1996) 447

2) U. Schwertmann and R. M. Cornell, Iron Oxides in the Laboratory, VCH, New York (1991)

3) S. Komarneni, N. Kozai, W. J. Paulus, Nature, 410 (2001) 771

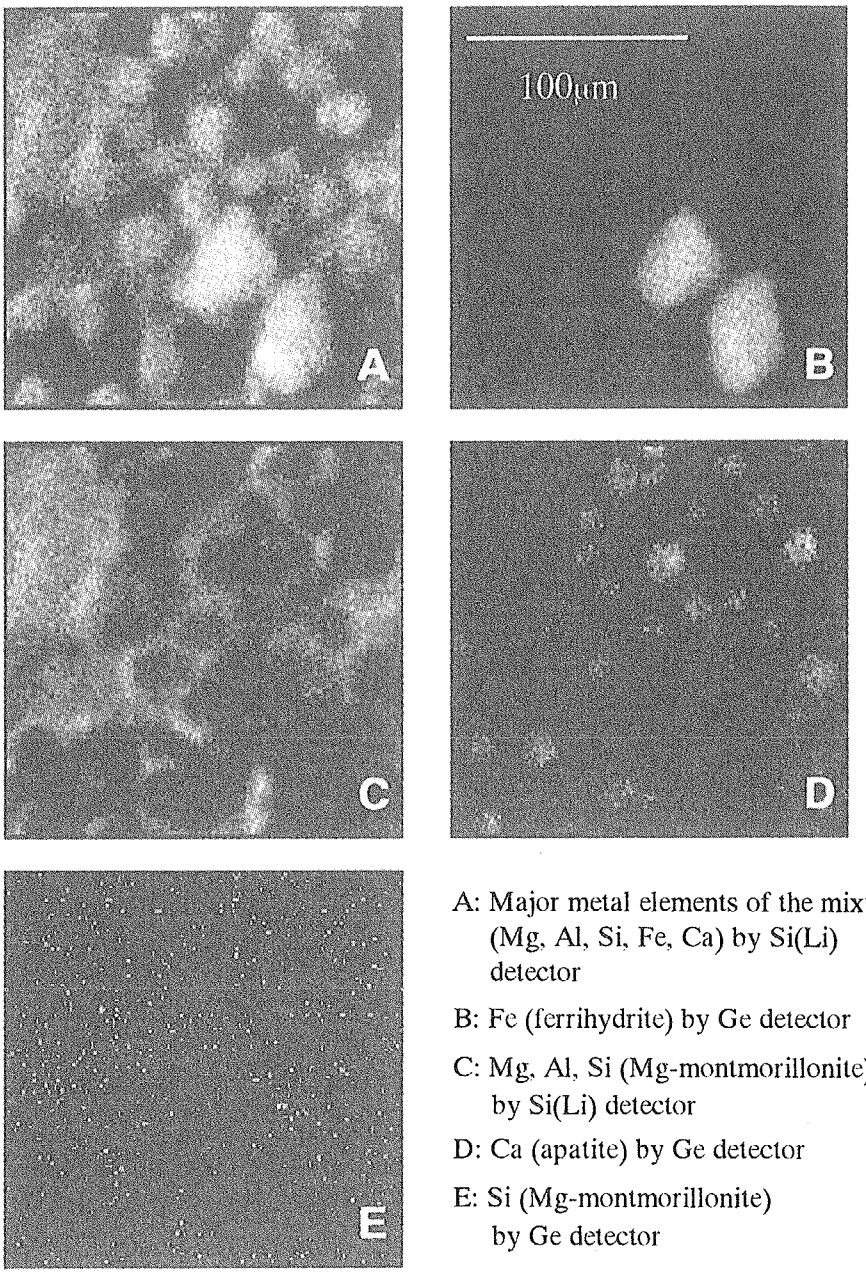

A: Major metal elements of the mixture (Mg, Al, Si, Fe, Ca) by Si(Li) detector

B: Fe (ferrihydrite) by Ge detector

C: Mg, Al, Si (Mg-montmorillonite) by Si(Li) detector

D: Ca (apatite) by Ge detector

E: Si (Mg-montmorillonite) by Ge detector

Fig. 1 Distributions of elements in the mixture of Mg-montmorillonite, ferrihydrite, and apatite obtained by micro-PIXE. The above pictures indicate the same region of the mixture spread on a carbon plate. A brighter region shows higher concentration of a given element.

5. Material Analysis

5.1 Formation process and stability of radiation-induced non-equilibrium phase in silicon (III)

S. Ohnuki*, E. Shioya*, M. Takeda**, T. Suda*, S. Watanabe*, A. Miyashita**, M. Ishino***, O.Yoda***
Dept. Mater. Sci., Fac. Engin., Hokkaido Univ. Sapporo 060-8628, Japan*
Dept. Mater. Sci. Miyagi Technical Collage, Natori 981-1239, Japan**
Advanced Photon Reseach Center, JAERI***

1. Introduction

An important material issue of multi-layers structure is the stability of such nano-scale structure. Compared with bulk materials, the atomic diffusion in the multilayer materials can be enhanced by high-energy particle irradiation. Therefore, thermal annealing and particle irradiation could be helpful for studying the stability of nano-multilayer.

In Mo/Si system, there are three typical intermetallic compounds, i.e. of $MoSi_2$, Mo_5Si_3 and Mo_3Si, which are different in crystal structure and composition, but the phase stability under irradiation is not surveyed in nano-scale. In this study, we focused on the non-equilibrium phase formation and diffusion process in multilayer materials by using HRTEM.

2. Experimental Procedure

Multilayer samples with alternation of Mo and Si were prepared by ion beam sputtering method on Si substrates[1]. The thickness of each layer with typically less than 10 nm and the total thickness with 100 nm were selected for having nominal compositions of inter-metallic compounds in Mo/Si system. TEM specimens were prepared by the conventional cross-sectional method using ion thinning. The HRTEM was performed with JEM-2010F. 1 MeV Si^+ ion beam was irradiated in TIARA Tandem facility Takasaki, and "in-situ" observation of microstructure was carried out in a 1250 kV HVEM (JEM-ARM 1300) at Hokkaido University.

3. Results and Discussion

3.1 Amorphization due to ion-irradiation

Figure 1 shows a typical sequence of amorphization in Mo_3Si multi-layer during ion-irradiation at room temperature. Obviously the amorphous layer is developed from Mo/Si interface. This result implies that the amorphization results in atomistic mixing and diffusion due to ion-irradiation.

3.2 Amorphization during e-irradiation

"In-situ" high-resolution observation was performed under electron-irradiation at room temperature. Figure 2 shows a mixing process in multilayer, Mo_5Si_3, under electron irradiation. Although periodic structures were basically stable after thermal annealing up to 773 K, we observed that c-Mo layers were mixed with a-Si, and all area turned to amorphous structure with homogeneous contrast after irradiation. It should be noted that the position of the layers shifted to the left side after irradiation, which means the shrinkage due to irradiation.

Figure 3 shows the shrinkage as a function of irradiation time. The shrinkage finished very quickly and the reduction rate was around 10-15 %, which depended on the Mo/Si fraction. In general, amorphization may increase the volume, but covalent bonding materials are exceptional. For example, c-Si reduces the volume with several percents after amorphization. However, this reduction occurred during the mixing of a-Si and c-Mo. It seems that this phenomenon is related to the mixing process between the larger size atom and the smaller size atom. In Ti/TiC multilayer, the value of the inter-diffusion coefficient is higher by many orders of magnitude than that expected from extrapolation of high temperature bulk data[2].

Figure 4 is typical FFT results from halo ring, which shows coarse and dense amorphous structures formed by e-irradiation. The dense amorphous phase is supposed to be ideally amorphous.

4. Summary

We tried to accelerate local diffusion using ion and electron irradiation at room temperature. The transition layer grew from the interface and finally the whole multi-layer became amorphous structure. The intensive inter-diffusion between layers was confirmed by EDS analysis.

Our results suggest that a non-equilibrium phase may develop at interfaces in multilayer materials composed of elements quite deferent in atomic weight and crystal structure. Low temperature diffusion in amorphous structure could be important for the understanding of the observations.

An intensive shrinkage, about 10-15%, was confirmed during electron-irradiation at RT. Two types of amorphous zones were developed; bright and dark. The dense amorphous phase is supposed to be ideally amorphous.

REFERENCES

1) A. Ulyanenkov et al. *Journal of Applied Physics* 87 (2000) 7255-7260.
2) I. Dahan et al. *Thin Solid Film* 377-378 (2000) 687 –693.

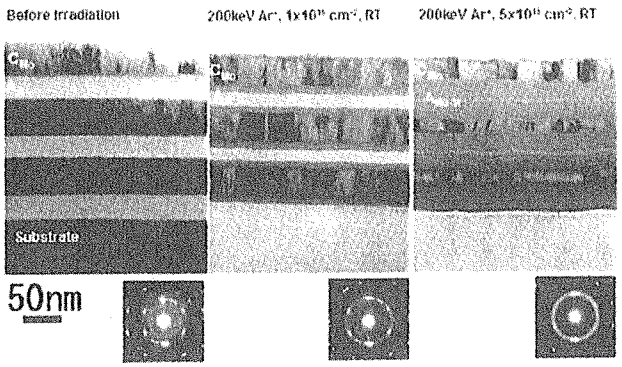

Fig. 1 Amorphization at the interface of multi-layers irradiated with 200keV Ar^+ at RT

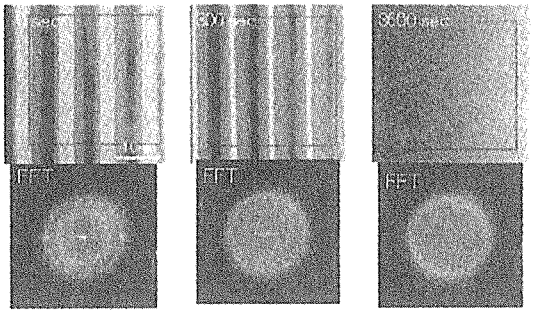

Figure 2 Amorphization process due to e-irradiation at RT.

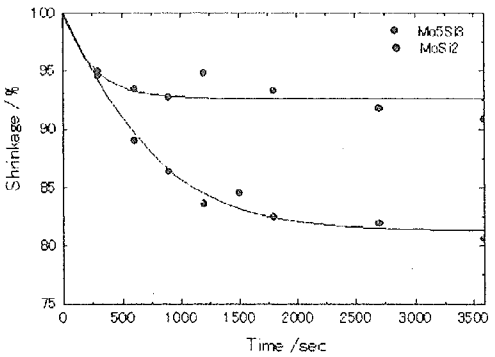

Figure 3 The shrinkage of amorphous layers during e-irradiation at RT.

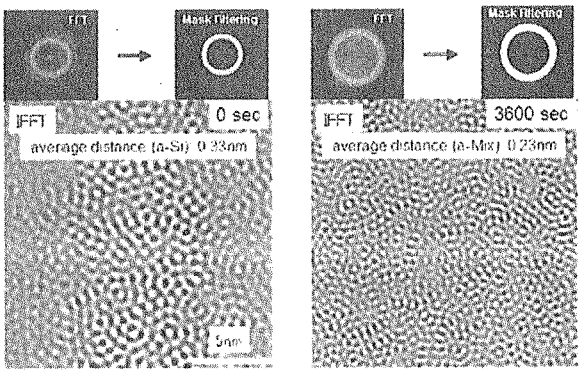

Figure 4 FFT images from halo ring, which indicates the formation of dense amorphous structure.

5.2 Hydrogen Up-take in Gas Ion Implantation Induced Porous Surface Layers

S. Nagata*, S. Yamamoto**, B. Tsuchiya*, K. Toh*, N. Ohtsu*, T. Shikama*
Institute for Materials Research, Tohoku University*
Department of Material Development, JAERI**

1. Introduction

The implantation of gas ions such as helium can produce porous cavity structure, which has a potential to modify the surface properties of functional materials[1]. Concerning hydrogen, it is well accepted that ion irradiation provides strong hydrogen trapping sites[2] and significantly affects the hydrogen transport process. Recently we found that the He irradiation at higher doses caused hydrogen enrichment in the He saturated layer of W and Mo single crystals in a high vacuum, without post hydrogen ion implantation[3-5]. The up-taken H concentration reached 10~20 at. % within the He saturated layer of the specimen at room temperature. Moreover, isotopic difference was observed between H and D uptake rates; H atoms were preferentially up-taken in the He saturated layer even in the D_2 and D_2O atmosphere. Although the significant H up-take and isotope difference can be attributed to the proton conductive oxide formation as well as the He bubble formation in the heavily irradiated surface, a detail of the mechanism for the anomalous hydrogen accumulation has not been known. In the present work, we examine the gas ion implantation effects on the W and Mo to clarify the hydrogen up-take mechanism.

2.Experimental procedure

Specimens used were W and Mo single crystalline disks of 8 mm diameter and 0.5 mm thickness. They were cut from single crystal rods made by the floating zone melting method, with <100> or <111> crystallographic axis. To obtain mirror like surface, the specimens were electro polished in 0.1 N NaOH solutions and in a 1:3 mixture of sulfuric acid and methanol, for W and Mo, respectively.

Ion implantations were carried out using a 400 kV ion implantation facility at TIARA, with He, Ne, Kr, Xe ions of 50 ~ 280 keV, at room temperature. The maximum dose was about 2 x 10^{22} ions/m^2, with a typical current density of about $3x10^{18}$ ion/m^2s. During the ion implantation, the residual gas pressure was kept about 2 x 10^{-5} Pa. Low energy He (10 keV) irradiation was performed using an ion gun with a velocity filter. Concentration depth profiles of hydrogen isotopes in the surface layer of the specimen were measured by Elastic Recoil Detection Analysis (ERDA) using 2.8 MeV He^{3+} beams. An ion beam with 1mm diameter was incident on the specimen at an angle of 75 degree to the surface normal and the recoiled He and hydrogen isotopes were detected at an angle of 30 degree with respect to the analyzing beam. The depth resolution of hydrogen in the present ERD experiments was estimated to be 25 nm at the surface of W. Changes of the surface morphology due to the ion implantation were investigated by Scanning Electron Microscope (SEM) and Atomic Force Microscope (AFM) observation.

3.Results and Discussion

Concentration depth profiles of up-taken H in the surface layer of various ion implanted W crystals were shown in Fig. 1, measured by the ERDA technique after the ion implantation.

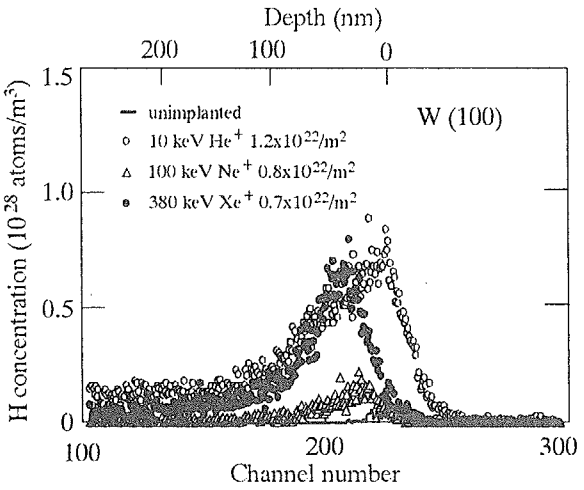

Fig. 1. Recoil spectra of H atoms in the surface layer of W crystals obtained by ERDA technique.

The depth profile of H in the He implanted specimen extends to the top most surface in comparison with the calculated range distribution. A long tail of H distribution observed for the ion-irradiated specimen was probably due to the deterioration of the depth resolution, caused by morphological changes of the irradiated surface. No large difference was observed for H accumulation in specimens irradiated by 100 keV Ne, 200 keV Ar, 380 keV Kr ions. The up-taken H profiles for heavier ions (Ne, Ar, Kr, Xe) irradiation nearly corresponds to their projected range profiles in spite of sputtering effects; the sputtering rates of W by these ions bombardment are expected to be larger than 1[6]. From the RBS spectra, the ratio of retained implanted atoms to the substrate W atoms was roughly estimated to be about 0.1 for Ar, Kr, Xe implantation, and was less for Ne.

Fig. 2 shows a typical SEM micrograph of surfaces of the W crystals irradiated by 100 keV Ne ions to a dose about 8 x 10^{21} ions/m^2 at 295 K. The edge of the irradiated area is seen; the left half and right half of the image correspond to the irradiated and un-irradiated region respectively. Pinholes with a size of about 100

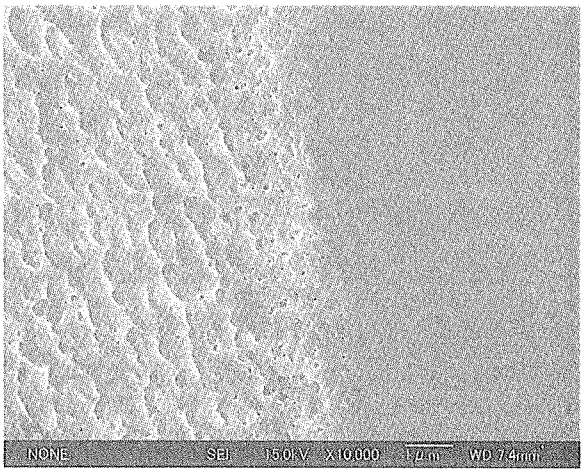

Fig.2. SEM micrograph showing unirradiated (right) and irradiated (left) region of the W crystal, after implantation of 100 keV Ne to a dose of 8 x 10^{21}/m^2 at room temperature.

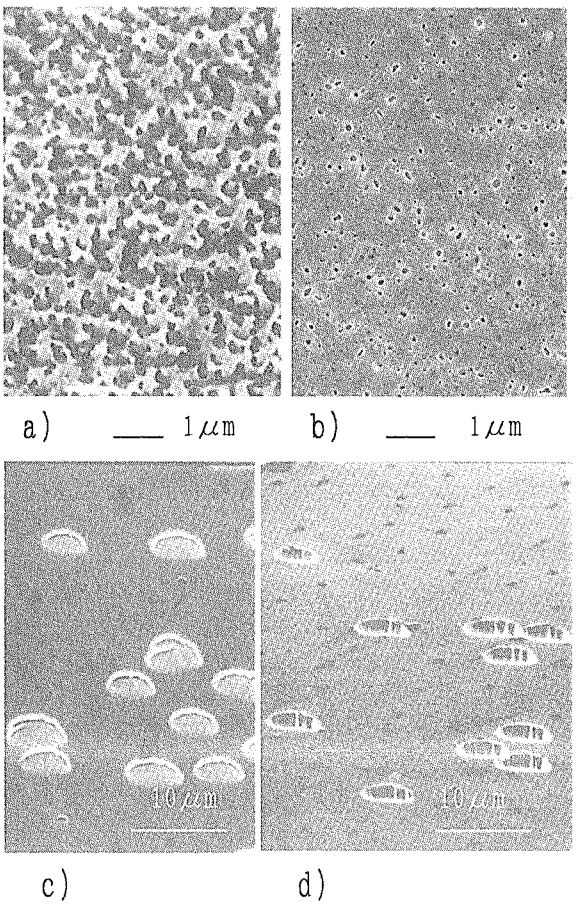

Fig. 3. SEM micrographs of the W single crystals irradiated by 100 keV Ne, 380 keV Kr (b), 380 keV Xe (c). A SEM micrograph for the 60 degree tilted for the 380 keV Xe irradiated specimen as the same as (c).

nm in waved structures were observed in the irradiated surface. The porous surface like "seaweed" was confirmed in the same specimen as shown in Fig. 3 (a). The irradiation of 380 keV Kr created tiny halls in the flat surface without waved structure as shown in Fig. 3(b). For the 200 keV Ar ion irradiated specimen, the blisters are regularly dome-shaped with about 1μm and some of them lost their covers. Those are similar to the blister formation observed for He implantation. Although the ion implanted surface has porous structure, or similar to the He irradiation induced microstructure, hydrogen accumulation in Ne, Ar and Kr irradiation resulted little accumulation of hydrogen.

A unique image was found for 380 keV Xe ion implanted surface, where the H atoms were enriched, as shown in Fig. 3(c). A number of large 'shells' with a size of several μm was created in the relatively flat surface. The original smooth surface was maintained except for the 'shell' structure, while the sputtering rate would be large for Xe ion irradiation. Fig. 3(d) shows a SEM micrograph taken as the specimen was tilted about 60-degrees. Each 'shell' seems to be arranged with the same symmetry on as the crystal lattice of the host W atoms. Structural and compositional microanalysis for this ion-irradiated surface is in progress.

4.Conclusions

To study the hydrogen up-take behavior in the gas ion implanted metal surface, we measured the concentration depth profiles of hydrogen in the He, Ne, Ar, Kr, Xe ion implanted W single crystals. Although, the ion implantation caused various porous structures depending on the ion species, enhancement of hydrogen up-take was found only for He and Xe ion irradiated surfaces. Further investigation is needed to clarify the correlation of the hydrogen up-take with structure and composition in the ion irradiated surface.

References

1) P.B. Johnson, P.W. Gilberd, A. Markwitz, Y. Morrison, CR. Varoy, Mprdan Phyiscs Letters B, 28&29 (2001)1391-1401.
2) S.T. Picraux, J. Bottiger and N. Rud, Appl. Phys. Lett. 28 (1976) 179.
3) S. Nagata, B. Tsuchiya, T. Sugawara, N. Ohtsu, T. Shikama, Nucl. Instr. Meth. in Phys. Res. B 190 (2002) 652-656.
4) S. Nagata, B. Tsuchiya, T. Sugawara, N. Ohtsu, T. Shikama,, J. Nucl. Mater. 307-311 (2002) 1513-1516.
5) S. Nagata, B. Tsuchiya, N. Ohtsu, T. Sugawara, T. Shikama, K. Tokunaga, M. Takenaka, E. Kuramoto, J. Nucl. Mater., 313-316 (2003) 279-283.
6) H.H. Andersen, H.L. Bay, J. Nucl. Mater. 93&93 (1980) 625-633.

5.3 Sulfur-doping in titanium dioxide by ion implantation technique

T. Umebayashi*, T. Yamaki**, T. Sumita***, S. Yamamoto**,
A. Miyashita**, S. Tanaka** and K. Asai*
Department of Quantum Engineering and Systems Science, The University of Tokyo*
Department of Material Development, JAERI**
Technology Research Department, NASDA***

1. Introduction

Although titanium oxides (TiO_2) is the most promising photocatalytic material [1], it is active only under ultraviolet (UV) light irradiation because of its wide bandgap (~3.0 eV). The effective utilization of visible light, therefore, is one of the important subjects for the increased applicability of TiO_2 as a photocatalyst.

Recently, the S-doped anatase TiO_2, including S substituted for O, was synthesized by the oxidative heating of the TiS_2 powder [2]. The S-doping shifted the optical absorption edge to a lower energy-side, thereby increasing the photoreactivity in the visible light region. The S-doped TiO_2 is expected to be available as the novel visible light photocatalyst [3), 4)]. However, the oxidative heating of TiS_2 is a difficult method to control the concentration of the dopant and its dependant profile, which should govern the photocatalytic activities of the doped TiO_2. Control of these factors can be best carried out by ion implantation. In this study, the S-doped TiO_2 single crystal was synthesized by ion implantation and its optical properties and electronic structures were investigated.

2. Methods

Optically polished single-crystalline TiO_2 (rutile; 10 x 10 x 0.5 mm) with a <001> crystallographic axis was used for our experiments. The implantations were carried out with 200 keV S^+ at room temperature (RT). The implanted crystals were annealed at 600 °C in air for 6 hours. After the annealing, the Rutherford backscattering spectrometry and ion channeling analysis (RBS-C) measurements were performed with a 2 MeV $^4He^+$ beam from a 3 MV single-stage accelerator. The charge state of the dopants was investigated by x-ray photoelectron spectroscopy (XPS) with an ESCALAB-MK II (VG Scientific) using an Mg X-ray source (Mg K α, $h\nu$ = 1253.6 eV). The differential absorption spectra were measured by a UV/VIS spectrophotometer.

The electronic structures of the S-doped TiO_2 were studied using first principles density functional (DF) band calculations by the full potential linearized augmented plane wave method with the super-cell

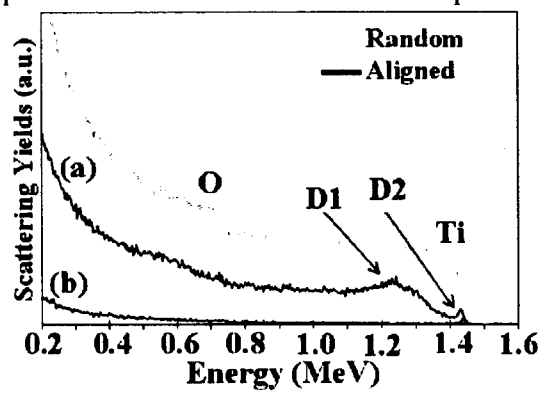

Fig. 1. 2 MeV $^4He^+$ RBS-C spectra of TiO_2 single crystals implanted with 200 keV S^+ (8 x 10^{15} ions/cm^2) at RT for (a) As implanted and (b) annealed samples at 600°C in air for 6 h. Gray lines: random spectra; black lines: <001> aligned spectra.

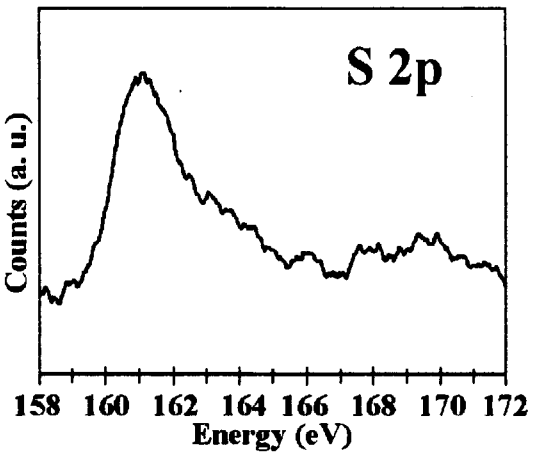

Fig. 2. X-ray photoelectron spectrum for the S 2p state of the S-implanted and subsequently annealed TiO_2.

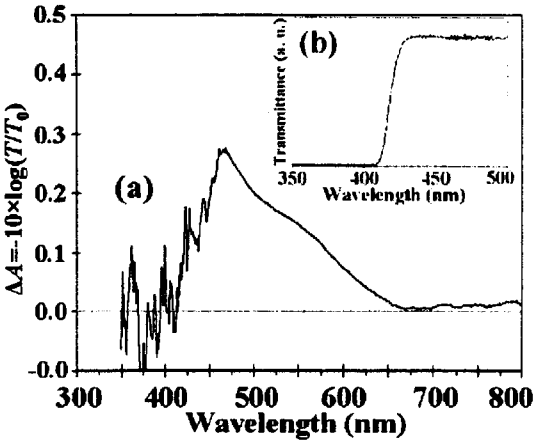

Fig. 3. (a) Differential absorption spectrum ΔA=-10× log(T/T_0), where T and T_0 are the transmittance of the S-doped and undoped TiO_2 crystal, respectively. (b) Transmittance spectrum of the undoped TiO_2 crystal.

approach [5]. Our model consists of 2 unit-cells stacked along the c-axis, where one O atom was replaced by the S atom. The details of the calculation methods have been described in previous reports [6, 7].

3. Results and discussion

Figure 1 shows the random and <001> aligned RBS-C spectra after the implantation of 8 × 10^{15} S^+/cm^2 at RT. Based on the analysis of the Rutherford universal manipulation program (RUMP) code [8], the signal of S occurs around 1.22 MeV. The S signal was not detected for the implanted crystal. As shown in the aligned spectrum of the as-implanted sample, two damage peaks (D1 and D2) were observed around 1.4 and 1.2 MeV and both of them did not reach the random level. The former peak is due to the surface damage, while the latter is attributed to the displacement damage in the solids generated by the S implantation. According to the RUMP simulation, the displacement damage lies at a depth of 220 nm. A large amount of S atoms would occur in a deeper area in the as-implanted crystal. The aligned spectrum of the sample annealed at 600 °C for 6 hours, where the damage peak disappeared, indicates that radiation damage recovered due to the annealing.

Figure 2 shows the XPS spectrum for the S 2p core level of the S-implanted crystal annealed at 600 °C for 6 hours. This spectrum was referenced to the C 1s state at 284.8 eV. The signal observed at 161 eV is associated with S forming Ti-S bonds in the TiO_2 [9]. A trace amount of S would remain in the annealed sample as substitutional atoms at the O sites.

Combining the above RBS-C and XPS results, we concluded that the S-doped TiO_2 was synthesized by the S implantation and subsequent annealing at 600 °C.

Figure 3 shows the differential absorption spectrum $\Delta A(\lambda)$ = -10× log(T/T_0), where T and T_0 are the transmittance of the implanted and unimplanted TiO_2 crystal, respectively. In the pure crystal, optical absorption is observed below 410 nm which corresponds to the bandgap energy. In contrast to this crystal, the S-doped crystal absorbed the light below 650 nm. This visible light absorption would be due to the S-doping.

Figure 4 shows the calculated total and partial density of states (DOS) of the VB and CB for the pure and S-doped TiO_2. When

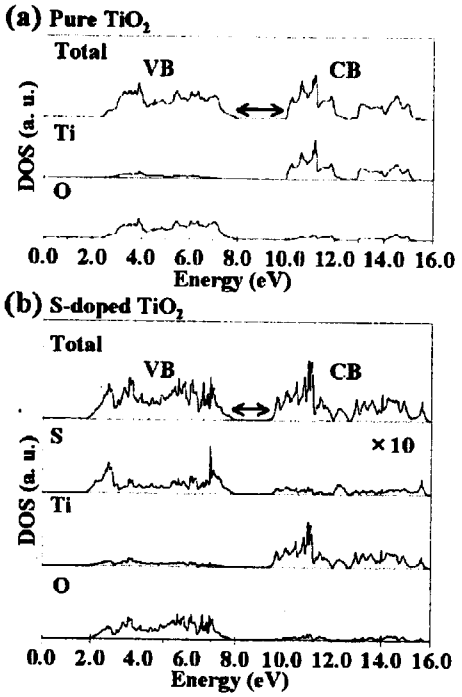

Fig. 4. Total and partial DOS of the (a) pure and (b) S-doped TiO_2.

TiO_2 is doped with S, the S 3p states are somewhat delocalized, thus greatly contributing to the formation of the VB with the O 2p and Ti 3d orbitals. Consequently, the mixing of the S 3p states with VB increases the width of the VB itself. This results in a decrease in the bandgap energy due to S doping. The calculated bandgap energies were 1.31 eV for the S-doped TiO_2 and 1.93 eV for the pure TiO_2. Our calculation results consistently confirm that the S atoms doped into the substitutional site of rutile TiO_2 are effective for the bandgap narrowing.

TiO_2 doped with a transition metal, i.e., Cr, V, Mn, Fe, etc., also absorbs a photon in the visible light region. This visible light absorption is caused by an impurity level in the bandgap [7), 10)]. In contrast with the case of the transition metal doping, the bandgap narrowing leads to the optical-absorption in the visible light region for the S-doped TiO_2.

4. Conclusion

(i) S-doped TiO_2 was synthesized by 200 keV S^+ implantation and subsequent thermal annealing at 600 °C in air for 6 hours.

(ii) In the S-doped TiO_2, the optical-absorption occurred in the visible light region.

(iii) S-doping into TiO_2 causes an increase in the width of the valance band, resulting in bandgap narrowing.

References

1) A. Fujishima and K. Honda, Nature 238 (1972) 37-38.

2) T. Umebayashi, T. Yamaki, H. Itoh and K. Asai, Appl. Phys. Lett. 81 (2002) 454-456.

3) T. Umebayashi, T. Yamaki, S. Tanaka and K. Asai, Chem. Lett. 32 (2003) 330-331.

4) T. Ohno, T. Mitsui and M. Matsumura, Chem. Lett. 32 (2003) 364-365.

5) P. Blaha et al., A Full Potential Linearized Augmented Plane Wave Package for Calculating Crystal Properties, Karlheinz Schwarz, Techn. Univ. Wien, Vienna, (1999).

6) T. Umebayashi, T. Yamaki, S. Yamamoto, A. Miyashita, S. Tanaka, T. Sumita and K. Asai, J. Appl. Phys. 93 (2003) 5156-5160.

7) T. Umebayashi, T. Yamaki, H. Itoh and K. Asai, J. Phys. Chem. Solids 63 (2002) 1909-1920.

8) L. R. Doolittle, Nucl. Instr. and Meth. B 9 (1985) 344-351.

9) D. Gonbeau, C. Guimon, G. P. Guillouzo, A. Levasseur and G. Meunier, R. Dormoy, Surf. Sci. 254 (1991) 81-89.

10) T. Umebayashia, T. Yamaki, T. Sumita, S. Yamamoto, S. Tanaka and K. Asai, Nucl. Instr. and Meth. B 206 (2003) 264-267.

5.4 Irradiation Effect on Crystalline C_{60} Films with Low Energy Self-Ions

Hiroshi Naramoto, Vasily Lavrentiev, Kazumasa Narumi and Seiji Sakai
Advanced Science Research Center, JAERI

1. Introduction

Since the synthesis of C_{60} molecules, there appeared many kinds of reports treating C_{60} as starting materials. Transition metal atoms are interesting partners for chemical modification of C_{60} molecules because both are expected to play the complementary roles in the process of charge transfer. The charge transfer induces the weekly bound chemical compounds competing with the strain accumulation associated with the phase separation. This process can be supposed to the complex system suitable for the spontaneous structure evolution study. The recent effort has shown that the evolved structures are endowed with interesting electrical functions [1,2].

The structures obtained are weakly bound, and should be changed into the endurable ones for the use as functional materials. Energy beam illumination at the spatially specified points will give us an additional means to design the functional materials. In the present report, the effort on the irradiation-effect-study with self ions is described made for a last fiscal year. The ion irradiation is a violent technique beyond the binding energy of the relevant system but the careful application has been shown to be useful [3].

In the present study, the energy of C_{60} ions was chosen so as to be just below the critical one for the break-up of C_{60} cages [4-6]. The simple process of graphitization by high energy ion bombardments is beyond our interests.

2. Experimentals

FCC Crystalline C_{60} films with ~100nm order thickness were prepared on (0001) α-Al_2O_3 around 70-120 °C under 10^{-8} Torr by operating a Knudsen cell at the temperature range of 440-460 °C. The source material for C_{60} is relatively high quality with 99.99 % purity. For the present chemical modification study the bombardments of C_{60}^+ ions (50keV, 200 nA/cm^2) from a Freemann-type ion source were carried out at room temperature. Different from the usual ion irradiation experiment, in C_{60}^+ ion irradiation the negative potential for the secondary electron suppression was not applied for the proper evaluation of ion current under the strong influence of desorbed particles. The irradiated surfaces were analyzed by employing micro-Raman spectrometry, Atomic Force Microscopy (AFM), Fluorescent spectrometry and step-profiling with a Dectak machine. The step height change was evaluated referring to the pristine region in the same sample that was prepared by covering partly on a sample surface when irradiation.

3. Results and Discussion

In the course of irradiation the special cares were paid for ion beam integration because the materials properties of C_{60} films are expected to change from insulator into conductor depending on the nature of irradiation effect. Actually, the apparent incident ion current has increased after the incubation period where the release of desorbed molecules is operative. In this

course of study we found that the step height evaluation is more sensitive way to detect the subtle change of C_{60} surface with Raman analysis.

Fig. 1 illustrates the step-height change as a function of the fluence of C_{60}^+ ion. One can recognize the two stages feature. At the 1st stage, the step-height increase is detected but this is apparent phenomena coming from roughening on the irradiated area because Dektak machine is only sensitive to the height change but limited to the spatial resolution. The Raman analysis shows the intensity increase of $A_g(2)$ peak without appreciable peak-shift. This result suggests the improvement of C_{60} crystal quality. It is reasonable to consider the ejection of adsorbed oxygen molecules and the subsequent rearrangement as evidenced by the AFM micrographs in Fig. 2. As illustrated at the top part of Fig. 2, even just after the low fluence irradiation ($1.5x10^{15}/cm^2$), there appears the drastic topographic change from rounded C_{60} granules into well-facetted ones. This process could induce the apparent step-height increase.

At the 2nd stage, one can observe the linear decrease of step-height from zero to 40 nm within the fluence of $1.6x10^{16}/cm^2$ at room temperature. The corresponding change of Raman spectra features is as follows: The $A_g(2)$ peak corresponding to tangential mode of C_{60} intra-vibration was down-shifted linearly from 1462 to 1458 cm^{-1} by the irradiation up to $1.63x10^{16}/cm^2$. This change suggests strongly the polymerization associated with the rearrangement of partly broken C_{60} molecules through the collision process. The AFM analysis suggests also the existence of lineage structure but not for long polymerized chains. The step-height changes are fitted on the same line even though the samples with different thicknesses (200 nm-2100 nm) were used for the present experiment. This result implies that the irradiation effect remained even after sputtering is localized to almost the top surface-layer. The sputtering process was analyzed based on Winter-Sigmond approach and it is concluded that the step-height change is associated with C_2 molecule ejection from C_{60} molecule. The additional experiment gives us the favorable result that the sputtering ratio between α-Al_2O_3 and C_{60} in the present experiment is so close to the results for the sputtering ratio between α-Al_2O_3 and carbon.

References:

1) V. I. Lavrentiev, H. Abe, S. Yamamoto, H. Naramoto and K. Narumi, Physica B: Con. Matter 323 (2002) 303-305.
2) S. Sakai, Y. H. Xu, Tri Hardi Priyanto, V. Lavrentiev, K. Narumi and H. Naramoto, Proc. of Mater. Res. Soc. (2003, Boston).
3) H. Naramoto, X. D. Zhu, J. Vacik, Y. H. Xu, K. Narumi, S. Yamamoto and K. Miyashita, Phys. of the Solid State 44 (2002) 668-673.
4) X. D. Zhu, Y. H. Xu, H. Naramoto, K. Narumi, K. Miyashita, J. Phys. :Con. Matter 14 (2002) 5083.
5) X. D. Zhu, H. Naramoto, Y. H. Xu, K. Narumi, K. Miyashita, J. Chem. Phys. 116 (2002) 10458-10461.
6) X. D. Zhu, H. Naramoto, Y. H. Xu, K. Narumi, K. Miyashita, Phys. Rev. B 66 (2002) 165426.

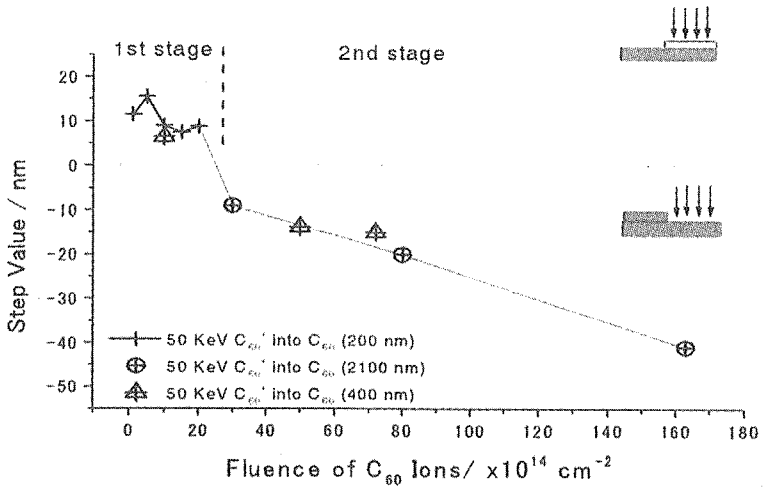

Fig. 1: Step-height change as a function of 50keV C_{60}^{+} ion fluence for three different samples. The 1st stage corresponds to apparent step-height increase associated with reordering of C_{60} molecule, and the 2nd stage does to sputtering associated with C_2 molecule ejection and the subsequent rearrangement on the surface.

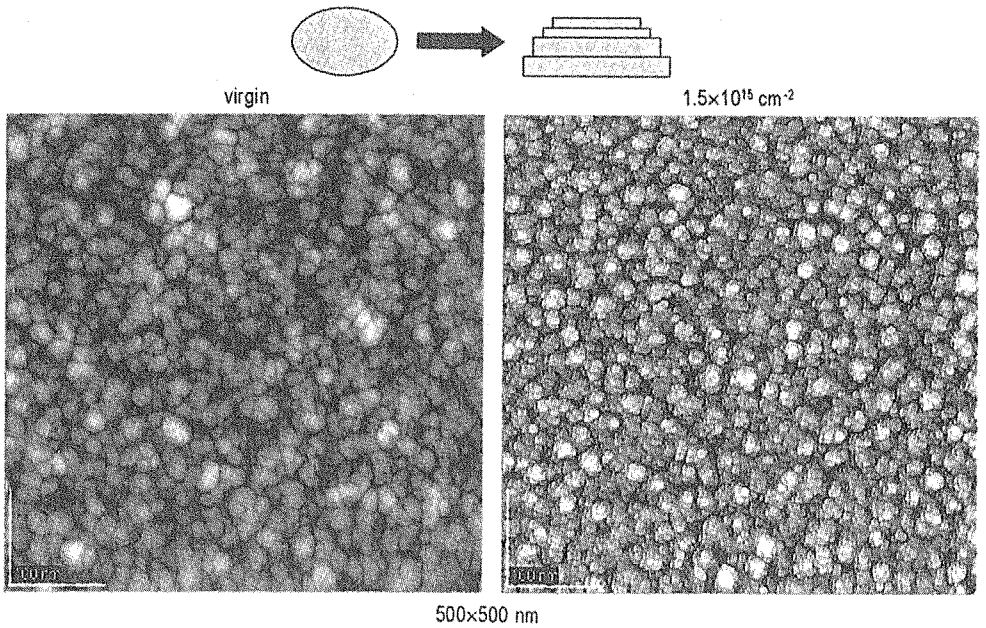

Fig. 2: AFM pictures taken from virgin (left) and irradiated region (right) on the sample irradiated within the low fluence region (1.5×10^{15}/cm^2). One can recognize the clear topographic change from granulitic into terrace-stacked surfaces.

5.5 Cobalt Ion Implantation into Nano-Porous Carbon Structures

V. Lavrentiev, H. Naramoto, K. Narumi and S. Kitazawa
Advanced Science Research Center, JAERI, Takasaki

1. Introduction

The mechanisms study of electronic interaction between carbon and transition metals (Me) has been essential and attractive during several decades. The discovery of C_{60} fullerene critically improved the interest because of the variety of possible Me-C_{60} electronic hybridizations suggesting intriguing nano-structures [1]. At the same time the wealth of possible Me-C_{60} bonding predicts the high sensitivity of final structure to the thermodynamic conditions and, as a consequence, to the preparation method. Recently we successfully combined Co and C_{60} using the simultaneous deposition technique [2]. Here we have tested the ion implantation to create buried Co-C_{60} layers important for application[3]. Expecting the destructive effects of the energetic ions we performed the similar ion implantation into glassy carbon (GC) to have the reference samples. A comparison between these low-density C-materials has provided the complementary information helpful during analysis of the post-implantation structural effects using approach reported in 4).

2. Experimental

Implantation of cobalt into C_{60} film and GC has been performed using 100 keV Co^+ ions at room temperature (RT) under UHV conditions (TIARA facilities, JAERI, Takasaki). Ion current during implantation process was kept at around 5 μA. Implantation doses were kept to be 3×10^{16} Co^+/cm^2 and 1×10^{17} Co^+/cm^2 in case of C_{60} film and GC, respectively. The value of Co concentration in C_{60} has been chosen to provide Co/C atomic ratio (0.02/0.98) generally used for creation of fullerene-based structures (see, for instance, 5)). Fullerene films have been grown at RT on (0001) α-Al_2O_3 up to thickness of 1200 nm by the thermal sublimation of pure C_{60} powder (99.99 mass. %C_{60}) in UHV vacuum. The glassy carbon samples were supplied by Tokai Carbon Co., Ltd. After Co-implantation the samples were annealed several times at 500°C. We analyzed the samples after each annealing step. The implanted samples were analyzed with Rutherford Backscattering Spectrometry (RBS) and Raman Spectrometry. Depth profiles of implanted Co have been simulated by RUMP codes.

3. Results and Discussion

Raman analysis of as-implanted C_{60} and GC revealed the broad peak between 900 and 1700 cm^{-1} reflecting the decomposition of C_{60} molecules and nano-graphitic units in glassy carbon and the appearance of disordered carbon in Co-irradiated area. The area is rather different in C_{60} and GC in spite of comparable average density (1.7 and 1.5 g/cm^3, respectively) implying the different nano-scale distribution of "vacuum" in these nano-porous materials. After the first post-implantation annealing, the composition in subsurface region of the samples remarkably changed. Although implanted Co in GC got received the reasonable shift to the sample surface the thermal response of that in C_{60} was opposite (Fig. 1). The depth profiles show that after the first annealing Co ions are situated within perfect fcc-C_{60} lattice. The appearance of 1448 cm^{-1} Raman peak suggests the charge transfer and the resultant Co-C_{60} bonding in the created buried layer.

The analysis of the implantation modified layers in C_{60} and GC after the thermal treatments revealed other interesting phenomena. We found the strong competition between thermal and chemical effects during the structure evolution in Co-doped amorphous carbon, resulting in the abnormal shift of Co away from the surface. The correlation between Raman and RBS results suggests the diffusion of Co atoms through C=C double bonds as a possible mechanism of the post-implantation structure evolution.

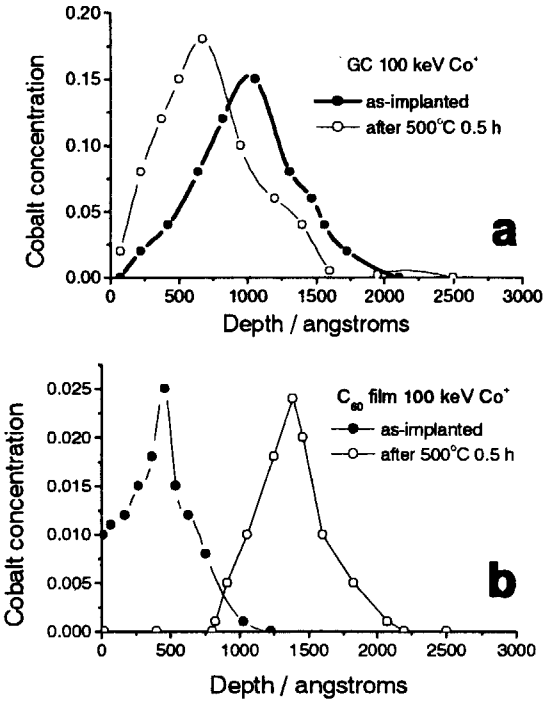

Figure 1: Depth profiles of cobalt implanted into GC (a) and C_{60} film (b) in as-implanted samples and after annealing at 500°C for 0.5 hours.

References

1) A. N. Andriotis et al., Phys. Rev. **B 62** (2000) 9867-9871.

2) V. Lavrentiev H. Abe, S. Yamamoto, H. Naramoto, K. Narumi, Surf. Interface Anal. **35** (2003) 36-39.

3) V. Lavrentiev, H. Abe, S. Yamamoto, H. Naramoto, K. Narumi, Physica **B 323,** (2002) 303-305.

4) A.C. Ferrari and J. Robertson, Phys. Rev. **B 61** (2000) 14095-14107.

5) A. Tess et al., Science **273** (1996) 483-487.

5.6 Ion-irradiation-induced Color Centers and Anti-Stokes Luminescence in Diamond

Y. Xu*, H. Naramoto*, K. Miyashita**, T. Kamiya***, S. Yamamoto***, T. Sakai****, T. Hamano****, and T. Suda****
Advanced Science Research Center, JAERI*,
Gunma Industrial Technology Center**,
Department of Material Development, JAERI***,
Advanced Radiation Technology Center, JAERI****

1. Introduction

Since diamond films were synthesized even at low pressure in 1968[1], the broad applications of diamond, particularly in optoelectronic devices, have been expected, attributing to its outstanding electronic and optical properties. During the time, ion beam technique has been extensively applied to analyze and to improve the structure and properties of diamond films. However, many kinds of defects are induced during ion irradiation, due to the severe energy dissipation beyond the binding energies.

In the present report, we describe the color centers induced by H^+ ion irradiation, which is usually used in ion beam analysis technique such as PIXE. To characterize the depth distribution of point defects in ion-irradiated diamond, a micro-Raman spectroscope with sub-micrometer spatial resolution was employed, and anti-Stokes luminescence has been observed from a selected area with high concentration of 3*H* color centers.

2. Experiment

A synthetic single crystal diamond (type II*a*) was used in this experiment. The concentration of the main impurity of nitrogen is less than 10 ppm. Ion bombardments were made into the diamond platelet from the side-face with a 2 MeV H^+ micro-beam at room temperature (100 p*A*, 1μm in diameter). The scanning area for bombardment was kept to be about 50× 50 μm^2 for the convenience of finding the irradiation spot for micro-Raman measurement. The doses employed are about $10^{16}/cm^2$.

A micro-Raman spectrometer with a confocal scanning microscope equipped with a 488 nm Ar^+ laser as the light source was used. In this spectrometer, a good spatial resolution (about 0.2 μm) is achieved using the confocal system. Moreover, an AFM scanning system is combined with the spectroscope. So, the position adjustment and Raman point mapping of the sample can be easily realized. In addition, another micro-Raman spectroscope with a 514 nm Ar^+ laser as the light source was also used to measure the samples for a comparison.

3. Results and Discussion

Figurer 1(a) shows a typical Raman spectrum of H^+-ion-irradiated diamond excited by 488 nm Ar^+ laser excitation. Very strong peaks can be observed, but these peaks correspond to neither the Raman peaks of diamond and graphite, nor that of amorphous carbon. Because the peaks at the same wavelength are observed when sample is excited by 514 nm wavelength (Figure 1(b)), all of the peaks at 504 nm, 518.6 nm, 534.7 nm, 541 nm, and 553 nm are considered to be induced through the photoluminescence. Comparing the peak positions and intensities with the reference data, it is confirmed that these peaks correspond

to the zero-phonon line or one-phonon lines of 3*H* color centers in diamond. In the emission spectrum, a peak at 742 nm is also observed. This peak is from luminescence too, being associated with *GR*1 color centers.

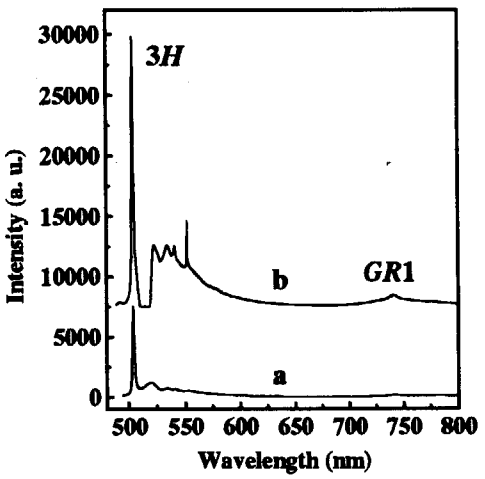

Figure 1. Raman spectra of H^+-irradiated diamond with a 488 nm Ar^+ laser (a) and a 514 nm Ar^+ laser (b).

Because H^+ ions were irradiated into the side-face of the diamond platelet, the depth-profiles of ion-irradiation-induced defects can be easily characterized from the top-face of the diamond platelet. Figure 2 (a) shows the intensity changes of 3*H* and *GR*1 color centers along the depth from the irradiated side. It should be pointed out that the intensities of 3*H* and *GR*1 at the specified position were simultaneously obtained, and that each datum is only related with the information of vary small area due to the high spatial resolution of Raman spectroscope. It is observed that the intensities for both 3*H* emission and *GR*1 emission increase along the depth and get the maximum at about 22.3μm, while the intensity of *GR*1 emission changes more slowly than that of 3*H* emission along the depth. A relation of $I_{3H} \propto I_{GR1}^{2.62}$ is found, when we plot the 3*H* intensity (I_{3H}) with *GR*1 intensity (I_{GR1}), as shown in Fig. 2 (b). Although 3*H* luminescence is considered to be associated with interstitial-type color centers in diamond, whether they are single isolated, di-, or other interstitials has not been identified up to now [2), 3)]. However, it can be inferred that the 3*H* emission probably is related with tri-interstitials, based on the result in Fig. 2, as knowing that *GR*1 emission comes from single isolated neutral vacancy [4)].

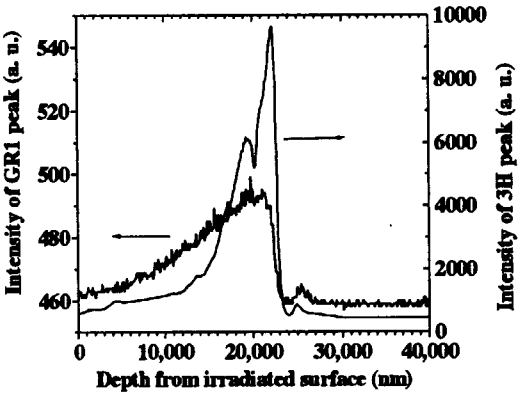

(a)

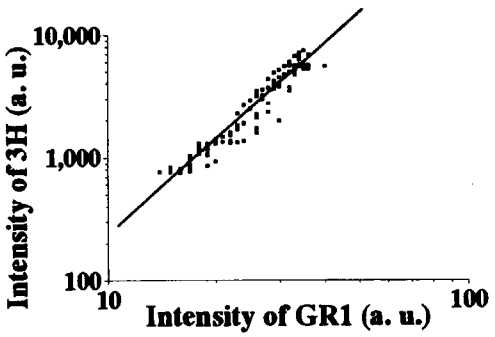

(b)

Figure 2. (a) Intensity changes of 3*H* and GR1 with the depth of ion implantation. (b) Relationship between the intensities of 3*H* and GR1.

Now, returning back to Fig 1 (b), a strong peak at 504 nm is observed even though the excitation wavelength is as long as 514 nm. This emission is called as anti-Stokes luminescence (ASL). To our knowledge, such strong ASL phenomenon has not been reported in diamond

up to now. At ASL, the energy of the emitted photons is higher than that of the incident photons, therefore, it is necessary for the system to obtain additional energies, except for the incident photon energy, during the absorption and emission process of photons. Generally, ASL is caused by multi-photon absorption, Auger recombination, or thermal energy absorption, *etc*. It is reasonably considered in the present case that ASL arises from a simultaneous phonon-absorption process during photon absorption which leads to the electronic transition from the ground states to the excited states.

References

1) B. V. Derjaguin et al., J. Cryst. Growth 2 (1968) 380.
2) J. W. Steeds et al., Diamond Relat. Mater. 8 (1999) 1847.
3) J. P. Goss et al., Phys. Rev. B 63 (2001) 195208.
4) G. Davies et al., Phys. Rev. B 46 (1992) 13157.

5.7 Ion-Irradiation-Induced Resistance to Photopolymerization of C_{60} Thin Films

Kazumasa Narumi*, Yonghua Xu*, Kiyoshi Miyashita** and Hiroshi Naramoto*
Advanced Science Research Center, JAERI*
Gunma Prefectural Industrial Technology Research Laboratory**

1. Introduction

Ion-irradiation effect of solid state C_{60} has been investigated by many researchers and the primary effect is destruction of the molecule: Energetic-ion impact leads to destruction of cage structure in a C_{60} solid[1-3]. FTIR and Raman analyses have revealed that no intermediate fragments of a C_{60} molecules are generated by ion impact[1-3]. On the other hand, solid state C_{60} can be transformed by UV-visible light to a polymeric phase[4]. It has been proposed that in the photopolymer, C_{60} molecules are linked by covalent bonds via a photochemical 2 + 2 cycloaddition reaction in which the double bonds on neighboring C_{60} molecules are broken and reformed as a four-membered ring. This process can be monitored by characteristic peak splittings and shifts in Raman and other vibrational spectra with regard to pristine C_{60}.

In the present study, ion-irradiation effect on photopolymerization in a C_{60} solid is investigated with the use of Raman spectroscopy. We observe the resistance of ion-irradiated films to the photopolymerization, which is explained by the fact that the number of a C_{60} pair satisfying the topochemical requirement for photochemical reaction in solids decreases by ion-induced decomposition of the C_{60} molecules accompanied by lattice disorder.

2. Experimental

Thin films of C_{60} were prepared by molecular beam epitaxy on Si(111) substrates. A surface oxide of the substrate was removed by immersing in a 5% HF solution. Pure C_{60} powder of 99.99 % (Term USA) was loaded into a Knudsen cell in a deposition chamber whose base pressure was 1×10^{-6} Pa. During the deposition, the temperature of the substrates was kept at 165 'C and a deposition rate was about 0.6 nm/min. The pressure in the chamber was lower than 5×10^{-6} Pa during the deposition. After the deposition, the specimens were irradiated at room temperature with 7-MeV $^{12}C^{2+}$ ions from the 3-MV Tandem accelerator of JAERI/Takasaki in an irradiation chamber, whose base pressure was 1×10^{-5} Pa. The films were about 190 nm thick so that almost all of C ions could pass through the film. Current density was around 200 nA/cm^2. Raman spectra were measured in air with Renishaw Ramascope 2000 μ-Raman system using a fixed grating angle and 514.5 nm radiation from an Ar^+ laser. The spot size of the laser was estimated to be about 3μm.

3. Results and Discussion

Figure 1 shows the dependence of Raman spectra around the "pentagonal pinch" mode for an unirradiated film on power density of the Ar^+ laser. Each of the spectra was measured with accumulation time of 120 s with the power density indicated in the figure. The Ar^+ laser illuminated the specimen just only during the accumulation of a spectrum. The Raman intensity of the line at 1469 cm^{-1} decreases with increasing power density, while a shoulder at the lower-frequency side of the line becomes prominent. The result of Lorentzian-line-fit analysis for the spectrum measured with 7100 W/cm^2 is shown in the inset, which demonstrates

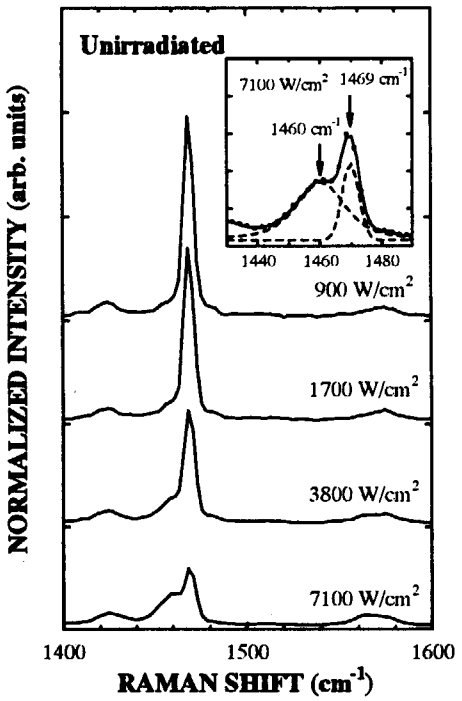

Fig. 1 Dependence of Raman spectra for an unirradiated specimen on power density of the Ar^+ laser. Inset shows Lorentzian-line-fit analysis of the Raman spectrum measured with 7100 W/cm^2.

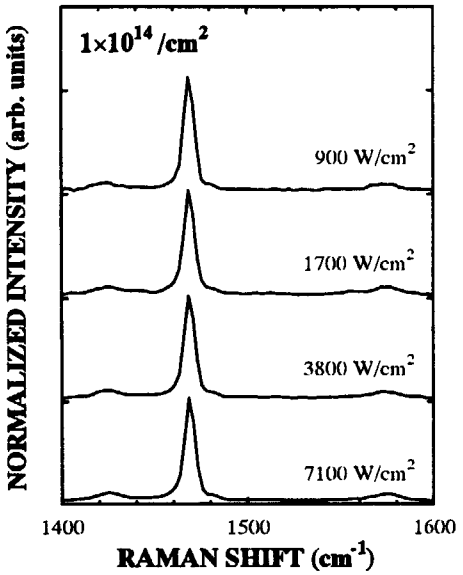

Fig. 2 Dependence of Raman spectra for a specimen irradiated with the fluence of 1.0×10^{14} cm^2 on power density of the Ar^+ laser.

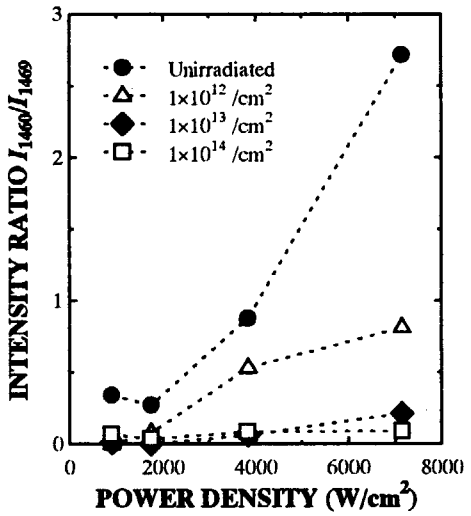

Fig. 3 Laser-power dependence of integrated-intensity ratio of the Raman band due to a polymeric phase to that of the line at 1469 cm^{-1} peak for four different fluences. Broken lines are guide to the eye.

that the shoulder is attributed to the Raman band at 1460 cm^{-1} due to a polymeric phase of C_{60}[5]. Figure 1 indicates that the Ar^+ laser illumination photopolymerizes C_{60} in the film during the collection of a spectrum.

On the other hand, Fig. 2 shows the change of the Raman spectrum for a C_{60} film irradiated with 1.0×10^{14} /cm^2, where all of the spectra were measured on the same conditions as those in Fig. 1. Contrary to the result shown in Fig. 1, the spectra do not depend on the laser power and the Raman band due to a polymeric phase is hardly observed. Figure 3 shows ratio of integrated peak intensity of the Raman band due to a polymeric phase to that of the line at 1469 cm^{-1} as a function of the laser power for four different ion fluences. Integrated peak intensity was determined by the Lorentzian-curve-fitting analysis of the obtained Raman spectra. As inferred easily from Fig. 1, the ratio for the unirradiated film increases with increasing power density of the laser. Such a change is also observed except for the film irradiated with 1×10^{14} /cm^2 and the variation becomes smaller as the ion fluence increases. On the other hand, for the film irradiated with 1×10^{14} /cm^2, the ratio is so small and hardly depends on the power density of the laser as inferred from Fig. 2.

Figure 3 clearly indicates that ion-irradiated films are resistant to photopolymerization and that the resistance increases with increasing ion fluence. This can

be qualitatively explained by the topochemical requirement for the photochemical 2 + 2 cycloaddition reaction in solids and destructive collisions of the C_{60} molecules with energetic ions accompanied by lattice disorder. At first, let us consider photochemical reaction in a C_{60} solid. According to the topochemical requirement for photochemical reaction in molecular solids, the photopolymerization is active when two carbon double bonds on adjacent molecules are oriented parallel to one another and separated by less than 0.42 nm[6, 7]. In the fcc structure of a C_{60} crystal, the distance between adjacent molecules is as small as 0.29 nm[8]. A C_{60} molecule has 30 double bonds and spins freely about randomly oriented axes on fcc lattice positions at room temperature; thus the probability that two double bonds on adjacent molecules are oriented parallel to one another is high. Therefore, the topochemical requirement is satisfied in a C_{60} crystal. On the other hand, ion irradiation of C_{60} films leads to complete decomposition of each molecule into its constituent atoms[1-3]. In the present study, the number of the C_{60} molecule surviving ion bombardment decreases exponentially with increasing ion fluence: it was estimated that about 30 % of C_{60} molecules in an as-deposited film was destroyed after the irradiation of the fluence of 1×10^{14} /cm^2. Thus the number of the molecules involved in photopolymerization decrease with increasing ion fluence. Furthermore, the decomposition of molecules induces lattice disorder. The disorder of the crystal lattice induces change of the distance between adjacent molecules. Because of these two reasons, the number of the adjacent-molecule pairs satisfying the topochemical requirement decreases with increasing ion fluence. Therefore, the photopolymerization is suppressed for the ion-irradiated films.

In conclusion, we mention application of the effect observed in the present study: It has potential to make it possible to control polymerization although the effect accompanies the destruction of the molecules. In addition, the same effect is expected in the case of pressure-induced polymerization, because the covalent linking between the C_{60} molecules has also been proposed to be via the 2 + 2 cycloaddition reaction in the pressure-induced C_{60} polymers[9].

References

1) R.G. Musket, R.A. Hawley-Fedder and W.L. Bell, Radiat. Eff. Defects **118** (1991) 225.
2) S. Prawer, K.W. Nugent, S. Biggs, D.G. McCulloch, W.H. Leong, A. Hoffman and R. Kalish, Phys. Rev. B **52** (1995) 841
3) J. Kastner, H. Kuzmany and L. Palmetshofer, Appl. Phys. Lett. **65** (1994) 543.
4) A.M. Rao, P. Zhou, K.-A. Wang, G.T. Hager, J.M. Holden, Y. Wang, W.-T. Lee, X.-X. Bi, P.C. Eklund, D.S. Cornett, M.A. Duncan and I.J. Amster, Science **259** (1993) 955.
5) P.C. Eklund, A.M. Rao, P. Zhou, Y. Wang and J.M. Holden, Thin Solid Films **257** (1995) 185.
6) K. Venkatesan and V. Ramamurthy, Photochemistry in organized &Constrained Media, ed. V. Ramamurthy (VCH, Weinheim, 1991) Ch. 4, p. 133.
7) P. Zhou, Z.-H. Dong, A.M. Rao and P.C. Eklund, Chem. Phys. Lett. **211** (1993) 337.
8) M.S. Dresselhous, G. Dresselhous and P.C. Eklund, Science of Fullerenes and Carbon Nanotubes, (Academic Press, San Diego, 1996) Ch. 7, p. 171.
9) M. Núñez-Regueiro, L. Marques, J-L. Hodeau, O. Béthoux and M. Perroux, Phys. Rev. Lett. **74** (1995) 278.

5.8 Defect Creation due to X-ray Irradiation and Electron Irradiation in $EuBa_2Cu_3O_6$

N. Ishikawa*, Y. Chimi*, A. Iwase*, H.Wakana**, T. Hashimoto**, O. Michikami**

Department of Materials Science, JAERI*

Faculty of Engineering, Iwate University**

1.Introduction

High energy (several keV) X-ray causes electronic excitation which may cause atomic displacements, but so far little experimental proof is reported for atomic displacements after high-energy X-ray irradiation. If the electronic excitation due to X-ray irradiation causes atomic displacements, then this may be attributed to the creation of high energy δ electrons and/or Coulomb repulsion between ionized constituent atoms. The atomic displacements due to high energy δ electrons can be simulated by directly irradiating energetic electrons to samples. The objective of this work is to detect the small amount of atomic displacements due to high-energy X-ray, and to simulate the effect of δ electrons by irradiating the target with energetic electrons. In the previous work, we found that increase in electrical resistivity is observed in $EuBa_2Cu_3O_y$ (y=6-7) as a result of defect creation due to electron irradiation, and the sensitivity to electron irradiation is greatly increased by decreasing the oxygen content. From this result it can be learned that oxygen-deficient $EuBa_2Cu_3O_y$ (y=6) is a appropriate specimen to detect a small amount of defect creation due to some irradiation. Based on this recognition, we tried to detect the effect of irradiation with high-energy (several keV) X-ray by using the oxygen-deficient $EuBa_2Cu_3O_y$.

2.Experimental Procedure

In order to prepare the oxygen-deficient samples a c-axis oriented $EuBa_2Cu_3O_y$ (y=7) thin film was prepared on MgO substrate, and it was heated in low oxygen partial pressure. The oxygen-deficient $EuBa_2Cu_3O_y$ was expected to have oxygen content of nearly y=6, since its c-axis lattice parameter was larger by 1.2% than that of $EuBa_2Cu_3O_y$ (y=7). The specimens were irradiated at 100K with 9.07keV X-ray. The X-ray irradiation was performed at Photon Factory of the High Energy Accelerator Research Organization (KEK, Tsukuba). In order to avoid the possible irradiation effect of the electrode, the rectangular-shaped slit was placed on the sample, and only the sample part was irradiated. In-situ measurement of change in resistivity during the irradiation was performed at 100K. The electrical resistivity is measured by the conventional four-probe method. We performed also the irradiation with 0.46MeV electrons from a 3MV single-ended accelerator in TIARA, JAERI-Takasaki, in the same way as the irradiation with X-ray. The energy of 0.46MeV was chosen because this is the lowest energy achievable by the accelerator for simulating the δ electron irradiation.

3.Results and Discussion

Figure 1 shows the resistivity change as a

function of irradiation time in $EuBa_2Cu_3O_y$ (y=6) irradiated with 9.07keV X-ray. Resistivity increase is observed only during the irradiation, indicating the lattice defects are created due to ionization by the irradiation. It is surprising in a sense that such a low density electronic excitation can lead to atomic motion. The resistivity change shows a saturating behavior. Figure 2 shows the resistivity change as a function of electron fluence in $EuBa_2Cu_3O_y$ (y=6) irradiated with 0.46MeV electrons. From this result it is found that the increase in resistivity due to electron irradiation is also monotonic and slightly saturating. Both saturating behaviors indicate that both of the irradiations create defects part of which is annihilated by recombining with the defects already created by the previous irradiation.

It is supposed that the δ electrons created by X-ray irradiation can be a cause of atomic motion from the results of electron irradiation experiments. It is already known that for electron irradiation elastic displacements are the cause of defect creation[1]. For X-ray irradiation, electrons are created as a result of ionization, and it is still controversial whether or not electrons created by X-ray irradiation give sufficient energy for atoms to displace. Quantitative analysis is necessary to examine whether the mechanism of atomic displacements due to electron irradiation is really the same as those due to δ electrons created by high energy X-ray irradiation.

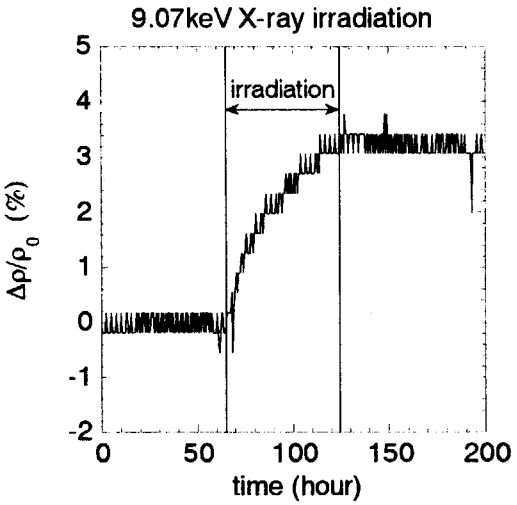

Fig.1 Change in resistivity normalized by the resistivity before irradiation plotted as a function of time for $EuBa_2Cu_3O_y$ (y=6) irradiated with 9.07keV X-ray. The irradiation time is indicated in the figure.

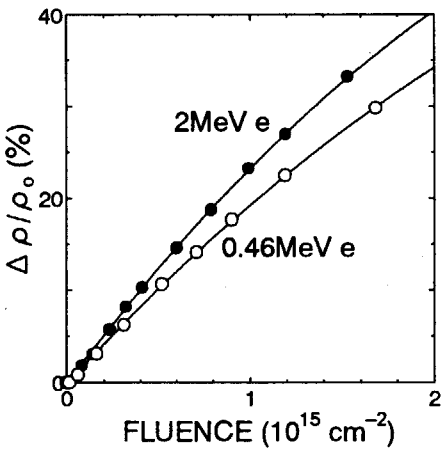

Fig.2 Change in resistivity normalized by the resisitivity before irradiation plotted as a function of fluence for $EuBa_2Cu_3O_y$ (y=6) irradiated with 0.46MeV electrons. The result for 2MeV irradiation is also shown for reference.

Reference

1)N. Ishikawa, Y. Chimi, A. Iwase, K. Tsuru and O. Michikami, J. Nucl. Mater. 258-263 (1998) 1924.

5.9 Electron Beam Energy Dependence of Cross-Section for Production of Frenkel Pairs in Nanocrystalline Gold

Y. Chimi*, A. Iwase*, N. Ishikawa*, M. Kobiyama**, T. Inami**, S. Okuda***
Department of Materials Science, JAERI*
Department of Engineering, Ibaraki University**
Emeritus Professor, University of Tsukuba***

1. Introduction

Nanocrystalline materials consist of crystal grains with much smaller size (below several-tens nm) than those in ordinary polycrystalline materials. Therefore, nanocrystalline materials are expected to be irradiation-resistant due to a large volume fraction of grain boundaries, which might work as effective sinks for irradiation-produced defects. We have studied irradiation behavior of nanocrystalline gold (nano-Au) with energetic particles[1),2)], and have found that nano-Au is irradiation-resistant under the condition that irradiation-produced defects can be diffused thermally, but at low temperature where diffusion of defects is suppressed the defect production is easier by irradiation in nano-Au than in polycrystalline gold (poly-Au). This result can be explained by assuming lower displacement threshold energy (E_d) in nano-Au than in poly-Au.

In the present work, in order to study the lowering of E_d in nano-Au, dependence of cross-section for production of Frenkel pairs on electron beam energy is investigated.

2. Experimental Procedure

A nano-Au foil (~8.6 μm thick) was prepared by the gas deposition method. Estimated average grain size of the specimen was ~20 nm. The specimen was irradiated below ~17 K with 0.5 or 2.0 MeV electrons from a 3 MV single-ended accelerator in TIARA, JAERI-Takasaki. The change in electrical resistivity of the specimen was measured *in situ* at ~11 K as a function of electron fluence. Electrons with two kinds of energy, 0.5 and 2.0 MeV, were irradiated by turns. For comparison, a poly-Au foil (11.2 μm thick), which had been annealed at 873 K for ~1h in a vacuum below 4×10^{-7} Torr before irradiation, was placed adjacent to the nano-Au foil, and those foils were irradiated and measured simultaneously.

3. Results and Discussion

Figure 1 shows the change in electrical resistivity, $\Delta\rho$, of nano- and poly-Au specimens as a function of electron fluence, Φ. This figure indicates accumulation behavior of irradiation-produced defects in the specimens. For poly-Au specimen, little change in resistivity during 0.5 MeV electron irradiation is observed, and this is ordinary behavior in consideration of E_d = 43 eV for gold[3)]. For nano-Au specimen, on the other hand, resistivity change rate, $d(\Delta\rho)/d\Phi$, is much larger than that for poly-Au. Moreover, the value of $d(\Delta\rho)/d\Phi$ depends strongly on electron beam energy; $d(\Delta\rho)/d\Phi$ during 0.5 MeV electron irradiation is larger than that during 2.0 MeV electron irradiation. In order to estimate the cross-sections for production of Frenkel pairs, $d(\Delta\rho)/d\Phi$ is plotted against $\Delta\rho$ as shown in Fig. 2. For the analysis, the following general rate equation was used;

$$\frac{d(\Delta\rho)}{d\Phi} = \rho_F\left(\frac{dC}{d\Phi}\right) = \rho_F(\sigma_d - \sigma_r C), \quad (1)$$

where C is the concentration of

irradiation-produced Frenkel pairs, ρ_F the resistivity contribution of Frenkel pairs (250 μΩcm/u.c.[3]), and σ_d and σ_r the cross-sections for production and annihilation of Frenkel pairs, respectively. On the assumption that ρ_F for nano-Au is the same as poly-Au, dependence of σ_d for each specimen on electron beam energy is shown in Table 1. For 2.0 MeV electron irradiation, σ_d calculated by using NRT model with E_d = 43 eV, σ_d^{cal}, is 1.4×10^{-23} cm^2, so that the damage efficiency, $\xi \equiv \sigma_d / \sigma_d^{cal}$, becomes 1.9 and 11 for poly- and nano-Au, respectively. The value for nano-Au is much higher than that for poly-Au. This result can be explained by lowering of E_d in nano-Au[2]. For nano-Au, moreover, σ_d for 0.5 MeV electron irradiation is ~1.5 times larger than that for 2.0 MeV electron irradiation. This energy dependence is quite opposite to that for poly-Au, so that it is impossible to estimate E_d in nano-Au by means of a conventional method[4]. Therefore, this energy dependence cannot be explained only as effective lowering of E_d in nano-Au. The reason for this interesting phenomenon is still unknown.

Table 1. Dependence of cross-sections for production of Frenkel pairs, σ_d, for each specimen on electron beam energy.

Energy	σ_d for poly-Au	σ_d for nano-Au
0.5 MeV	———	2.3×10^{-22} cm^2
2.0 MeV	2.7×10^{-23} cm^2	1.5×10^{-22} cm^2

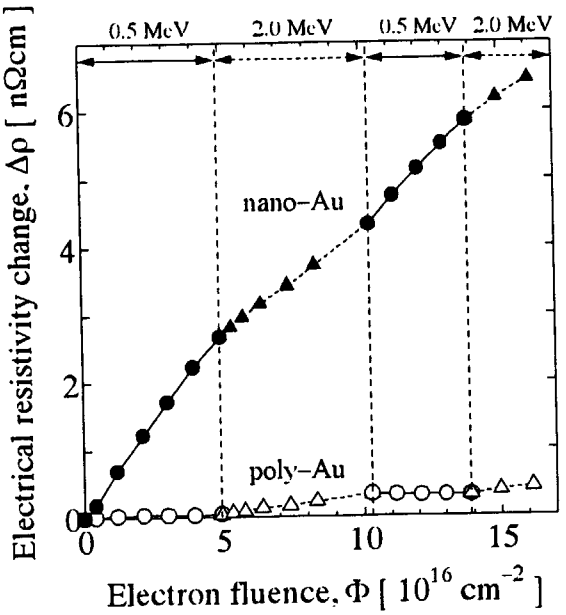

Fig. 1. Change in electrical resistivity, Δρ, of nano- and poly-Au specimens as a function of electron fluence, Φ.

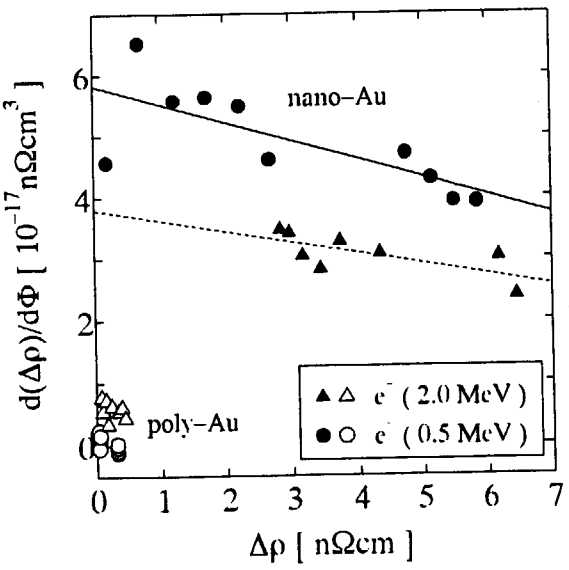

Fig. 2. Resistivity change rate, d(Δρ)/dΦ, for nano- and poly-Au specimens as a function of resistivity change, Δρ.

References

1) Y. Chimi, A. Iwase, N. Ishikawa, M. Kobiyama, T. Inami, S. Okuda, J. Nucl. Mater. **297** (2001) 355.

2) Y. Chimi, Doctor of Engineering thesis, Osaka University, January 2003 (in Japanese).

3) P. Ehrhart, P. Jung, H. Schultz, H. Ullmaier, in: H. Ullmaier (Ed.), Atomic Defects in Metals, Landolt-Börnstein, Numerical Data and Functional Relationships in Science and Technology, Springer, Berlin, 1991, Group III, vol. 25.

4) F. Seitz, J.S. Koehler, in: F. Seitz, D. Turnbull (Eds.), Solid State Physics, vol. 2, Academic Press, New York, 1956, p. 305.

5.10 Study on Processes of Radiation-Enhanced Segregation in Fe-Cu Model Alloys for Pressure Vessel Steels of Light Water Reactors

Y. Chimi*, A. Iwase*, T. Tobita**, N. Ishikawa*, M. Suzuki**, S. Ishino***
Department of Materials Science, JAERI*
Department of Reactor Safety Research, JAERI**
Department of Applied Science, Tokai University***

1. Introduction

Fe-Cu alloys are well-known as model alloys for studying a mechanism of irradiation embrittlement in pressure vessel steels of light water reactors. One of the major reasons of the irradiation embrittlement is that segregation of solute Cu atoms in the material is enhanced by irradiation, which is called "Radiation-Enhanced Segregation". Thermal diffusion of irradiation-produced defects accompanied with transportation of Cu atoms correlates to the segregation. Especially, irradiation with γ-ray emitted from fission reaction contributes strongly to the radiation-enhanced segregation, since γ-ray irradiation produces Frenkel pairs through energetic electron irradiation via Compton scattering and/or pair creation in the pressure vessel steels. We have studied the processes of the radiation-enhanced segregation of Cu atoms in Fe-Cu model alloys for pressure vessel steels [1–4]. In the present work, as a simulation of γ-ray irradiation, energetic electrons are irradiated to Fe-Cu alloys with several Cu concentrations in order to introduce Frenkel pairs effectively. The segregation of Cu atoms is studied by measuring the change in electrical resistivity of the Fe-Cu alloys, focusing on the dependence of Cu concentration.

2. Experimental Procedure

Four kinds of Fe-Cu alloys with different Cu concentration (0.02, 0.1, 0.6 and 1.2 wt.%) were used as specimens. The chemical composition of the specimens is shown in Table 1. The specimens were solution-annealed at 1123 K for 10 min under a vacuum, and then quenched into helium gas. This process made Cu atoms dissolve supersaturatedly in the iron lattice. The size of the specimen was 1 mm × 10 mm × 30 μm. Fe-Cu alloy ribbons, which had the same Cu concentration as the specimens, were spot-welded to the specimens as lead wires for electrical resistivity measurement. The specimens were mounted on aluminum substrates by using epoxy resin (Araldite) in order to insulate the specimens from the substrates. The specimens were irradiated at ~300 K with 2.0 MeV electrons from a 3 MV single-ended accelerator in TIARA, JAERI-Takasaki. The change in electrical resistivity of each specimen, Δρ, was measured *in situ* at 300K as a function of electron fluence during irradiation.

3. Results and Discussion

Figure 1 shows the change in electrical resistivity of the specimens as a function of irradiation dose. For each specimen, Δρ decreases linearly with increasing dose except for an increase in Δρ at the beginning of irradiation. This decrease in Δρ means that the solute Cu concentration in the iron lattice decreases due to the segregation of Cu atoms. The increase in Δρ at the beginning, on the other hand, implies that the defect clusters, which will be nucleation sites for the segregation of Cu

atoms, are growing up during irradiation. The dependence of resistivity decreasing rate on Cu concentration above 10 μdpa is shown in Fig. 2. The decreasing rate seems to be larger for higher Cu concentration. According to experimental results of low-temperature irradiation, however, it appears that the resistivity contribution of a Frenkel pair depends on Cu concentration. Therefore, the resistivity contribution per unit Cu concentration may also depend on Cu concentration. We have to treat the results of Cu concentration dependence very carefully.

References

1) T. Tobita, M. Suzuki, A. Iwase, K. Aizawa, J. Nucl. Mater. **299** (2001) 267.
2) K. Morita, S. Ishino, T. Tobita, Y. Chimi, N. Ishikawa, A. Iwase, J. Nucl. Mater. **304** (2002) 153.
3) A. Iwase, T. Hasegawa, Y. Chimi, T. Tobita, N. Ishikawa, M. Suzuki, T. Kambara, S. Ishino, Nucl. Instr. and Meth. B **195** (2002) 309.
4) S. Ishino, Y. Chimi, Bagiyono, T. Tobita, N. Ishikawa, M. Suzuki, A. Iwase, J. Nucl. Mater. (2003), in press.

Table 1. Chemical composition of specimens in wt.%.

Specimen	Cu	C	Si	O	N	Fe
Fe-0.02wt.%Cu	0.022	0.003	0.003	0.015	0.0006	Balance
Fe-0.1wt.%Cu	0.1	0.002	0.003	0.014	0.0005	Balance
Fe-0.6wt.%Cu	0.61	0.002	0.002	0.015	0.0006	Balance
Fe-1.2wt.%Cu	0.19	0.002	0.001	0.013	0.0006	Balance

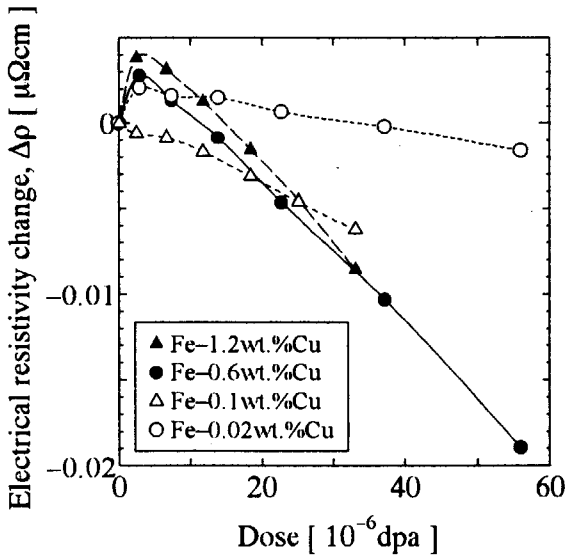

Fig. 1. Change in electrical resistivity of specimens as a function of irradiation dose.

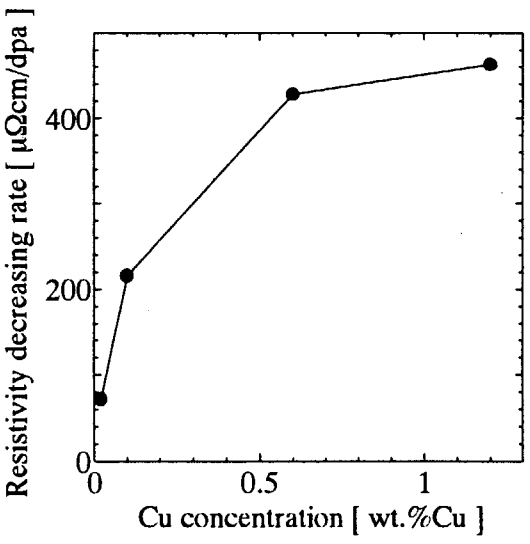

Fig. 2. Cu concentration dependence of resistivity decreasing rate.

5.11 Radiation Effects on Li-Vacancy Ordering in NaTl-type Li Compound

M.Yahagi*, T. Hashimoto*, H. Sugai**, A. Iwase***, Y. Chimi***,
N. Ishikawa***, H. Hamanaka**** and K. Kuriyama****
Faculty of Engineering, Aomori University*,
Department of Research Reactor, JAERI**,
Department of Materials Science, JAERI***,
College of Engineering and Research Center of Ion Beam Technology,
Hosei University****

1. Introduction

β-LiAl has a large constitutional defect concentration at room temperature[1]. The defect structure is composed of vacancies in the Li sublattice (free V_{Li}), Li anti-structure atoms in the Al sublattice (free Li_{Al}), and complex defects (V_{Li}-Li_{Al}). However, this compound maintains a well-defined structure (NaTl structure[2]) over a homogeneity β phase (48-56 at.%Li). It is assumed that the low value (~0.15 eV)[3] of the activation energy for the diffusion of Li^+ ion is associated with a large concentration of free V_{Li} on the Li sublattice. Therefore, β-LiAl has been considered as a possible electrode materials for rechargeable lithium batteries[4,5] , because the Li^+ ions can move easily through these free V_{Li}.

β-LiAl has some distinctive features as follows ; the electrical resistivity is considerably affected by these defect structures[1]. Furthermore, an abrupt change in the resistivity[6] and heat-capacity[7] at 95K is closely correlated with the low-temperature order-disorder transition of Li vacancies.

The radiation effects by electron irradiation in β-LiAl with about 48.2 at.%Li make it clear that Frenkel-type defects composed of Li interstitial and V_{Li} pair are produced by the knock on of Li atoms which orderly arrange in Li sublattice sites, but there are a few of Frenkel-type defects, consist of Al interstitial and Al vacancy pair, produced by electron irradiation[8].

In this report, we describe the radiation effects for Li anti-structure atoms in Al sublattice in β-LiAl with about 49.0 at.%Li, due to Li atom ejected by electron irradiation.

2. Experimental Procedure

β-LiAl was prepared by direct reaction of equimolar amounts of Li (99.9% pure) and Al (99.999% pure) as reported earlier[9]. Li content of sample was estimated to be about 49.0 at.%Li from the value of the resistivity. Electron irradiation was performed at below 40K using a 3MV single-ended accelerator in TIARA (JAERI-Takasaki). 2 MeV-electron were used in this study. The fluence dependence of electrical resistivity was measured at below 40K using the van der Pauw method after stopping electron irradiation for a time.

3. Results and Discussion

Figure 1 shows the electron-fluence dependence of resistivity ρ_A of β-LiAl at temperature below 40K. ρ_A is the average of the resistivity measured over a temperature from 14 to

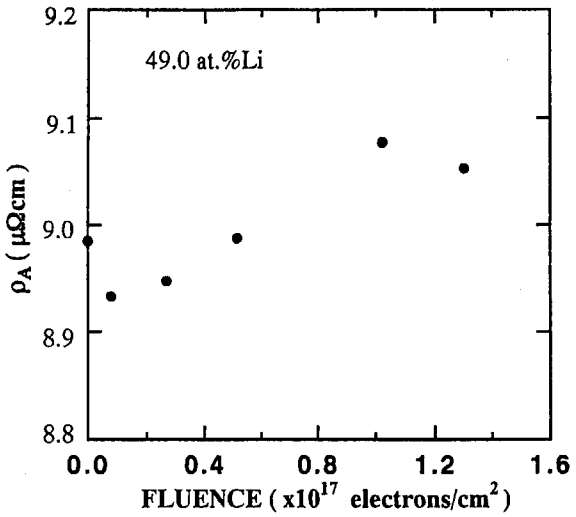

Fig.1 Electron-fluence dependence of resistivity for β–LiAl with C_{Li} = 49.0 at.%Li.

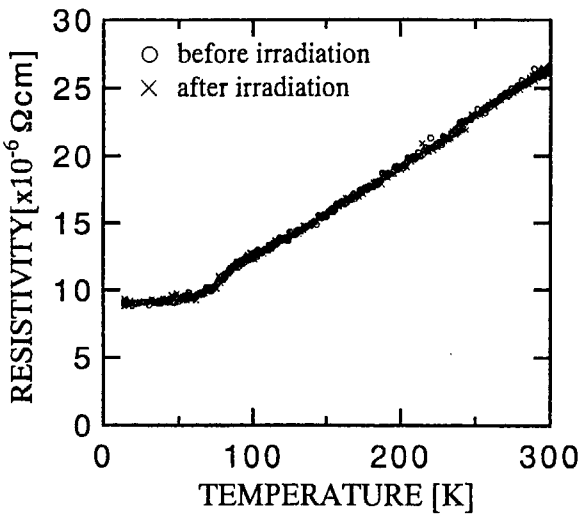

Fig.2 Temperature dependent electrical resistivity of β-LiAl before and after irradiation.

33 K. Figure 2 shows the temperature dependence of resistivity of β- LiAl before and after electron irradiation. The electron-fluence is about 1.3x10^{17} electrons /cm^2.

As shown in Fig. 1, ρ_A increases slightly with the electron-fluence. This tendency seems to have the same tendency as one reported previously[8]. This specimen (49.0at.%Li) contains the defect concentration of free V_{Li} (2.35%) and V_{Li}-Li_{Al}(0.33%). The Latter V_{Li}-Li_{Al} complex defects cause an increase in the resistivity, since this defect (valency -3) consist of V_{Li} (valency -1) and Li_{Al} (valency -2) is much more effective as scatteres than V_{Li} (valency -1)[1]. If Li_{Al} in V_{Li}-Li_{Al} complex defect is ejected by electron irradiation, V_{Li}-V_{Al} complex defects are created and the valency will be -4. Therefore, it is assumed that the resistivity of β-LiAl with 49.0 at.%Li after electron irradiation shows high resistivity than that in β-LiAl with 48.2 at.%Li (a few of V_{Li}-Li_{Al} complex defects) as reported previously[8]. However, there is no difference in the resistivities of β-LiAl with 48.2 and 49.0 at.%Li after electron irradiation. This result suggests that Li_{Al} in V_{Li}-Li_{Al} complex defect is not ejected by electron irradiation, and Frenkel-type defects composed of Li interstital and V_{Li} pair are only produced by the knock on of Li atoms which orderly arrange in Li sublattice sites.

The temperature dependence of resistivity after electron irradiation coincides with that before electron irradiation as shown in Fig.2. This behavior is similar to that for β-LiAl with 48.2at.%Li except on the region of the ordering temperature. This suggests that there are a few of Frenkel-type defects, consisting of Al interstitial and Al vacancy pair produced by electron irradiation.

Hereafter, we wish to clarify a relation between a interaction of V_{Li}-V_{Li} and the diffusion mechanism of Li^+ ion in β-LiAl according to the energy-dependence and Li-content dependence of electron irradiation.

References

1) H.Sugai, M.Tanase, M.Yahagi, T.Ashida, H.Hamanaka, K.Kuriyama, and K.Iwamura, Phys. Rev. B52 (1995) 4050.
2) E.Zintl and G.Brauer, Z. Phys. Chem. B20 (1933) 245.
3) H.E.Schone and W.D.Knight, Acta Metall. 11 (1936) 179.
4) C.H.Wen, B.A.Boukamp, R.A.Huggins,

and W.Wepner, J.Electrochem. Soc. 126 (1979) 2258.
5) C.J.Wen and R.A.Huggins, J. Electrochem. Soc. 128 (1981) 1636.
6) K.Kuriyama, T.Kamijoh, and T.Nozaki, Phys. Rev. B22 (1980) 470.
7) K.Kuriyama, S.Yanada, T.Nozaki, and T.Kamijoh, Phys. Rev. B24 (1981) 6185.
8) M.Yahagi, et al., JAERI-Review 2002-035, (2002)191-192.
9) M.Yahagi, J. Cryst. Growth. 49 (1980) 396.

5.12 Mechanical Properties of High-Density Nanocrystalline Au after Low-Temperature Irradiation

H. Tanimoto*, T. Yamada*, N. Yagi*, H. Mizubayashi*, A. Iwase**,
N. Ishikawa*** and Y. Chimi***
Institute of Materials Science, The University of Tsukuba*
Research Institute for Advanced Science & Technology, Osaka Prefecture University**
Department of Materials Science, JAERI***

1. Introduction

Whereas an increased volume fraction of the grain boundaries (GBs) may modify the properties of nanocrystalline (n-) materials, the present knowledge on the GB regions is very limited. Recent mechanical studies on high-density n-metals reveal that the Young's modulus of n-metals is not much lower than that of the conventional polycrystalline (poly-) metals.[1-3] For example, the Young's modulus of the high-density n-Au at 10 K is almost the same to the value of poly-Au after taking into account the crystalline texture.[3] In contrast, it is found that the anelastic strains revealed for the strain, ε, range above 10^{-4} in the prolonged time scale of the order of 10^4 sec, start to increase above 200 K, where the slow anelastic process in the GB regions is excited.[4] On the other hand, the increase in the anelastic strain above 200 K is also found in the dynamic measurements at 10^2 Hz, where the fast anelastic process in the GB regions is excited. In the present work, we pursued the fast anelastic process by means of the vibrating reed method at about 200 Hz. That is, we measured the strain amplitude dependence (SAMD) of the resonant frequency, f, and the internal friction, Q^{-1}. Further, the low temperature irradiation was made to get an insight into the GBs through a probable modification by irradiation.

2. Experimental Procedure

High-density n-Au and n-Cu ribbons 0.02 ~ 0.1 mm thick, 1 mm wide and 23 mm long were prepared by the gas-deposition (GD) method.[3] The density was measured by the Archimedes' method using high-purity ethanol, indicating that the relative density to the theoretical value (ρ/ρ_0) is more than 99 % for n-Au and about 94-98% for n-Cu. The mean grain size, d, estimated from the peak broadening of the X-ray diffraction was about 20 ~ 40 nm for n-Au and 10 ~ 30 nm for n-Cu. No contamination was detected from the electron probe microanalysis and the thermal gas-desorption measurement in vacuum.

The temperature dependence of f and Q^{-1} was measured by the electrostatic and electromagnetic methods. The 2MeV electron irradiation at temperature, T, below 15 K was carried out by using the 3MeV single-ended electrostatic accelerator of TIARA, JAERI. The 20MeV proton irradiation at $T < 5$ K was carried out by using the tandem accelerator of University of Tsukuba.

3. Results and Discussion

Figure 1 shows an example of the SAMD observed for the n-Au specimens in the as-prepared state at various temperatures. The outline of the SAMD is as follows : For $\varepsilon < 10^{-4}$, f observed at 90 K shows a monotonous decrease of about 1 % with increasing ε, and f at 303 K shows a decrease for ε below 4×10^{-5} and then saturation for ε above 4×10^{-5} (Fig. 1(a)). Q^{-1}

shows a monotonous increase with increasing ε for all the temperatures (Fig. 1(b)). The SAMD of f and Q^{-1} observed at 258 K is intermediate between those at 90 and 303 K. In Fig. 1(c) for $\varepsilon > 10^{-4}$, f at 293 K remains almost constant for $\varepsilon < 3\times10^{-4}$, and then increases by about 1 % showing saturation with increasing ε to 8×10^{-4}. On the other hand, f at 90 K remains almost constant for the present strain range. The SAMD of f observed at 223 K is intermediate between those found at 90 K and 293 K. For the strain range shown in Fig. 1(d), Q^{-1} shows a monotonous increase as like as Q^{-1} shown in Fig. 1(b).

The SAMD of f seen in Fig. 1 is so different from that of conventional poly-Au specimens. No plastic deformations are detected for the n-Au specimens after the SAMD measurements for ε up to 2×10^{-3} at 300 K, although the microyielding takes place for ε below 10^{-5} for conventional polycrystalline Au specimens.[6] After the low-temperature irradiation, the Q^{-1} spectrum was remained unchanged, in contrast, f showed a large monotonous increase which showed a recovery by annealing after the irradiation.[7] In Fig. 2, a relative change in the Young's modulus observed at 6 K ($\Delta E/E_0$, E_0 ; the Young's modulus before irradiation) is plotted as a function of the accumulated Frenkel-pair defect concentration (C_{FP}). For the single crystal refractory BCC metals, we found that the Young's modulus showed a small decrease by the accumulation of the Frenkel-pair defects, i.e. $(\Delta E/E_0)/(C_{FP}) \sim -10$.[8] The increase in $\Delta E/E_0$ observed for the n-metals by irradiation showed a large recovery after annealing to 300 K. These changes in $\Delta E/E_0$ by irradiation and annealing suggest the accumulation of irradiation-induced defects and the annealing out, respectively.

From the combination of the observed results for the SAMD in f and the low temperature irradiation experiments, we surmise that the characteristic SAMD of f found for the n-Au specimens is associated with a certain anelastic process other than dislocation motions, where the GB regions may play some role.[9] It is noted that the SAMD of f reported for amorphous alloys is qualitatively similar to that observed for the n-Au specimens shown in Fig. 1, and is explained by the cooperative motion of many atoms.[5] For the atomic diffusion in the GB regions, the cooperative motion of three or four atoms are suggested after the computer simulations[10,11], indicating that one part of the GB regions may be soft mechanically. Possible explanation for the characteristic SAMD of f found for the n-Au specimens is a cooperative motion of a crystallite which is surrounded by the GB regions being mechanically soft in a relative sense. However, quantitatively, the SAMD of f for the n-Au specimens is much smaller than that found in amorphous alloy, suggesting that the fractional volume of such soft GB regions should be very low. The large increase in $\Delta E/E_0$ by irradiation and the recovery after annealing may be attributed to the local structural change such as the trapping and detrapping of interstitial atoms by the vacancy-type defects at the GB regions. In order to clarify the detailed mechanisms, the further study is now in progress.

References

1) P. G. Sanders, J. A. Eastman and J. R. Weertman, Acta Mater. 45(1997)4019.

2) X. Y. Qin, X. R. Zhang, G. S. Cheng and L. D. Zhang, Nanostruct. Mater. 4(1998)661.

3) S. Sakai, H. Tanimoto and H. Mizubayashi, Acta Mater. 47(1999)211.

4) S.Sakai, H.Tanimoto, K.Otsuka, T.Yamada, Y.Koda, E.Kita and H.Mizubayashi, Scripta Mater. 45(2001)1313.

5) H. Mizubayashi, T. Okamoto, K. Koyama and M. Horiuchi, Acta Mater. 46(1998)1257.

6) G. Fantozzi, C. Esnoug, W. Benoit and C. Bonjour, Proc. 4th Inter. Conf. on the Strength of Metals and Alloys, (Nancy, France, 1976), p.351.

7) H. Tanimoto, H. Mizubayashi, H. Fujita and S. Okuda, J. de Phys. 6(1996)C8-199.

8) H. Tanimoto, H. Mizubayashi, R. Masuda, S. Okuda, T. Iwata, H. Takeshita and H. Naramoto, phys. stat. sol. (a) 132(1992)353.

9) H. Tanimoto, S. Sakai and H. Mizubayashi, Mater. Trans. 44(2003)94 : Mat. Sci. Eng. A, in press.

10) M.R. Sørensen, Y. Mishin and A.F. Voter, Phys. Rev. B 62(2000)3658.

11) P. Keblinski, D. Wolf, S. R. Phillpot and H. Gleiter, Phil. Mag. A 79(1999)2735.

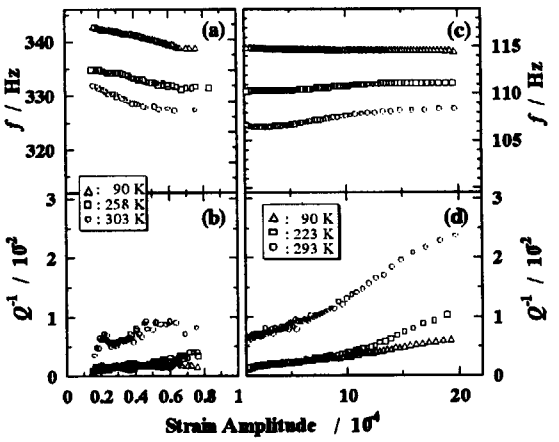

Figure 1. Strain amplitude dependence of the resonant frequency, f, and the internal friction, Q^{-1}, observed for the n-Au specimens, where (a) and (b) are measured by the electrostatic method, and (c) and (d) by the electromagentic method.

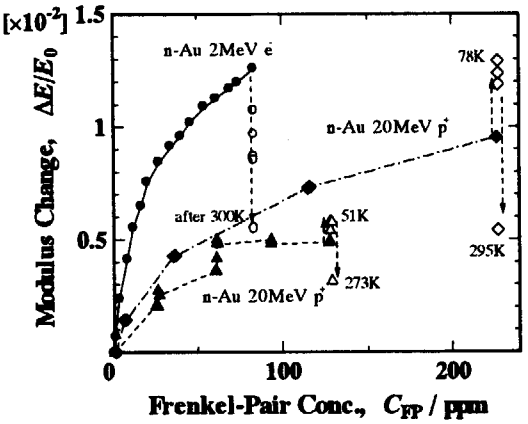

Figure 2. Relative change in the dynamic Young's modulus ($\Delta E/E_0$) measured at 6K during low-temperature irradiation and after the following annealing. E_0 is E observed at 6 K before irradiation.

5.13 ESR CHARACTERIZATION OF ION IMPLANTATION DOPING OF WIDE-GAP SEMICONDUCTOR CRYSTALS: PHOSPHORUS DONORS IN SiC

J. Isoya*, N. Mizuochi*, T. Ohshima**, N. Morishita**, T. Kamiya**
Institute of Library and Information Science, University of Tsukuba*
Department of Material Development, JAERI**

1. Introduction

Wide-gap semiconductor crystals, which have specific properties that are not feasible by silicon, are promising materials for electronic devices of high-frequency, high-power, high-temperature applications and for those used in a harsh environment. The most critical issue in wide-gap semiconductor technologies is to establish the methods of introducing p-type/n-type dopants as well as growing both bulk single crystals and epitaxial layers of high quality. Silicon carbide (SiC) is suited for MOSFETs since stable oxide is formed by thermal oxidation. In SiC, due to the difficulty of doping by thermal diffusion, ion implantation is a potential method of selective area doping in the device fabrication. In SiC, some of radiation damages and secondary defects produced by annealing might be stable up to rather high temperatures. Thus, selection of the implantation conditions and that of the post-implantation annealing conditions are critically important to reduce the radiation damages and to drive the implant into the required lattice site.

In addition to nitrogen, which is unintentionally incorporated during the crystal growth, phosphorus acts as a shallow donor. To improve the doping efficiency by varying the conditions of phosphorus ion implantation and those of post-implantation annealing, microscopic characterization of implanted phosphorus ions as well as those of implantation-induced defects is important. We have applied ESR method to elucidate at microscopic level the thermal behaviour of implanted ions and radiation damages. To characterize the activation of phosphorus ions, it is critically important to observe the ESR signals from phosphorus shallow donors in which the phosphorus atoms substitute for silicon atoms. We have succeeded in observing the ESR signals of shallow phosphorus donors, which was reported previously only in samples doped by neutron transmutation [1,2], first time in both MeV (9-21MeV) and KeV (340 KeV) phosphorus ion implanted 6*H*-SiC [3]. ESR signals of radiation damages in implanted samples are often not sufficiently strong to observe weak ^{29}Si (I=1/2, 4.7%) and ^{13}C(I=1/2, 1.1%) hyperfine lines. We have determined the detailed structures of defect species produced as radiation damages by using their strong ESR signals in the samples irradiated with electrons.

2. Experiments

Rectangular plates (3 × 10 × 1.5 mm^3) of *n*-6*H*-SiC crystals (Nippon

Steel Corp.) were irradiated along the [0001] axis with phosphorus ions (5×10^{13} cm^{-2} at each of 9 steps of energy between 9 and 21 MeV) using a 3 MV tandem accelerator. Post-implantation annealing was performed at 1650 °C for 30 min in Ar atmosphere by using a RF-heating system.

For electron-irradiation, both *n*-6*H*-SiC and *n*-4*H*-SiC crystals were exposed to 3MeV electrons at 50°C up to the total dose of 4×10^{18} cm^{-2}.

The ESR spectra were recorded on a Bruker ESP300 X-band spectrometer by using an Oxford Instrument ESR-900 to control the sample temperature.

3. Results and Discussion

The electric activation of implanted phosphorus ions at various implantation temperatures [room temperature (RT), 400 °C, 800 °C and 1200 °C] has been studied at the fluence in which the mean concentration of phosphorus in the implanted layers was ~1×10^{18} cm^{-3}. The implantation at multi-fold energy between 9 and 21 MeV enabled to attain a sufficient ESR sensitivity with its wide depth-profile.

To compare the concentrations of the radiation damages produced among the samples implanted at different temperatures, it is convenient to use the absorption spectra obtained by integration of the first-derivative form in which the area underneath the curve corresponds to the number of spins (Fig.1). The unimplanted sample exhibits strong signals from shallow nitrogen donors contained as impurity (~10^{17}cm^{-3}). In the case of the implantation at RT, a considerable amount of defects are accumulated. The concentration of the ESR-active defects observed in the as-implanted state decreases with the increase of the implantation temperature. By using hot implantations, the amount of the defects which remained after the implantation is considerably lowered.

The ESR spectrum of *n*-6*H*-SiC which was annealed at 1650°C after the implantation at 800°C is shown in Fig.2. Each of two spectra labeled P_a and P_b consists of two-lines arising from ^{31}P (I=1/2, 100%) hyperfine structure. In the crystal lattice of 6*H*-SiC, there are three inequivalent sites (a hexagonal site *h* and two quasicubic sites k_1 and k_2) for each of silicon and carbon. The P_a and P_b spectra were identified to be originating from the isolated shallow phosphorus donors on each of two quasicubic silicon sites, respectively [2]. ESR spectrum from the shallow phosphorus donor on hexagonal silicon site is likely to be hidden underneath the strong signals of the nitrogen shallow donors. The ratio of the isolated shallow phosphorus donors (the sum of P_a and P_b) relative to the amount of the implanted phosphorus ions is estimated to be ~0.08.

In all target temperatures, RT, 400°C, 800°C and 1200°C, ESR spectrum arising from isolated shallow phosphorus donors has been observed after post-implantation annealing at 1650°C but was not observed in as-implanted state. The relative ratio of concentration of the isolated shallow phosphorus donors for implantation temperatures RT, 400°C, 800°C and

1200°C is 1:0.8:1.5:0.8. While the concentration of the ESR-active defects after implantation strongly depends on the target temperature, ESR spectrum of the shallow phosphorus donors has been similarly observed for all the implantation temperatures studied.

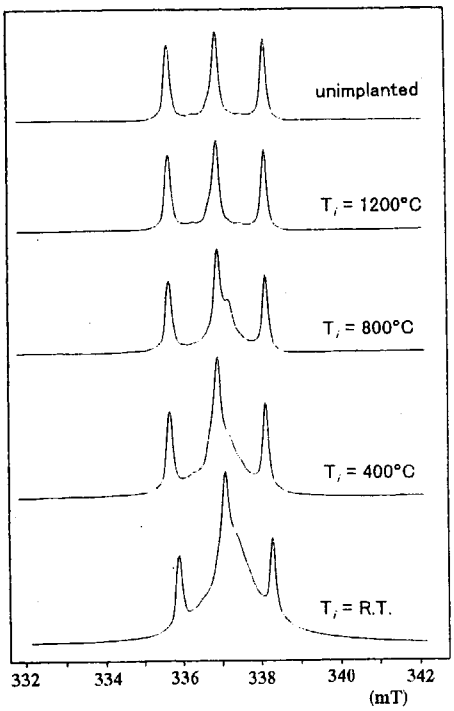

Fig.1 ESR spectra (60K, B//[0001]) of *n*-6*H*-SiC implanted with high energy phosphorus ions at various temperatures.

In the negatively charged silicon vacancies produced in electron-irradiated *n*-4*H*-SiC and *n*-6*H*-SiC, detailed analysis of angular dependence of the ^{13}C hyperfine lines has revealed the C_{3v} symmetry and has distinguished silicon vacancies at hexagonal and quasicubic sites (Fig.3).

References

[1] A. I. Veinger, A. G. Zabrodskii, G. A. Lomakina and E. N. Mokhov, Sov. Phys. Solid State 28, 917 (1986)

[2] P. G. Baranov, I. V. Ilyin, E. N. Mokhov, H. J. von Bardeleben and J. L. Cantin, Phys. Rev. B66, 165206 (2002)

[3] J. Isoya, T. Ohshima, A. Ohi, N. Morishita, and H. Itoh, Nuclear Inst. and Methods in Physics Research B 206C, 965 (2003)

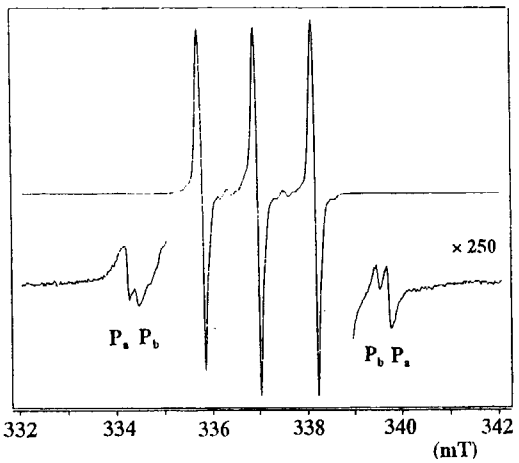

Fig.2 ESR spectrum (80K, B//[0001]) of *n*-6*H*-SiC implanted with high energy phosphorus ions at 800°C with subsequent annealing at 1650°C

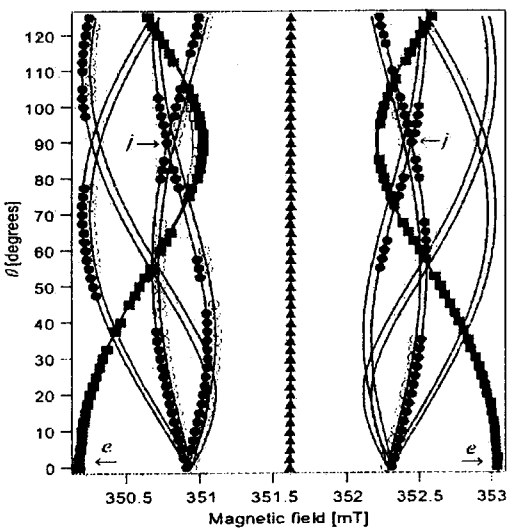

Fig.3 Angular dependence of the line positions of the ^{13}C hyperfine lines of the nearest neighbor carbon atoms around the negatively-charged silicon vacancy in 4*H*-SiC

5.14 Identification of ion-implantation-induced defects with the use of hydrogen-doped Si crystals

N. Fukata*, M. Suezawa*, A. Kawasuso** and M. Maekawa**
Institute for Materials Research, Tohoku University*
Department of Material Development, JAERI **

1. Introduction

Hydrogen in semiconductors is known to have various action, such as passivation and activation of electrical activities of impurities and also the enhancement of impurity diffusion [1]. Hydrogen is also useful to identify defects from the detection of complexes of hydrogen and defects with the measurement of optical absorption spectrum [2, 3]. Vibrational frequencies of hydrogen atoms included in those complexes are very high because of its light mass and the sensitivity of detection with optical absorption method is high.

Ion implantation method plays a crucial role for device fabrication process. Implantation-induced damages, however, are not well understood.

Purposes of our research were to identify defects generated by carbon-implantation, to study annealing behaviors of those defects and to clarify the effect of hydrogen on the annealing behaviors from measurements of optical absorption spectra with the use of hydrogen-doped Si crystals.

2. Experimental

Specimens were prepared from a high-purity floating-zone grown Si crystal (Carrier concentration at room temperature was about $4x10^{12}$ cm^{-2}). After mechanical shaping and chemical polishing, they were doped with hydrogen. Hydrogen doping was performed by annealing specimens in hydrogen gas at 1390°C for 1 h followed by quenching in water (abbreviated as HTH hereafter). Hydrogen atoms form molecules (H_2) in Si crystals at room temperature. H_2 concentration is around $1x10^{16}$ cm^{-3} [4]. To increase hydrogen concentration near surface, some specimens were treated in hydrogen plasma. Namely, we doped hydrogen by soaking specimens at appropriate temperature in hydrogen plasmas. We paid special attention to protect specimens from damages caused with plasma exposure by adopting so-called remote plasma method. We termed this an atomic hydrogen treatment method (abbreviated as AHT, hereafter). Then, carbon ions (C^+) were implanted with an accelerating voltage of 300 kV. Implanted doses were between $1x10^{14}$ and $1x10^{17}$ cm^{-2}. We measured optical absorption spectra of those specimens with a Fourier transform infrared spectrometer at room temperature or 5 K with resolution of 0.25 cm^{-1}.

Results and discussion

Figure 1 shows optical absorption spectra at room temperature of specimens after AHT (a) and carbon-implantation (b). A peak at around 2110 cm^{-1} in (a) is due to vibration of hydrogen atoms included in hydrogen platelets, i.e., a hydrogen precipitates which were formed during AHT. Due to carbon-implantation, this peak disappeared and a new band was observed at about 2000 cm^{-1}. This band is similar to that observed in hydrogenated amorphous silicon. Hence, we think that this band is due to vibration of hydrogen atoms trapped by amorphous region formed by implantation.

Next, we measured optical absorption spectra without AHT. We did not detect peaks observed in Fig. 1. Hence, hydrogen platelets were not formed with HTH. After carbon implantation, we did not detect the peak due to amorphous. This is due to small concentration of hydrogen after HTH. As mentioned above, H_2 concentration due to HTH is around $1x10^{16}$ cm^{-3} and the peak intensity due to amorphous was too small to be detected with optical absorption method: The amorphous region formed by implantation is too small because of small implantation range. As shown in Fig. 2, optical absorption peak due to H_2 was observed even in an HTH specimen because total number of H_2 was large. Figure 2(b) is the spectrum of H_2 in AHT specimen. Peak height in Fig. 2(a) is similar to that in Fig. 2(b). It means that the net concentration of H_2 due to AHT was not high but, as shown in Fig. 1, the local concentration was high.

Summary

To study properties of implantation-induced defects, we performed optical absorption measurement of carbon-implanted Si crystals. We have not been successful in detection of optical absorption peaks due to complexes of hydrogen and simple point defects, such as vacancies.

References

1) See, for example, Hydrogen in Semiconductors, Eds. J. I. Pankove and N. M. Johnson (Academic Press, 1991, Boston).
2) M. Suezawa, Physical Review B 63 (2000) 035201-1 ~ -7.
3) M. Suezawa, Physical Review B 63 (2000) 035203-1 ~ -6.
4) R. E. Pritchard, M. J. Ashwin, J. H. Tucker, R. C. Newman, E. C. Lightowlers, M. J. Binns, S. A. McQuaid and R. Falster, Physical Review B 56 (1997) 13118-13125.

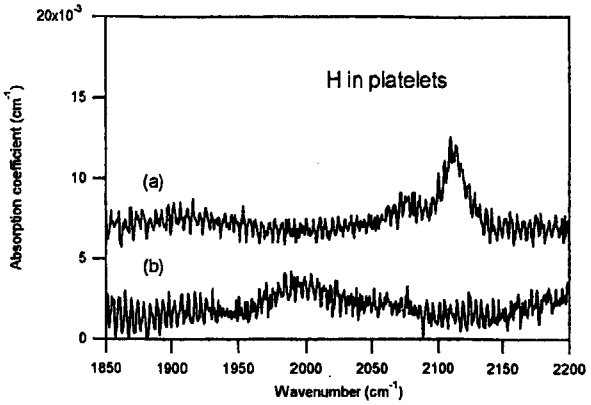

Fig. 1 Optical absorption spectra at room temperature observed in (a) before and (b) after implantation. Specimens were doped with hydrogen with both HTH and AHT.

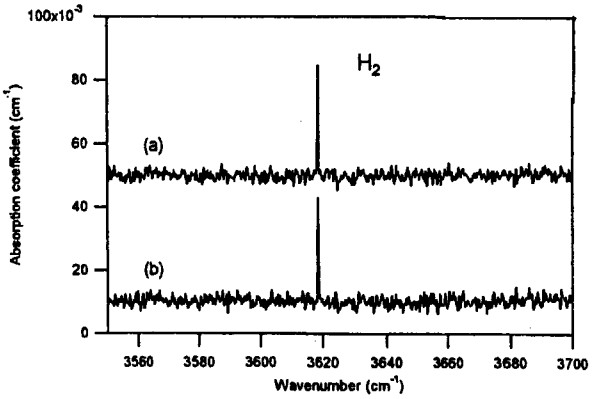

Fig. 2 Optical absorption spectra at 5 K observed in (a) before and (b) after implantation.

5.15 Evaluation of Three Dimensional Microstructures on Silica Glass Fabricated by Ion Microbeam

H. Nishikawa*, T. Souno*, M. Hattori**, Y. Ohki**, E. Watanabe***,
M. Oikawa****, K. Arakawa****, and T. Kamiya*****
Department of Electrical Engineering, Shibaura Institute of Technology*,
Department of Electrical Engineering and Bioscience, Waseda University**
Department of Electrical Engineering, Tokyo Metropolitan University***
Advanced Radiation Technology Center, JAERI****
Department of Material Development, JAERI*****

1. Introduction

Ion beam irradiation on silica glass can induce defect creation and compaction. Since the compaction leads to refractive index changes up to an order of 10^{-2}, we have studied this phenomenon using an ion microbeam technique for fabrication of micrometer-scale optical elements on silica glass[1),2)].

Rapid growth of the data traffic on the internet drives the development of wavelength division multiplexing (WDM) technique. Optical filters using fiber Bragg gratings (FBG) is one of the most important optical elements for the WDM. Writing with ion beam is advantageous over a conventional UV writing technique of the FBG[3)], since no special pre-treatment of silica glass is involved for enhanced photosensitivity. Also, a better stability of induced grating structure is assured by ion implantation. In this study, we report the results of radiation effects induced by ion microbeam irradiation on silica glass.

2. Experimental

Samples are high-purity silica ([OH]: 1200 ppm) with dimensions of 3×3×10 mm^3 and 10×10×1 mm^3. The H^+ and Si^{5+} ions, accelerated at energies of 1.7 MeV and 18 MeV respectively, were implanted into the silica samples using 3 MV single-ended and 3 MV tandem accelerators equipped with microbeam lines (TIARA, JAERI Takasaki, beam diameter: ~ 1 μm). Radiation effects induced by ion microbeam were investigated by means of a micro-Raman spectroscopy, an atomic force microscopy (AFM), and an optical microscopy. In addition, a microscopic two-beam interferometer was used to evaluate refractive index changes in microbeam irradiated regions in silica glass.

3. Results and Discussion

Shown in Fig. 1 is a phase microscope image obtained from the side surface of silica glass on which the H^+-beam was scanned at different widths. At the stopping range of H^+, the lateral spread of refractive index changed region represented as a bright area in Fig. 1, is estimated to be 8 μm for the microbeam-scanned width of 1 μm (see the rightmost rectangular region). On the other hand, although refractive index

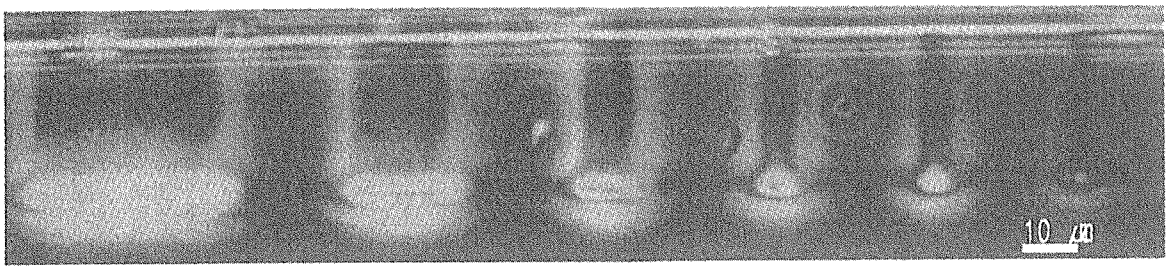

Fig. 1 Phase microscope image obtained for the side surface of the silica glass irradiated by microbeam (H^+, energy: 1.7 MeV, dose: 1×10^{17} ions/cm^2) with different irradiation widths of 40, 20, 10, 5, 3, and 1 μm from left to right.

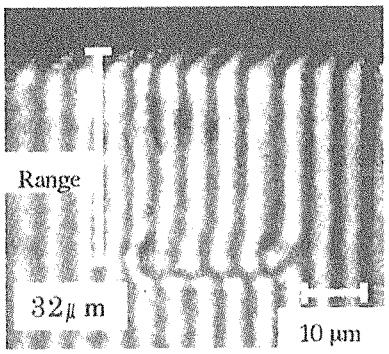

Fig. 2 Interference fringes taken by a microscopic two-beam interferometer.

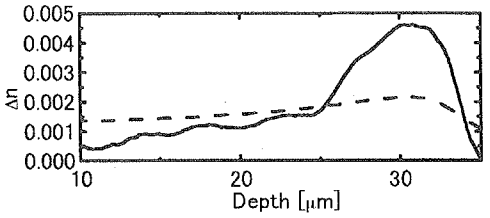

Fig. 3 Refractive index change (Δn) measured by a microscopic two-beam interferometer (solid line) and that estimated by an atomic force microscope (broken line).

change is not so significant, the lateral spread near the irradiation surface is smaller, when compared with the stopping range.

Figure 2 shows an image obtained by a microscopic two-beam interferometer for the beam-scanned area with 20 μm width. At the stopping range of ions, large displacements of the interference fringes were observed at the stopping range of ions. Since the displacement of the fringe is proportional to refractive index change Δn, it is possible to estimate Δn as a function of the depth from the surface. Shown in Fig. 3 is the depth distribution of Δn (solid line) estimated from the interference fringes in Fig. 2. Also shown is Δn (broken line) obtained from the compaction of silica glass, which is calculated from the surface grooves measured at the side and front surfaces by AFM measurements using the Lorentz-Lorenz relationship.

The result from the microscopic two-beam interferometer shows the maximum of the H^+-microbeam-induced Δn at the depth of 32 μm. This is in agreement with the result of Δn estimated by AFM. We also note that Δn with an order of magnitude of lower value is induced at the track of ions than the stopping range.

Figure 4 shows Raman spectra at the 40 μm-width microbeam-scanned area measured at different depths from the surface. At the stopping range (32μm) of H^+, a significant increase was observed for the Raman scattering intensity at 606 cm^{-1} due to three-membered rings, which are smaller than regular ring sizes of five-

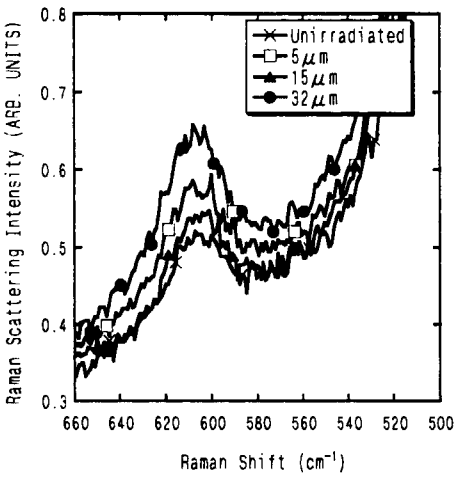

Fig. 4 Raman spectra obtained for the region of irradiation width of 40 μm at different depths from the surface (H^+, 1.7 MeV, dose: 10^{17} ions/cm^2).

or six-membered rings in silica glass network. This supports the mechanism of refractive index changes due to the compaction of silica glass induced by ion beam irradiation.

Periodic modulation of refractive index at intervals as small as 0.5 μm at the core of a waveguide is required to fabricate the Bragg gratings, which can selectively reflect a certain wavelength of light in the WDM system for optical communication. Therefore, the lateral spread of the refractive index changes should be minimized for the direct writing of the Bragg gratings using ion microbeam, while a sufficient Δn of 10^{-3} order is achieved as shown in Fig.3. A possibility for the better resolution in direct writing by H^+ microbeam is use of radiation effect at the track rather than the stopping range.

Although data are not shown, we have also observed radiation effects in silica glass by heavy-ion microbeam such as Si^{5+} including defect formation and refractive index changes which are localized at the surface with smaller lateral spread. This suggests another possibility of heavy-ion microbeam for the writing of gratings on the surface of planar optical waveguides. The use of sub-micron ion beam is also under consideration.

References

1) M. Hattori, M. Fujimaki, Y. Ohki, T. Souno, H. Nishikawa, T. Yamaguchi, E. Watanabe, M. Oikawa, T. Kamiya, and K. Arakawa, 8th International Conference on Nuclear Microprobe Technology & Applications, P1-29, p.57 (2002)

2) T. Souno, H. Nishikawa, T. Yamaguchi, E. Watanabe, M. Hattori, M. Fujimaki, Y. Ohki, M. Oikawa, T. Kamiya, and K. Arakawa, 8th International Conference on Nuclear Microprobe Technology & Applications, P2-19, p.101 (2002)

3) K. O. Hill, Y. Fujii, D. C. Johnson, and B. S. Kawasaki, Appl. Phys. Lett. 32, 647 (1978)

6. Nuclear Science and RI Production

This is a blank page.

6.1 Development of Positron-emitting Bromine Nuclides Production Using An Isotope Separator

B. FATEH*, N. S. ISHIOKA*, S. WATANABE*, T. KUME* and T. SEKINE**

Department of Ion-beam-applied Biology, JAERI*

Department of Irradiation Technology and Public Relation, RADA**

1. Introduction

Halogen isotopes such as ^{18}F, $^{123,125,131}I$ and $^{75,76,77}Br$ are used in nuclear medicine and biology increasingly. Among them, Br isotopes have suitable characteristics such as stable bonding to carbon atoms than of the iodine and suitable half-life for studying of slow metabolic processes. ^{76}Br is an alternative of ^{18}F for labeling radiotracers with application in positron emission tomography, PET[1]. ^{76}Br has a half-life of 16.2 hr, positron decay of 57.2% and its compound labeled can be used in plant studies using positron emitting tracer imaging system, PETIS.

Several methods for carrier-free production of the bromine isotopes have already been described by several researchers, either directly from arsenic targets by alpha particles[2] and from enriched selenium targets by Se (p,xn) Br reactions[3], or indirectly by decay of their krypton precursors. The krypton isotopes can be produced in good yields by the bromine target[4]. The bromine target such as NaBr has several advantages: no toxicity, good yield, simple separation of the products from the target and no need of using expensive enriched target materials. Nevertheless, production of ^{76}Br associated with production of other Br isotopes as an interfering reaction. It must be considered that there is no chemical method for the separation of different isotopes of one element. The isotope separation after irradiation of a target has not been considered as a practical method of radioisotope production. In practical point of view, the ionization efficiency of mass separators ion source is low. But, recently a compact ECR ion source has realized high ionization efficiency. The ECR are used for production radioactive beams for gaseous or high-vapor-pressure materials with ionization efficiencies (charge state 1^+) of 10-65%[5]. Therefore, it is reasonable to expect a high yield isotope separation for Kr atoms using ECR ion source.

The present paper describes some experiments on the production of high pure Br isotopes (especially ^{76}Br) based on the mass separation of their precursors (Kr radio-nuclides). The separated Kr isotopes were implanted into the Al foils. After several hours, all implanted Kr isotopes decayed to Br isotopes. In this paper, some chemical experiments on separation of Br isotopes from Al foils are described.

2. Experimental

The irradiations were performed with the 45 MeV proton beam at AVF cyclotron (TIARA) on pressed pellets of anhydrous NaBr (1cm ϕ, 6 mm thickness) of natural isotopic composition for 3 min at the

currents of 1 μA. After irradiation, the pellets were transferred to dry distillation apparatus (Fig.1) connected to vacuum pumps and equipped with trapping vessel emerged in liquid nitrogen. The NaBr targets were placed in a quartz cylinder of an oven.

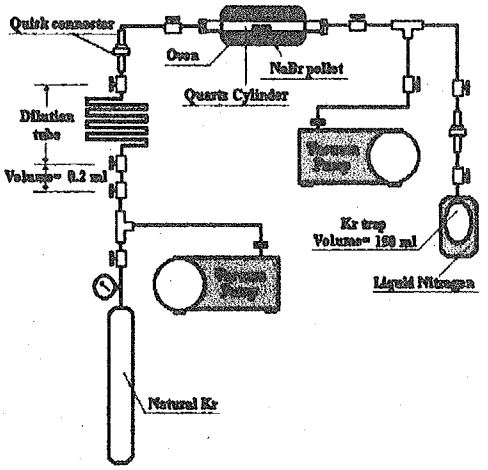

Fig. 1 System for dry distillation and radiokryptons trap

After evacuation of the whole system, 6 μl natural Kr was added to the quartz cylinder in order to increase the trapping efficiency. This small amount of the natural krypton was supplied by transferring of 0.2 ml Kr to the short tube and then 30 times dilution using long tubing (Fig. 1). Furthermore, the Kr trap vessel has been evacuated by diffusion pump to make high vacuum (10^{-6} Pa) inside the trap.

In the next step, heater was turned on and when the temperature reached to 600°C the valves between dry distillation apparatus and trap were opened and Kr atoms were trapped. Then the trap was connected to isotope separator (ISOL system) and Kr atoms supplied from the trap were ionized in the ECR ion source. Kr ions were accelerated to the energy of 38 keV, mass separated and implanted into the Al foils mounted on isotope collector (Fig. 2).

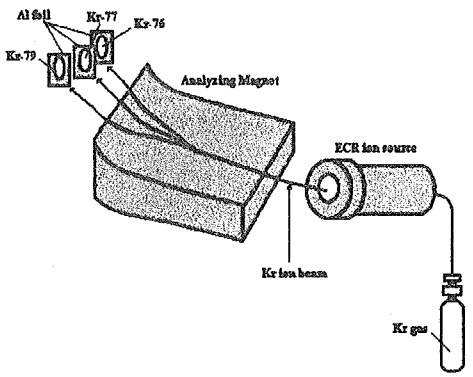

Fig. 2. Isotope separation and Kr implantation (ISOL system)

After decaying of implanted ^{76,77}Kr, the Al foils contain ^{76}Br and ^{77}Br were dissolved separately in 300μl conc. HCl. After dissolving the foil, 6.8 ml distilled water was added to the solution. Two chemical methods were carried out using anion exchange (Bio-rad, AG-1X8) and cation exchange (Bio-Rad, AG50W-X8) resins. In the first method, solution was transferred through the column contained 3 ml of AG50W-X8 resin, preconditioned with 0.5 N HCl and eluted with 0.5 N HCl. In the second method, solution was transferred through the column contained 3 ml of AG-1X8 resin preconditioned with 0.5 N HCl and eluted with 8N HCl. The elution curves were obtained for both methods. In each step, samples were taken and measured by Ge detector.

3. Results and Discussion

Our experiments have shown that the radiokrypton remained enclosed in the NaBr matrix very efficiently, even under vacuum, because of efficient cooling system and low beam current. In dry distillation unit, when the temperature reached to 760°C, the trapping had been

practically completed and more than 95% of Kr atoms trapped in a stainless steel vessel (volume=150ml). The result of Kr isotope separation is shown in Table 1. Isotopic purities of the products were obtained: 99.92, 99.99, 100% for ^{77}Kr, ^{76}Kr and ^{79}Kr, respectively, with the overall separation efficiency: 15±2%.

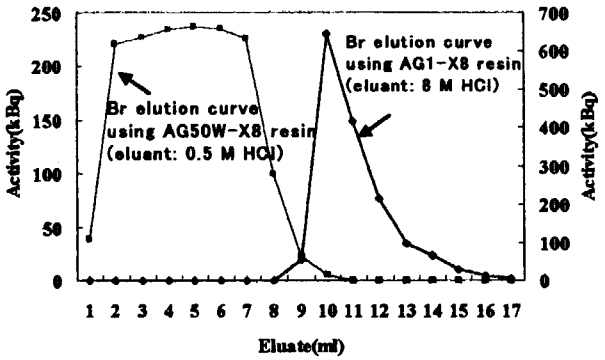

Fig. 3 Br elution curves of two chemical methods

The results of chemical separation of Br from Al foils are shown in Fig. 3. First method based on AG50W-X8 resin, provided bromine solution in low concentration HCl (0.5 M) and the chemical efficiency of more than 95%. In the second method based on AG1X-8 resin, the elution curve was sharper than the first method but the chemical separation efficiency was 80% and the final solution had higher HCl concentration (8 M). Our experiments showed that aluminum ion is not accompanied with Br ions in the final solutions of the both methods.

Due to high ionization efficiency ECR ion source, production of Kr and the Br isotopes through this method for local uses and biological research purposes is quite reasonable because high pure radioisotopes are needed for labeling and biological studies.

Application of high efficiency isotope separator equipped with an ECR ion source for isotope production have several advantages: simultaneous production of various kinds of isotopes, radio-chemically high-pure products, the possibility of the online production and no need to use the enriched targets.

Table 1. The results of Kr isotope separation using ISOL system (N. D.: None Detectable)

Implanted Ion	^{76}Kr (%)	^{77}Kr (%)	^{79}Kr (%)	Collected Activity
^{76}Kr	>99.99	<0.01	N. D.	165 kBq
^{77}Kr	<0.08	>99.92	N. D.	70 MBq
^{79}Kr	N. D.	N. D.	100	7.5 MBq

Acknowledgment: The authors wish to express appreciation to Japan Society for the Promotion of Science (JSPS) for supporting this research activity.

Refernces

1) Yngve U., Khan T. S., Bergstrom M. and Langstrom B., J. Labelled Comp. and Radiopharm., **44** (2001), 561-573.
2) Blessing G. and Qaim S. M., Int. J. Appl. Radiat. Isot., **35** (1984), 927-931.
3) Tolmachev V., Lövqvist A., Einarsson L., Schultz J. and Lundqvist H., Int. J. Appl. Radiat. Isot., **49** (1998), 1537-1540.
4) Nozaki T., Iwamoto M. and Itoh Y., Appl. Radiat. Isot., **30** (1979), 79-83.
5) Stefanini A., SPES Project Study, L.N.L.-I.N.F.N. (REP) **145/99** (1999), 67-68.

6.2 Synthesis of Endohedral ^{133}Xe-Fullerol

S. Watanabe*, N. S. Ishioka*, H. Shimomura**, H. Muramatsu**, T. Kume*
Department of Ion-Beam-Applied Biology, JAERI*
Faculty of Education, Shinsyu University**

1. Introduction

Endohedral radioisotope-fullerenes have a possibility of being new radiopharmaceuticals. In order to realize this, hydrophilic fullerene derivatives that can be transported only to desired tissues such as cancer cells have to be synthesized in addition to the encapsulation of radioisotopes emitting β- or γ-rays available for therapy or diagnosis. Cagle *et al.*[1] reported the synthesis method of endohedral ^{166}Ho-fullerol (^{166}Ho@$C_{82}(OH)_x$) and the concentration of the ^{166}Ho@$C_{82}(OH)_x$ into bone tissue as a result of animal experiments. Since ^{166}Ho emits a β- ray with a maximum energy of 1.8 MeV, it seems that ^{166}Ho@$C_{82}(OH)_x$ can be applied to the therapy of cancer of a bone.

We have recently reported a production method of endohedral ^{133}Xe-fullerene by ion implantation.[2, 3] ^{133}Xe decays with a half-life of 5.25 d, emitting a β-ray with a maximum energy of 0.346 MeV and a conversion electron competing in the 81-keV γ transition. Therefore, endohedral ^{133}Xe-fullerol (^{133}Xe@$C_{60}(OH)_x$) could be also applied to the therapy of cancer of a bone. In the present paper, we describe the synthesis method of ^{133}Xe@$C_{60}(OH)_x$ by addition reaction of hydroxyl groups to endohedral ^{133}Xe-fullerene (^{133}Xe@C_{60}).

2. Experimental

Fullerene targets for ion implantation were made by vacuum evaporation of C_{60} on Ni foils. Implantation of ^{133}Xe ions into the targets was carried out with an isotope separator[4] at acceleration energies of 30 keV. After ion implantation, the fullerene part on the target was dissolved in *o*-dichlorobenzene. The solution was filtered through a millipore filter to remove insoluble materials.

The synthesis of ^{133}Xe@$C_{60}(OH)_x$ was carried out by the method described by Cagle *et al.*[1] with minor modifications. The *o*-dichlorobenzene solution including ^{133}Xe@C_{60} was stirred for 12h with tetrabutylammonium hydroxide (TBAOH, 40% in water) and concentrated aqueous KOH solution by a rotary evaporator. After the stirring, the *o*-dichlorobenzene solution was removed *in vacuo* at 80° C. Then the remaining solution was stirred with water for 8h. To remove the TBAOH and the KOH, the solution was passed down a size-exclusion gel chromatography column with Sephadex G25 Fine using water as an eluent. The effluent was analyzed by high performance liquid chromatography (HPLC) with a RP-18 column (Merck). Elution was done with water at a flow rate of 1 ml/min. The concentration of fullerol ($C_{60}(OH)_x$) in the effluent was continuously monitored by a UV detector. The effluent after UV measurement was collected in glass vials each for 1 min until 20 min and the ^{133}Xe radioactivity in each vial was measured by γ-ray spectrometry.

3. Results and Discussion

Figure 1 shows elution curves of ^{133}Xe and $C_{60}(OH)_x$ obtained. The strong correlation observed between the ^{133}Xe and $C_{60}(OH)_x$ peaks corroborates the formation of $^{133}Xe@C_{60}(OH)_x$. In the effluent, only 2% of the ^{133}Xe radioactivity was detected as the $^{133}Xe@C_{60}(OH)_x$. The other radioactivities of ^{133}Xe were released from the $C_{60}(OH)_x$ molecule as ^{133}Xe gas during the synthesis of $^{133}Xe@C_{60}(OH)_x$ except for about 5% of the ^{133}Xe radioactivity remaining in the flask of the rotary evaporator as precipitate.

This can be explained as follows. $^{133}Xe@C_{60}(OH)_x$ is synthesized by addition reaction which hydroxyl groups attack to the double bonds of carbon atoms in a $^{133}Xe@C_{60}$ molecule. As the addition reaction proceeds, the number of the double bonds decreases and also the strength of the bonds between carbon atoms weakens. Consequently the $^{133}Xe@C_{60}(OH)_x$ molecule expands, easily releasing a ^{133}Xe atom from itself.

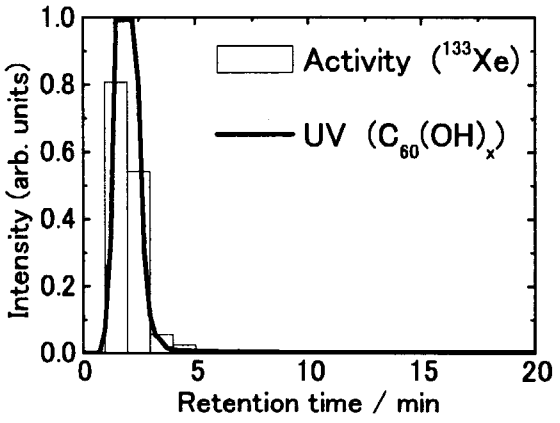

Fig.1. HPLC elution curves of ^{133}Xe and $C_{60}(OH)_x$.

References

1) D. W. Cagle *et al.*, Proc. Natl. Acad. Sci. USA, 96 (1999) 5182.

2) S. Watanabe *et al.*, J. Radioanal. Nucl. Chem., 255, (2003) 495.

3) S. Watanabe *et al.*, Nucl. Instr. and Methods Phys. Res. B., 206, (2003) 399.

4) T. Sekine *et al.*, J. Radioanal. Nucl. Chem., 239 (1999) 127.

This is a blank page.

7. Microbeam Application

This is a blank page.

7.1 Formation of a Focusing High-energy Heavy Ion Microbeam

M. Oikawa*, T. Kamiya**, T. Satoh*, M. Fukuda*, S. Kurashima*, N. Miyawaki*
Advanced Radiation Technology Center, JAERI*
Department of materials development, JAERI**

1. Introduction

For microbeam applications in biomedical science such as radio microsurgery, high-energy single-ion hit irradiation techniques with a spatial resolution of around the 1 μm level are required for striking particular sites within intracellular structure. The ability to do so presents a powerful tool for research into the effects of radiation on single cell structures using 3 - 5 MeV hydrogen or helium ions from electrostatic accelerators [1),2)]. At the TIARA facility [3)], a focused high-energy heavy ion scanning microbeam system was designed and installed on a vertical beam line (HX1) of the AVF cyclotron accelerator, for external beam, single cell irradiation using the single-ion hit technique. The advantage of this new system compared to those currently in operation, is that very high linear energy transfer (LET) ionization tracks can be generated in biological media using ions of more than 10 MeV/u in energy. A vertical microbeam line is also advantageous since it reduces problems associated with cell movements under gravity and hence overall target complexity as compared with a horizontal system such as the one at GSI [4)], where additional techniques are required to maintain cell position. Prior to this work, a collimated microbeam and single ion hit system has already been developed on a separate vertical beam line (HZ1) [5)], and cell irradiation experiments have been performed using this system [6)]. However, this existing system is limited by its spatial resolution and irradiation speed, which are 10 μm and 2 sample positions per minute, due to ion scattering from the edge of the final collimator and the time required for stage manipulation and sample positioning, respectively. This line does however; possess a fully automated single-ion hit system [5)].

The new system uses a set of quadruplet quadrupole magnets for focusing with an accuracy of around 1 μm. To reduce the contribution of chromatic aberration in determining the overall spot size, it is necessary to minimize the energy spread $\Delta E/E$ to less than 10^{-4} for typical heavy ion beams provided by the cyclotron (generally the energy spread is usually > 10^{-3}). To ensure a highly stable voltage during the acceleration phase, a flat top (FT) acceleration technique was introduced into the cyclotron RF system [7)]. The system also has an X, Y beam scanner, so that a larger number of micron scaled samples like biological cells can be irradiated in single ion mode to improve statistics. A thin film window was used to extract beam into atmosphere. The problem of scattering can be ignored if the window is thin enough and samples are set as close to the window as physically possible. In actual cell irradiation experiments, it is necessary to detect the cell to be irradiated as well as the striking single ions as efficiently and precisely as possible. To reduce the exposure time per cell and increase throughput for large batches were high reliability is required, a

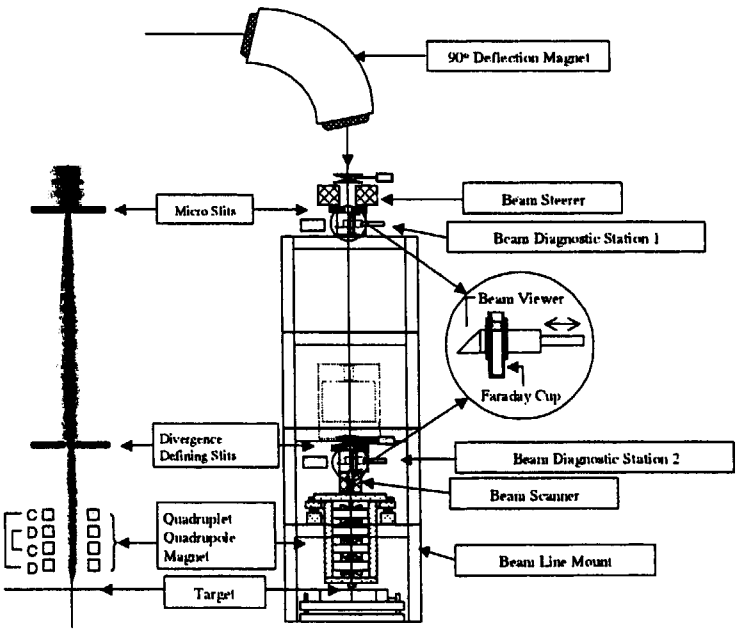

Fig. 1. Schematic View of Microbeam System on the Vertical Beam Line of the AVF Cyclotron.

real-time single-ion hit position detection system was also required.

2. Detail of high-energy heavy ion microbeam system

The schematic of the microbeam line is as shown in Fig. 1. As noted earlier all samples are mounted on the atmosphere side of a thin film window at the rear of the chamber. A high-energy heavy ion beam from the cyclotron is deflected 90 degrees with a bending magnet and lead into a vertical beam line. The slit systems forming object and aperture are also indicated in Fig. 1. The micro-slits used to form the micron-sized object are composed of two wedged shape slits that cross perpendicularly to one another on the beam axis (made by Technisches Büro S. Fischer with a minimum slit aperture < 1 μm and maximum aperture of 150 μm). Divergence defining slits are composed of four ordinary slit chips. The motion of each slit is controlled by a stepper motor driven precision stage (positional resolution of 0.5 μm). In order to monitor the beam profile or current passing through each slit system, a beam viewer and Faraday cup are installed on a single diagnostic rod manipulated by a two-step pneumatic actuator. For beam viewing, a CaF_2(Eu) scintillator having a high luminescence efficiency of 50 compared to that of NaI(Tl) 100 was chosen, resulting in beam currents as low as ~100 fA being observed on a high sensitivity camera. The focusing lens is a quadruplet

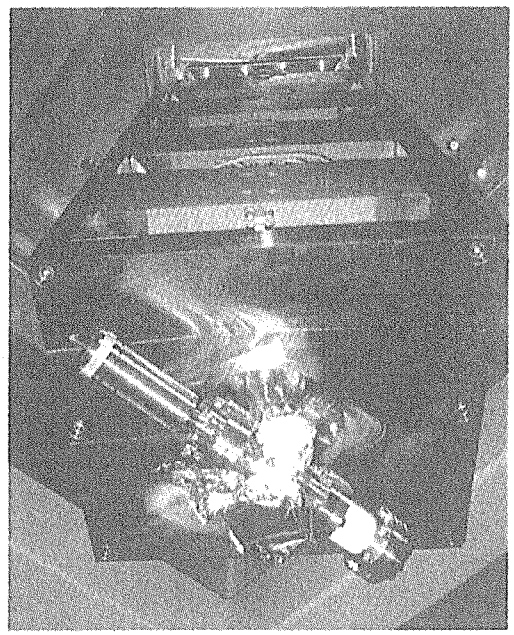

Fig. 2. Quadruplet Quadrupole Magnet.

of quadrupole magnets with a bore radius of 20 mm and mechanical pole length of 150 mm as shown in Fig. 2. The lenses are configured to converge, diverge, converge and diverging with the both the first and fourth lenses, and second and third lenses, coupled. The working distance is 300 mm resulting in a horizontal and vertical demagnification of 5. So as to minimize irregularities in the quadrupole fields, an assembly tolerance of ±50 μm was set during manufacture. Such a small tolerance is also necessary for reducing the risk of geometrical misalignment of the magnet poles, or yokes, as there is no means for adjusting each magnets relative position. The magnet current supplies are stabilized to $\Delta I/I$ values of less than $\pm 1 \times 10^{-5}$ so as to maintain a stable beam spot focus. Air-core coils placed just above the first focusing element are used to either target the beam, or, scan the beam over a 1 mm × 1 mm area of the sample in the case of the most rigid beam being used.

3. Outline of the real-time single ion hit detection system

Fig. 3 shows an outline of the real-time single-ion hit position detecting system, combined with the automated single cell irradiation system both developed in previous work [5]. In order to obtain the exact position of each single ion hit, the flash of luminescence from a scintillator placed under the sample is observed by an optical microscope and super high sensitivity CCD camera and superimposed over a sample image collected by the same camera and magnification. However, as shown in previous studies, the intensity of the CCD signal from such faint luminescence is lower than background noise. In order to reduce noise from the luminescence image, single-ion detection signals have been used to define the CCD acquisition times thereby further eliminating the effects of scattered ions or irregular ion injection. X, Y scanning control signals are also used to limit the active region of the CCD to that directly around the target position. Single-ion detection signals are obtained using secondary electrons from the vacuum side of the beam exit window. Since CaF_2(Eu) has high optical transparency and non-deliquescency as well as luminescence efficiency it was deemed an obvious first candidate for use in this system.

4. Summary

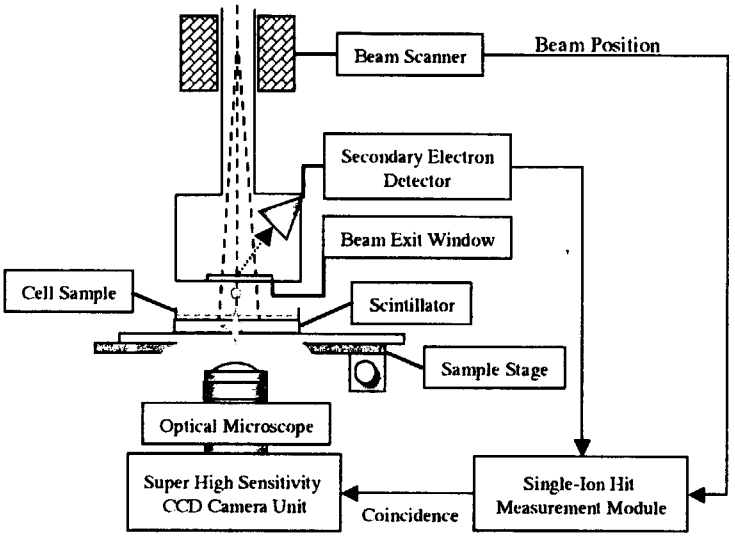

Fig. 3. Conceptual Scheme of The Real-Time Single Ion Hit Position Detection System.

A focusing high-energy heavy ion microbeam system has been designed and installed on a vertical beam line of the TIARA AVF cyclotron accelerator. Optimization of the microbeam focusing system was performed using 260 MeV Ne^{7+}, which is the most suitable condition for acceleration with the FT technique, in the second stage of the development for the minimum beam size of 1 μm. A real-time single-ion hit position detection system has been designed and requires further investigation to be fully optimized. We obtained the prospect in which the single-ion hit position detecting is possible by using the particular camera configuration in the preliminary examinations. The final goal for this development will be to establish a high-speed automated single cell irradiation system and combine it with the real-time single-ion hit position detecting system.

References

1) M. Folkard, B. Vojnovic, G Schettino, M. Forsberg, G Bowey, K. M. Prise, B.D. Michael, A.G Michette, S. J. Pfauntsch, Nucl. Instr. and Meth., B 130 (1997) 270.

2) R. Geard, D. J. Brenner, G Randers-Pehrson, S. A. Marino, Nucl. Instr. and Meth., B 54 (1991) 411.

3) R. Tanaka, Proc. 5th Japan-China Joint Symp. on Accel. for Nucl. Sci. and Their Appl., Osaka, Japan (1993) 201.

4) B. E. Fischer, M. Cholewa, H. Noguchi, Nucl. Instr. and Meth., B 181 (2001) 60.

5) T. Kamiya, W. Yokota, Y. Kobayashi, M. Cholewa, M. S. Krochmal, G Laken, I. D. Larsen, L. Fiddes, G Parkhill, K. Dowsey, Nucl. Instr. and Meth., B 181 (2001) 27.

6) Y. Kobayashi, T. Funayama, M. Taguchi, S. Wada, M.Tanaka, T. Kamiya, W. Yokota, H. Watanabe, K.Yamamoto, TIARA Ann. Rep. 2000, JAERI-Review, 2001-039 (2001) 73.

7) M. Fukuda, S. Kurashima, N. Miyawaki, S. Okumura, T. Kamiya, M. Oikawa, Y. Nakamura, T. Nara, T. Agematsu, I. Ishibori, K. Yoshida, W. Yokota, K. Arakawa, Y. Kumata, Y. Fukumoto, K. Saito, Nucl. Instr. and Meth., B210 (2003) 33.

7.2 Replication of Individual Snow Crystals for Their Subsequent Chemical Analysis Using Micro-PIXE

M. Kasahara, C.- J. Ma, M. Okumura,
T. Kojima*, T. Hakoda*, T. Sakai** and K. Arakawa**
Graduate School of Energy Science, Kyoto University
Department of Material Development, JAERI*
Advanced Radiation Technology Center, JAERI**

1. Introduction

A snow crystal is a single frozen ice grain which generally results from a process known as nucleation in which atmospheric water vapor condenses on a solid particle or nucleus at temperature below 0℃. The formation of snow crystals most commonly occurs by a process known as heterogeneous nucleation. This scavenging process of aerosol particles is called nucleation scavenging. In addition to this nucleation scavenging, snow can capture and transfer large quantities of other particulate matter from the atmosphere. This mechanism is a result of aerosol particles becoming attached to the snow crystals by Brownian motion, inertial, hydrodynamic, phoretic and electric forces. Thus, snow like rain is one of the most important natural processes in cleaning the particulate matter that are present in the atmosphere. However, the snow scavenging has many unsolved problems because the shape of snow crystals is so complicated that it is very difficult compared with raindrops to deal with them experimentally and theoretically.

In this study, to collect snow crystal individually, a particular replication technique was newly applied. The physical characteristics of individual snow crystals were determined by microscopic measurement. Furthermore, in order to study the particle scavenging properties and the chemical characteristics of snow crystals, Particle induced X-ray emission (PIXE) and micro-PIXE analyses were newly applied in this study.

2. Experimental procedure

Collodion, a thick and colorless syrupy liquid, is made by dissolving the nitrocellulose involving 11-12% of nitrogen into the mixed solution of ether and alcohol. It was widely used by surgeons as a liquid bandage and photographic film as a coating owing to its strength and adhesion. The physical and chemical properties of collodion are summarized in Table 1. For the purpose of forming the replica of snow crystal, thin collodion film was prepared. About 200 μl of collodion solution (3%) is mounted onto a 47 mm diameter non-hole polycarbonate filter (Nuclepore^{c}) just before sampling. When snow crystals fall onto the thin layer of collodion film (130± 10 μm) they gently settled without bounce off. The formation of individual snow crystal replicas on the collodion film was described in elsewhere[1]. This procedure not only allows us to get information about the physical property but also enable us to analyze the retained components in and/or on snow crystal replica. Samplings was performed at height of 25 m above ground level of a Kyoto University building located in Uji during the wintertime of 2001. Micro-PIXE measurements were performed with a scanning 2.6MeV H^+ micro beam accelerated by 3MV single-end accelerator. For the analysis of whole snow crystals, PIXE analysis was performed with a proton beam of 6 mm diameter and 2.0 MeV energy from a Tandem Cockcroft accelerator in Quantum Science and Engineering Center, Kyoto University.

Table 1. The physical and chemical properties of collodion

Appearance	Clear, colorless liquid	Vapor Density	4.5 (air = 1)
Odor	Characteristic fruity odor	Vapor Pressure	440 mm Hg (at 20°C)
Solubility	0.2 % in water	Ingredient	- Nitrocellulose (For trinitrate): $C_6H_7O(OH)_3O+3OHNO_2$
Specific gravity	0.77		
pH	No information found		- Diethyl ether ($C_2H_5OC_2H_5$)
Boiling point:	34.6 °C		- Ethyl alcohol (C_2H_5OH)

3. Results and Discussion

Though most of snow crystal was collected as snowflake because of ground level sampling, unagglomerated crystals were also observed. Separated clean snow crystal replicas formed on the collodion film are shown in Photo 1. Individual ice crystals collected in this study are ranged from 0.12 mm to 2.5 mm.

Fig. 1 shows an example of PIXE spectrum of a single dendritic sectored snow crystal replicated on the collodion film. It was possible to resolve the significant several elemental peaks corresponding to channel number of PIXE spectrum. Though apparent peaks of chloride and iron at collodion film blank which can affect

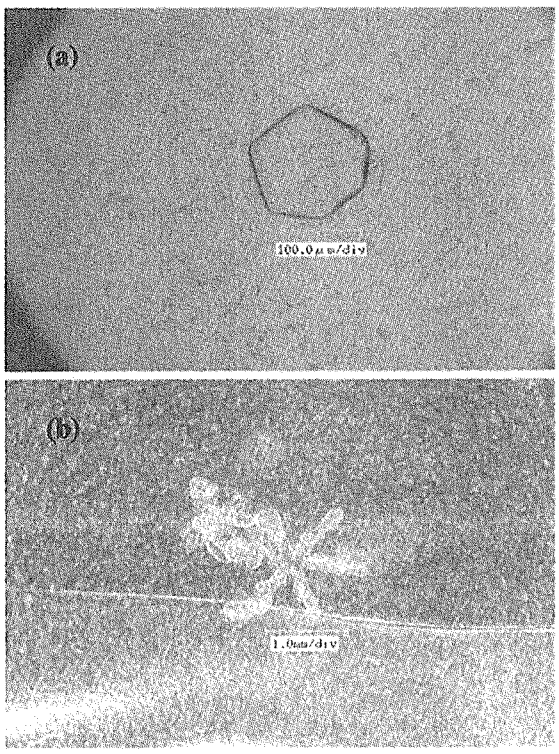

Photo 1 Snow crystals collected on the collodion film. (a) and (b) are hexagonal plate and dendritic sectored plate, respectively.

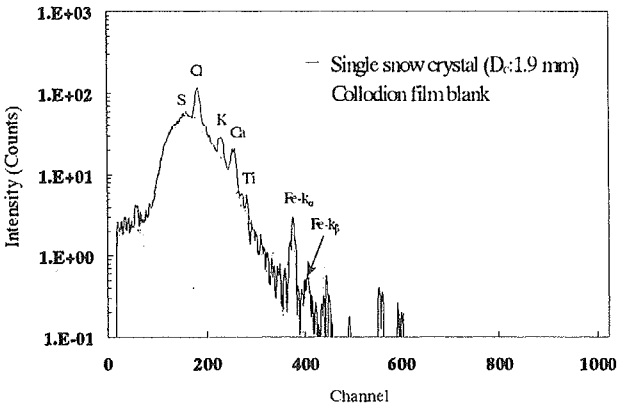

Fig. 1 PIXE spectrum of a single dendritic sectored snow crystal collected on the collodion film. Dc means the diameter measured by the circumscribed circle.

on the detection ability of PIXE analysis was found, these relatively distinct background levels could be corrected by the ratio of integrated level of background counts to those of signal. Fig. 2 shows the variation of major elemental masses as a function of the circumscribed diameter of dendritic sectored snow crystal. Each elemental data set is the average masses of 10~20 snow crystals. Dust originated components like silicon, potassium, calcium, and iron were found as major elements in each size of individual snow crystals. Their average masses are 3.76×10^{-1} μg, 2.18×10^{-1} μg, 3.84×10^{-1} μg, and 2.83×10^{-1} μg, respectively in 0.6 mm diameter crystals. Also sulfur shows the significant mass with average 3.61×10^{-1}μg in 0.6 mm diameter crystals. The mass of silicon (2.83×10^{-1} μg) showing the maximum is 25 times higher than that of iron (1.13×10^{-2} μg) in 2.3 mm diameter crystal. Fig. 3 was formed on a 100 μm×100 μm scanning area including an edge part of hexagonal snow crystal replica.

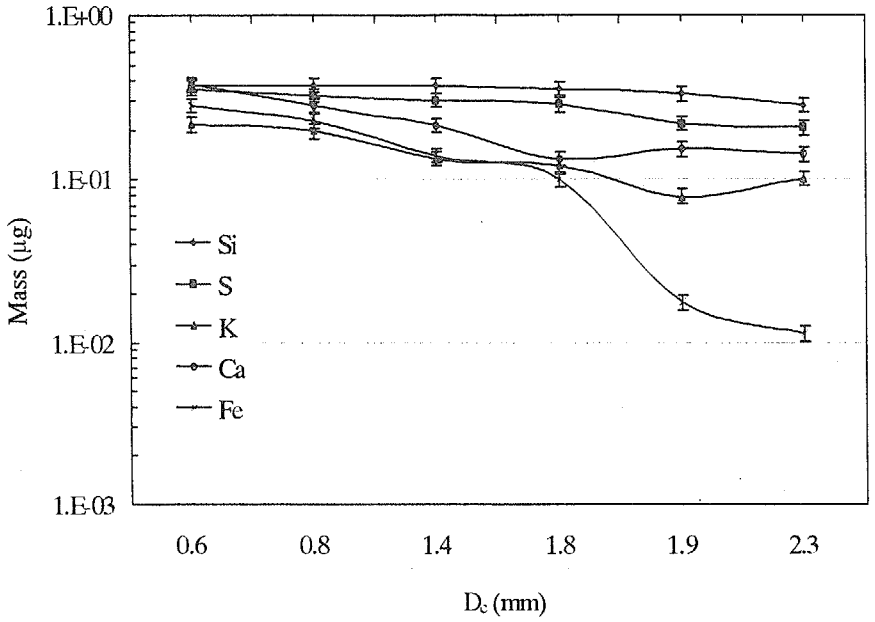

Fig. 2 Variation of major elemental masses as a function of snow crystal diameter. Dc means the diameter of dendritic sectored plate crystal measured by the circumscribed circle. The vertical bars represent the standard error values of the average mass.

Row and column are pixels corresponding beam scan area and the scale bar shows the intensity of characteristics X-ray count. Iron and sulfur were distributed at the whole rim portion of snow crystal. On the other hand, the distribution of potassium was formed at a part of rim line ranged from 25 to 75 and from 50 to 75 row and column pixel axes, respectively. Also the mask of three kinds of elemental maps was drawn at right down in Fig. 3. From this elemental mask and maps taken by micro-PIXE analysis, we can presume the chemical inner-structure and the elemental mixing state in and/or on single snow crystal.

References

1) C.-J. Ma, M. Kasahara, S. Tohno and T. Sakai, Japan Society Atmospheric Environment 38 (2003) 89-99.

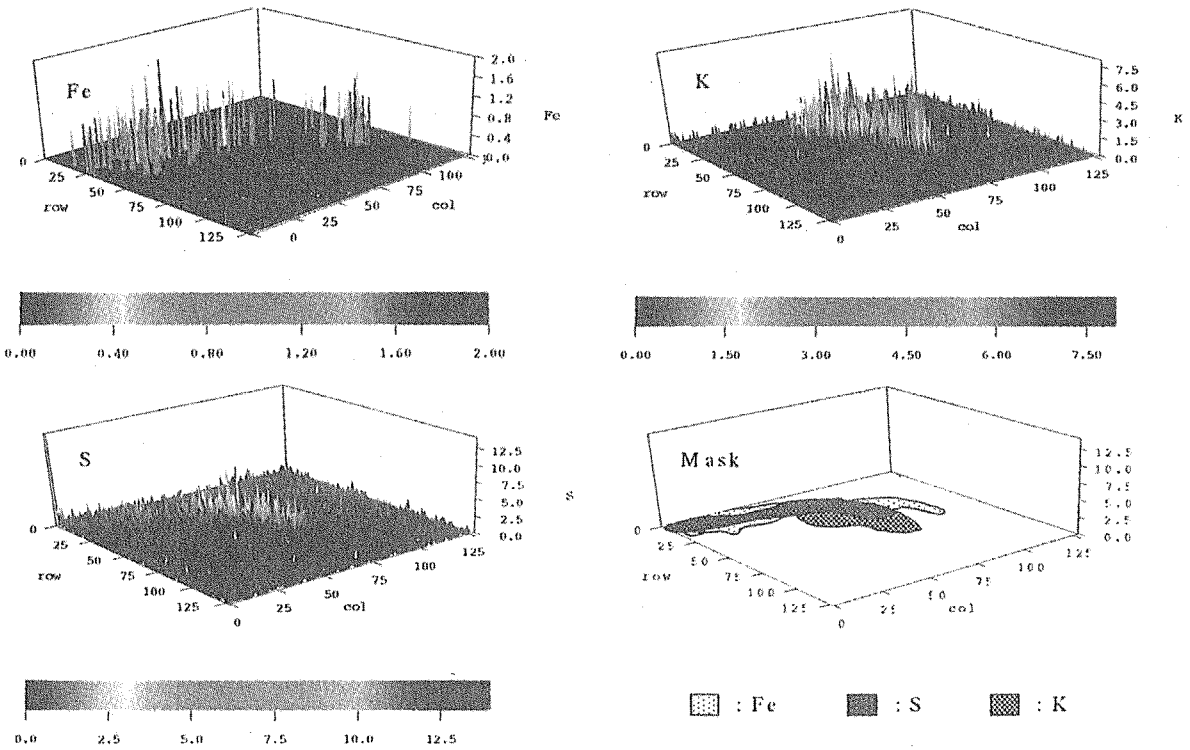

Fig. 3 An example of 3D micro-PIXE elemental maps taken on an edge part of hexagonal snow crystal replica formed on collodion film. Microbeam scanning area is 100 μm×100 μm. Scale bars represent the intensity of characteristics X-ray count.

7.3 Development of Single Ion Detectors using Thin Films

T.Kamiya*, M.Oikawa** and T.Satoh**
Advanced Radiation Technology Center, JAERI**
Department of Material Development, JAERI*

1.Introduction

Since an energetic heavy ion can introduce a localized radiation effect or damage in material along its track in microscopic scale, a combination of the single ion hit technique and a heavy ion microbeam with a high spatial resolution is a powerful tool to investigate individual phenomena induced by single-ion injections to local areas of samples, which have micron-scale structures such as semiconductor devices or biological cells. On the other hand, by confining irradiation damages in such narrow localized area can be a useful landmark to indicate how large area or region of the device to be concerned with charge collection events as reported in the previous works[1),2)]. Such information is important in the study of single event phenomena in real LSI device.

This is the first work on a micro-scale test device of silicon carbide (SiC) pn diode. SiC is a wide band-gap semiconductor, which is regarded as one of the materials suitable for power electronic devices because of its excellent thermal and physical properties in space or high radiation fields. The device was bombarded with 12 MeV nickel ions with a dose profile of 1 μm in FWHM. Computer simulation to reproduce transient current (TC) pulse height reduction was also performed using a Monte Carlo model.

2. Sample and experimental setup

The sample was a p^+n diode with a diameter of 100 μm fabricated on a 10 μm p-type 6H-SiC epitaxial film grown on a p-type 6H-SiC substrate (0.3 mm). This device was firstly tested using 15 MeV O ions by Ohshima et al[3)], but no damage was observed in the transient signals even if the ions were irradiated onto a spot with a 1 μm beam size.

In this work, a larger reverse bias of 30 V was applied to the diode to increase the depletion layer width to 2.5 μm, which is comparable to the range of 12 MeV Ni^+ ions in SiC (Fig. 1). The irradiation conditions of ions and energy were selected, so as to introduce the largest displacement damage effects within the depletion layer thickness in the biased junction. Accumulated displacement damage induced by previous ions reduces the charge collections, which take place along the ion trajectory in such region. If the lateral extent of the region concerning

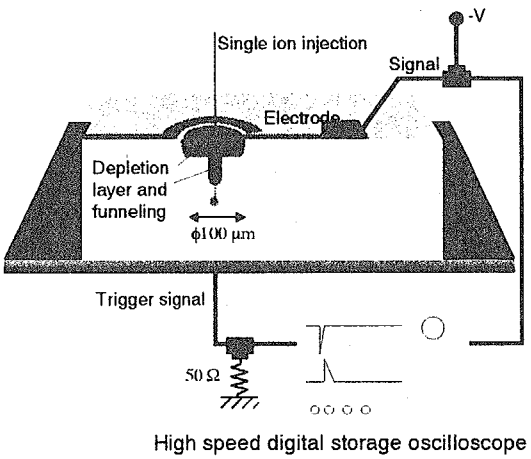

Fig. 1 A cross-sectional view of the SiC diode test devise and schematic illustration of the TIBIC measurement set up.

to the charge collection is larger than the beam size, bombardment will result in continuous degradation of the TC pulse signals. By analyzing this degradation we will show that the lateral extent of the charge collection could be obtained.

In this experiment, the numbers of 12 MeV Ni^+ were introduced one by one to a spot within the SiC diode with a special resolution of 1 μm (FWHM). The amount of charges generated in the diodes during the single ion irradiation was measured using the TIBIC data collection system in conjunction with a high-speed digital oscilloscope [4].

3. Results and discussions

Figure 2 shows the result due to irradiation of 12 MeV Ni^+ focused to a spot on the SiC diode sample with a beam size of 1 x 1 μm^2 (FWHM). Damage effects could be observed for the first 200 ions. A solid line in Fig. 2 shows a fitting using the Weibull distribution function (eq. 1) for the first 200. The data were analyzed with this function in analogy of survival of living things or defect rate in manufacture.

$$I = I_0 \exp\left(-\frac{n^m}{\alpha}\right), \qquad (1)$$

where I_0 is the numbers of charges generated in a diode by a single-ion injection. Some of the charges can reach the electrodes but others are trapped or recombined by vacancies induced by previous single-ion injections. The number of charges, I, survives at nth ion injection according to eq. (1) with shape parameter m and scale parameter α. The parameter m was found to be 0.3. The parameter m less than 1 indicates incipient failure type adapted to the manner of degradation of I. This result suggests that lateral extent of charge collection is larger than that of damage region induced by microbeam single ion hit.

This experiment of charge

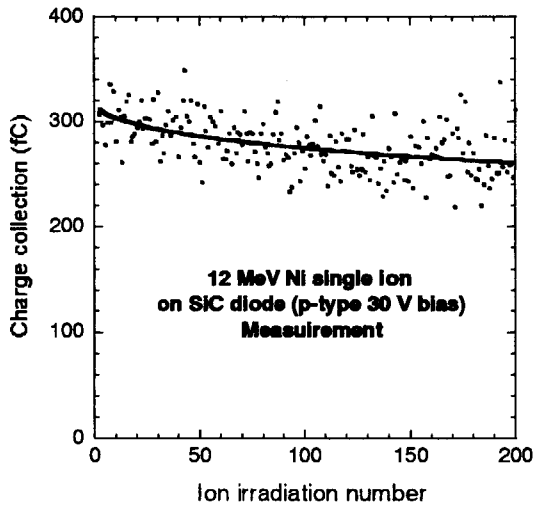

Fig. 2 Change of TC signals measured for a SiC diode as a function of the number of incident 12 MeV Ni ions. A rigid line indicates a fitting curve using the Weibull distribution function with a shape parameter m of 0.42 and scale one $\alpha = 44$.

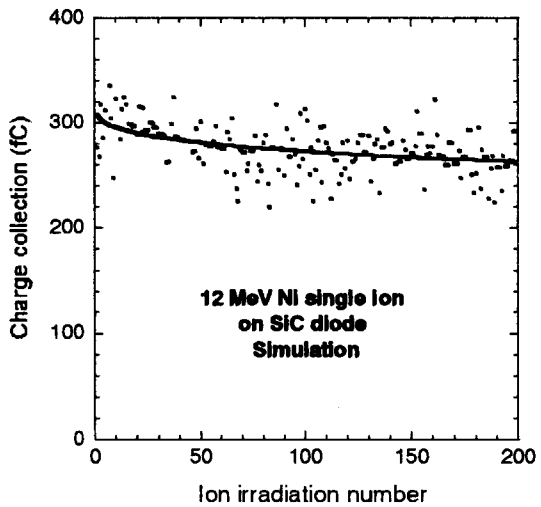

Fig. 3 Change of TC signals simulating the measured data for a SiC diode as a function of the number of the incident ions. The rigid line indicates the fitting curve using Weibull distribution function with a shape parameter, m of 0.30 and scale one $\alpha = 26$.

collection and radiation damage induced by 200 single-ion injections to a diode were simulated by applying a simple model for the survival of transient ion induced charges in an imaginary sample field, that was reported in a previous paper 2). Figure 3 shows the result of the numerical calculation reproducing measurements with 12 MeV Ni microbeams and parameters obtained using the Weibull distribution function. Although the model for the simulation seems to be too simple to evaluate the phenomenon exactly, the calculated result can well reproduce the measured one, when the lateral extent of the charge collection is about three times as large as that of the radiation damage by the microbeam with a spot size of 1 μm (FWHM) in diameter.

In order to obtain information on the longitudinal extent of charge collection, the range of ions in a diode is an important parameter to be compared with the depth of funneling, which increases the electric field's ability to attract the charges to one of the electrodes. If particles have a range greater than the device active volume, they do not leave much damage, but just a dense track of electron-hole pairs there. If heavy ions stop in such active region of the device, they leave not only charges along the ion track but also defects at the end of the range. Therefore, precise investigation on the longitudinal extent of charge collection in SETC can be made with this kind of measurement using the heavy ion microbeam single ion hit technique.

4. Summary

When a micro-scale test device of silicon carbide (SiC) pn diode was irradiated by single 12 MeV nickel ions with a lateral width of dose profile at 1 μm in FWHM, successive irradiation damage effects were observed in attenuation of the charge collection. The data was fitted to a Weibull distribution function and from the computer simulations using the Monte Carlo model for a single-ion injection indicated that the lateral extent of charge collection is more than twice as the microbeam spot size of 1 μm (FWHM) in diameter. The extent of charge collection in depth direction has also been discussed in conjunction with the thickness of a sensitive layer and the range of projectiles. Further measurement will be necessary with varying the range in samples. This work using a TC measurement technique demonstrated that geometrical information of single event transient charge current phenomena was obtained by analyses of damaged effect in measurements using micron-sized area irradiations with high-LET single-ions.

References

1)T.Kamiya, T.Sakai, Y.Naitoh, T.Hamano and T.Hirao, Nucl. Instr. And Meth. B158 (1999) 255.
2)T.Kamiya, T.Sakai, T.Hirao and M.Oikawa, Nucl. Instr. And Meth. B181 (2001) 280.
3)T.Ohshima, K.K.Lee, S.Onoda, T.Kamiya, M.Oikawa[1)], J.S.Laird, T.Hirao and H.Itoh, Nucl. Instr. And Meth. B210 (2003) 201.
4)J.S.Laird, T.Hirao H.Mori, S.Onoda, T.Kamiya, and H.Itoh, Nucl. Instr. And Meth. B181 (2001) 87.

7.4 Effect of the Thin Layer (Bonding Agent) on the Fluorine Penetration in the Tooth using PIGE

H. Yamamoto*, M. Nomachi**, K. Yasuda***, T. Sakai****Y. Iwami*, S. Ebisu*, Y. Sugaya**, M. Oikawa****, T. Satoh**** and T. Kamiya****
Graduate school of Dentistry, Osaka University*,
Graduate school of Science, Osaka University**,
Wakasa-wan Energy Research Center***,
Advanced Radiation Technology Center, JAERI****

1. Introduction

We have succeeded to establish a quantitative measurement method of fluorine (F) in a micro region of a tooth by using PIGE at JAERI[1,2]. The method is the effective tool for studying the biomaterial as the tooth[3].

In the dental clinical treatment, there is a technique to coat the surface of caries cavity of a tooth with the thin resin film before applying the resin materials. This technique is useful to adhesive the hydrophobic F-releasing material to the hydrophilic tooth surface. The lack of strong adhesion between the filling material and a tooth induces the leakage and the penetration of bacteria, which are the origins of second caries. In this study, we will report the effect of thin layer (Bonding agent) on F penetration in a tooth.

2.Experimenal procedure

2. 1 Experimental set-up

The experimental facility of the 1.7 MeV proton beam accelerated by the TIARA single-ended accelerator at JAERI-Takasaki, was used for this work. Precise conditions of the measurement were already published in the previous report [1,2].

2.2 Specimens

Class V cavities were prepared at the cement-enamel junction in the buccal face of extracted human teeth and the cavities were

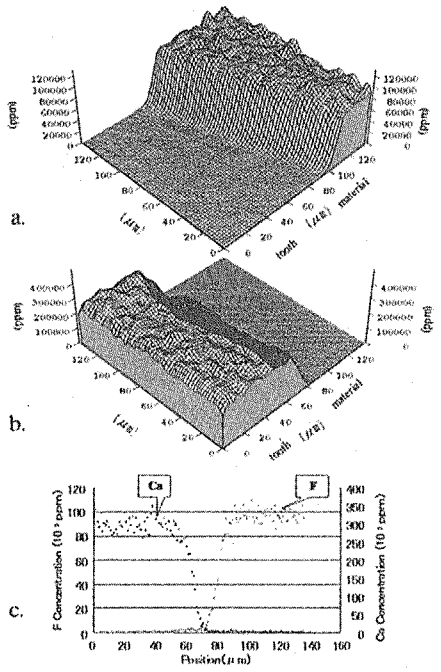

Fig.1. Group I (filling Beautifil with BA). F (a) and Ca (b) distribution maps (F source; fluoroaluminosilicate). Concentration (c) of F and Ca at 20 μm in width around the central part of the measured area.

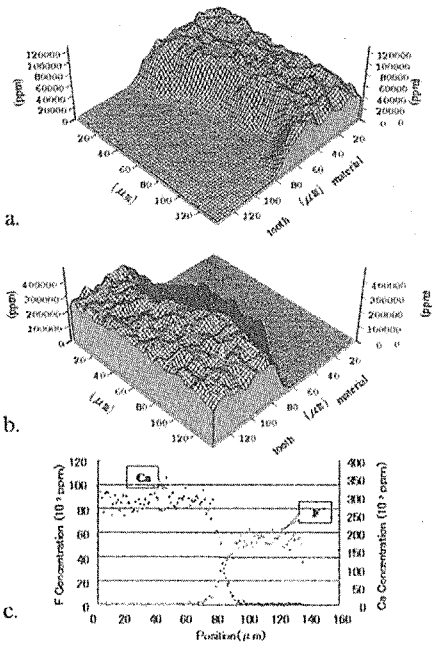

Fig.2. Group II (filling Beautifil without BA). F (a) and Ca (b) distribution maps (F source; fluoroaluminosilicate). Concentration (c) of F and Ca at 20 μm in width around the central part of the measured area.

filled with the F-releasing composite resin ; a) Beautifil (Shofu), b) Teethmate F-1 (Kuraray), c) Clearseal F (Kuraray). F sources of these materials are each a) fluoroaluminosilicate, b) methacryloyl F-methylmethacrylate copolymer, c) methacryloyl F-methylmethacrylate copolymer and NaF. As group I, the thin resin layer (Liner Bond II Σ Binding agent, Kuraray. It is abbreviated with the following BA) was applied in the cavity surface and light-cured before filling the materials. As group II, without BA, these materials were directly filled in the cavity. These resin materials harden by the visible ray. The viscosity of BA is low.

The precise pre-treatment of the specimens were the same as previous experiments and precisely described in the previous reports [1,2].

SEM photos observed the width of BA.

3. Results and Discussion

In Fig.1-6 are shown the obtained results as the 2D mapping form. In all specimens with BA, the F penetration from the F-releasing materials to the teeth was less than that of without BA for all specimens (Mann-Whitney, <0.05). Fig 7 shows the F concentration at the cavity surface, which is at the position in the middle in inclination region of the calcium concentration. In some case of group I, F concentration was below the detection limit of PIGE. For example, in the case of Beautifil, the following correlation was observed between F concentration in the tooth and BA width: F; 4000~37000ppm(without BA), F; < 7000ppm (0<BA width<~25μm), F; <1000ppm(BA width>~25μm). In the case of Teethmate F-1 without BA, F concentration was the highest at the dentin surface same as the previous data[3], like a kind of mountain rage is running alongside the dentin surface. In the case of Teethmate F-1 with BA, the two same heaps of F were observed at the dentin surface and between the F-releasing resin composite and BA. In the case of Clearseal F, F distribution in the material was inhomogeneous and decreased slowly from the boundary toward the tooth, and

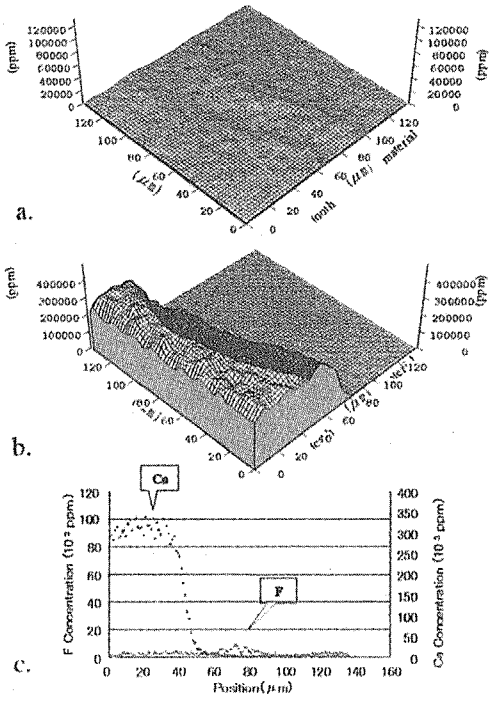

Fig.3. Group I (filling Teethmate F-1 with BA). F (a) and Ca (b) distribution maps (fluorine source; methacryloyl F-methylmethacrylate copolymer). Concentration (c) of F and Ca at 20 μm in width around the central part of the measured area.

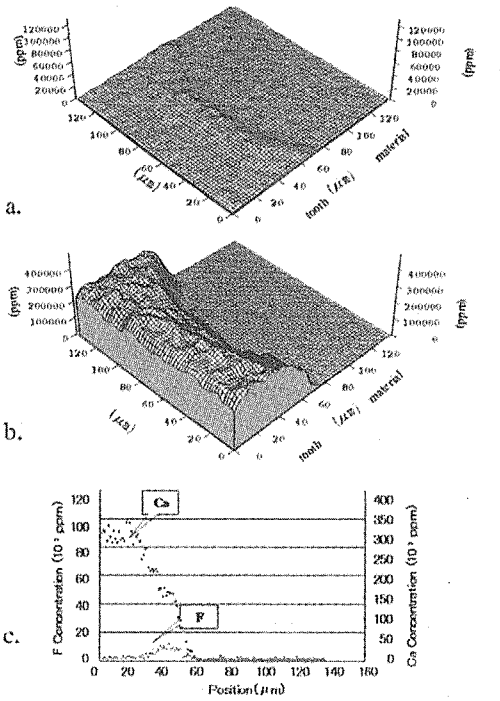

Fig.4. Group II (filling Teethmate F-1 without BA). F (a) and Ca (b) distribution maps (fluorine source; methacryloyl F-methylmethacrylate copolymer). Concentration (c) of F and Ca at 20 μm in width around the central part of the measured area

then at the dentin surface the small heap was observed.

The difference of F distribution in the tooth and material seemed to depend on the F concentration in the material and the mechanism of F releasing from the materials. The detail analysis of the phenomena examination is certain yet.

It was shown that F penetration from the material to a tooth could occur even under the existence of thin resin layer, but F concentration was lower comparing to without the thin layer. PIGE in TIARA enabled to measure the F concentration at the conditions under which the measurement has not been reported.

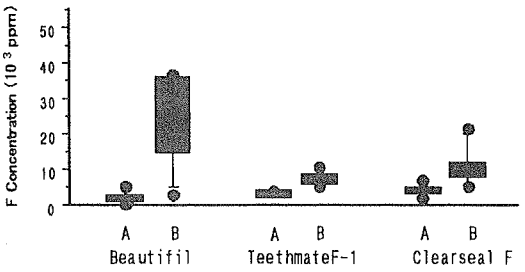

Fig.7. F concentration at the cavity surface. A; filling with BA. B; filling without BA.

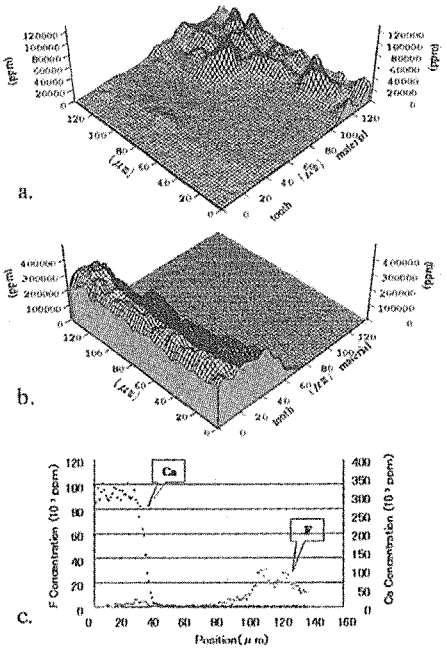

Fig.5. Group I (filling Clearseal F with BA). F (a) and Ca (b) distribution maps (F source; methacryloyl F-methylmethacrylate copolymer). Concentration (c) of F and Ca at 20 μm in width around the central part of the measured area.

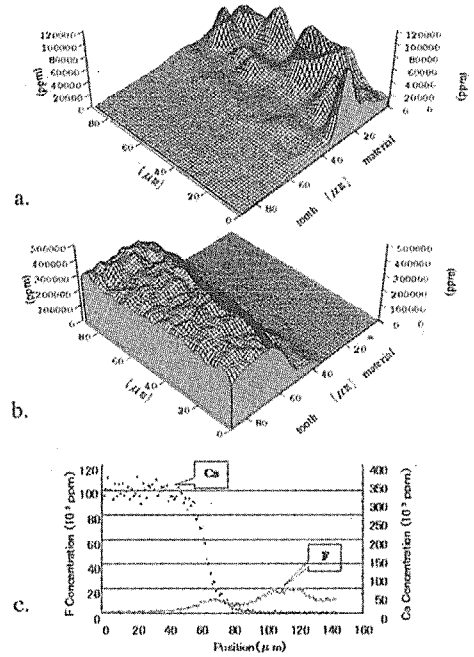

Fig.6. Group II (filling Clearseal F without BA). F (a) and Ca (b) distribution maps (F source; methacryloyl F-methylmethacrylate copolymer and NaF). Concentration (c) of F and Ca at 20 μm in width around the central part of the measured area.

4. Acknowledgements

We would like to thank members of TIARA, JAERI TAKASAKI for operating the accelerator facility.

References

1) M. Nomachi et al., TIARA Ann. Rep. 1998, JAERI-Review 1999-025 (1999) 226-228.
2) M. Nomachi et al., TIARA Ann. Rep. 2000, AERI-Review 2001-039 (2001) 244-246.
3) H.Yamamoto et al TIARA Ann. Rep. 2001, JAERI-Review 2002-035 (2002) 258-260.

7.5 Damage of Biological Samples by In-air Micro-PIXE

Y.Komori*, K.Ishii*, Y.Barbotteau*, K.Mizuma*, H.Yamazaki*, S.Matsuyama*, T.Nagamine**, K.Suzuki**, H.Kuwano***, M.Nakajima***, T.Kamiya****, T.Sakai****, T.Satoh****, M.Oikawa****, K.Arakawa****

Department of Quantum Science and Energy Engineering, Tohoku University *

Department of Nursing, Gunma University **

First Department of Surgery, Gunma University***

Advanced Radiation Technology Center, JEARI****

1. Introduction

The cross sections of x-rays emitted from atoms excited by ion-beams are very large (10^3b-10^4b), so we can use these x-rays to analyze trace elements (-ppb abundances). Moreover, by focusing the beam spot within 1μm (micro-beam) and scanning the sample, the elemental distributions in the sample are observed (micro-PIXE analysis). We developed an in-air micro-PIXE analysis system and obtained the elemental distributions of the bovine aortic endothelial cell.[1] This research aimed to develop the system capable of examining the metabolic mechanism in cells. As the current density of micro-beams is extremely high, damage to the sample might occur such as dissipation of elements and distortion of the sample. In vacuum micro-PIXE, the cell shrinks by 20% [2] and reduction of elemental yields P, S, Cl and K have been reported[3]. Using In-air micro-PIXE camera, it is possible to avoid the complete drying up of the sample, and the distortion of the sample and diffusion of electrolytic elements can be prevented. Moreover, the rise in temperature in the sample can be reduced by cooling with He gas. so Consequently the sample damage is reduced compared with in-vacuum micro-PIXE. The effect of sample damage by In-air micro-PIXE was examined through the observed change in structure, shape and elemental distribution.

In addition, we analyzed the human gullet cancer cell TE-1 cultured in a medium that contained cisplatin by In-air micro-PIXE.

2. Experiment

The micro beams exit to air through a Mylar film of 4μm thickness and irradiate bovine aortic endothelial cells (BAECs) ,which were cultured on the Mylar film, then cryofixed and freeze- dried.[4] Before and after irradiation, the three dimensional structures were observed with a confocal laser scanning microscope (KEYENCE VK8500), and the structural changes were identified. The change of the elemental yield was estimated by integrating the list data. Proton micro-beams of which the current was 100-150pA and the beam spot size was 1μm, were scanned on the areas of $45\times45\mu m^2$ and $90\times90\mu m^2$. We analyzed the samples on the vacuum side and ,by turning the Mylar window, on the in-air side for a direct comparison.

Human gullet cancer cells TE-1 were cultured

for 24hours in a medium that contained cisplatin(25μg/ml), and prepared by the conventional method[4] and analyzed. The total dose was 1240nC and the exposure time was 210min.

3. Results and Discussion

The actin filament, which is a kind of the cytoskeleton, was observed under a fluorescence microscope before and after sample preparation. The stability of structure and shape of the cytoskeleton was confirmed in the process of sample preparation. Fig.1 shows the images and the height distributions of cells, measured with a laser microscope before and after irradiation in-air analysis. The result shows that under in-air irradiation the size and three dimensional structure of the cell is conserved, although a minor change is seen at the surface of the cell.

Next, the temporal change of the x-ray yield was checked for each element. It was observed that the yields of P, K, Fe, Zn, and Br did not vary in both cases of in-vacuum and in-air irradiation. On the other hand, a decrease was observed for S in vacuum and in air with $45\times45\mu m^2$ scanning irradiation.

Figs.2 and 3 show the x-ray yield variation of S during irradiation. The initial yield value is normalized to one. However, by $90\times90\mu m^2$ in-air scanning irradiation, a decrease in S is not observed. In contrast it decreased by 20% under in-vacuum $90\times90\mu m^2$ scanning irradiation. By in-air analysis, the rise in temperature is reduced, the sample shape is unchanged and the volatile compounds have not diffused compared to in-vacuum irradiation. Moreover, the elemental distributions are unchanged during in-air and in-vacuum irradiation.

Fig.4 shows the element distribution images of a human gullet cancer cell TE-1 cultured with cisplatin. The element platinum included in the cisplatin is observed well.

4.Conclusion

The beam damage to biological samples can be reduced by in-air micro-PIXE compared with in-vacuum micro-PIXE. Especially, the three dimensional structures are well preserved. The x-ray yields remain unchanged with exception of the element for S, but x-ray yield for S decreased under in-vacuum irradiation and in-air with a small $45\times45\mu m^2$ scanning area irradiation. This latter elemental loss may be due to a strong rise in temperature for the small scanning area. It is concluded that one must pay attention to the experimental condition under beam irradiation. We would like to point out that the accumulation of cisplatin in the nucleus was confirmed for the first time in human gullet cancer cells TE-1.

References

1) K.Ishii, A.Sugimoto, et al., Nucl. Instr. And Meth. B181 (2001) 448-453.
2) F.Watt, P.S.P.Thong, et al. Nucl. Instr. and Meth. B130 (1997) 188-191.
3) K.Themner, Nucl. Instr. and Meth. B49 (1990) 52-59.
4) A.Sugimoto, K.Ishii, et al., I.J.PIXE. 9 (1999) 151-160.

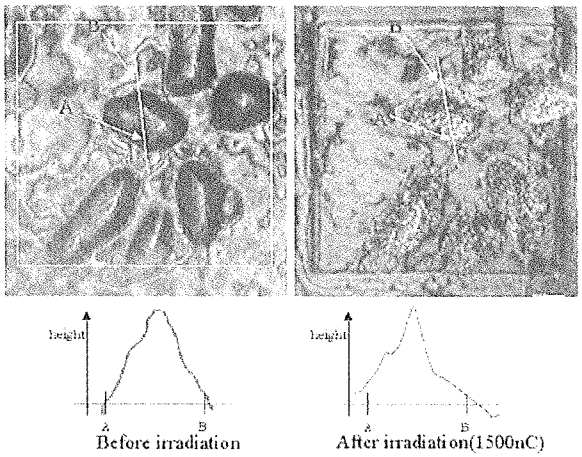

Fig.1 Observation by confocal laser microscope

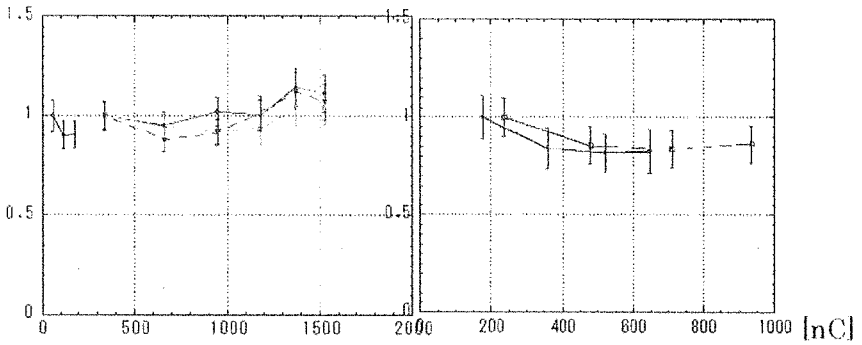

Fig.2 The change of x-ray yield of S. (in air, $90\times90\mu m^2$ scanning area)

Fig.3 The change of x-ray yield of S. (in vacuum, $90\times90\mu m^2$ scanning area)

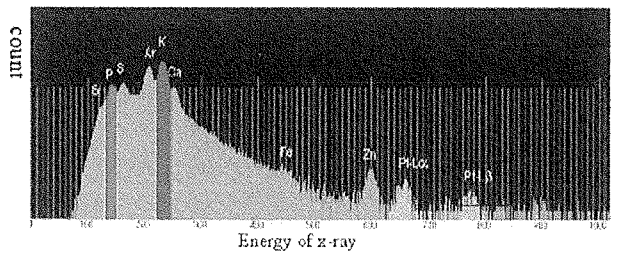

Spectrum of human gullet cancer cell TE-1.

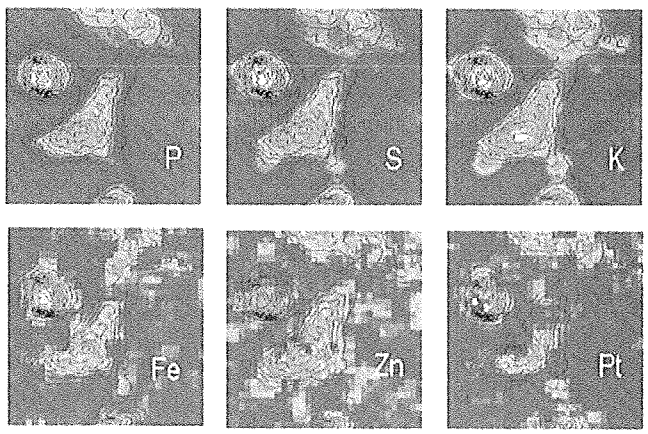

Fig.4 Elemental distributions of human gullet cancer cell TE-1.

This is a blank page.

8. Radiation Shielding for Accelerator Facilities

This is a blank page.

8.1 Characterization of ^{38}Cl and ^{39}Cl Formed by High-Energy Neutron Irradiation

S. Yokoyama*, H. Noguchi*, K. Sato*, Su. Tanaka**, T. Iida***, S. Furuichi***, Y. Kanda****, Y. Oki***** and T. Kaneto*****
Department of Health Physics*, Advanced Radiation Technology Center**, JAERI,
Graduate School of Nuclear Engineering, Nagoya University***,
Radiation Science Center, High-energy Accelerator Research Organization****,
Research Reactor Institute, Kyoto University*****

1. Introduction

In high-energy proton accelerator facilities, the air in the accelerator and target rooms is exposed to primary and secondary high-energy particles during the machine operation. Various radionuclides produced by the nuclear spallation of the air nuclei are present as both aerosol and gas. These become a potential source of radiation exposure. To estimate internal doses due to the inhalation of radioactive aerosols and gases, the physicochemical characteristics of radioactive aerosols and gases, in particular, the particle size of aerosols and the chemical form of gas, are very important parameters. It is therefore necessary to clarify the particle size distribution of aerosols, the mechanism of the radioactive aerosol formation and the chemical form of the aerosol and gas.

We have studied on the formation mechanism of radioactive aerosols by irradiating Ar gas containing non-radioactive aerosol particles with high-energy neutrons at TIARA[1), 2), 3)]. The results show that the formation of radioactive aerosols can clearly be explained by the attachment of radioactive atoms produced from Ar by the radiation-induced reactions, on a surface of coexisted non-radioactive aerosols. And the formation is independent of the size and physicochemical property of coexisted aerosol particles and the irradiation neutron energy. In this study, the physicochemical properties of chloric gases, which are commonly formed in the air of high-energy proton accelerator facilities[4)], were examined by the neutron irradiation of Ar gas at TIARA and the selective filter collection technique. Also examined were the physicochemical properties of radionuclides formed in the air of the AVF cyclotron room of TIARA.

2. Experimental methods

The neutron irradiation experiment was carried out using LC0 course in light-ion 3 room of TIARA. The neutrons were generated by the monoenergetic neutron source facility. An irradiation chamber (diameter 20 cm and length 100 cm) filled with high purity Ar gas (> 99.995 %) and di-octyl phthalate (DOP) aerosol was placed on the beam axis. The Ar gas containing the aerosol was irradiated with a 40 MeV quasi-monoenergetic neutron beam for 90 min. A neutron fluence rate in the monoenergetic peak at the acrylic window of the irradiation chamber was 1.9×10^{4} $cm^{-2}\cdot s^{-1}$. After the irradiation, the radioactive aerosols and gases in the chamber were collected using a sampler consisting of a particulate filter (Millipore filter, filter type: AA, pore size: 0.8m,MilliporeCo.),Na_2CO_3-impregnated filters, which can concentrate acidic gas (2 stages) and activated carbon fiber (ACF) filters (4 stages). A stainless steel container (160 cm^3) with activated charcoal (about 20 g) was placed behind the ACF filters and cooled by dry-ice/acetone to collect gases passed through the ACF filters. In addition, to examine the deposition of radionuclides on an inside wall of the irradiation chamber, the wall was covered with a thin aluminum sheet. The radionuclides deposited on a surface of the aluminum sheet were wiped with a filter paper after

collecting radioactive aerosols and gases in the chamber. The radioactivity of the filters and the gas trapped in the stainless steel container was measured using a gas-flow counter and ionization chamber, respectively. The γ-spectrum of the filter was measured by a germanium semi-conductor detector.

Radioactive aerosols and gases in the air of the AVF cyclotron room of TIARA were sampled in the radiation monitoring room through a pipe connected with a vent of the cyclotron room at a flow rate of 50 or 100 l/min. A particulate filter (HE40T), Na_2CO_3-impregnated filters (2 stages) and ACF filters (4 or 5 stages) were used to separate the aerosol and gases.

3. Results and Discussion

Figure 1 shows the distribution of radioactivity of the aerosol and gases collected on the Millipore filter, Na_2CO_3-impregnated filters and ACF filters. The radionuclides were found to be ^{38}Cl and ^{39}Cl formed from (n, 2np) and (n, p) reactions, respectively, by the neutron irradiation to ^{40}Ar gas. The radionuclides of ^{38}Cl and ^{39}Cl are detected in all the filters. The activity trapped in the first stages of Na_2CO_3-impregnated filter and ACF filter is obviously higher than those in the other stages. This means that ^{38}Cl and ^{39}Cl formed by the neutron irradiation to Ar gas exist as acidic gas and gas collected on the ACF filters. The ^{38}Cl and ^{39}Cl aerosols would be produced by the attachment of ^{38}Cl and ^{39}Cl atoms or these gases to DOP aerosol.

About 40 % of the gas collected on the four ACF filters was detected in the 2nd – 4th stages. In addition, a considerable amount of radioactive gas was also trapped in the stainless steel container behind the ACF filters. These results suggest that gas passed through the ACF filters would be formed by the neutron irradiation to Ar gas.

The radioactivity of ^{38}Cl and ^{39}Cl deposited on the surface of the aluminum sheet placed on the inside wall of the chamber was one order of magnitude higher than that of the ACF filter. This indicates that the ^{38}Cl and ^{39}Cl would easily attach to the aerosols and wall.

These results would be basic data for the assessment of the internal dose due to inhalation of the radionuclides. However, the accurate quantitative determination of ^{38}Cl and ^{39}Cl deposited on the inside wall of the chamber and passed through the ACF filters will be necessary to elucidate the proportions of gaseous chorine forms generated by the neutron irradiation.

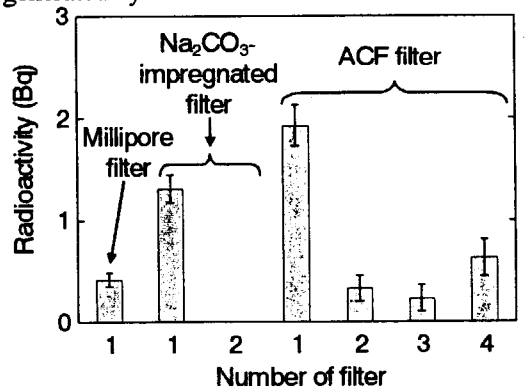

Fig. 1 Distribution of ^{38}Cl and ^{39}Cl activity on the filters.

Figures 2, 3 and 4 show the gamma-ray spectra of radioactive aerosols and gases in the air of the AVF cyclotron room of TIARA during the transport of 80 MeV proton beam to LC0 course. The radionuclides of ^{38}Cl and ^{39}Cl were detected in both of the Na_2CO_3-impregnated and ACF filters, but not in the HE40T filter. This means that the ^{38}Cl and ^{39}Cl atoms or gases generated in the air of the cyclotron room would hardly attach to the aerosol. The radionuclides of ^{38}S and ^{82}Br were also detected in the Na_2CO_3-impregnated and ACF filters, respectively. The ^{38}Cl and ^{82}Br gases would be generated by the neutron irradiation to stable isotopes of chlorine and bromine included in the covering material over cables around the accelerator and so on and release to the air from the material [5), 6)].

Table 1 shows the operating condition of AVF cyclotron during the collection of ^{38}Cl and ^{39}Cl in air of the cyclotron room. The ^{38}Cl and ^{39}Cl gases were observed in the room air during the transport

of 45 and 80 MeV H^+ to the LC0 course. The neutron dose rate measured by a room monitor during the transport of H^+ was several times higher than that during the transports of C^{5+} and He^{2+}. This indicates that the quantity of the radionuclides generated in the air of the accelerator room depends on the operating condition of the accelerator.

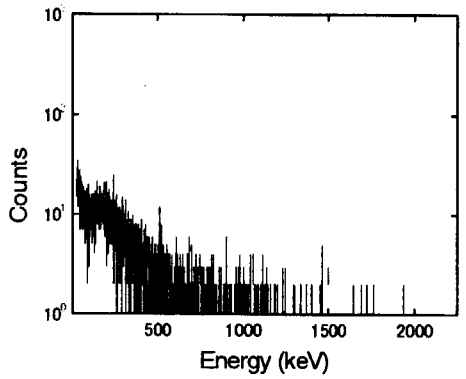

Fig. 2 Gamma-ray spectrum of aerosols collected on the HE40T filter.

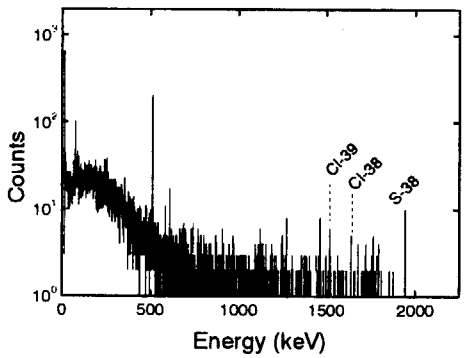

Fig. 3 Gamma-ray spectrum of acidic gases collected on the Na_2CO_3-impregnated filter.

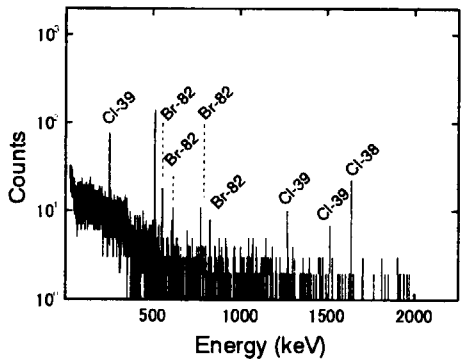

Fig. 4 Gamma-ray spectrum of gases collected on the ACF filter.

4. Summary

The characteristics of ^{38}Cl and ^{39}Cl produced by the 40 MeV neutron irradiation at TIARA to Ar gas containing aerosol were examined. It was found that ^{38}Cl and ^{39}Cl exist as aerosol, acidic gas and gases collected on the ACF filters and in the cold trap. Considerable amounts of these radionuclides were deposited on the inside wall of the irradiation chamber, indicating that the deposited activity cannot be ignored to estimate the proportions of gaseous chlorine forms generated by the neutron irradiation.

Table 1 Operating condition of AVF cyclotron during the collection of ^{38}Cl and ^{39}Cl in the air of the room.

Ion Source	H^+	H^+	He^{2+}	C^{5+}
Energy (MeV)	45	80	100	220
Current (μA)	3	2	2.5	5
Detection of ^{38}Cl and ^{39}Cl	D	D	ND	ND

D: Detectable, ND: Not detectable

In the air of the AVF cyclotron room of TIARA, ^{38}Cl and ^{39}Cl are present as acidic gas and gas collected on the ACF filters but not as aerosol. The ^{38}S and ^{82}Br gases were also observed in the room air. These radionuclides would be formed by neutron activation of structural materials around the cyclotron and released in the air of the room from the materials. It is necessary to examine the source of the radionuclides formed in the air of the cyclotron room.

References

1) Endo, A. et al., Appl. Radiat. Isot., 56 (2002) 615-620.
2) Sato, K. et al., Proc. of AESJ fall meeting (Autumn), (I) (2002) 177 in Japanese.
3) Endo, A. et al., J. Radioanal. Nucl. Chem., 256 (2003) 231-237.
4) Muramatsu, H. et al., Appl. Radiat. Isot., 39 (5) (1988) 413-419.
5) Nakamura Y. and Yokota, W., JAERI-M94-054 (1994) in Japanese.
6) Ashikagaya, Y., Nakazawa, T., JAERI-Tech 2001-092 (2001) in Japanese.

8.2 Measurement of Secondary Charged Particle Spectrum from tens of MeV Neutron Induced Reactions (Evaluation of basic data for external dosimetry)

T.Sanami*, M.Hagiwara**, N.Hirabayashi**, T.Ohishi**, M.Baba**, H.Nakashima*** and S.Tanaka****

Radiation Science Center, High Energy Accelerator Organization*

Cyclotron Radioisotope Center, Tohoku University**

Center for Proton Accelerator Facilities, JAERI***

Advanced Radiation Technology Center, JAERI****

1.Introduction

Energy and angular distribution data for secondary charged particles from tens of MeV neutron reaction are indispensable to evaluate dosimetry and irradiation effects of devices or instruments. Our group have been measured double differential cross sections (DDX) of secondary charged particle production reactions. In last year, we start on the development of method to measure DDX of secondary particles heavier than helium (fragments). Production rate of fragments is lower than lighter particles, but it can make large energy deposition in μm order region because of significantly large LET. Thus, DDX data are important to estimate irradiation effects caused by relatively high local energy deposition, such as single event effect (SEE) on devices. Up to now, the experimental data of DDX for fragments are less due to experimental difficulty except few cross section date obtained by activation method. In addition, theoretical calculation which can treat fragment production is few, also. Thus, reliable data are highly desired about fragment production reactions.

In this study, we adopt a Bragg curve spectrometer (BCS) to neutron induced fragment production reactions. In last year, we separate fragments and measure its energy from Carbon with large efficiency, successfully. From this result, in this year, we test 1) thin sample to minimize energy loss of fragments and 2) develop digital signal processing (DSP) method to enhance S/N and particle separation.

2. Outline of experimental method

Detail of the method was described in last report. Figure 1 shows schematic view of BCS. The BCS is a cylindrical - shaped grid ionization chamber (GIC) filled with a low pressure Ar+10%CH_4 gas. A sample is set on the cathode plate inside the BCS. The sample are 5 cm diameter carbon (0.1 mm thickness), poly -propylene film (10 μm) and silicon plate (500 μm). The polypropylene film to measure fragments from the $^{12}C(n,x)$ reactions. The detector is set at 5 m from the Li(p,n) neutron production target on LC3 course, TIARA[1]. Peak neutron energy is set to 75 MeV. The output signal, anode, from BCS is divided to two after passing through pre-amplifier and fed to two different shaping time amplifier to obtain bragg peak height and total energy of fragments[2),3)]. Figure 2 shows two-dimensional spectrum of short (0.4 μs) and long (6 μs) shaping time for 200 μm thickness carbon sample. Fragments can be separated clearly.

3. Result

3.1 Thin sample measurement

Energy loss of fragment in sample should be

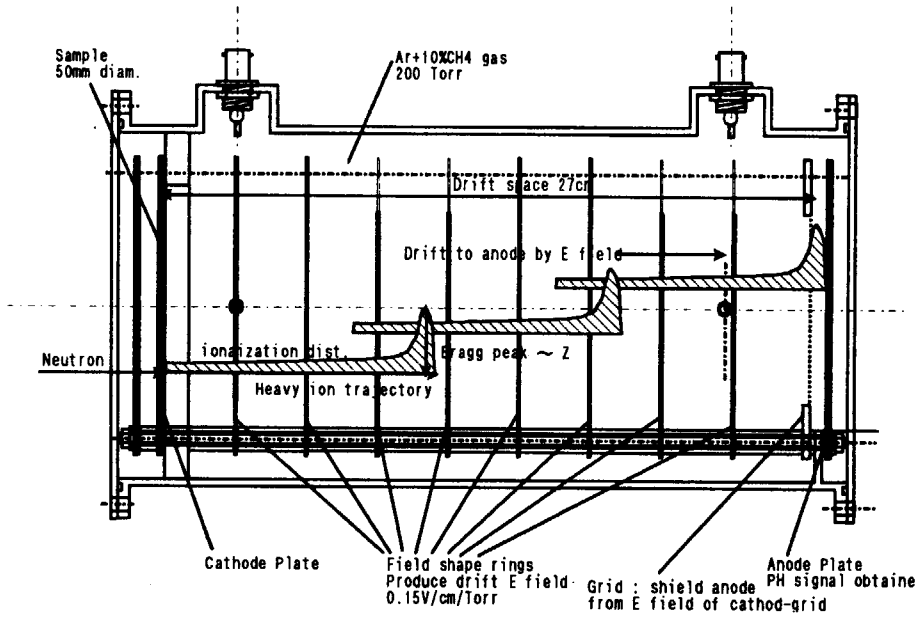

Fig. 1 Schematic view of BCS

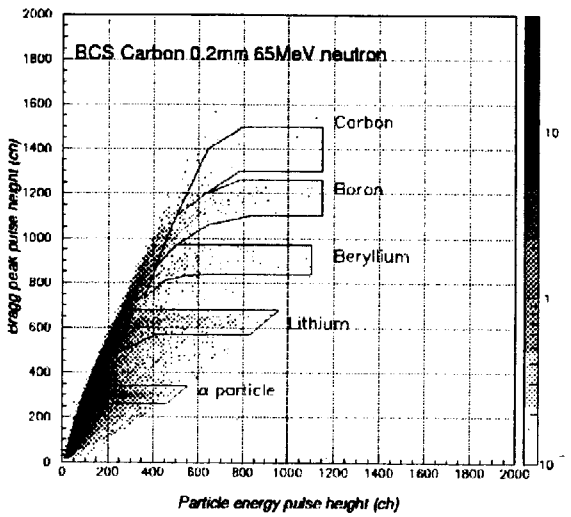

Fig.2 Two-dimensional spectra for 10μ polypropylene sample

corrected to obtain energy spectrum of fragment. In the case of thick sample, the correction has large errors and makes energy spectrum uncertainty. The problem is serious for fragment since its energy loss is large. On the other hand, thin sample causes low count rate. It is also serious for fragment measurement because of low production rate. Thus we have to choose sample thickness, carefully.

We test 10μm polypropylene film as carbon sample. The thickness makes energy loss correction less than 10% of its energy for lithium. Low energy beryllium, boron and carbon needs more energy correction. The film is not expensive and easy to handle in comparison with thin carbon. The gold foil is used as backing since the sample should be act cathode electrode also.

Figure 3 shows tentative results of Li energy spectra from 10 μm polypropylene, 500 μm silicon and 10 μm gold foil. Events from 10 μm gold foil are considered as background for one from 10 μm polypropylene. It means that we can obtain sufficient statistics in this condition. In the case of silicon sample, yield is low in comparison with polypropylene in spite of thick sample. In ether case, energy spectrum of He, Li, Be, B and C could be observed with acceptable S/N and counting rate.

3.2 Digital signal processing

Bragg curve spectroscopy is one of pulse shape discrimination technique. In addition, the pulse shape before shaping has not only information of Z number but also emitted angle or originate position of particles[4]. To obtain these

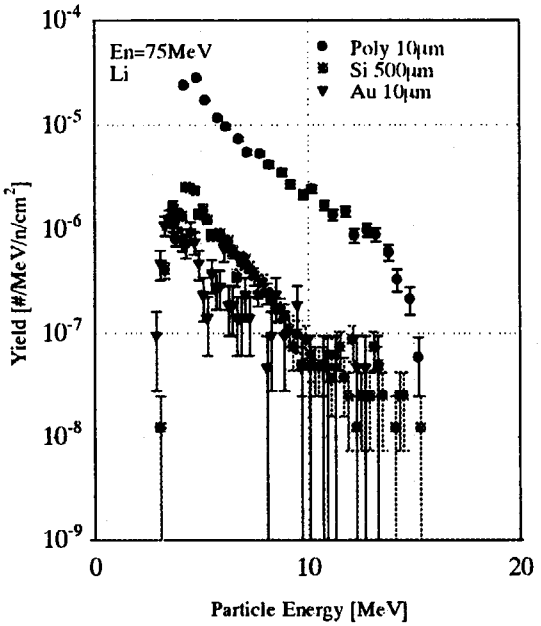

Fig. 3 Energy spectrum of Be

information for improvement of S/N, we adopt digital signal processing (DSP) method to this measurement.

Signals from Pre-amplifier are stored by LeCroy LT584L digital storage oscilloscope (DSO) with parameters of 8 bit vertical resolution, 10ns/point - 1000 point length (total 10 μs length) and 2 channel (anode and cathode)[5]. The DSO has large internal memory to store 2048 waveforms temporarily. After storing 2048 waveforms, all the waveforms are sent to PC through Ethernet interface. The procedure allows relatively high count rate up to 300 cps or more. DSO is triggered by coincidence signal between anode and cathode from ordinary NIM module electronics since count rate of anode signal exceeds 300 cps.

Figure 4 shows example of waveforms from

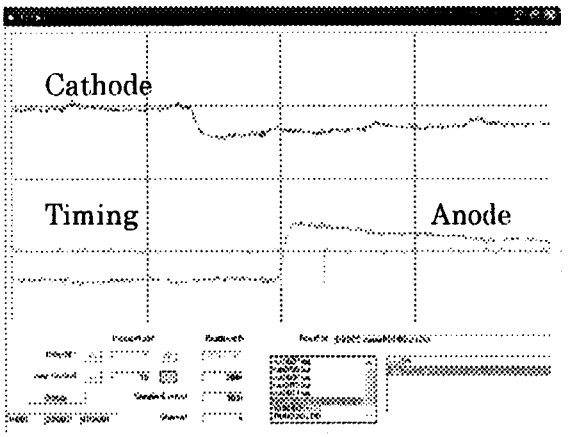

Fig.4 Example of waveforms from BCS

BCS. In offline analysis, pulse height of maximum and few μs from start are obtained as total energy and Bragg peak height for every waveforms. The data from DSO are confirmed by comparing with one from ordinal module systems. In addition, searching adequate shaping time and adopting fast Fourier transformation (FFT) to reduce electronic noise having high frequency are in progress.

Reference

1) M.Baba et.al., *Nucl. Instrm. Meth.*, **A428** (1999) 454

2) G.R.Gruhn, et.al., *Nucl. Instrm. Meth.*, **196** (1982) 33

3) N.J.Shenhav and H.Stelzer, *Nucl. Instrm. Meth.*, **228** (1985) 359

4) T.Sanami, M.Baba, K.Saito and N.Hirakawa, *Nucl. Instrm. Meth.*, **A440** (2000) 403

5) K.Takahashi et.al., *Proc. of 16th workshop on Radiation Detectors and Their Uses (KEK Proceedings 2002-12)* p85

8.3 Development of Phoswitch-Type Neutron Monitor Detector Applicable to Energies up to 100 MeV

T. Sato*, A. Endo*, Y. Yamaguchi* and Su. Tanaka**
Department of Health Physics, JAERI*
Advanced Radiation Technology Center, JAERI**

1. Introduction

High energy proton accelerator facilities have been constructed for applying to various fields of study, such as nuclear physics, material science and radiotherapy. In these facilities, it is very important to monitor doses from high energy neutrons since such neutrons can penetrate the radiation shields, and dominantly attribute to the doses of workers and members of the public[1]. However, conventional-type rem-counters, which are widely used as a neutron monitor in various kinds of radiation facilities, are not applicable to neutrons with energies above 20 MeV.

With this specific problem in mind, we have tried to develop a phoswitch-type neutron monitor detector applicable to neutrons with energies from the thermal energy to 100 MeV. Characteristics of the detector were studied experimentally in quasi-monoenergetic neutron fields of 40, 65 and 75 MeV at TIARA and moderated neutron fields of the ^{241}Am-Be source at Facility of Radiation Standard (FRS) in JAERI. A detailed structure of the detector and experimental results are presented below.

2. Structure of Detector

The structure of the phoswitch-type detector is shown in Figure 1. The detector is composed of cylindrical (12.7 cm in diameter and 12.7 cm in length) liquid organic scintillator BC501A covered with a ^{6}Li+ZnS(Ag) sheet.

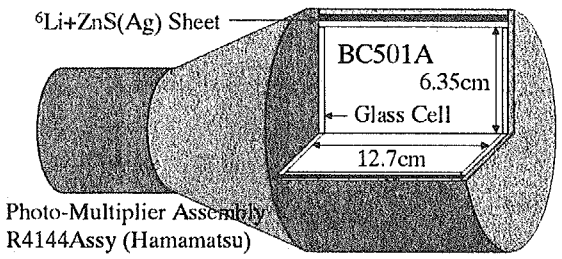

Figure 1 Schematic view of detector structure.

When a neutron with energy over several hundreds of keV strikes the detector, it can produce secondary protons which are capable of causing scintillation of BC501A. Lower energy neutrons, on the other hand, are detected by scintillation of the ZnS(Ag) sheet stimulated by α particles which are produced by neutron capture reactions of ^{6}Li. The signals from the two scintillators are amplified by a photo-multiplier R4144. Those signals are discriminated by measuring their pulse shapes, since the mean decay time of those from BC501A is much smaller than those from ZnS(Ag) sheet – approximately 100 nsec and 3 μsec, respectively.

Dose from higher energy neutrons is evaluated from light output of BC501A by applying the spectrum weighted dose function[2], G-function, which relates the light output to the neutron dose. The function can be calculated from fluence to dose conversion

coefficients and the response function of the detector. For the conversion coefficients, we adopted the values for the ambient dose equivalent at the depth of 10 mm – H*(10). The response function of BC501A was calculated by the SCINFUL-CG[3] and Cecil's codes[4] for neutron energies below and above 80 MeV, respectively.

3. Experiment

The experimental arrangement for studying the particle discrimination profile of the detector is illustrated in Figure 2. The detector is located at a distance of 60 cm from the ^{241}Am-Be source at FRS. A paraffin block with 15 cm thickness was placed in front of the detector as a neutron moderator.

Signals due to the scintillations of the ZnS(Ag) sheet and BC501A were discriminated by analyzing their rise time of the dynode signals from the detector. The gamma contaminations among the signals due to the scintillations of BC501A were excluded by the conventional neutron-photon discrimination technique – measuring the ratio of the total and slow components of the anode signals.

The characteristics of the detector in terms of the dose evaluation ability were studied experimentally in quasi-monoenergetic neutron fields of 40, 65 and 75 MeV at TIARA. The experimental setup is shown in Figure 3. The detector was located at a distance of 12.9 m from the Li target. The fluence of neutrons with the peak energies were calibrated by fission chambers placed near the target.[5]

In the data analysis, signals due to the incidence of fast neutrons were picked up and

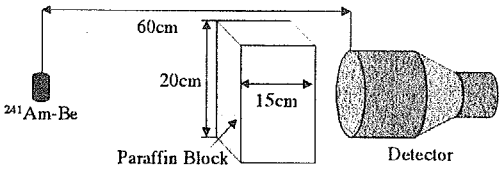

Figure 2 Experimental setup at FRS.

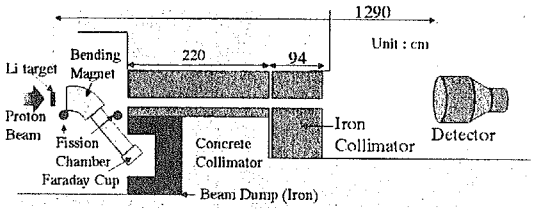

Figure 3 Experimental setup at TIARA.

the energy of the neutrons was determined by the time-of-flight (TOF) method. The dose from neutrons with the peak energy was obtained from the pulse height distribution of the corresponding neutrons by applying the G-function.

4. Results and Discussion

Figures 4 and 5 give graphical presentations of the particle discrimination profile of the detector. The data presented in Figure 4 indicate that signals due to the scintillations of the ZnS(Ag) sheet and BC501A can be clearly discriminated. The gamma contamination can be excluded by analyzing the ratios of total and slow components of the anode signals as shown in Figure 5. The difference of the ratios between gamma and neutron incidences, however, becomes smaller with decreasing of their light outputs, and the gamma contaminations among the signals with light outputs below 0.2 MeVee cannot be excluded. Therefore, dose from neutrons with energies below 1 MeV is unable to be evaluated from the pulse height distributions, since such low energy

neutrons cannot cause scintillation with light outputs above 0.2 MeVee.

Figure 6 shows the pulse height distribution of 40 MeV neutrons measured at TIARA, together with that calculated by SCINFUL-CG. It is evident from the figure that those results agree with each other. The neutron dose obtained from the pulse height distribution by applying the G-function is 11.9 (μSv/h), while the corresponding value calculated from the neutron fluence calibrated by the fission chambers is 11.2 (μSv/h). These values agree with each other, and the agreement between the two doses – one by the G-function and the other by the neutron fluence – can be observed in the cases of the other incident energies. We therefore conclude that the detector can be used for monitoring of high energy neutron doses.

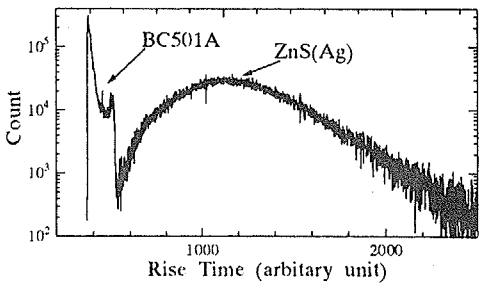

Figure 4 Rise time distribution of dynode signals.

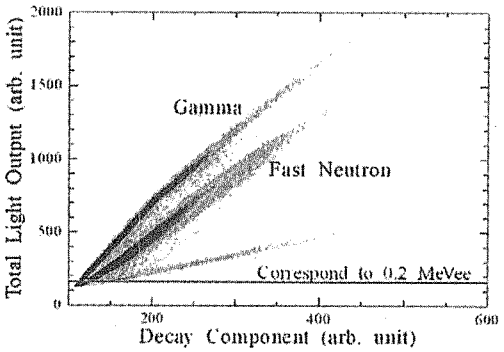

Figure 5 Two-dimensional plot of the total and slow component of anode signals.

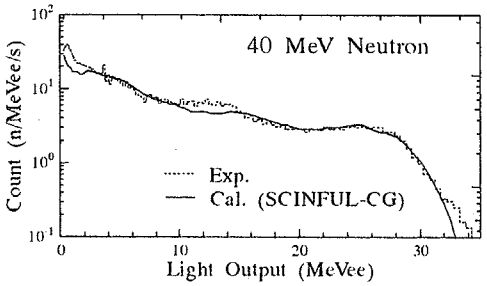

Figure 6 Pulse height distribution of 40 MeV neutrons.

5. Conclusions

The phoswitch-type detector is capable of measuring photons, thermal and high energy neutrons with an excellent property of the pulse-shape discrimination between them. Dose from neutrons above 1 MeV can be obtained from the pulse height distribution by applying the G-function. The conversion coefficient from the number of scintillations of ZnS(Ag) sheet to low energy neutron dose must be determined in order to use the detector as a neutron monitor for wider energy range – from the thermal energy to 100 MeV.

References

1) Y. Miyamoto, K. Ikeno, S. Akiyama and Y. Harada, JAERI-Tech 2002-86 (2002).
2) Y. Oyama, K. Sekiyama, and H. Maekawa, Fusion Technol. 26(3), pt2, 1098 (1994).
3) E. Kim, A. Endo and Y. Yamaguchi, J. Nucl. Sci. Technol. Suppl. 2, 693 (2002).
4) R. A. Cecil, et al., Nucl. Inst. and Meth. A161, 439 (1979).
5) M. Baba, et al., Nucl. Inst. and Meth. A428, 454 (1999).

This is a blank page.

9. Accelerator Technology/TIARA General

9.1 Construction of intense positron source based on AVF cyclotron for high brightness positron beam

M. Maekawa, A. Kawasuso, T. Ishimoto, Z. Q. Chen
Advanced Science Research Center, JAERI

1. Introduction

Positron beam is widely used as a powerful tool to detect vacancy-type defects or to analyze the topmost surface structure in non-destructive way with high sensitivity. In our research group, we have been developing reflection high-energy positron diffraction (RHEPD) apparatus for the analysis of surface structure of semiconductors and several types of slow positron beam apparatuses for the depth profiling of defects[1,2]. These apparatuses are used with the sealed positron sources. Although the machine geometry can be simplified and excellent beam stability can be realized using the sealed sources, the beam brightness is not enough for the observation of the transient phenomena on the surface or the small regions in a micrometer range. To break this limitation, we attempt to construct an intense positron source which used the nuclear reaction $^{27}Al(p,n)^{27}Si$ for high brightness positron beam. This method is inferior in absolute beam intensity compared with the large-scale positron sources, such as using electron LINAC or the nuclear reactor. However, it is suitable for production of a high brightness positron beam because of following advantages; (i) easy beam handling due to simple and compact structure of positron production system, (ii) stable beam production based on a nuclear reaction.

2. Design of positron production system

In order to obtain a high brightness positron beam, it is needed to accelerate generated positrons to high energy and to focus it by the lens system. However, the design of such a lens system greatly depends on the initial conditions of the generated positrons. In this study, we first try to confirm the production of positrons and to clarify the initial condition of positrons using simple magnetic guiding beam line.

Figure 1 shows a schematic drawing of positron source. The proton beam supplied from the TIARA AVF cyclotron is irradiated to the

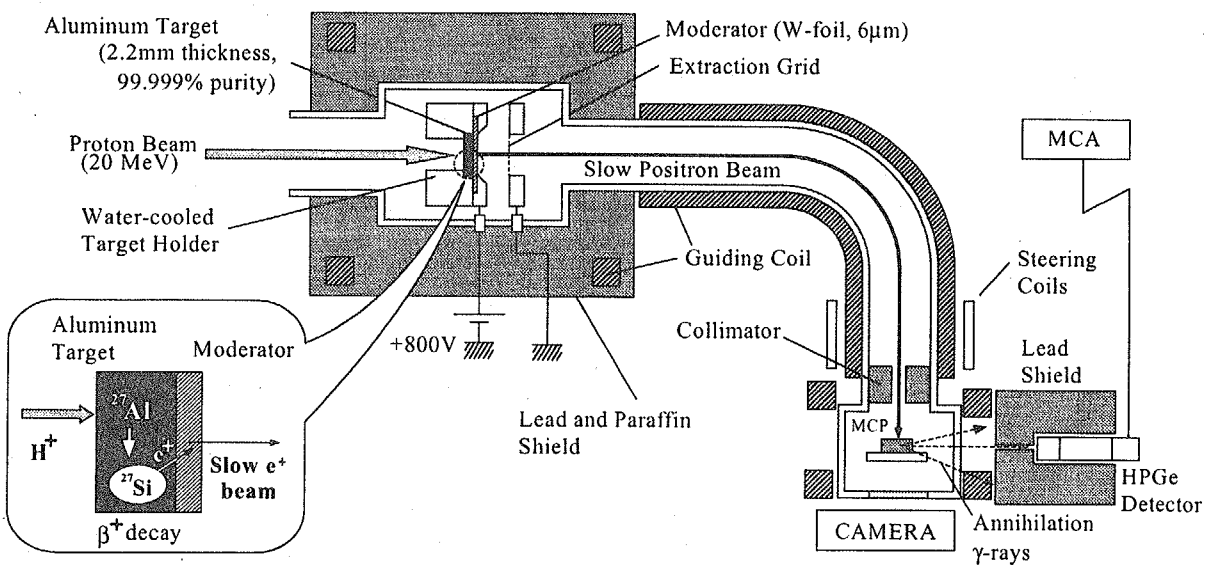

Fig. 1 Schematic of positron production system

high purity aluminum target (99.999% purity, 8 mm diameter), which mounted on the jacket with 5 mm collimator cooled with running water. In this target, the nuclear reaction ^{27}Al (p, n) ^{27}Si occurs and β^+ decay of ^{27}Si follows with a half-life of 4.3 sec. The percentage of the β^+ decay branching ratio of the ^{27}Si is 100 %. The fast positrons emitted from ^{27}Si are thermalized in a polycrystalline tungsten moderator with a thickness of 6 μm. This thickness is determined as the highest positron re-emission efficiency by the calculation using the diffusion equation considering the positron implantation profile emitted from ^{27}Si (~3.85 MeV) as shown in Figure 2 [3, 4]. Slow positrons emitted from the moderator surface are extracted by a grid electrode and transported to the beam monitor (MCP) by a magnetic guiding field (~0.01 T). To suppress backgrounds due to fast positrons, secondary electrons, ions and γ-rays coming from positron source directly, this guiding field includes a 90° bended section equipped a collimator. The whole of positron production system is covered by a lead and paraffin to shield gamma rays or neutrons.

The reported maximum cross section of the nuclear reaction ^{27}Al(p,n)^{27}Si is in the energy range of 14-16 MeV [5, 6]. Therefore, ion beam energy was selected to be 20 MeV here. The maximum range of 20 MeV protons in the aluminum is about 2.2 mm. To avoid direct damage of moderator by proton irradiation, the thickness of aluminum target used in this system is 2.4 mm. The saturated radioactivity of the ^{27}Si for a proton current of 1 μA is evaluated at 9.3 GBq by the IRAC code[7], and the radioactivity is distributed widely from the proton injected surface to a depth of about 2 mm as shown in Fig. 3. Since fast positrons of 9.3×10^9 e^+/s are generated from the ^{27}Si of 9.3 GBq, the expected intensity of slow positron beam is ~10^6 e^+/s when the conversion efficiency to slow positrons by the moderator is assumed to be 10^{-4} [8]. This intensity is two orders of magnitude higher than that of the conventional positron beam based on sealed positron source.

3. Results and discussion

The observed positron beam is shown in Fig. 4. The incident ion beam energy and current were 20 MeV and 70 nA, and positron transportation energy was 800 eV. The diameter of incident ion beam was adjusted about 5 mm. Thus, the positron beam can be generated without any special difficulty. Moreover, the intensity of the beam was very strong. The diameter of positron beam was 5 mm. The number of transported positrons was also measured using HPGe

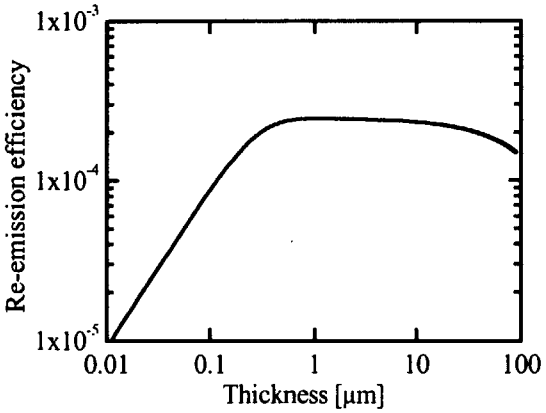

Fig. 2. Calculated moderation efficiency of a transmission-type tungsten moderator for the β^+ rays emitted from ^{27}Si.

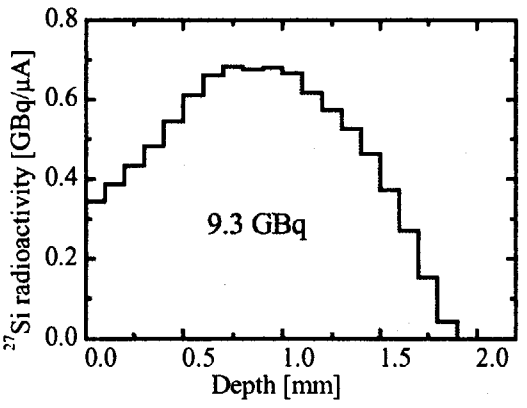

Fig. 3. Calculated distribution of ^{27}Si in aluminum target produced by 20 MeV proton beam.

detector counting the annihilation gamma rays (511 keV). The proton current dependence of positron beam intensity is shown in Fig. 5. The number of positrons showed fairly good linearity with incidence ion beam current. Estimated number of slow positron is about 10^7 e^+/s/μA. This is however one order of magnitude higher than the Hirose's report [9] or expected from the IRAC simulation. Due to the short transportation distance, the influence of backgrounds might be superimposed on the data because the soundings of positron production system under ion beam irradiation was a high radiation field containing with neutrons. Nevertheless, this result is promising towards the intense positron beam production using the cyclotron.

It is thought that the energy of the proton beam (20 MeV) used in the present time is different from the energy of the maximum cross-section for production of ^{27}Si. Sufficient target thickness was needed to avoid the transmission of proton beam and a consequent damage of the moderator. On the other hand, fast positrons escaping from the target will be effectively injected into the moderator using a thinner target. Probably, the conversion efficiency from fast to slow positrons is enhanced with lower ion energy and thinner target than used here. For this reason, the optimum energy to yield ^{27}Si is not necessarily suitable to maximize the slow positron beam intensity. Although in the present AVF cyclotron the proton energy is not continuously tunable, the optimal proton energy for the slow positron beam generation should be determined in feature.

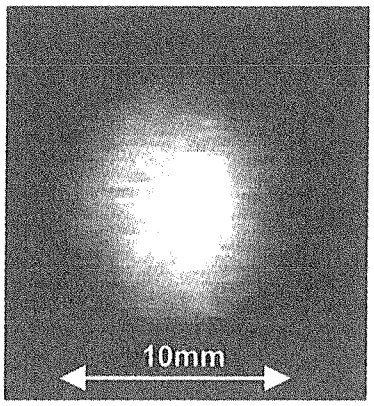

Fig. 4 Positron beam image observed with a MCP with 10mm diameter.

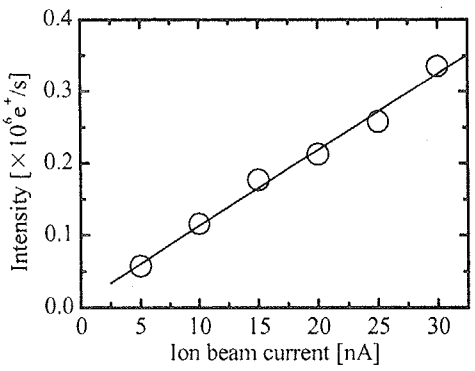

Fig. 5 Positron beam intensity as a function of the proton current.

References

1) A. Kawasuso, S. Okada and A. Ichimiya, Nucl. Inst. & Meth. **B171** (2000) 219-230.

2) M. Maekawa, A. Kawasuso, M. Yoshikawa and H. Itoh, Appl. Surf. Sci. **216** (2003) 365-370.

3) A. Vehanen and J. Makinen, Appl. Phys **A36** (1985) 97-101.

4) W. Brandt and R. Paulin, Phys. Rev. **B15** (1977) 2511-2518.

5) J. D. Anderson, S. D. Bloom and C. Wong, Phys. Rev. **117** (1696) 177.

6) P. M. Racolta, L. Popa-Simil, N. Miron and C.I.Muntele, Nucl. Inst. & Meth. **B139** (1998) 461.

7) S. Tanaka, M. Hukuda, K. Nishimura, M. Watanabe, N. Yamano, JAERI-Data/Code 97-019 (1997).

8) K. G. Lynn et.al., Appl. Phys. Lett. **47** (1985) 239-240

9) M.Hirose, M. Washio and K. Takahashi, Appl. Surf. Sci. **85** (1995) 111.

9.2 Measurement of Secondary Charged Particle Emission during Irradiation of MeV Energy Cluster Ions

Y. Saitoh *, A. Chiba*, K. Arakawa*, K. Narumi ** K. Hirata ***, H. Shibata**** and A. Itoh*****

Advanced Radiation Technology Center, JAERI*
Advanced Science Research Center, JAERI **
National Institute of Advanced Industrial Science and Technology ***
Research Center for Nuclear Science and Technology, The University of Tokyo****
Quantum Science and Engineering Center, Kyoto University*****

1. Introduction

Recently, a non-linear effect was observed in energy loss of MeV energy boron and carbon cluster ions passing through foil targets[1),2)]. Large enhancement of sputtering yields from metal targets was also reported for gold cluster ions[3)]. It is generally recognized that a massive energy deposition into a very small volume introduced by cluster ion irradiation will cause this kind of non-linier phenomena[4)]. From a viewpoint of industrial applications such as materials modification, we must control accurately the fluence of cluster ions implanted into a target. It is, however, often difficult to know accurate fluence from apparent beam current on a target, since the beam current measured for cluster ions tends to change significantly depending on target materials, being different from the case of single ion beam. For instance, in our ion-implantation apparatus equipped with a secondary electron suppression system, apparent beam currents on metal targets were negative values for C_8^+ cluster ion beam, while those were positive for a single C^+ ion beam[5)]. It suggests evidently an effect of secondary particle emission and macroscopic quantities like an apparent beam current are significantly affected by this effect. It is, therefore, important to know the property of secondary particles emitted from a target under irradiation of MeV energy cluster ions. In this work, emission of secondary electrons and positive ions from Si and Au targets have been investigated in detail using MeV energy carbon cluster beams. Beam currents on a target and on a suppression electrode were measured simultaneously at various suppression voltages.

2. Experimental

The experiments were carried out using the TC beam line of the 3MV tandem accelerator at the TIARA facility[6)] in JAERI. Incident beams were well collimated to 1 mm in diameter before entering the experimental chamber. The target sample of silicon surface was processed with hydrofluoric acid to clean up an oxide layer.

At first, we measure the emission efficiency of secondary electrons. In this case negative bias voltages were placed on the target plate, and beam currents on the target were measured at various bias voltages. The apparent total beam current I_t measured in this way is equal to the sum of incident beam current I_b and escaping secondary electron current I_e measured as a positive value ($I_t=I_b+I_e$). For an incidence of C_n^+ ions, emission efficiency of secondary electrons Y, defined as the number of secondary electrons per carbon atom, is obtained by

$$Y = (I_t - I_b)/(I_b \times n) \quad (1)$$

Note that the incident beam current I_b was measured accurately with a high-aspect ratio Faraday cup by removing the target plate from the beam line. The Faraday cup used here is 20 mm in diameter and 400 mm in depth, and the bottom part of the cup is inclined by 45 degrees with respect to the beam axis. Care was taken to ensure that the incident beam current was nearly constant during these independent measurements.

Next, secondary emission of positive ions (and neutrals) was investigated. As the purpose of the present work is to know the influence of secon-

dary particle emission on the beam current measurement under an actual experimental situation of ion-implantation condition, the target samples were set in the holder simulating our ion-implantation apparatus. In this case the bias voltage to the target is 0 V. The target is surrounded by an Al shielding box and an electron-suppression electrode to avoid inflow of scattered ions or electrons produced outside the box. The incident beam is introduced through two holes of 5 mm in diameter. A solid angle of these holes is about 1.7 msr with respect to the target center. Electric currents I_t on the target and I_s on the shielding box are measured simultaneously with digitalcurrent meters (ADVANTEST R8240 digital electrometer) and acquired with a personal computer.

3. Results and Discussion

Figure 1 shows apparent ion beam currents I_t versus target bias voltage measured using the secondary electron measuring system for carbon cluster beams of C_1, C_4 and C_8 on a Si target, where the data are normalized using accurate beam currents I_b obtained by the Faraday cup. It appears that each value is almost constant in nearly a whole range of bias voltage investigated. Using Eq. (1), emission efficiency Y of secondary electrons was obtained, as shown in Fig. 2, for Si and Au targets. The electron emission efficiencies for both targets decrease with increasing cluster size. The ratios of $Y(C_n^+)/nY(C^+)$, which is the electron emission yield per atom in the cluster normalized to the yield of single atom, were 0.77

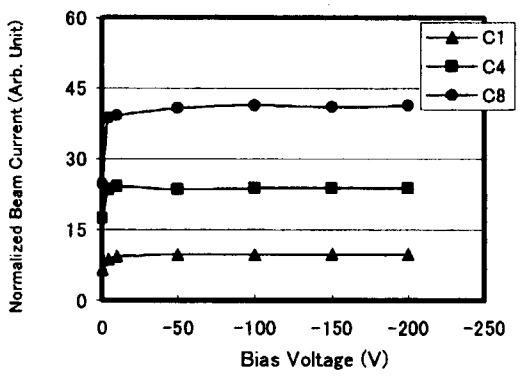

Fig. 1 The measured carbon cluster beam current of C1, C4 and C8 on the Si target, which was normalized by the Faraday cup current, versus the bias voltage from 0 to -200 V, respectively

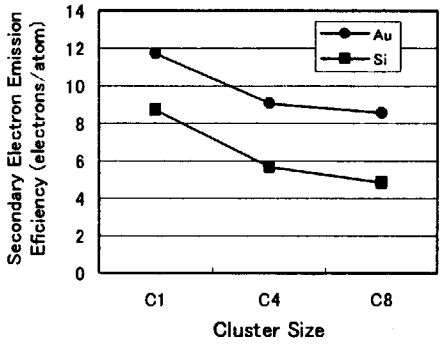

Fig. 2 The electron emission efficiencies for Si and Au targets.

and 0.73 for gold target, and 0.65 and 0.55 for silicon target in irradiation of C_4 and C_8 beam, respectively. A similar non-linear tendency has been reported for Au cluster ions in the present energy region[7),8)]. This phenomenon is explained in such a way that outer-shell electrons of a target atom are ionized at first by front atoms of a cluster ion, resulting in a reduction of the number of available electrons to be ionized by rear cluster atoms[9)]. Fig. 3 shows apparent beam currents I_t on a Si target measured using the ion-implantation apparatus[9)], where the data are plotted as a function of the voltage placed on the suppression electrode. Each value of I_t shown in the figure is divided by I_{tal}, the sum of I_t and I_s. It was confirmed that the sum currents I_{tal} were practically the same as the Faraday cup currents I_b, implying no run-away charged particles out of the shielding box. One can see that the apparent currents vary rather strongly at lower voltages and become nearly constant at higher voltages above -50 V. It is found that a saturated value is 97% for C_1^+ incidence, while those are only 75% and 50% for C_4^+ and C_8^+ ions, respectively. The results are explained as follows.

One cluster ion brings only one positive charge to the target. However, bombardment of each constituent atom of a cluster causes increase of secondary ions and neutrals leaving the target in spite of suppression of secondary electrons. Practically, the influence of the secondary particles was negligible for measurement of usual single ion beam current. But for that of cluster ion

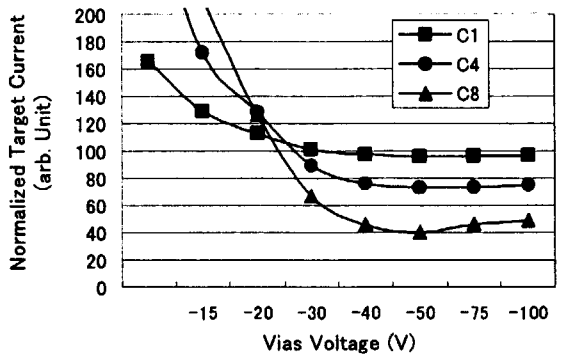

Fig. 3 The intensity of the target current I_t measured with the beam current measuring system as the carbon cluster irradiation on a silicon target versus the bias voltage supplied to the electrode.

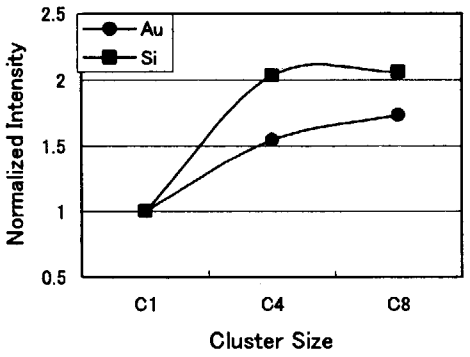

Fig. 4 The intensities of the electrical current I_s in the voltage of -100 V for C1, C4 and C8 irradiation to the silicon and gold targets, respectively.

current, the amount of secondary particles without electrons might be large enough to decrease the apparent beam current. Figure 4 shows the intensity of the electrical current I_s in the voltage of -100 V for C_1, C_4 and C_8 irradiation to the Si and Au targets, respectively. Each I_s was divided by I_{tal} times n, and normalized by the value in its C_1. So, it involves the relative efficiency of secondary ion and neutral emission per atom. The non-linear effect clearly appeared in fig. 4. The efficiency increases with increase of the number of constituent atoms of a cluster in contrast to the electron efficiency mentioned above. The tendency is not different from previous report [10].

4. Conclusions

We found non-liner effects in secondary particle emission from solid targets irradiated by MeV energy carbon cluster ions. Emission efficiency of secondary electrons per carbon atom was found to decrease with increasing cluster size. The secondary particle measurement and TOF analysis[9] suggests that the non-linear effect appeared in the amount of sputtered atoms and molecules adsorbed at the target surface. They brought positive charge from the target and decreased apparent cluster beam current.

References

1) K.Baudin, A.Brunelle, M.Chabot, S.Della-Negra, J.Depauw, D.Gardès, P. Håkanoss, y. Le Beyec, A. Billebaud, M. Fallavier, J. Remillieux, J.C. Poizat, J. P. Thomas, Nucl. Instrum. and Methods. B 94, 341 (1994).
2) K. Narumi, K. Nakajima, K. Kimura, M. Mannami, Y. Saitoh, S. Yamamoto, Y. Aoki, H. Naramoto, Nucl. Instrum. and Methods. B 135, 77 (1998).
3) H. H. Andersen, A. Brunelle, S. Della-Negra, J.Depauw, D. Jacquet, and Y. Le Beyec, Phys. Rev. Lett. 80, 5433 (1998).
4) Ch.Tomaschko, D. Brandl, R. Kügler, Schurr, H. Voit, Nucl. Instrum. and Methods. B 103 (1995) 407.
5) Y. Saitoh, Y. Nakajima, JAERI-Review 2001-039, 283 (2001).
6) Y. Saitoh, K. Mizuhashi, S. Tajima, Nucl. Instrum. Methods A 245, 61 (2000).
7) K. Baudin, A. Brunelle, S. Della-Negra, J. Depauw, Y. Le Beyec, E. S. Parilis, Nucl. Instrum. Methods B 117, 47 (1964).
8) M. Fallavier, R. Kirsch, J. C. Poizat, J. Remillieux, J. P. Thomas, Nucl. Instrum. Methods B 164-165, 920 (2000)
9)Y. Saitoh, Y. Nakajima, JAERI-Review 2002-035 (2002).
10) A.Brunelle, S. Della-Negra, J. Depauw, D. Jacquet, Y. Le Beyec, and M. Pautrat, Phys. Rev. A 63, 0229 (2001).

9.3 Study of Secondary Ion Emission Processes and Radiation Effects of MeV Energy Cluster Ions on Solid Targets

H. Shibata*, A. Itoh**, T. Majima**, Y. Saitoh***, A. Chiba***, K. Arakawa***, K. Narumi****
Research Center for Nuclear Science and Technology, The University of Tokyo*
Graduate School of Engineering, Kyoto University**
Advanced Radiation Technology Center, JAERI***
Advanced Science Research Center, JAERI****

1. Introduction

The interaction between high energy cluster ions and matter has been interested in basic physics and application fields[1-5]. Because cluster ions can bombard a very small area of a solid surface by many atoms simultaneously and release large energy in a very short time (from femto- to pico-second region) [4]. This situation cause non-linear effects or synergetic effects, which is unusual for single atom collision with solid targets.

High energy cluster ions beams used for study of secondary charged particle emission processes were produced by the TIARA tandem accelerator. A time of flight (TOF) mass spectrometer was used for secondary ion measurement and a chopper has been installed in an injector beam line to generate a pulsed cluster ion beam.

In this report we present a preliminary results of secondary ion emission from solid targets bombarded by carbon cluster ions.

2. Experimental

The experimental system of TOF mass spectrometry was composed of a pulsed ion beam generating system and an ion flight time measurement system.

A chopper and two sets of slits installed in an injector beam line generated pulsed ion beams by chopping continuous cluster ion beams from an ion source. A square wave from a master pulse generator controlled a high voltage applied to a parallel plate for chopping the beam. In this study pulsed cluster ion beam of 0.5 MeV/atom (~ 42 keV/amu) C_1^+ ~ C_8^+ ions were used.

The duration and width of the pulse used in this experiment were 100 μs and 100 ns, respectively. C_4^+ and C_8^+ ions were produced in the ion source and C_1^+, C_2^+ and C_6^+ ions were fragments of C_8^+ ions after passing through charge stripper gas. As averaged beam currents of pulsed beams could not be measured, continuous beam currents were measured to be around pA for C_8^+ ions. The vacuum in a beam line and a chamber was kept at ~ 10^{-7} Pa to prevent cluster ions from breaking.

A linear type TOF mass spectrometer and a TAC (Time to Amplitude Converter) system for time measurement were adopted as secondary ion mass spectrometric system. The TOF mass spectrometer composed of an extractor, a drift tube, an acceleration electrode and a multi-channel plate (MCP) detector. A TTL output from the pulse generator was used as a start pulse and a secondary ion signal from the MCP was used as a stop pulse of the TAC measurement system. Typical mass spectrum was accumulated for 30 minutes.

In the last year we used rod shaped targets and secondary ions were extracted at 90 degrees to the incident beam direction using the repeller and the extractor. However, as it was difficult to get the reproducible spectra, sheet shaped targets have been used and bombarded at incident angle of 45 degrees this year. The secondary ions were extracted to the normal direction from the target. A preliminary results of secondary ion emission from graphite (HOPG), Nb/α-Al_2O_3, Si (100), Al_2O_3 targets bombarded by C_1^+ and C_8^+ cluster ions will be discussed.

3. Results and Discussion

Secondary ion mass spectra emitted from a graphite (HOPG) target bombarded by C_1^+ ions and C_8^+ cluster ions are shown in Fig.1. The ordinate is the secondary ion yields normalized to the beam currents in arbitrary units, and the abscissa is the channel number of multi-channel analyzer, which corresponds to the flight time of ions (full scale: 50 μs). Several dominant peaks are seen in the spectra. These are H^+, H_2^+, H_3^+, C^+, Na^+, K^+ and so on. Almost of these peaks are caused by surface contaminants. So, we need to

clean the surface of the targets.

Figure 2 shows the ratio of yields of secondary ions from the graphite target bombarded by C_8^+ cluster ions to that by C_1^+. Very large value of yield ratio for each mass peak is seen. Although some are over thousand, the average is hundreds for almost all peaks.

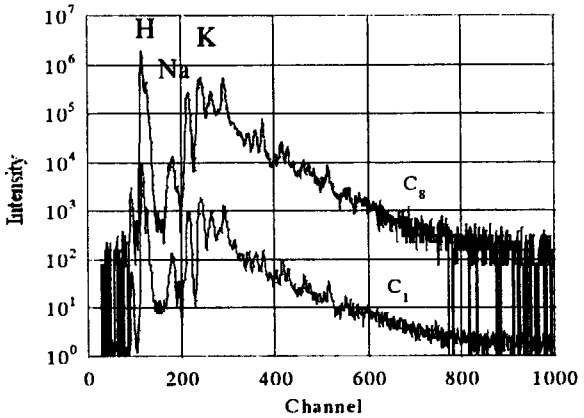

Fig.1. Secondary ion mass spectra emitted from a graphite (HOPG) target bombarded by C_1^+ ions and C_8^+ cluster ions.

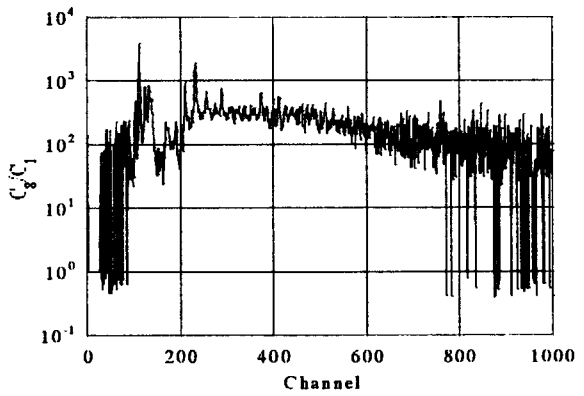

Fig.2. The ratio of yields of secondary ions from the graphite target bombarded by C_8^+ cluster ions to that by C_1^+.

Figure 3 shows the secondary ion mass spectra emitted from an Al_2O_3 target bombarded by C_1^+ ions and C_8^+ cluster ions. Very interesting phenomenon occurs in this figure. For C_1^+ ions, the peak of H^+ moves slightly to shorter time direction, and the whole spectrum shrinks on the time domain. This phenomenon is caused by charging up from ion beam to the insulator target. C_8^+ cluster ions do not affect the charge up of the alumina target so much. It seems that the degree of the charge up of insulator targets depends on the cluster size. Hirata et al. also has found this phenomenon for polymer targets[6, 7].

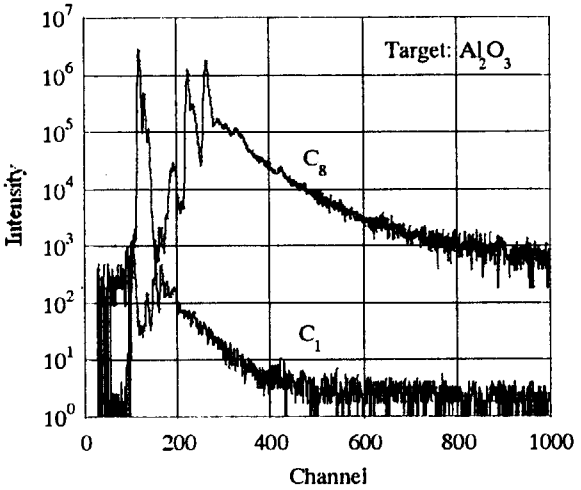

Fig.3. Secondary ion mass spectra emitted from an Al_2O_3 target bombarded by C_1^+ ions and C_8^+ cluster ions.

The problems concerning about experimental condition remain as follows; 1) the cleaning of the target surface is needed, because the surface condition sometimes changes the profiles of spectra, 2) the pulse width would be narrowed to get higher mass resolution.

References

1) Y. Le Beyec, Int. J. Mass Spectrom. Ion Proc. **174** (1998) 101.
2) S. Della-Negra, et al., Nucl. Instrum. Meth. B **74** (1993) 453.
3) M. Döbeli et al., Phys. Rev. B **94** (1994) 388.
4) K.Boussofiane-Baudin et al., Int. J. Mass Spectrom. Ion Proc. **130** (1994) 73.
5) M.Toulemonde et al, Nucl. Instrum. Meth. B **112** (1996) 26.
6) K.Hirata et al., Appl. Phys. Lett. **81** (2002) 3669.
7) K.Hirata et al., Nucl. Instrum. Meth. B, in press.

9.4 The Effect of Ion Doping on Ionic conduction of sol-gel phosphosilicate glasses

S.Ishiyama* and M.Asano**

Department of Advanced Nuclear Heat Technologies, JAERI*

Department of Material Development, JAERI**

1. Introduction

Phosphosilicate glasses $(P_2O_5)_x(SiO_2)_{1-x}$ composed of glass materials have advantages in lightweight, heat-resistance and non CO toxification as solid electrolyte in the middle thermal range (under 500 °C)[1], then it is expected one of 4th generation SOFC materials as a high proton conductivity material.

For phosphosilicate glasses, there are many studies taking advantages of the optical property for applications of optical fiber as Raman lasers [2)-7)]. In the study for the phosphosilicate glass, the sol-gel method has advantage in random structure of the glass organization for proton conductivity[2]. In order to investigate dynamic effects of structural change by implanted ion on the proton conduction mechanism for the improvement in ionic conductivity in phosphosilicate glass. The structure of the sol-gel synthesis is a peculiar porous material[3),4)]. Then, Authors has been examined the correlation between RIL and structural change and conduction function in ion irradiation in order to clarify complicated change in glass structure and the mutual influence by measuring radiation-induced luminescence (RIL) during the ion irradiation for the proton conductivity glass at in-situ,.

In this paper, the 1 MeV H^+ and 3MeV Zr^{+4} ion beams were irradiated on silica glasses (SiO_2) and phosphosilicate glasses were prepared by sol-gel method to investigate dynamic effects of structural change and ion conductivity.

2. Experimental Procedure

2.1 Materials

The silica and phosphosilicate glass were prepared using tritraethylorthosilicate (TEOS); $Si(OC_2H_5)_4$ and trimethylphosphate; $PO(OCH_3)_3$ solution. TEOS was hydrolyzed for 1 h with water under magnetic stirring at room temperature. Ethanol was used as solvent system and formaldehyde ($HCONH_2$) as a catalyst. The molar ratio of TEOS: C_2H_5OH: H_2O: HCl was 1: 1: 1: 0.01. For the phosphosilicate glass, an alkoxide $PO(OCH_3)_3$ solution was added to the hydrolyzed TEOS solution as the molar ratio of C_2H_5OH: H_2O: HCl = 4: 4: 0.03 and stirred for 1 h at room temperature. The obtained transparent sols were left in glass containers. Final gels were obtained in air for 3 - 4 weeks. The dried gels were then heated to 600°C at a rate of 50°C/h and held at this temperature for 5 h. Three kinds of glass were synthesized in present study and these component were listed in Table 1.

Table 1 Composition of sol-gel glasses.

Sample No.	AP_2O_5-$BSiO_2$	
	A	B
1	0	100
2	5	95
3	10	90
4 (Water dip)	10	90

2.2 Irradiation conditions

The ion irradiation experiments were performed using the 3 MV tandem accelerators in TIARA at JAERI Takasaki. The H^+ and Zr^{+4} ion irradiations were performed using fluencies of 5 x 10^{15} ions/cm^2 at 1 MeV and 1.25 x 10^{14} ions/cm^2 at 3MeV at room

temperature, with a beam current density of $0.2\mu A/cm^2$ and $20nA/cm^2$, respectively. The ion beams direction was almost normal of the target surface.

3. Results and Discussion

Fig.1 shows ion conductivity of H^+ ion doped phosphosilicate glasses of $5P_2O_5$-$95SiO_2$ and its porous one ($5P_2O_5$-$95SiO_2$*) at the temperature rang from 300K-350K. The phosphosilicate glasses show higher conductivity as increase of P_2O_5 content and porous volume in the glass, however in the case of H^+ doped SiO_2 glasses, its shows lowest conductivity and no change was found before and after ion doping. It is found that the conductivity of $5P_2O_5$-$95SiO_2$ glass increased after H^+ doping, however that of porous glass $5P_2O_5$-$95SiO_2$* decreased after irradiation.

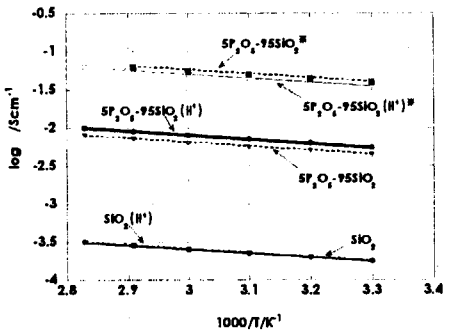

Fig.1 Ion conductivity in H^+ doped glasses.

These results indicated that H^+ density in the glass after doping was not drastically change to effect ion conductivity of the glasses and long time irradiation test is to be requested for the purpose.

Fig. 2 shows ion conductivity of Zr^{+4} ion doped $10P_2O_5$-$90SiO_2$ glasses at the temperature rang from 300K-350K. $10P_2O_5$-$90SiO_2$* is a sample of $10P_2O_5$-$90SiO_2$ which was dipped in water for 24 hours before ion conductivity measurement and drastic change was found in Zr^{+4} doped $10P_2O_5$-$90SiO_2$ samples before and after water dipping. This fact indicated that Zr^{+4} ion combined elements in the glasses and form Zr-O-P bonding, and contributed stability of P_2O_5-SiO_2 glass in water.

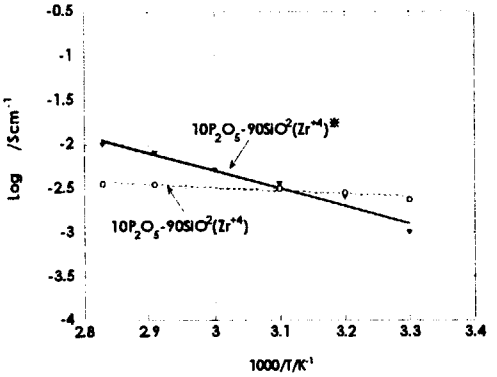

Fig.2 Ion conductivity of Z^{+4} doped glasses.

References

1) M. Nogami, Y.Goto, Y.Tsurita and T.kasuga, J. of Am. Ceram. Soc., 84[11]2553-2336(2001).

2) A.Matsuda, T.Kanzaki, Y.Kotani, M.Tatsumisago and T.Minami, Electrochimica Acta 47,939-944(2001).

3)L.Skuja, J. Non-Cryst. Solids 239, 16-48(1998).

4)L.Skuja, K.Tanimura and N.Ito, J. Appl.Phys. 80,3518-3525(1996).

5)T.Yoshida, T.Tanabe, T.Li and H.Yoshida, Nucl. Instr. And Meth, B191, 382-386(2002).

6)V.G.Plotnichenko, V.O.Sokolov,V.V.Koltashev and E.M.Dianov, J.Non-Cryst. Solids, 306,209-226(2002).

7)H.J.Fitting, T.Barfels, A von Czarnowski and A.N.Trukhin, Mater.Sci. Eng. B71, 109-114 (2000).

9.5 Formation of keV ~0.1 μm Ion Beam using Double Acceleration Lenses

Y. Ishii, A. Isoya, K. Arakawa

Advanced Radiation Technology Center, JAERI

1. Introduction

A submicron ion beam system has been developed using an electrostatic focusing lens system (acceleration lens system) and a duoplasmatron-type ion source [1] to form a few tens keV H_2^+ beam with 0.1 μm width. The beam width measurement system for submicron ion beams was also developed by applying the knife-edge method [2].

The 33 keV H_2^+ beam with 0.28 μm width was already formed by the divergence angle reduction of the ion beam extracted from an ion source in the system using a short distance acceleration between plasma sheath and an extraction electrode, plasma sheath acceleration method [1].

The direct extraction method of a parallel ion beam from plasma using the tapered anode hole with the Pierce angle was developed in the ion source to produce smaller divergence-angle ion beams than those by plasma sheath extraction method and form the smaller beam width than 0.28 [μm]. The beam width could be smaller because the beam trajectory calculation showed the long distance from an effective object point to the lens system and the smaller beam width at its point using the parallel beam extraction method. The effect of beam extraction method on the beam divergence reduction was verified by the ion beam generation experiments. The minimized divergence angle was estimated from these experiments.

2. Parallel beam extraction from the ion source

The parallel beam extraction method, the tapered non-magnetic anode with angle of 67.5° (Pierce angle) to a light-axis, was introduced in the ion source as shown in Fig.1. Figure 1 (A) shows the enlarged illustration of the anode.

The reduction of beam divergence angle was tried by three processes as follows, the direct beam extraction from the high vacuum space near the anode hole, the beam acceleration in the uniform electric field between the anode and the extraction electrode and the parallel electric field with three electrodes placed at downstream of the extraction electrode, as shown in Fig.1.

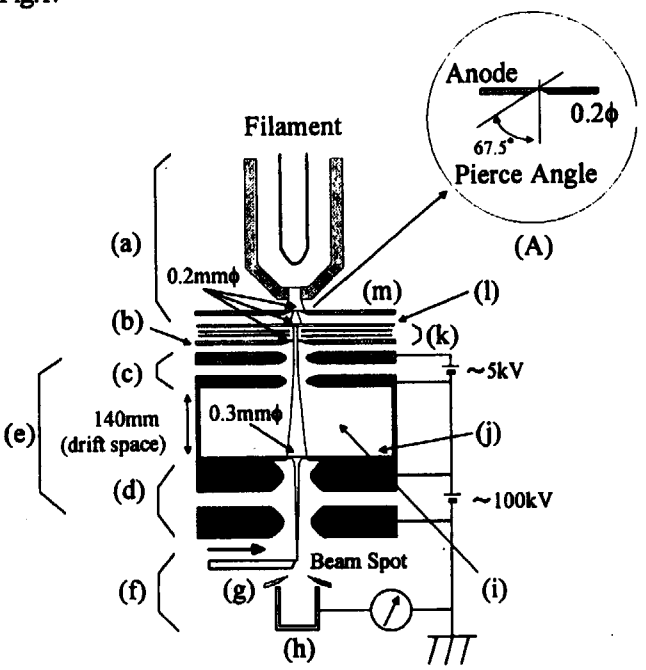

Fig.1 Schematic diagram of the submicron ion beam system. (A) with detailed figured of the non-magnetic anode in the duoplasmatron-type ion source. (a): the duoplasmatron-type ion source, (b): the first throttle electrode, (c): first acceleration lens, (d): second acceleration lens, (e): the acceleration lens system, (f): submicron ion beam system, (g): sharp knife-edge, (h): Faraday cup, (i): beam measurement chamber, (j): the second throttle electrode, (k): parallel acceleration electrode, (l): extraction electrodes, (m): anode.

3. Performance of the parallel beam extraction

The beam divergence angle was measured to evaluate the parallel beam extraction system. The divergence angel was estimated from the experimental data as shown in Fig.2 by the assumptions as follows; the two ion densities injected into the anode and the extraction electrode were uniform and the ratio of beam current passing through each electrode hole is proportional to that of the area between injection beam and a hole of each electrode. The calculated divergence angle was reduced to the extraction voltage over 400 V and minimized to

the 3.8×10^{-3} rad at 600 V as shown in Fig.2. The divergence angle of the 10^{-3} rad order was sufficient to form the final beam with the width of 0.1 μm order. The extraction voltage over 400 V was, thereby, applied to the extraction electrode to reduce the beam divergence angle.

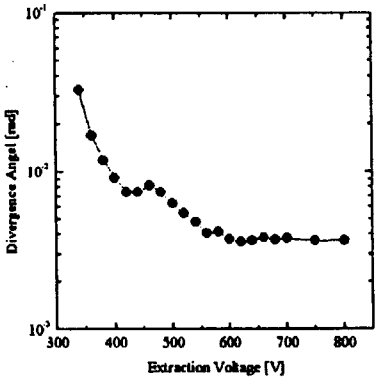

Fig.2 Divergence angle of beams injected in the acceleration lens system as the function of the extraction voltage.

4. Measurement of the beam width

The beam width was measured employing a submicron ion beam measurement system with resolution of 0.02 μm [2]. The system is composed of a sharp knife-edge and a Faraday cup. The beam width was evaluated from the beam current measured by the Faraday cup, gradually cutting the beam with the shifting sharp knife-edge.

For production of small divergence angle ion beam, the extraction voltage of over 400 V was applied to the extraction electrode in the ion source after 1 hour worming-up. A 6 kV and a 46 kV acceleration voltages calculated from the beam trajectory simulation were applied to the first and the second acceleration lenses to focus the production ion beam with small divergence angle to submicron width, respectively. In addition, those voltages were fine-tuned to get the minimum width.

The measurement of decreasing beam current to estimate the beam width was shown in Fig.3 as a function of the knife-edge position.

The three extrapolation lines of the maximum current, the zero current and the fitting linear line of the decreasing current curve were fitted using the least square method and linear lines as shown in Fig.3 with the solid lines. The minimum extrapolation line was drawn on zero current as over-estimate side. The beam width was defined as a length of the abscissa between the two cross sections among the three linear lines by taking account of an effective portion of a halo [2]. Such a defined width corresponds to about 10% over estimation value as compared to the FWHM value calculated by fitting the measurement data using Gaussian distribution. The beam width was in 0.16 ± 0.02 μm including a part of halo.

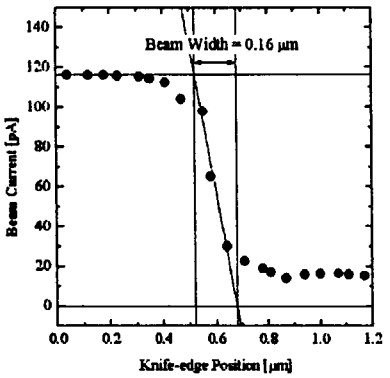

Fig.3 Beam current change as a function of the knife-edge position. The H_2^+ beam energy was about 46 keV. The beam width was estimated from the abscissa values of two intersection points of three extrapolation lines (the maximum current, the decreasing beam current and zero current) drawn by the least-square fitting method.

5. Summary

The H_2^+ of a 46 keV beam was formed by minimization of the divergence angle based on the direct acceleration method. The beam width of 0.16 ± 0.02 μm, half of the one formed by the plasma sheath acceleration method, was obtained at the beam spot.

References

1) Y.Ishii, A.Isoya, K.Arakawa, T.Kojima and T.Tanaka, Nucl. Instr. and Meth. B181(2001)71

2) To be published in Nucl. Instr. and Meth.

9.6 Measurement of the Cyclotron Magnetic Field and the Beam Energy Spread for Microbeam Production by the Flat-top Acceleration

S. Okumura, I. Ishibori, M. Fukuda, N. Miyawaki, S. Kurashima, T. Agematsu, T. Nara, K. Yoshida, Y. Nakamura, K. Arakawa
Advanced Radiation Technology Center, JAERI

1. Introduction

In the JAERI AVF cyclotron, a microbeam production with a lens system of quadrupole magnet is under way. Reduction of the energy spread of the beam, from dE/E = 1-5×10^{-3} to 2×10^{-4}, is required to reduce the effect of chromatic aberration in the lens system. We are, therefore, developing the flat-top acceleration system[1] to minimize the energy spread of the beam. High stable magnetic field, dB/B < 2.0×10^{-5}, is needed to maintain the beam phase within the allowable range for the flat-top acceleration. And also, measurement of the energy spread of the beam is required to tune the parameters in the flat-top acceleration system and to confirm the minimization of the energy spread of the beam for the microbeam production.

2. Cyclotron Magnetic Field

We found that an increase in temperature of the iron body of the magnet induced a prolonged fluctuation of the magnetic field[2-3]. Stabilization of the iron body temperature was achieved by precise temperature control of the cooling water for thermal isolation plates installed between the iron body and a main coil[4].

In the operation with the flat-top acceleration, it is required to maintain the stable magnetic field from start-up for optimizing parameters of the cyclotron. It was not verified that the magnetic field in the opening stages of the operation was within the allowable range, while the long-term stability of the magnetic field was confirmed when the temperature control of the iron body was introduced.

The magnetic field was measured from start-up, shortly after completion of the cycling the magnetic field, without tuning the coil currents. The current of the main coil was also measured to examine a correlation between the magnetic field and the current of the main coil. From the result, the magnetic field decreased depending on the variation of the coil current within the allowable range for the flat-top acceleration.

3. Beam Energy Spread

Energy resolution ΔE/E less than the order of 10^{-4} is required for measurement of the energy spread of the beam. Although particle detectors such as semiconductor radiation detectors have a high resolving power, it is difficult to maintain the high resolving power in variety of the beams. In a dispersive magnet system, it is easy to achieve high resolving power in variety of the beams by improving the resolution of the image size.

We have a dispersive magnet system, which consists of a bending magnet and quadrupole magnets. The momentum resolution of the magnet system R = p/Δp can be calculated from the slit widths at the object and the image positions, Xo and Xi, respectively, the magnification M, and the dispersion D. By using a normal transport parameters, Xo = Xi = 1 mm (minimum), M = 1 and D = 2mm/10^{-3}, the momentum resolution R is estimated to be 2×10^{3}, which means the energy resolution ΔE/E is 1×10^{-3}. We have measured the energy spread of several beams without the flat-top acceleration using the magnet system. The results show that the energy spreads range from 1×10^{-3} to 3×10^{-3}.

It is required to decrease the slit widths for improve the energy resolution. We have a plan to install new micro-slits with a minimum slit width of 10 μm.

References

1) M.Fukuda et. al., Rev. Sci. Instrum. 74 (4) (2003) 2293 - 2299.
2) M.Fukuda et. al., JAERI Review 99-025, 251-253.
3) S.Okumura et. al., The 12th Symp. On Accel. Sci. and Tech., Wako, Japan (1999) 78-80.
4) Y.Nakamura, et al., JAERI-Review 2000-024, 282-284.

9.7 Beam Development for Flat-top Acceleration in the JAERI AVF Cyclotron

S. Kurashima, N. Miyawaki, M. Fukuda, S. Okumura, T. Nara
T. Agematsu, I. Ishibori, K. Yoshida, Y. Nakamura and K. Arakawa
Advanced Radiation Technology Center, JAERI

1. Introduction

The JAERI AVF cyclotron provides a variety of ion beams especially for the research in biotechnology and materials science. Several cyclotron technologies such as cocktail beam acceleration, a uniform irradiation in a wide area and beam pulsation have been developed so far. These technologies have been pioneering the frontiers of ion beam applications.

A flat-top acceleration system for the JAERI AVF cyclotron has been designed to minimize the energy spread mainly for a microbeam production. The energy spread of the cyclotron beam is required to be reduced to $\Delta E/E = 2 \times 10^{-4}$ to produce a microbeam with a spot size of 1 μm by focusing the beam with a set of quadrupole magnets. The flat-top acceleration using fundamental and fifth-harmonic frequencies for an acceleration voltage is an excellent technique to reduce the energy spread. The flat-top acceleration system, consisting of a fifth-harmonic resonator, a power amplifier and an RF controller, has been installed in the main RF resonator in March, 2002. A power test at a fundamental frequency of 17.475 MHz has been carried out, and the flat-top waveform was successfully observed at the dee voltage pick-up [1]. In order to achieve the energy spread of $\Delta E/E = 2 \times 10^{-4}$ [2], several technical developments are required as listed in table 1. The tolerable stability of the fifth-harmonic voltage and the cyclotron magnetic field, $\Delta V/V = 0.06$ % and $\Delta B/B \leq 0.001$ %, respectively, have already been achieved. In this paper, we report the stabilization of the fundamental acceleration voltage and preliminary beam development of 260 MeV $^{20}Ne^{7+}$ using the flat-top acceleration technique.

Table 1: Requirements for achieving the energy spread of $\Delta E/E = 2 \times 10^{-4}$ except the flat-top acceleration system.

Requirement	Tolerance
Stability of acceleration voltage	$\Delta V/V \leq 0.02$ % for fundamental $\Delta V/V \leq 0.1$ % for harmonic
Stability of cyclotron magnetic field	$\Delta B/B \leq 0.002$ %
Beam phase width	$\Delta\phi \leq 10$ deg. RF
High performance beam buncher	80 % compression of injected beam within 10 deg. RF
pricise measurement of the beam energy	$\Delta E/E \leq 0.01$ %

2. Stability improvement of the fundamental voltage

As shown in Table 1, the stability of the fundamental voltage is needed to be $\Delta V/V \leq 0.02$ %. However, the voltage stability was originally designed as ±0.1 % in specification. The voltage stability depends mainly on variation of the temperature around the RF low-level controller. The temperature varied a few degrees through the cyclotron operation, since the temperature controller, attached to the RF control rack for the RF low-level controller, had insufficient capability. Heat insulation of the control rack was required to be reinforced as well. The newly installed temperature controller with heat reduction capability of 1300 W can keep the temperature variation within ±0.1 degrees around a thermo-sensor. The variations of the fundamental voltage and the temperature around the RF low-level controller are shown in

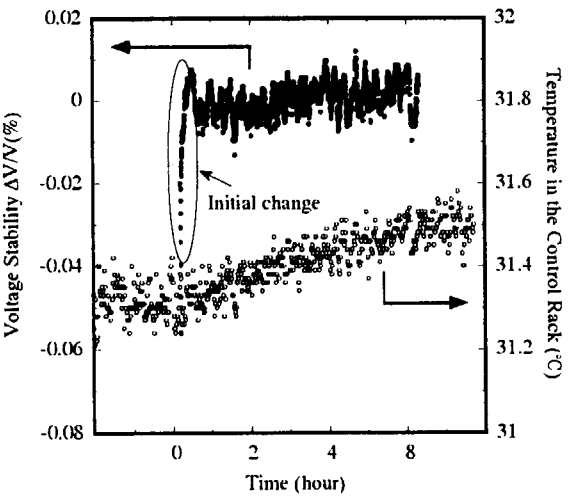

Fig. 1 Variation of the fundamental voltage for acceleration and the temperature in the RF control rack after the improvement of temperature stabilization.

Fig. 1. As a result, the voltage stability of $\Delta V/V \leq 0.02$ % has been achieved by controlling the temperature variation within ±0.2 degrees

3. Development of the flat-top accelerated beam

We have succeeded in accelerating 260 MeV $^{20}Ne^{7+}$ ions at a fundamental frequency of 17.475 MHz by superimposing the fifth-harmonic voltage on the fundamental one. In this preliminary beam development, we searched for the optimum fifth-harmonic voltage to minimize the number of beam bunches extracted from the cyclotron. A single-turn extraction is an indispensable condition to obtain the energy spread of $\Delta E/E = 2 \times 10^{-4}$. A radial spread of the beam in the cyclotron is suppressed by the flat-top acceleration owing to the uniformity of energy gain.

A DC beam extracted from an ion source was pulsated by a beam chopper using a rectangular voltage wave form. The pulse width of the beam was modulated to around 100 ns. After the beam was injected into the cyclotron, two or three beam bunches with a period of 57.2 ns were produced by periodic acceleration. One of the evidence for the single-turn extraction is that the number of the beam bunches extracted from the cyclotron corresponds to the initial bunch number. A beam bunch distribution for the acceleration using the fifth-harmonic voltage of 1.6 kV, obtained by measuring beam phases with a plastic scintillator placed on a beam transport line, is shown in Fig. 2. Only two significant peaks were observed in the distribution, which indicated that the number of the beam bunches was invariable after the extraction. In ordinary acceleration using a sinusoidal voltage wave form, the number of beam bunches enormously increases after extraction that is so-called multi-turn extraction. Although the energy spread of the extracted beam was unknown, it was obvious that the energy spread of the flat-top accelerated beam was smaller than the ordinary acceleration.

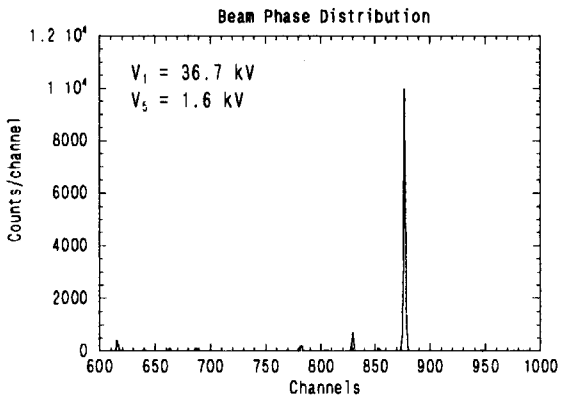

Fig. 2 A beam phase distribution of the 260 MeV $^{20}Ne^{7+}$ ion beam, accelerated at a frequency of 17.475 MHz using the fundamental voltage of 36.7 kV and the fifth-harmonic voltage of 1.6 kV. The injection beam was pulsated with a pulse width of around 100 ns.

REFERENCES

[1] S. Kurashima, et al., "Development of the Flat-Top Resonator for the JAERI AVF Cyclotron", TIARA Annual Report 2001 (JAERI-Review 2002-035), 298 (2002).

[2] M. Fukuda, et al., "Flat-top Acceleration System for the Variable-Energy Multi particle AVF Cyclotron", Rev. Sci. Instrum. **74**, 2293 (2002).

9.8 Present Status of JAERI AVF Cyclotron System

Y. Nakamura*, T. Nara*, T. Agematsu*, I. Ishibori*, S. Kurashima*, M. Fukuda*, S. Okumura*, N. Miyawaki*, K. Yoshida*, K. Arakawa*, S. Tajima*, K. Akaiwa**, To. Yoshida**, S. Ishiro**, A. Matsumura**, Y. Arakawa**, Tu. Yoshida**, S. Kanou**, A. Ihara** and K. Takano**

Advanced Radiation Technology Center, JAERI*
Beam Operation Service, Co., Ltd.**

1. Introduction

The JAERI AVF cyclotron system[1)-3)] has been also operated smoothly without serious troubles as well as past a few years. Figure 1 shows the shift of the operation time for recent 10 years since 1993 when it exceeded over 3000 hours at first. So far, the operation time more than 3000 hours has been kept certainly although various reconstruction, improvement, renewal, replacement and so on were carried out. Especially in last year, the longest operation time of 3433 hours was recorded.

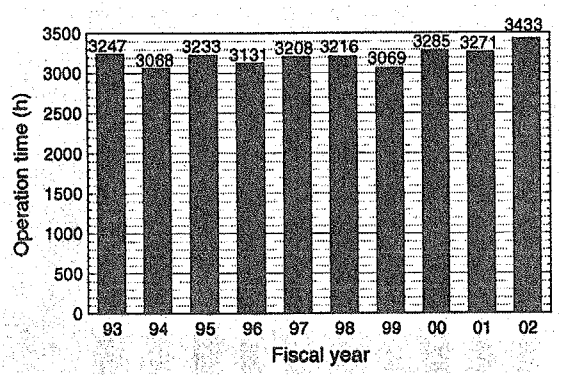

Fig. 1 The shift of the operation time for recent 10 years.

The time for scheduled beam tuning is shown in Fig. 2. The overall beam time allotted to the biotechnology research has been remarkably increased in recent years. While the yearly operation time is roughly same, the time for beam tuning rapidly increased from 360 hours to 700 hours during 7 years.

The frequencies of the changes for ion species, beam energy, course and harmonics also increase gradually. The number of the beam course change reached to 290 times during last fiscal year. Therefore, our cyclotron system may be recognized as the busiest cyclotron in the world.

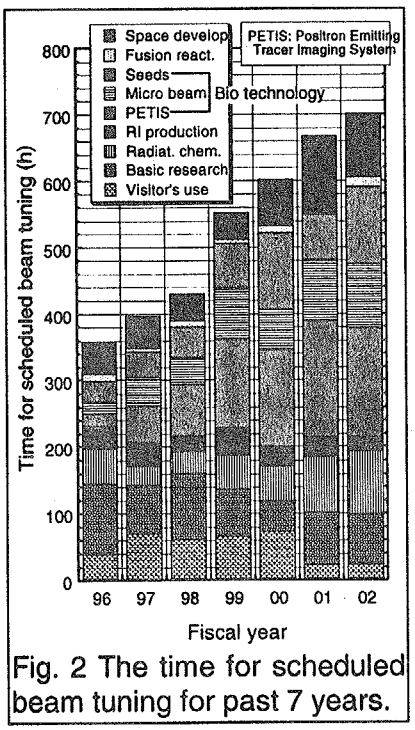

Fig. 2 The time for scheduled beam tuning for past 7 years.

2. Present Status

2.1 Development and Improvement

A flat-top (FT) acceleration system[4),5)] has been operated for practical use after the installation on March in 2002. This FT system can generate the fifth-harmonic voltage of around 1.5 kV, required for flat-topping, at both resonators of #1 and #2. We are improving the beam quality of 260 MeV $^{20}Ne^{7+}$ which is one of the candidates of ion species for micro-beam formation.

In order to realize the precise beam transport for the micro-beam formation, a new gradient corrector[6)] with bending function was fabricated after the careful design using three-dimensional analytical code (TOSCA) and the orbit calculation. An appearance of the gradient corrector before the installation in the cyclotron is shown in Fig. 3. An additional three-phase electricity of 420 V and 150 A was supplied to the gradient corrector system.

The multi-cusp ion source which is one of three ion sources, usually generates the light ion species of proton and deuteron, has been already operated for 12000 hours over 13 years. On account of a long-term operation, the performance such as beam intensity and stability comes to deteriorate gradually. Therefore, we are planning to replace the multi-cusp ion

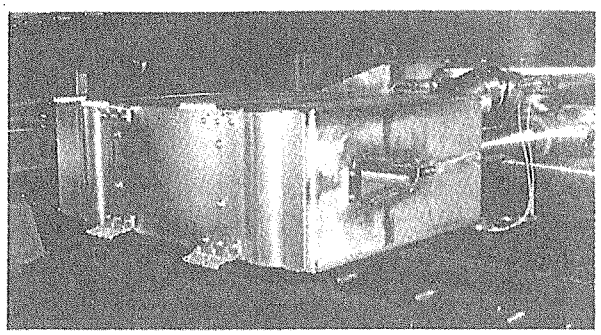

Fig. 3 An appearance of the new gradient corrector before installation.

source by the new one in near future. This new ion source is being designed so as to improve about above the performance. And its working range may be also expanded largely. Prior to the fabrication of this ion source, the short beam line and analyzing magnet were installed in the ion source test-bench room at the basement as shown in Fig. 4.

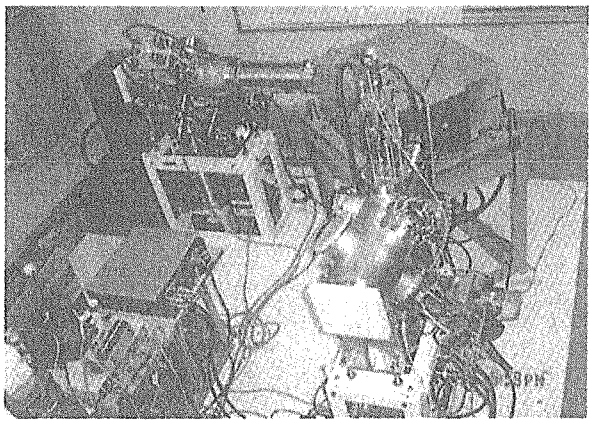

Fig. 4 The installation of the short beam line and analyzing magnet for the new ion source.

2.2 Maintenance and Repair

Comprehensive periodical maintenance including the installation of the new gradient corrector for 4 weeks and beam tuning for 1 week in summer, the routine maintenance of several power supplies for 1 week, the reconstruction and installation for 3 weeks in spring were performed in last fiscal year.

In the middle of last May, the polarity change of the steering magnet in the beam transport line became impossible. At first, although we investigated the changing sequence for this magnet, it was sound. At least, we found that a small auxiliary power supply in the power supply box was out of order. In last March, all of sixty-four small power supplies were replaced with new ones.

In late May, the beam time for 320 MeV $^{12}C^{6+}$ was cancelled owing to the serious attenuation of the beam current at central region in the cyclotron. This beam attenuation was originated from the air leakage at the bellows of the Faraday cup placed just before the cyclotron.

After the periodical maintenance in summer, since worse vacuum condition in the cyclotron had continued, a 500 MeV $^{197}Au^{31+}$ was not available because of the beam attenuation resulting from the increase of charge exchange. This condition has been not solved fundamentally yet although we tried to do some countermeasures such as a helium leak test, a repair of the driving shaft for magnetic channel, reassemble of the plug through the earth plate and so on.

A main RF tube (4CW50000E), which had revealed the aggravating sign in regard to its bias voltage, was broken completely at the middle on last Nov. One of used tubes was assembled in a hurry.

During the irradiation of an intense 100 MeV $^{4}He^{2+}$ beam, three gate valves were shut and the indication of the vacuum gauge disappeared suddenly along the LA course. The cause of this trouble was the malfunction of the sequencer (C500H) which governs to the sequence and information for vacuum control. We did not possess the original program ourselves although this C500H was adopted RAM type. However, the control program which was preserved over 10 years by the medium of floppy disc could not be read out actually. Therefore, the control program had to be rewritten finally based on the ladder sequence on the chart. It is presumed that the soft wear error was induced in the C500H by the exposure of strong neutrons and gamma rays.

The vacuum pressure in the cyclotron rapidly increased up to 2×10^{-3} Pa because small water leakage occurred in the baffle slit at the exit for the magnetic channel. The extraction of ion beam became difficult. At this time, since the residual assignment period in the operational schedule was rather short, the experimental utilization was resumed after separating the failed water cooling line and confirming the safety. As shown in Fig. 5, this baffle slit was exchanged later to new spare one made of molybdenum.

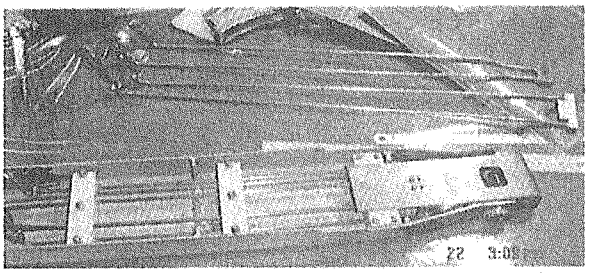

Fig. 5 Lower : baffle slit fitted up at the exit of the magnetic channel, Upper : its spare one.

3. Beam Acceleration Test

After the installation of the new gradient corrector, the test operation for beam tuning was done energetically in the middle of August.

Sixty-three kinds of ion species accelerated by the JAERI AVF cyclotron so far are summarized in Table 1.

According to the strong requirement from several users, the beam intensities of 20 MeV, 30 MeV and 80 MeV H^+ were improved to 11.5 μA, 6.2 μA and 4.4 μA from 5 μA, 5 μA and 3 μA, respectively.

For the main purpose of the micro-beam formation in near future, the intensity of 260 MeV $^{20}Ne^{7+}$ beam was reinforced drastically to 9.8 μA from 0.33 μA using the "HYPERNANOGAN" instead of the "OCTOPUS".

A new ion species of 320 MeV $^{102}Ru^{18+}$ which is a sort of metallic ions, was extracted successfully at the beam intensity of 13 nA. The $^{102}Ru^{18+}$ ion was generated by MIVOC method in the HYPERNANOGAN.

Table 1 The list of ion species accelerated by JAERI AVF cyclotron. The symbol of "Text" in the table is defined by a ratio of the beam current at the Faraday cup just behind the cyclotron to that at 900 mm of the cyclotron radius. The "Tall" is a ratio of the beam current extracted from the cyclotron to that injected into.

species	Energy (MeV)	Intensity (eμA)	Text (%)	Tall (%)
H^+	10	12	80	27
	20	11.5	89	25
	30	6.2	78	22
	45	30	79	14
	50	5	44	14
	55	5	63	14
	60	5	57	22
	65	7	62	12
	70	5	42	12
	80	4.4	72	13
	90	10	48	7.7
D^+	10	11	29	3.7
	20	5.6	80	16
	25	15	88	31
	35	40	59	13
	50	20	49	7.2
$^3He^{2+}$	60	8.2	68	18
$^4He^+$	25	3.6	M/Q=4	13
$^4He^{2+}$	20	5.5	69	12
	30	10	42	10
	50	20	62	22
	100	10	32	10
	108	1.6	M/Q=2	
$^{12}C^{3+}$	75	2	M/Q=4	
$^{12}C^{5+}$	220	0.25	77	22
$^{12}C^{6+}$	320	0.008	M/Q=2	
$^{14}N^{3+}$	67	4	43	10
$^{15}N^{3+}$	56	0.70	M/Q=5	5.0
$^{16}O^{4+}$	100	5	M/Q=4	22
$^{16}O^{5+}$	100	4	34	21
$^{16}O^{6+}$	160	1.9	58	21
$^{16}O^{7+}$	225	1	82	13
$^{16}O^{7+}$	335	0.1	41	6
$^{16}O^{8+}$	430	0.0045	M/Q=2	
$^{20}Ne^{4+}$	75	1.5	M/Q=5	6.6
$^{20}Ne^{5+}$	125	0.01	M/Q=4	
$^{20}Ne^{6+}$	120	1.6	53	18
$^{20}Ne^{6+}$	200	0.8	Scaling	10
$^{20}Ne^{7+}$	260	9.8	70	22
$^{20}Ne^{7+}$	270	0.28	Scaling	14
$^{20}Ne^{8+}$	350	1.5	63	23
$^{20}Ne^{10+}$	540	10^5 cps	M/Q=2	
$^{22}Ne^{6+}$	165	0.007	M/Q=4	
$^{36}Ar^{8+}$	195	2.5	73	13
$^{36}Ar^{10+}$	195	0.1	43	1.2
$^{36}Ar^{18+}$	970	10^5 cps	M/Q=2	
$^{40}Ar^{8+}$	150	2.4	M/Q=5	6.2
	175	3	73	15
$^{40}Ar^{10+}$	250	0.2	M/Q=4	
$^{40}Ar^{11+}$	330	0.7	86	22
$^{40}Ar^{13+}$	460	0.03	63	24
$^{40}Ca^{9+}$	200	2	61	11
$^{56}Fe^{11+}$	210	1.4	M/Q=5	16
$^{56}Fe^{15+}$	400	0.59	66	28
$^{58}Ni^{15+}$	390	0.012	M/Q=4	
$^{82}Kr^{20+}$	490	10^7 cps	M/Q=4	
$^{84}Kr^{17+}$	320	0.08	M/Q=5	5.0
$^{84}Kr^{18+}$	400	0.04	60	2
$^{84}Kr^{20+}$	520	0.06	72	22
$^{84}Kr^{21+}$	525	0.0032	M/Q=4	
$^{102}Ru^{18+}$	320	0.013	50	2.7
$^{129}Xe^{23+}$	450	0.2	72	11
$^{197}Au^{31+}$	500	0.023	49	3

M/Q = 2, 4 and 5 : a series of cocktail beams
Colored pattern : modified data on previous table

References

1) Y. Nakamura, T. Nara, *et al.*, Proceedings of International Workshop on Accelerator Operation, Hayama and Tsukuba, Kanagawa and Ibaraki, Japan (2003)
2) Y. Nakamura, T. Nara, *et al.*, TIARA Annual Report 2001 (JAERI-Review 2002-035) (2002) pp. 300-302
3) Y. Nakamura, T. Nara, *et al.*, Proc. 16th Int. Conf. Cyclo. Their Applic., East Lansing, MI, USA (2001) pp. 129-132
4) M. Fukuda, S. Kurashima, *et al.*, Review of Scientific Instruments, No.4, Vol.74, (2003) pp. 2293-2299
5) S. Kurashima, M. Fukuda, *et al.*, TIARA Annual Report 2001 (JAERI-Review 2002-035) (2002) pp. 298-299
6) S. Okumura, M. Fukuda, *et al.*, this annual report

9.9 Study of the Beam Meander at JAERI AVF Cyclotron

T. Agematsu, M. Fukuda, Y. Nakamura, I. Ishibori, T. Nara, S. Okumura,
S. Kurashima, N. Miyawaki, K. Yoshida, K. Arakawa and S. Tajima
Advanced Radiation Technology Center, JAERI

1. Introduction

On JAERI AVF Cyclotron, it is needed to study a problem that is a meander of the beam envelope along the micro-beam lines and the other beam lines. The causes of the beam meander mainly come from that the position and direction of the beam are not alignment with designed beam trajectory. Also the miss alignment of the devices at the cyclotron system is similar to the problem of beam position and direction. To study this problem, we evaluated the value of the miss alignment for the several magnets near the cyclotron exit.

2. Evaluation Case at HZ Beam Line

The beam line HZ has been used for R&D on biotechnology. In order to form the micro-beam there are three narrow collimators in this line. The size of first, second and third collimator is 5mm, 0.5mm and 10μm in diameter respectively. In actual operation, we could transport the beam to the micro-beam chamber by adjusting the steering magnets of the beam line. However, it was very difficult to pass through beam into the collimators, because the beam was meandering through the beam duct.

To clear the problem and to evaluate the meander of the beam envelope, we have simulated the beam trajectories by using Visual Assistance system Unit (VAU) [1]. Of course, the beam was roughly transported in actual operation. However, if we set up the operated actual parameters to VAU beam simulator, the beam trajectories break down on the way as shown dotted lines in Fig. 1. On the other hand, the beam is transported smoothly by changing the initial conditions to +3mm from center on the vertical plane as shown solid lines in Fig. 1. The only 3mm beam shift at the initial condition is amplified to maximum 60mm beam position change at the beam line. Thus, we had supposed that the cause of meander is 3mm beam shift. After then we found that level of several magnets near the cyclotron was 3mm down from the cyclotron level. We corrected already the vertical level of the several magnets up to about +3mm to original position [2].

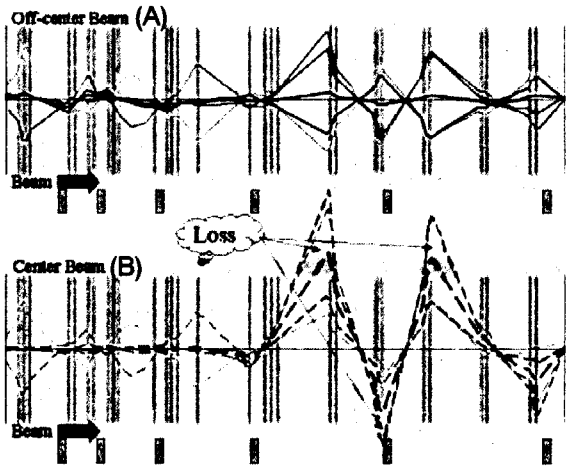

Fig. 1 Simulated beam trajectories on vertical plane with actual operating parameters at HZ beam line.

Solid lines (A) show the trajectories of off-centered beam by +3mm. Dotted lines (B) show the trajectories of centered beam. The beam trajectories are crash into the beam duct.

3. Correction Device on Horizontal Plane

For improvement of the beam meander on the horizontal plane, we installed a correction device that is the beam steering magnet inside

the gradient-corrector of the cyclotron extraction block [3]. Operators can easily control by using this steering magnet as compared with before this improvement.

4. Summary

We corrected the vertical miss alignment of the magnets. And we installed the steering magnet at the cyclotron extraction position so that the beam meander was decreased. Although, there are still remained slightly the beam meander on vertical and horizontal plane.

To consider the beam meander is important for all the beam lines. Because, small changing of the beam position and the beam angle will produce a large changing them along the beam line. These problems are applied to all the beam lines of the cyclotron. For example, just 3mm beam shift is amplified to 60mm at HZ beam line.

To provide high quality and high intensity ion beam, we should continue the studies concerning the changing of a beam position and the beam angle at the cyclotron exit. Perhaps, betatron oscillations of the cyclotron beam and the small miss alignment of devises at the cyclotron system are producing the beam meander. Same time, we should install the measurement system of the beam meander.

References

1) T.Agematsu, et al., 'An Operator Assistance System for Beam Adjustment of JAERI AVF Cyclotron', Proc. on Workshop on Accelerator Operation 2003,
http://conference.kek.jp/wao2003/
2) Y.Nakamura, et al. , JAERI TIARA Annual Report 2000, JAERI-Review 2001-039, p293
3) Y.Nakamura et al , 'Present Status of JAERI AVF Cyclotron System', in this TIARA report

9.10 Measurement of Accumulated Dose Around the Cyclotron

Y. Nakamura* and T. Kojima**

Advanced Radiation Technology Center, JAERI*
Department of Material Development, JAERI**

1. Introduction

The estimation of an accumulated dose at the surrounding devices of the JAERI AVF cyclotron is significant for the damage control of various electronic components. Many alanine and thermo-luminescence dosimeters were placed to estimate the accumulated dose and measured once a year in summer, roughly between two periodical maintenance occasions. And an integration measurement was continued using the same dosimeters after reading-out of dosimeters.

Although the average accumulated doses for a year were obtained by double corrections depending on the operation condition of the cyclotron and signal fading from the dosimeters, only a few electronic components were suffered through the radiation damage because we had already considered so as to avoid it.

2. Prediction of Accumulated Dose

A distribution of the accumulated dose for a year has been estimated to be wide range from a few Gy to several hundreds Gy by the shielding design[1] of TIARA facility. Table 1 summarizes neutron yields for light and heavy ions when their intensities are assumed based upon the actual operation condition. For example, 45 MeV H^+ with the intensity of 2 μA generates a number of neutrons more than 1500 times that for 220 MeV $^{12}C^{5+}$ with the intensity of 20 nA.

The table clearly illustrates that the neutrons induced by the light ions are almost predominant in the radiation environment of the cyclotron.

3. Selection of Dosimeters

We should choose the suitable dosimeters which have a wide dynamic range for accumulated dose under the mixed radiation field from neutrons and gamma-rays and high stability for long-term integrating measurement.

Alanine dosimeters[2,3] (AD's), made by Hitachi Cable Ltd., were used in consideration of a superior long-term stability of their signals. However, a rather large signal fading was observed on the half way especially at low dose region of a few (<10) Gy level. Two kinds of thermo-luminescence dosimeters (TLD's) were placed additionally, with AD's at many positions, which are UD-808PQ and UD813-P15 made by Matsushita Electric Co. Ltd. These dosimeters were fitted up surely at surrounding positions a little far away the cyclotron.

4. Conversion Factor from Exposure to Absorbed Dose in Silicon

An energy dependence of the AD has been reported in the reference[4] that the dose responses for the neutrons with energies up to 15 MeV are between 0.4 and 0.7 of those for Co-60 gamma rays. The response factor was estimated to be 0.55 as an average value. The contribution of the gamma rays occupied the all of absorbed dose has been also estimated to be 1-10%[1] in the JAERI cyclotron facility. Comprehensively, the correction factor for the AD was assumed to be 0.60

Table 1 Neutron yield for actual ion beams.

Kind of ions	Ion species	E/u	Beam intensity		Neutron yield	Relative value	Normalized
Unit		MeV/u	enA	pnA	neutron/ion	neutron·nA	value
Light ions	45 MeV, H^+	45.0	2000	2000	0.028	56	1.00
	50 MeV, $^4He^{2+}$	12.5	2000	1000	0.0031	3.1	0.055
	100 MeV, $^4He^{2+}$	25.0	2000	1000	0.022	22	0.39
Heavy ions	220MeV, $^{12}C^{5+}$	18.3	20	4	0.0093	0.037	6.6E-04
	260 MeV, $^{20}Ne^{7+}$	13.0	50	7	0.0035	0.025	4.5E-04
	175 MeV, $^{40}Ar^{8+}$	4.4	50	6	0.0001	0.0006	1.1E-05

Table 2 Operation time and ratio of ion species.

Period	Operation	Ratio of species (%)		Operation time	Relative
JFY-JFY	time (h)	Light	Heavy	to light ions (h)	value
91-92	2600	61.3	38.7	1593.8	1.157
92-93	3006.8	54.7	45.3	1644.7	1.194
93-94	3243.5	53.0	47.0	1719.1	1.248
94-95	3101.7	42.6	57.4	1321.3	0.959
95-96	3344.1	41.7	58.3	1394.5	1.012
96-97	3049.8	32.8	67.2	1000.3	0.726
97-98	3459.9	40.4	59.6	1397.8	1.015
98-99	2937.5	37.6	62.4	1104.5	0.802
99-00	3036.4	37.4	62.6	1135.6	0.824
00-01	3519.2	43.8	56.2	1541.4	1.119
01-02	2893.1	45.0	55.0	1301.9	0.945

In general, as many kinds of semiconductor devices rather weak against the radiation, the unit of the absorbed dose is convenient to indicate using Gy in the silicon. The mass energy absorption coefficient for silicon around the energy of 1.25 MeV of Co-60 gamma rays is almost the same as the one for air, 0.0266 cm^2/g. In consequence, the conversion factor from the exposure (X) in unit of Roentgen to adsorbed dose (D) in unit of Gy is written as,

$$D = 0.869/0.6/100 \cdot X = 0.0145 \cdot X .$$

5. Result of Measurement

The integrating dose measurement using the AD's was begun in March 1991, and continued until July 2002. The operation time and the ratio of ion species[5] are shown in Table 2. An average operation time for one year is 3178 hours during 11 years. The ratio of light ion to all ions varies from 33% to 61%. As mentioned before, because the light ion brings the bigger contribution of neutron production compared to the heavy ion, we calculate the relative value which corresponds to the operation time for light ion, as shown in Table 2. This value proportional to the absorbed dose is fluctuated between 0.73 and 1.25.

A few years later, quite big signal fading was observed for a number of AD's. Therefore, all of AD's were replaced by new ones in the summer of 1995 to prevent from complicate correction. The fading effect on the signal during long-term irradiation was evaluated to be 37.5 % per one year as an average value based upon the data from 42 AD's.

This fact means that the deviation of the actual dose which corresponds to the relative value shown in Table 2 is buried completely in the fading effect on AD. We got unwillingly an average value from two quantities observed by virgin AD's at two colored columns in Table 2. Finally, double corrections were applied using the relative value and the half value of 37.5 % for signal fading.

Figure 1 shows the average absorbed dose (DY) around the cyclotron for a year. The biggest DY of 1000 Gy was recorded at the TS1 where the beam extracted from the cyclotron was often stopped. The DY on the shielding wall surrounding the cyclotron vault is the magnitude of several Gy. The largest DY was observed at the first diagnostic station after the switching magnet along the LC course which is usually used to deliver light ion beams at high intensity. It looks like that these results reflect faithfully the actual condition of experimental utilization.

In the cyclotron-pit room at the basement just under the cyclotron body, the DY of 5-6 Gy was detected rather uniformly at several points. On the other hand, in the region at relatively low dose, the DY detected by TLD was about 10-30 % of the dose obtained by means of AD. A little larger fading effect also appeared in the TLD's measurement result.

6. Radiation Damage

As described in the introduction, our cyclotron system has been designed carefully for fear that the sensitive elements against radiation, such as optical devices, encoder, photo coupler and so on, may be put in the cyclotron vault as far as possible.

We have experienced only three troubles so far which are predicted obviously that they were caused by radiation damage. The list of devices suffered from the radiation damage is shown in Table 3. After the TMP controller was out of order at 35 Gy, it was already moved at the basement where the radiation level is relatively lower. The visicon type camera for the beam diagnosis worked normally up to 1400 Gy. This camera was installed near the TS1 station where is the severest radiation environment among the stations. The sequencer (C500H) installed in the light ion room 1

was broken down suddenly during the irradiation of intense 100 MeV $^4He^{2+}$ beam. Unfortunately, no dosimeter was set up by the sequencer.

Some electronic devices such as the telephones, CCTV cameras for watching the room and the pre-amplifier assembled into the detector for radiation monitor are installed on the shielding wall at several Gy for a year. These devices are still sound so far.

Prior to the installation of the cyclotron system, we examined their radiation damage[6] using gamma-rays and neutrons about a vacuum gauge controller and the universal device controller, which are the components used in the cyclotron system, as typical electronic devices which include in many kinds of semiconductor elements. Since two devices were functionally disordered at the absorbed dose about 40-100 Gy, we did not install these in the cyclotron vault.

Table 3 List of devices suffered from radiation damage.

Date	Device	Element (Type)	Accum. Dose Gy in Si	Remarks
Jan 1999	TMP controller	Photo coupler	35	Movement
Aug 2001	Camera	(Visicon type)	1400	Change to CCD
Jan 2003	Vacuum controller	Sequencer (C500H)	-----	Replace by new one

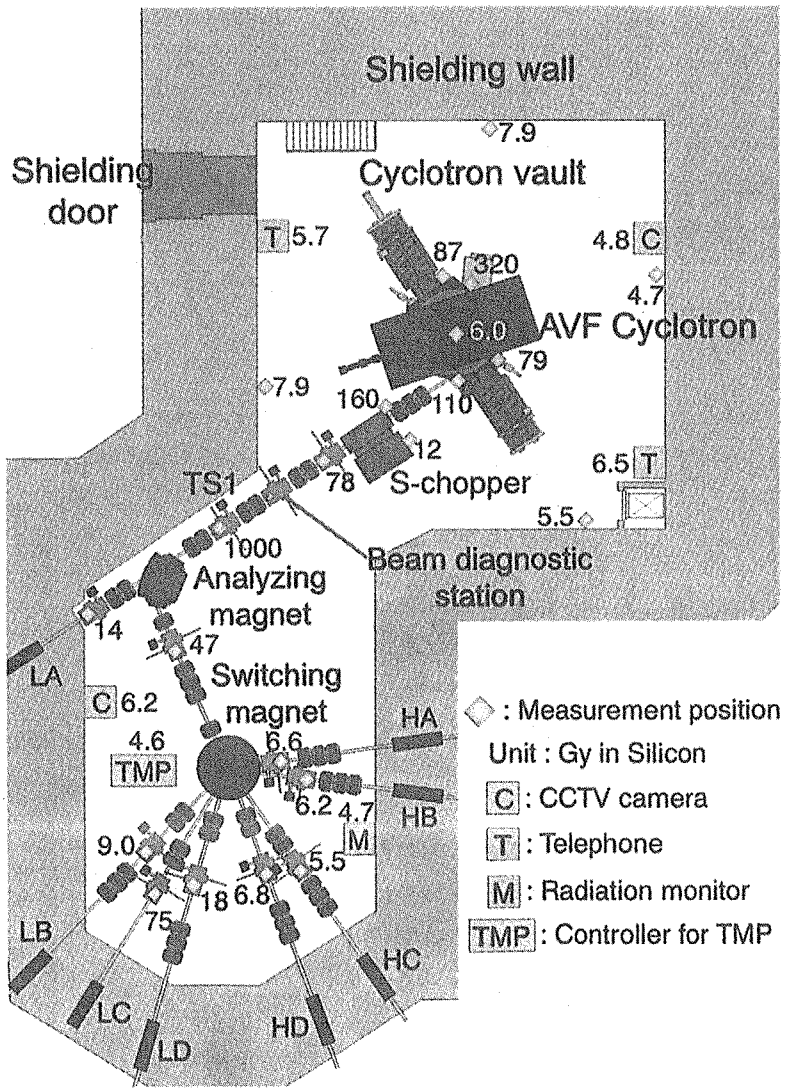

Fig.1 Average absorbed dose for a year around the cyclotron.

Acknowledgment

Authors wish to thank Mr. Tsuyoshi Yoshida for his original drawing of Fig. 1.

References

1) S. Tanaka, Private communication
2) T. Kojima, *et al.*, Appl. Radiat. Isot., 37, (1986) pp. 517-520
3) Y. Haruyama, *et al.*, RADIOISOTOPES, 44, (1995) pp. 507-513 (in Japanese)
4) H. Schraube, *et al.*, Appl. Radiat. Isot., 40, (1989) pp. 941-944
5) Y. Nakamura, T. Nara, *et al.*, Proc. 16th Int. Conf. Cyclo. Their Applic., East Lansing, MI, USA (2001) pp. 129-132
6) W. Yokota, Y. Nakamura, *et al.*, TIARA Annual Report 1992 (JAERI-M 93-241) pp. 204-206

9.11 Development of PC-based analogue signal analysis system

Takuro Sakai, Sadanori Uno and Kiyoshi Mizuhashi
Advanced Radiation Technology Center, JAERI

1. Introduction

It is necessary to monitor analogue signals, such as the terminal voltage fluctuation of the electrostatic accelerator, for stable daily accelerator operations. Conventional oscilloscopic measurement is utilized for this purpose in many accelerator facilities. However, this method only displays the waveform of analogue signals, another expensive instrument is required to perform quantitative spectrum analysis or deviation measurement. So, we have developed new inexpensive personal computer (PC) based analogue signal analysis system that provides real-time frequency component analysis and signal fluctuation measurement, as well as conventional waveform monitoring. This system has been installed TIARA 3MV tandem accelerator control console to optimize the accelerator parameters for stable operation.

2. Instruments

The terminal voltage fluctuation of the tandem accelerator is sensed by the capacitive pick-off (CPO) plate which is facing the high voltage terminal of the accelerator. The plate is coupled with the terminal as a capacitor, so that any terminal voltage fluctuation will reflect on this CPO plate by changing the collected charges [1]. The fluctuation signal is amplified by electric circuits to monitor the voltage stability.

The analogue signal analysis system consists of a commercial Windows-based PC (Dell OptiPlex GX60 equipped with Celeron 2.4GHz, 512MB

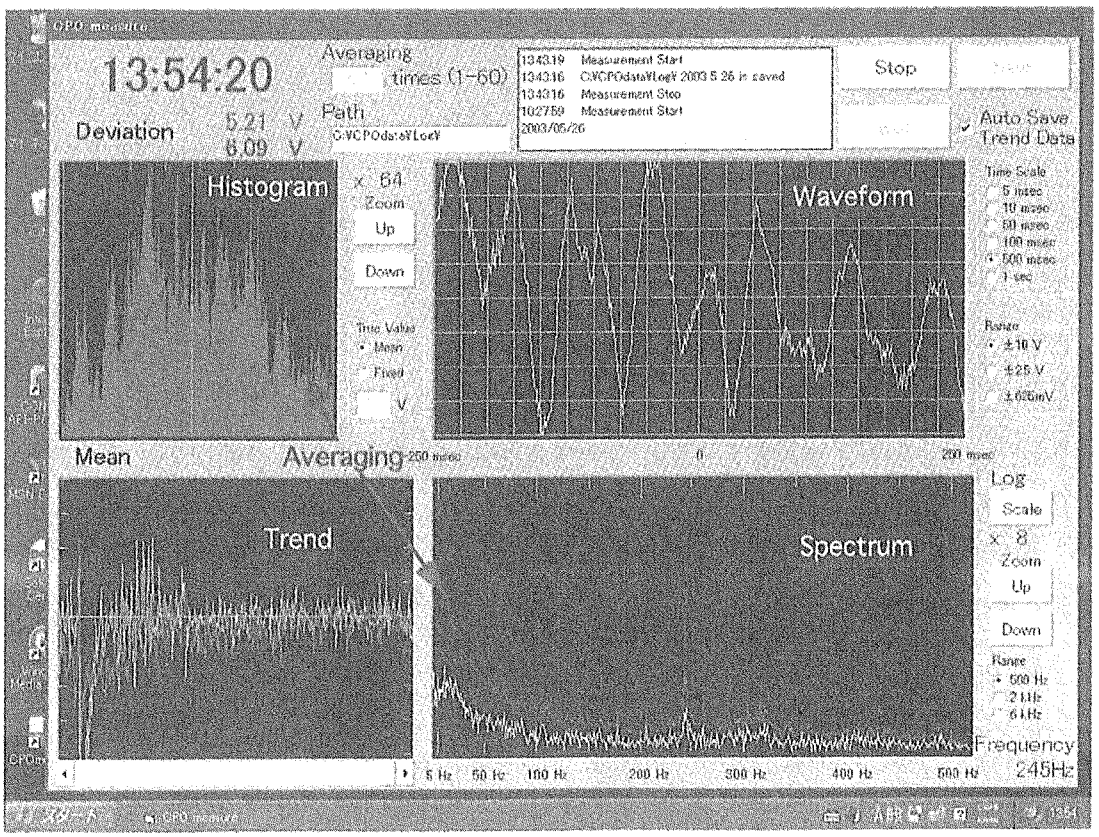

Fig. 1 The display of analogue signal analysis system

RAM) and an analogue to digital converter (Contec AD12-16(PCI)E with 12-bit digital resolution, 10 μsec/ch conversion time and 256k words buffer memory). The latest PC can now provide faster data handling with lower cost as a result of the recent rapid progress of computer technology [2-4]. The analogue signal is converted to digital value and processed by the PC in real-time. Waveform, frequency component and deviation histogram of the input signal are displayed instantly. The spectrum analysis is based on fast Fourier transform (FFT) method and the signal deviation is indicated in 256-channel histogram. This system also records the time resolved deviation of signal fluctuation like a pen-recorder device. Figure 1 shows the display of the analysis system.

3. Operations

The analogue signal analysis system has been used for the daily accelerator operation. Some examples of terminal voltage fluctuation measurement is described as below.

TIARA 3MV tandem accelerator (National Electrostatics Corp. 9SDH-2) is equipped with two pellet-chain for the high voltage generation. The pellet-chain works for both up-charging to the terminal shell and down-charging to the ground, so that smooth operation of the pellet-chain is essentially required for the terminal voltage stability. The waveform of the CPO signal, its deviation histogram and spectrum are taken with only driving each single pellet-chain to diagnose its operation. The histograms and spectra are shown in figure 2 and 3, respectively. The

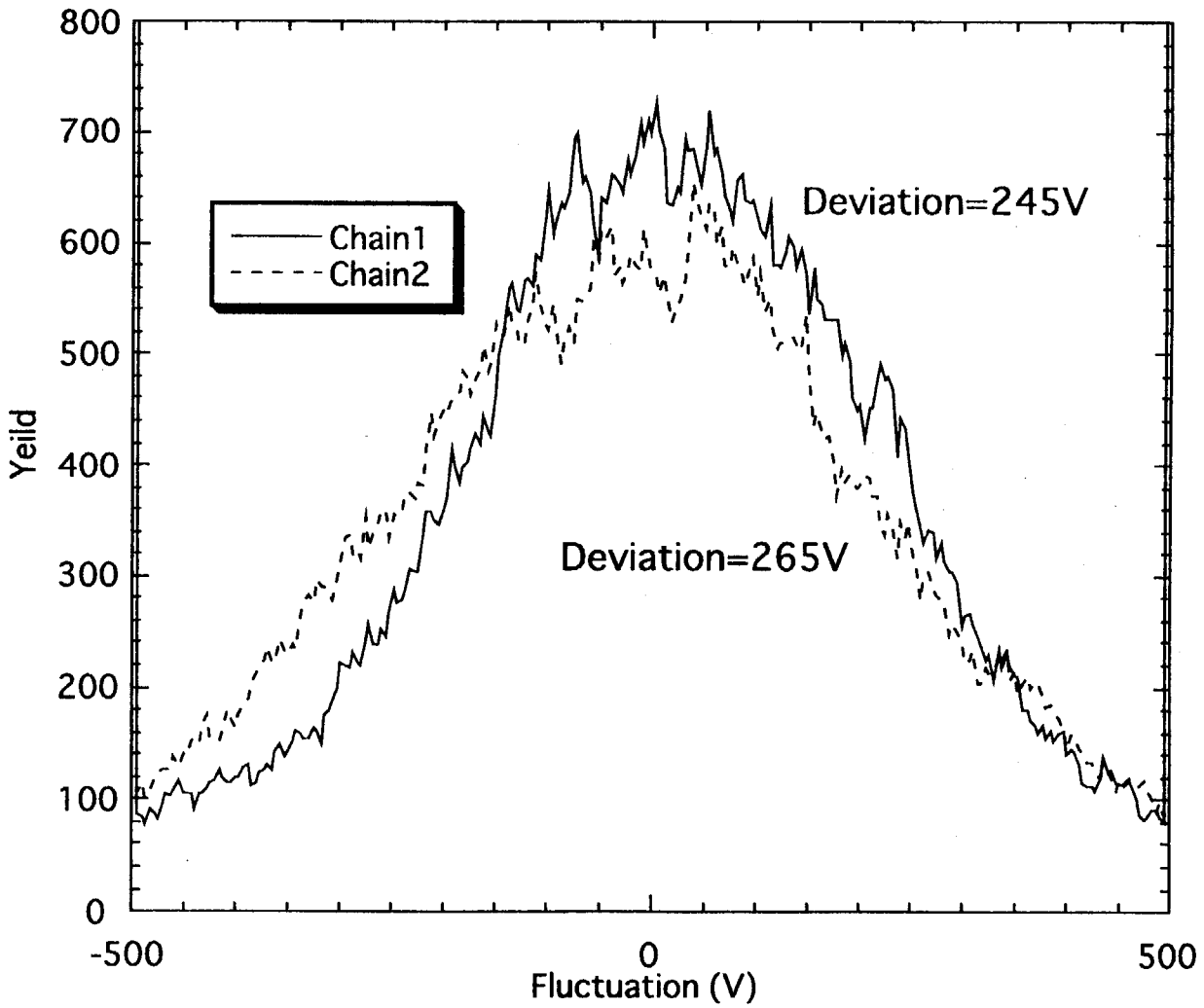

Fig. 2 The deviation histograms of the terminal voltage fluctuation

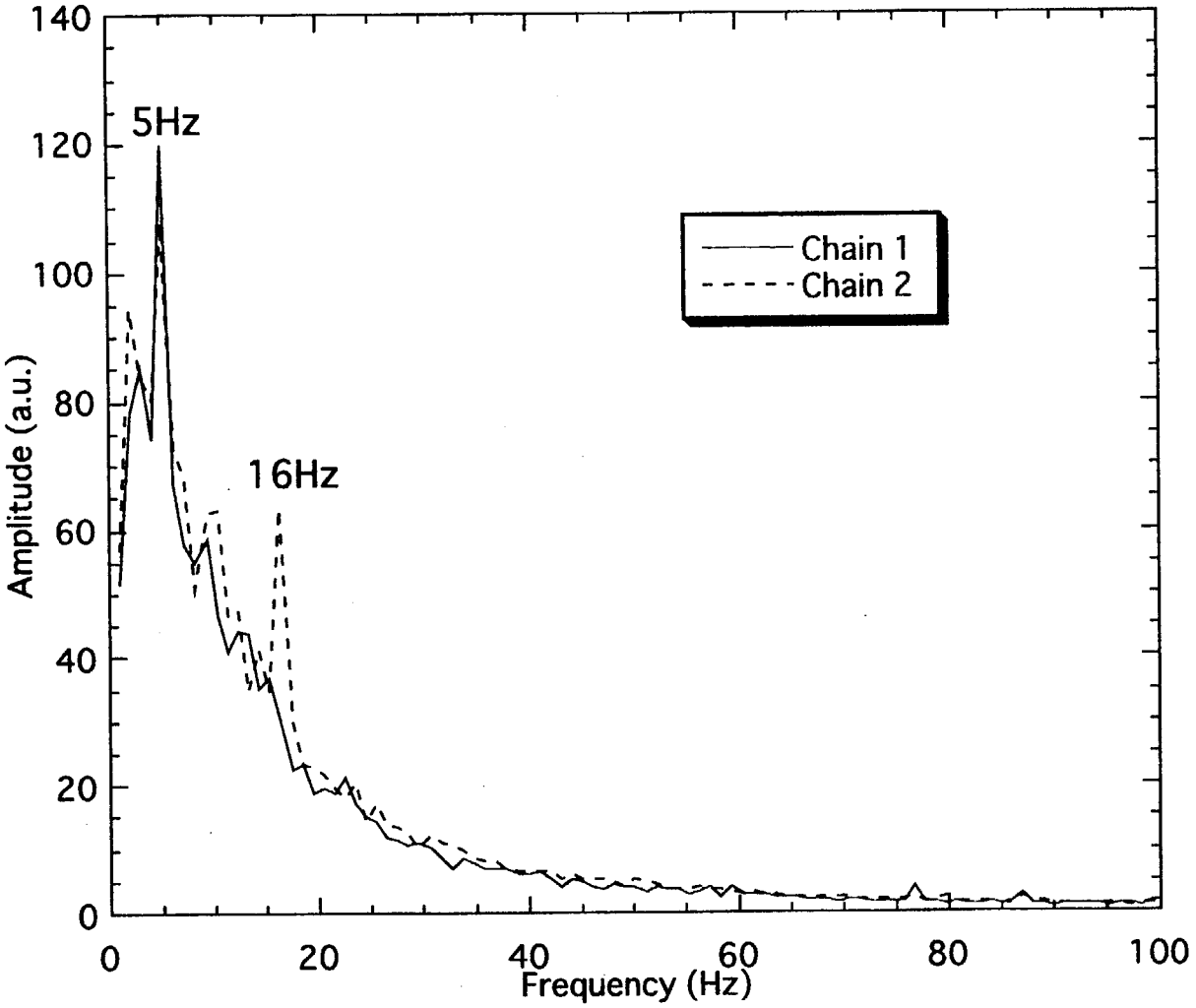

Fig. 3 The frequency components of the terminal voltage fluctuation

measurement conditions are, 1MV terminal voltage, 16 rounds per second (rps) pellet chain drive pulley rotating speed, no ion beam injection.

The histograms show that the pellet chain 2 driven voltage fluctuation is lager than that of pellet-chain 1. The spectra give more detail information. 5 Hz component is shown in both spectra. This frequency is twice as the pellet-chain cycle, so that this component is supposed to be derived from the pellet-chain driving. On the other hand, 16 Hz component is only appeared in pellet-chain 2 driven spectrum, and the frequency is consistent with the pulley rotating rate. So the drive or pickoff pulley of pellet-chain 2 is suspected to be unsettled.

These results proved that the newly developed analogue signal analysis system is useful not only for monitoring the voltage stability, but also for diagnosing the accelerator troubles in an early stage.

Acknowledgement

The authors are grateful to Dr. K. Arakawa and JAERI electrostatic accelerator group for their continuous assistance.

References

[1] J. Takács, Energy Stabilization of Electrostatic Accelerators, (John Wiley & Sons, Chichester, 1997)
[2] T. Sakai et al., Nucl. Instr. and Meth. B136-138 (1998) 390.
[3] M. Bogovac et al., Nucl. Instr. and Meth. B89 (1994) 219.
[4] G. W. Grime and M. Dawson, Nucl. Instr. and Meth. B104 (1995) 107.

9.12 Production of Fullerene (C_{60}) ions by Freeman Ion Source

K.Ohkoshi*, Y.Saitoh*, T.Orimo**, A.Ohmae**, I.Takada* and S.Tajima*
Advanced Radiation Technology Center, JAERI*
Beam Operation Co. Ltd.**

1. Introduction

A variety of ions from H^+ to Bi^+ have been available for various experiments by means of the 400kV ion implanter equipped with a Freeman ion source in TIARA facility[1]. Recently, the cluster ions has attracted attention in area of fundamental research such as non-linear irradiation effects on the surface of a target. Accordingly, the fullerene (C_{60}) ions were required by users in the research fields. We tried producing fullerene ions by the Freeman ion source[2].

2. Ion generation by the Freeman ion source

The Freeman ion source is used to generate the ions. The structure of the Freeman ion source is illustrated in Fig.1. The material gas or vapor is fed into a plasma chamber to make the arc plasma. The electrons emitted from the tungsten filament are accelerated toward the plasma chamber wall with 100V potential. The constant magnetic field of about 150 Gauss is applied in parallel with the filament to lengthen electron trajectory. The positive ions are extracted from the plasma chamber and are accelerated after mass analyzing.

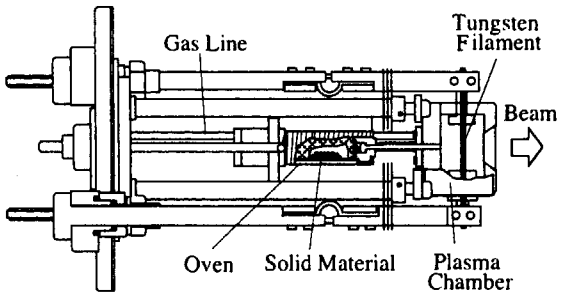

Fig.1 Freeman ion source.

3. Production of fullurene ions

The C_{60} powder of 95% purity is put into the oven of the Freeman ion source, and is vaporized by the oven (430℃). The Ar gas feeds to the plasma chamber to make the stable plasma. The vapor of fullerene are fed to the Ar plasma and ionized in the plasma chamber. The fullurene ions are extracted from the source. Figure 2 shows the mass spectrum of the ions extracted from the source. High intensity C_{60}^+, its fragments such as C_{58}^+, C_{56}^+, C_{54}^+, and their doubly charged ions are obtained.

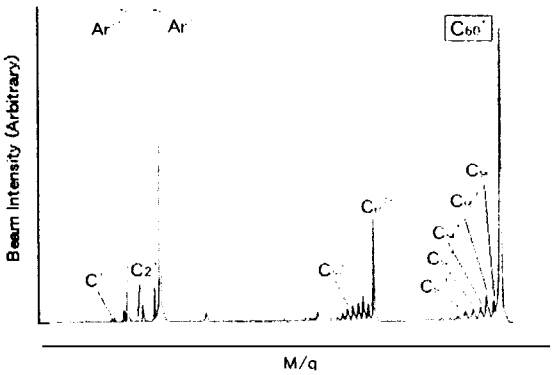

Fig.2 Mass spectrum of ions extracted from source.

A number of positive secondary ions are emitted from a surface of a target with the irradiation of cluster ions. It causes that the measured beam current with a usual Faraday cup equipped with electron suppresser electrode seems lower value compared with the true one because of the escape of the secondary ions. So, the beam current of C_{60} was measured with the high-aspect ratio Faraday cup shown in Fig. 3. The maximum beam current of C_{60}^+ is 2.1μA at 350keV.

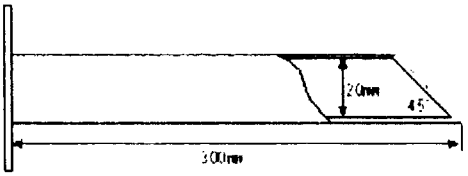

Fig.3 High-aspect ratio Faraday cup.

Two samples of C_{60} were tested to generate the C_{60} beam. One is the powder (95% purity), and the other is the grain (99% purity).

At first, the beam intensity of C_{60}^+ using

the powder sample is shown in Fig.4. The beam current of C_{60} decreased gradually to nA order by 6 hours operation. However, there was enough quantity of C_{60} powder in the oven after the operation.

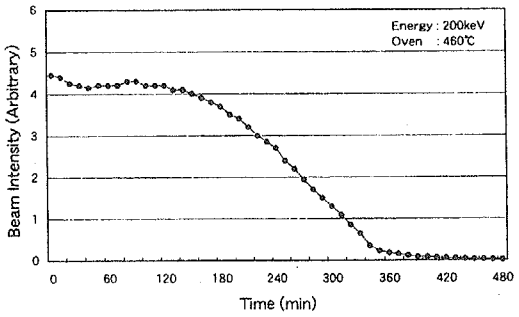

Fig.4 Fluctuation of C_{60}^{+} beam intensity using powder sample.

Next, the beam intensity of C_{60} using the grain sample is shown in Fig.5. The stable beam current of C_{60} was available for more than 8 hours.

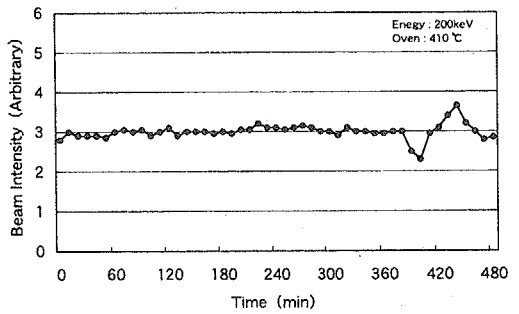

Fig.5 Fluctuation of C_{60} beam intensity using grain sample.

We investigate the oven temperature dependence of the beam current. The temperature in which maximum beam current is obtained using powder sample (500℃) is higher than that using grain sample (410℃) shown in Fig. 6.

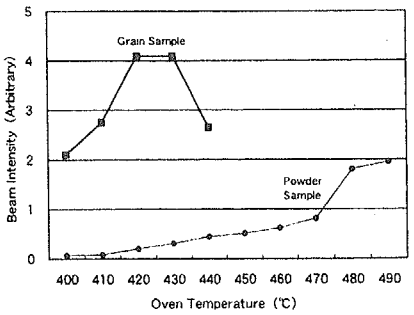

Fig.6 Relationship between oven temperature and C_{60}^{+} beam intensity.

As a result, the C_{60} beam is stabilized for a long time when energy and oven temperature are 200keV and 410℃.

We thought that the Fullerene is decomposed to an allotrope of carbon such as graphite in high temperature.

In the generation of C_{60} beam, the tungsten filament was carbonized by C_{60} plasma and had a crack in length of 15mm on the surface of the filament shown in Fig.7.

To avoid that, we exchanged from tungsten filament to tantalum one.

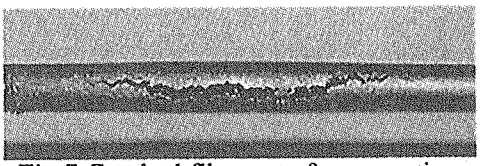

Fig.7 Cracked filament after operation.

4. Summary

We have succeeded in generating stably an intense C_{60} beam in the energy of up to 400 keV (more than 8 hour). It was found that stable generation of C_{60} ions in the source could be obtained using the grain sample instead of the powder sample. It appears that the grain size of C_{60} sample in the oven was important for stable ion beam generation. It also found that the crack growth on the filament could be avoided using the tantalum filament instead of the tungsten one.

We continue to generate the higher intensity and stable C_{60} beam.

References

1) Y.Saitoh, S.Tajima et al., Nucl. Instrum. Methods phys. Res. B89, 23 (1994).
2) J.H.Freeman, Nucl. Instrum. Methods 109, p477 (1973).

9.13 Automatic measurement of beam energy spread for JAERI Single-ended Accelerator

Y.Ishii, A.Chiba and I.Takada
Advanced Radiation Technology Center, JAERI

1.Introduction

Ion beam with a narrow energy spread is an essential factor for formation of a submicron ion beam by reducing a chromatic aberration in a focusing lens system. Beam energy spreads of $\pm 1x10^{-5}$ are required to produce a submicron beam of 0.1 μm or less in a light ion beam system in JAERI Takasaki. The production of such an ion beam with the narrow beam energy spread has been tried by JAERI Single-ended Accelerator connected to the light ion system. The accelerator with a voltage range between 1 and 3 MV has high voltage stability of $\pm 1x10^{-5}$ at 3 MV. The voltage stability is, however, different from the beam energy spread in a beam due to various increases of instability, such as ripple voltage for production of ion beam, small discharges for ion hits to electrodes in an accelerator tube and so on. The high accurate measurements of the beam energy spreads were, thereby, required to evaluate the stability of ion beam generated form the accelerator.

Beam energy spreads have been measured at four different beam energies of 0.992 MeV, 1.317 MeV, 2.100 MeV and 2.4 MeV using nuclear resonance reactions of ^{27}A $(p,\gamma)^{28}Si$ and $^{24}Mg(p,\gamma)^{25}A$ with narrow reaction widths on the basis of a 0° analyzing technique[1]. The former two beam energies are used in ^{27}A $(p,\gamma)^{28}Si$ and the latter ones were in $^{24}Mg(p,\gamma)^{25}A$. The measurement time, however, took more than 3 hours at each reaction energy because the ion beam energies injected in a target were changed within 200 eV over 30 step repeatedly at least 5 times and the measurements at each step were needed more than about 3 min. The measurements of beam energy spreads based on various operated conditions of the accelerator were difficult in a limited beam time. An automatic measurement technique of beam energy spread was introduced to reduce the measurement time. In the technique, beam scanning by alternating deflection voltage was applied for finely control of the injection beam energy instead of manual control. This technique led us to reduce the measurement times in about 1 hour at each energy and enables us to boost the study of beam energy spreads on the basis of accelerator operation conditions. The average beam energy spread was estimated in $2x10^{-4}$ using the automatic measurement system though it was not small.

2.Experiment

2-1.Setup

A direct ion beam injection into the target is required to measure the beam energy spread using the nuclear resonance reaction method. The reason is that a width of beam energy spread is determined by a resolution of an analyzing magnet if ion beam passes through its magnet. An experimental vacuum chamber was connected to a 0' beam line in order to inject ion beam into a target without energy analyzer as shown Fig.1. A 600 Å thin A foil, as a target, vapored on a 20x20x0.3 mm/mm Tantalum (Ta) plate was supported by an insulator rod to apply high voltage. A 2'x2' inch NaI γ-ray detector was set to the traveling direction of the H^+ beam and in about 20 mm form the target to obtain a large solid state angle to γ-ray detections.

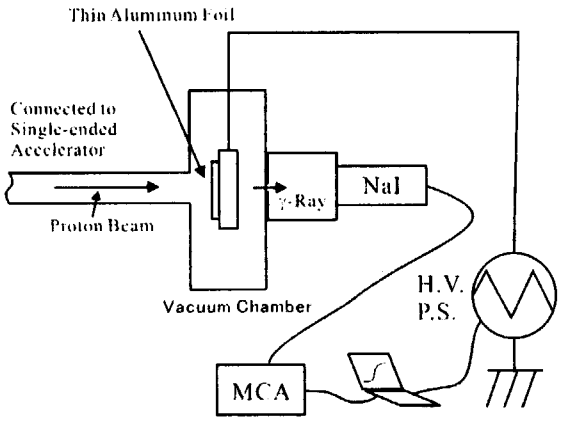

Fig.1 Schematic of the experimental chamber. The chamber was connected with 0' beam line.

H^+ beam generated from the single-ended accelerator was directly injected in the thin foil target to react the nuclear resonances. The injection beam

energy is controlled in the minimum voltage of 1 keV step. The control of the beam energy within 100 eV was, however, required to achieve the resolution of less than 10^{-4}. A high voltage power supply of maximum voltage of 5 kV with stability of $1x10^{-5}$ was connected with the thin A target to control injection H^+ beam energy within 1 keV by suppressing the beam energy. Furthermore the suppression voltage was successively changed into the alternating one with a triangle wave of 0.125 Hz.

2-2. Measurement of γ-yields

The micro-PIXE measurement system[2] was used for the measurement of γ-yield on the basis of the alternating suppression voltage. A suppression voltage to each reaction was automatically measured in a personal computer (PC) when a γ-ray was detected in the NaI. The measured voltage in the PC was decided from the voltage data divided by 128 and stored in the same number of memory cells in a personal computer. The detection of γ-ray was continued until total γ-ray count of $1.9x10^5$ [cps]. Each acquisition time until the counts was about 1 hour though depending on the ratio of γ-ray generations.

3.Result and Summary

A γ-ray yield carve of the nuclear resonance reaction energy at 2.4 MeV was shown in Fig.2 as a function of beam energy based on the suppression voltage. The acquisition time for the total γ-ray count of $1.9x10^5$ [cps] took about 1 hour. In the Fig.2, the filled circle and the broken line show the measurement values and the interpolation line based on an average data, respectively. The total circles are 128 points as the same number of memory cells. The width of beam energy spread in Fig.2 was defined as the value of a Full Width at Half Maximum (FWHM) of Gaussian distribution and estimated from fitting the deferential values of the yield curve to the beam energy using its distribution as shown in Fig.2 as the solid line. The differential curve value was shown in the right size of Fig.2. The beam width was $4x10^{-4}$ from the FWHM value. The beam widths were estimated to the other resonance nuclear reaction energies by the same fitting method using Gaussian function. Each measurement was carried out in about 1 hour. Although the width of beam energy spread was not small, it was in $6.3x10^{-4}$, because this measurement was concentrated into the development of measurement technique. The measurement technique was established by this time measurement.

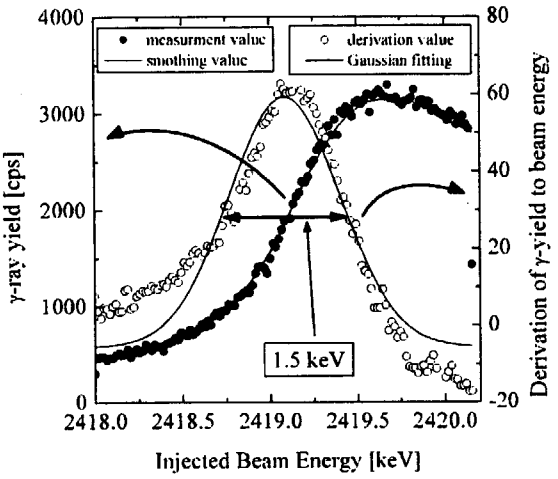

Fig.2 One example of measurement result.
Nuclear resonance reaction of $^{24}Mg(p,g)^{25}A$ at injection H^+ beam energy of 2.4 MeV.

The measurement accuracy might be considered to be decreased by reducing the data acquisition time. The accuracy of introduced measurement technique was, however, the same of that of the previous technique because statistical accuracy was significant form the peak counts over 3000 in the yield curve.

The introduced measurement technique led us to reduce the experimental time and enables us to boost the study of beam energy spreads on the basis of accelerator operation conditions..

Reference

1) Y.Ishii et al. JAERI-Review 2001-39.
2) T. Sakai, Nucl. Instr. and Meth. B136-138 (1998)390.

9.14 Development of Emittance Measurement Device Using Illuminant with Thin Scintillator

Atsuya CHIBA, Yasuyuki ISHII and Satoshi TAJIMA

Advanced Radiation Technology Center, JAERI/Takasaki

1. Introduction

It is very important with respect to formation of high intensity micro-beam and effective beam transportation that the voltage for electrostatic accelerator is stable and that the brightness of the ion source is high. In developing the high performance ion source, it is necessary to measure the accurate emittance. However, in the generally, a measurement of the emittance takes long time, therefore they are difficult to get the accurate emittance from the fluctuate beam. [1)]

We developed a new measuring device composed of a slit with multiple clearances, a movable illuminant and a CCD camera. [2)] It can measure the beam emittance easily and quickly, and the cost of the system was able to be held down low.

2.Measuring method

The beam emittance is estimated from the directional intensity distributions of the ions in a small segment of the ion beam. To measure the distributions of the ion beam, the light image on the illuminant activated by the beam passed through the multi-slit was taken twice into the personal computer at the different positions of the illuminant by CCD camera. The slit has 25 holes of 0.25mm gap at regular interval of 1.25mm. The divergence angle in a small segment of the ion beam is calculated from the relation between each width of a lighting part and moving distance of the illuminant. Figure 1 shows the measuring system and how to measure the divergence angle with a pair of the light images.

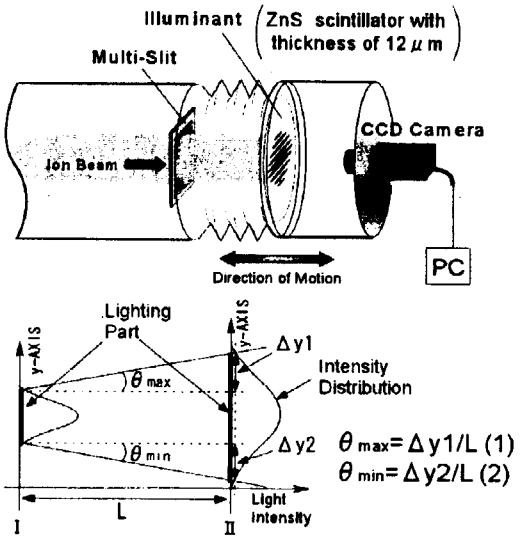

Fig.1. Schematic drawing of the emittance measurement device and calculation method of the divergence angle. Maximum angle θ_{max} and Minimum angle θ_{min} are deduced by the equation (1) and (2).

3.Property of illuminant

It is necessary to obtain the accurate divergence angle of the beam in order to measure the accurate emittance. In the general instruments, the divergence angle is derived from the relation between the current intensity distribution and the distance to the detector from the slit. The light intensity must be proportional to the

current intensity, because the divergence angle has been got from the light intensity distribution on this device. Then, we examined the relation between the current intensity and the light intensity on the illuminant. The current intensity distribution has been measured using super-fine wire slid on the cross section of the ion beam passed thorough the aperture, and the light intensity distribution has been derived from light image on the illuminant at the same cross section. Figure 2 shows schematic drawing of the measurement method, and the result is indicated in Fig.3. Width and shape of the intensity distribution of the light are almost equal to them of the current.

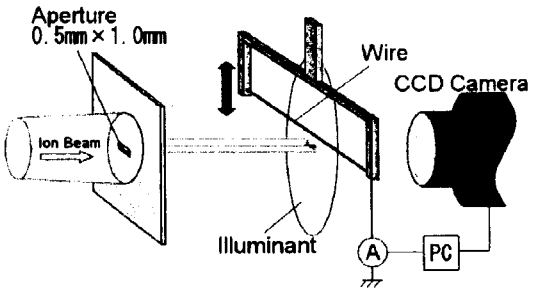

Fig.2. Schematic drawing of the intensity distribution measurement method.

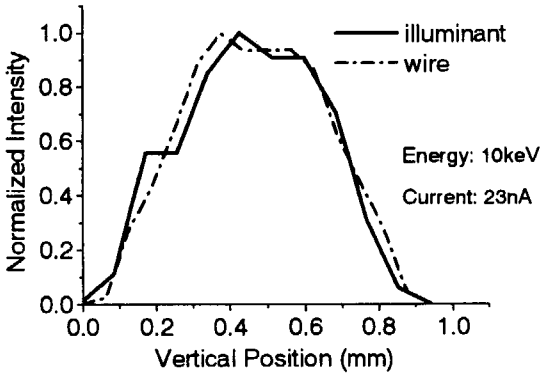

Fig.3. Comparison of intensity distribution of light and current. The resolution of the camera is 0.065mm/pixl.

Figure 4 shows the current intensity dependence of the light intensity. It was shown that the light intensity was proportional to the current intensity.

In addition, we must also investigate the damage to the illuminant by the ion beam. An efficiency of the light intensity was just decreased by irradiation as shown in Fig.5. The decreasing rate of light intensity was 3.7% in the irradiation of 10keV 0.2μA He^+ during about two minutes. It is not necessary to consider the effect of the damage to the illuminant, because the irradiation time to the illuminant at measurements of once is very short. The acquisition time of a light image is one second or less.

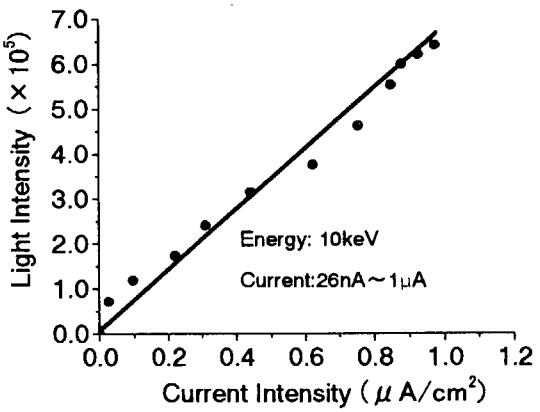

Fig.4. Relation between the current intensity and the light intensity. The vertical axis means the light intensity which is integral value of the gray level in the light image converted into monochrome.

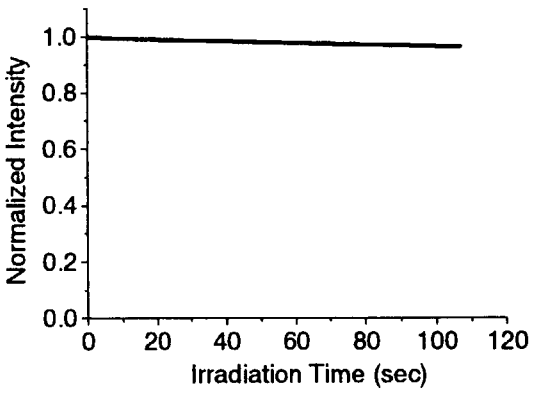

Fig.5. Change of the efficiency of the light intensity on the illuminant irradiated with 10keV 0.2 μA/cm² He^+.

4.Measurmint result of emittance

We tried to measure the emittance of the Helium ion beam from the RF source that is same type mounted on the 3MV single-ended accelerator in TIARA. Figure 6 shows the light image on the illuminant and Fig.7 is the light intensity distribution on the dotted line of the light image in Fig.6. The emittance diagram in Fig.8 was calculated by the comparison and analysis of the light image on the illuminant at the multiple positions on the beam axis.

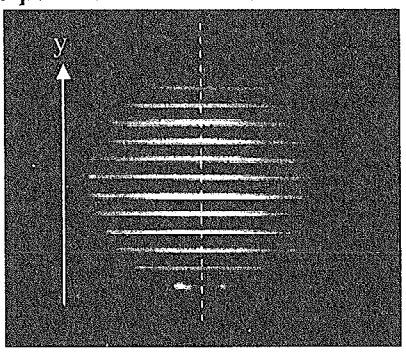

Fig.6. Light image on the illuminant.

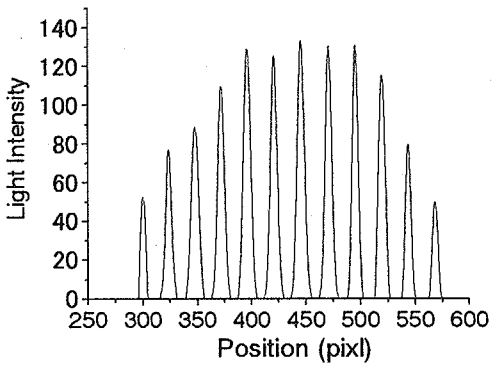

Fig.7. Distribution of light intensity on the dotted line in Fig.6. The horizontal axis has shown the y position of the light image.

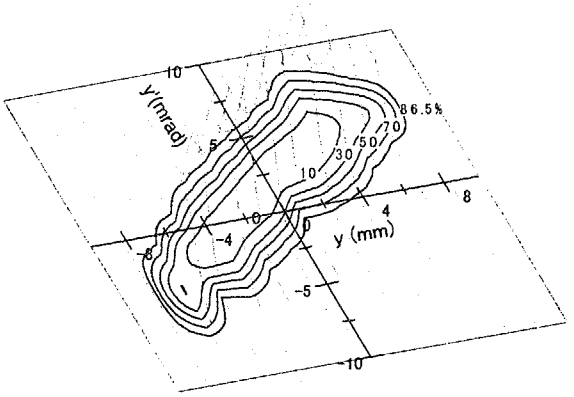

Fig.8. Beam emittance contours of extracted Helium ion beam of 10keV 4.7μA from RF source.

5.Summary

The light intensity obtained from the illuminant used in this device was proportional to the current intensity. In present measurement, it was possible to distinguish the light image clearly, and the measurement of the emittance was easily and quickly obtained by the simple system. The emittance value for 86.5% contours was 3.01 mm・mrad・MeV$^{1/2}$ for the RF ion source as same as the type mounted on the single-ended accelerator in TIARA. One measurement took about 20 seconds including the moving time of the illuminant.

References

1) G.D.Alton, J.W.McConnell, S.Tajima, and G.J.Nelson, Nucl. Instr. and Meth. in Phys. Res. B24(1987)
2) A. Chiba, Y. Ishii, S. Tajima, JAERI-Review 2002-035, p.312

This is a blank page.

10. Status of TIARA 2002

This is a blank page.

Utilization of TIARA Facilities

10.1

Su. Tanaka*, K. Nishimura*, M. Hosono*, H. Takizawa*, K. Yotsumoto**, H. Tachibana**, I. Kawashima**, S. Kaneya**, K. Daikubara***, M. Kawabata**, M. Iijima**

Advanced Radiation Technology Center, JAERI*
Radiation Application Development Association**
Research Center for Nuclear Science and Technology, The University of Tokyo***

1. Introduction

TIARA is a center of the ion accelerator facilities composed of four ion accelerators, the AVF cyclotron, the 3MV tandem accelerator, the 3MV single-ended accelerator, and the 400kV ion implanter. These accelerators have been fully served for ion beam applications since January 1994.

2. Utilization system

TIARA is opened for public use: it receives applications of the experimental subjects in wide areas once a year from outside users as well as JAERI staffs. The subjects and the allocated beam time are approved after the official investigation by Subcommittee for TIARA under Advisory Council for JAERI's Research Facilities, which has been organized since 1999. To attain an effective outcome of the research program, the beam time of each accelerator is fairly allotted to the subjects three times in a year based on the approved beam time.

Charges for the utilization are remitted in the case that a contract of the joint research between JAERI and a university or a company or that of the projective joint research between JAERI and universities is made. However, the results of research have to be published at the TIARA Research Review Meeting and in the JAERI TIARA Annual Report. There is another system of visitor use with charges but without the publication duty.

3. Experimental subject approved

Number of experimental subjects using cyclotron approved in FY2002 was 54 while the total number using three electrostatic accelerators was 52 as shown in Table 1. Table 2 shows the number allotted to users under various contracts.

Fig. 1 shows the change of number of experimental subjects in various research fields from FY1991 to FY2003.

4. Allotted time to users

The cyclotron has been continuously operated from Monday to Friday. The utilization time for the cyclotron is allotted in units of an hour.

Table 1 Number of experimental subjects in FY2002 at various research fields.

Accelerators / Fields of research	Number of subjects	
	Cyclotron	Electrostatic accelerators
Materials for space	5	6
Materials for fusion	1	10
Biotechnology	35	2
Inorganic material	0	25
RI & nuclear sci.	1	0
Organic material & Radiation chemistry	7	1
Basic technology	5	8
Total	54	52

Table 2 Number of experimental subjects in FY2002 at various relations with users.

Accelerators / Relations with visitors		Number of subjects	
		Cyclotron	Electrostatic accelerators
JAERI only	Takasaki Establishment	11	12
	Others	0	12
Cooperative research with university		17	18
Projective joint research between JAERI and universities		9	5
Joint research with private company or governmental Institute		17	5
Total		54	52

In case of the electrostatic accelerators, on the other hand, the utilization time is allotted in units of a day either from 9 a.m. to 7:30 p.m. (A mode), or from 9 a.m. to 10 p.m.(B mode).

As shown in Table 3 and Fig. 2, the cyclotron was used in the various research fields, while the electrostatic accelerators were mainly used in the field of inorganic materials and materials for fusion. The ratios of allotted time for JAERI staffs to total utilization time were 28% for the cyclotron and 45% for the electrostatic accelerators as shown in Table 4 and Fig. 3.

Table 3 Utilization of the accelerators in FY2002 at various research fields.

Accelerators / Fields of research	Utilization time at each period															
	Cyclotron (hours)				Tandem accelerator (days)				Single-ended accelerator (days)				Ion implanter (days)			
	02-1	02-2	02-3	total	02-1	02-2	02-3	total	02-1	02-2	02-3	total	02-1	02-2	02-3	total
Material for space	195	180	63	438	12	11	13	36	-	-	-	-	13	10	7	30
Material for fusion	110	97	61	268	19	18	15	52	16	16	12	44	14	10	12	36
Biotechnology	391.5	352.5	170	914	1	1	2	4	-	-	-	-	-	-	-	-
Inorganic material	-	-	-	-	11	11	8	30	19	8	19	46	21	24	18	63
RI & nuclear science	17	8	8	33	-	-	-	-	-	-	-	-	-	-	-	-
Organic material & Radiation chemistry	92	90	55	237	3	4	2	9	-	-	-	-	-	-	-	-
Basic technology	95	105	54.5	254.5	4	5	1	10	16	22	13	51	0	0	0	0
Machine study	122	116	56	294	3	3	4	10	3	6	4	13	2	3	3	8
Visitors use with charges	0	35	110	145	3	2	2	7	0	1	0	1	1	2	2	5
Total	1022.5	983.5	577.5	2583.5	56	55	47	158	54	53	48	155	51	49	42	142

Table 4 Utilization of the accelerators in FY2002 at various relations with users.

Accelerators / Relation with visitors		Utilization time at each period															
		Cyclotron (hours)				Tandem accelerator (days)				Single-ended accelerator(days)				Ion implanter (days)			
		02-1	02-2	02-3	total	02-1	02-2	02-3	total	02-1	02-2	02-3	total	02-1	02-2	02-3	total
JAERI	Takasaki Establishment	186	149	106	441	17	12	21	50	7	8	10	25	19	19	11	49
Only	others	0	0	0	0	3	5	2	10	17	7	7	31	5	3	3	11
Cooperative research with universities		211.5	186.5	92.5	490.5	10	11	3	24	14	18	18	50	10	13	12	35
Projective joint research between JAERI and universities		318	313	145	776	15	14	10	39	13	13	9	35	11	6	8	25
Joint research with company or governmental institute		185	184	68	437	5	8	5	18	0	0	0	0	3	3	3	9
Machine study		122	116	56	294	3	3	4	10	3	6	4	13	2	3	3	8
Visitors use with charges		0	35	110	145	3	2	2	7	0	1	0	1	1	2	2	5
Total		1022.5	983.5	577.5	2583.5	56	55	47	158	54	53	48	155	51	49	42	142

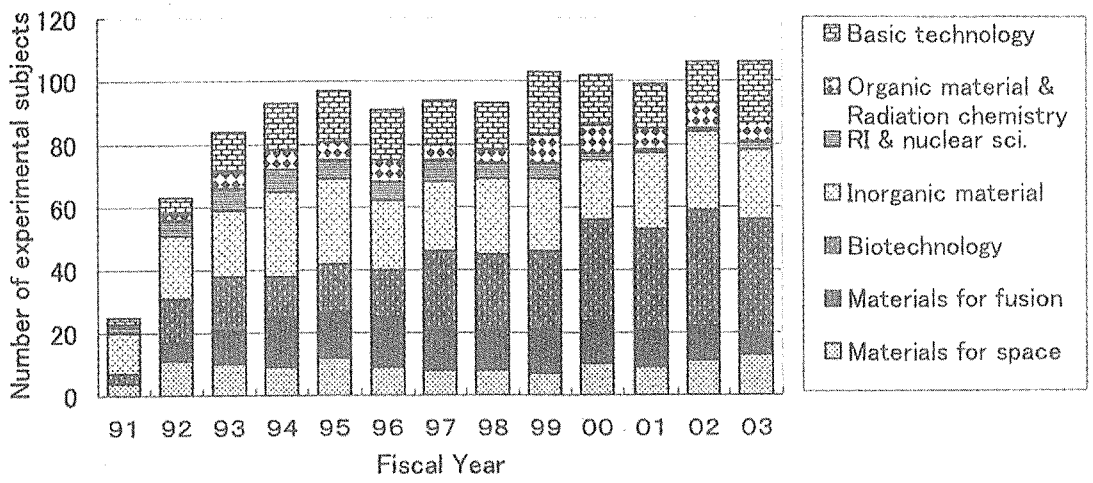

Fig. 1 The change of number of experimental subjects in various research fields.

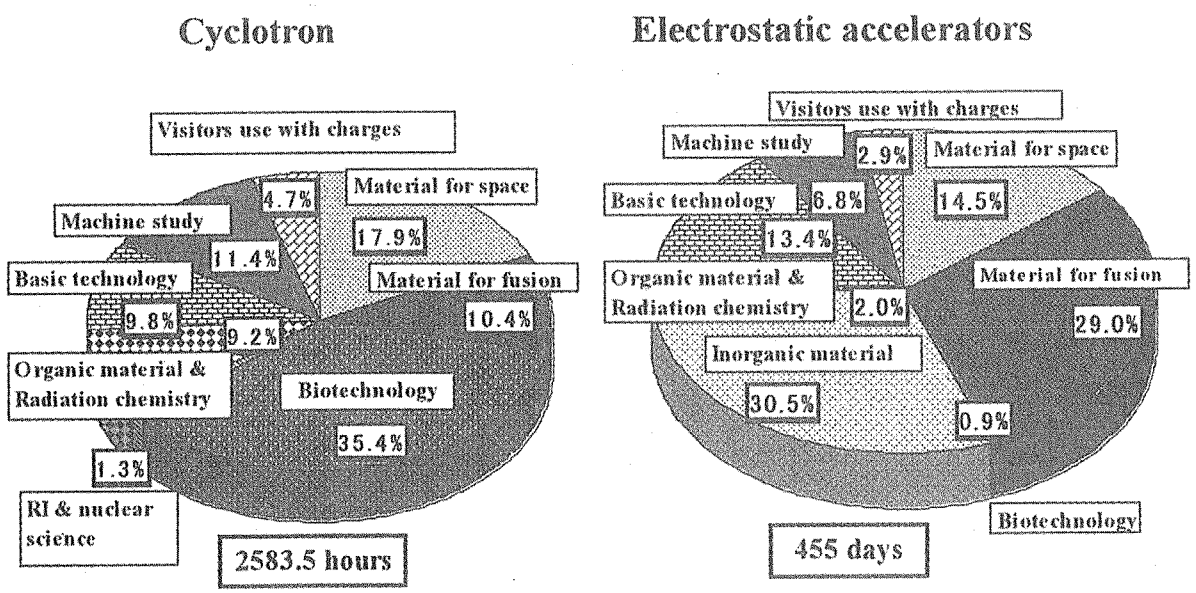

Fig. 2 Utilization of the accelerator in FY2002 in various research fields.

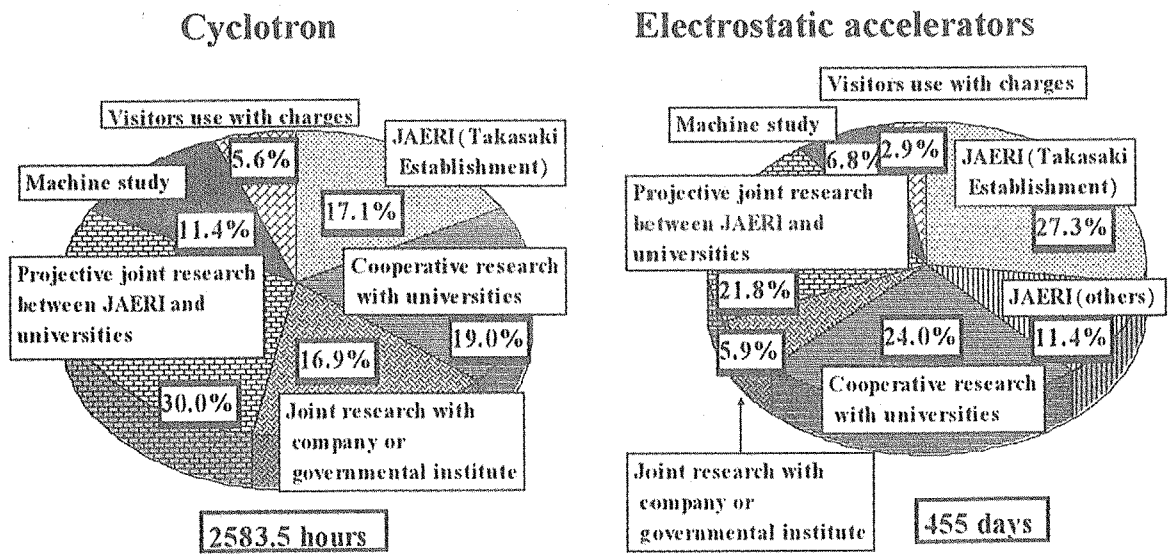

Fig. 3 Utilization of the accelerator in FY2002 in relation to the various types of users.

10.2 Operation of JAERI AVF Cyclotron System

Y. Nakamura*, T. Nara*, T. Agematsu*, I. Ishibori*, S. Kurashima*, M. Fukuda*, S. Okumura*, N. Miyawaki*, K. Yoshida*, S. Tajima*, K. Akaiwa**, To. Yoshida**, S. Ishiro**, A. Matsumura**, Y. Arakawa**, Tu. Yoshida**, S. Kanou**, A. Ihara** and K. Takano**

Advanced Radiation Technology Center, JAERI*
Beam Operation Service, Co., Ltd.**

The JAERI AVF cyclotron system was smoothly operated according to an allotted beam time. The total operation time in JFY 2002 amounted to the longest time so far, 3433 hours.

The utilization time of the ion species delivered for various experiments for the past 12 years is shown in Fig. 1. The ratios of operation time used for experiments including visitor's use with charge, machine tuning, beam development and machine study to total operation time were 67.8%, 23.3% and 8.9%, respectively.

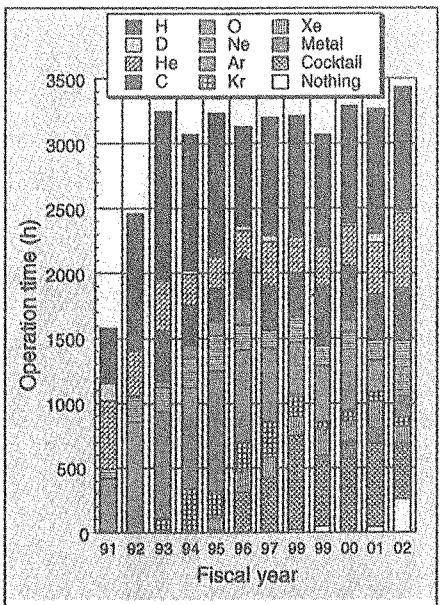

Fig. 1 Utilization time of ion species delivered for experiment.

Figure 2 shows the percentage beam time of accelerated ions. The percentage of heavy ions and cocktail ones occupied 64.0 %, while that of light ions was 28.4 %.

Regular yearly overhaul including the installation of a new gradient corrector was continued for five weeks in summer, 2002.

Several serious troubles are as follows: 1) plural small auxiliary power supplies in the power supply boxes were out of order, 2) the beam intensity of 320 MeV $^{12}C^{6+}$ in the cyclotron extremely reduced by an air leakage from the bellows of the Faraday cup positioned just before the cyclotron, 3) a worse vacuum condition in the cyclotron was not improved after the periodical maintenance in last summer, 4) an RF main vacuum tube (EIMAC, 4CW50000E) was broken, 5) a sequencer (C500H) for the evacuation system was in a bad condition during the intense beam irradiation of 100 MeV $^{4}He^{2+}$.

The intensities and extraction efficiencies for three kinds of proton beam were improved. Furthermore, a metallic ion of 320 MeV $^{102}Ru^{18+}$ was developed newly.

The frequencies of the change of harmonic number, particle species, beam energy and course are shown in Fig. 3. Especially, the frequency of the beam course change amounted to more than 290 times during JFY 2002. The frequencies of these changes increase gradually year by year.

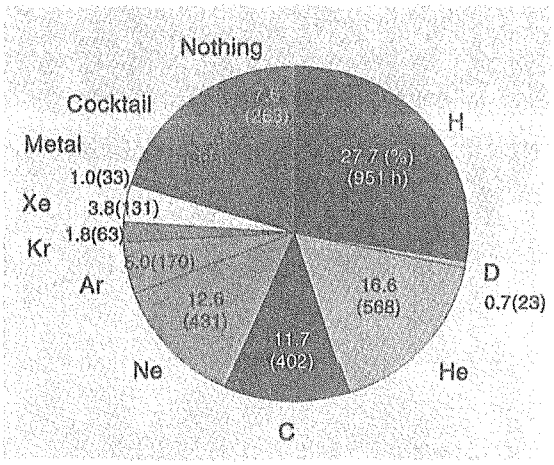

Fig. 2 Percentage beam time of accelerated ions in JFY 2002.

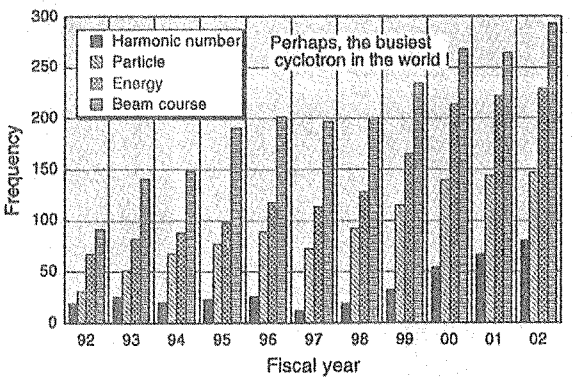

Fig. 3 Frequencies of the change of the harmonic number, the particle species, the beam energy and the beam course since 1992.

10.3 Operation of the Electrostatic Accelerators

I. Takada*, K.Mizuhashi*, S. Uno*, K. Ohkoshi*, A.Chiba*,
Y. Saitoh*, Y. Ishii*, T. Kamiya *, T. Sakai*, M.Ishii**, T.0rimo**,
T.Takayama**, M.Kouka**, A.Ohmae**, T.Kitano** and S.Kanai**

Advanced Radiation Technology Center, JAERI *
Beam Operation Service, Co., Ltd. **

1. Operation

The three electrostatic accelerators were operated smoothly for various experiments in FY 2002. The total operation time for each accelerator in this fiscal year was 2,066 hours for the tandem accelerator, 2,475 hours for the single-ended accelerator and 1,839 hours for the 400kV ion implanter, respectively. Monthly and yearly operation time for each accelerator are shown in Fig.1 and Fig.2.

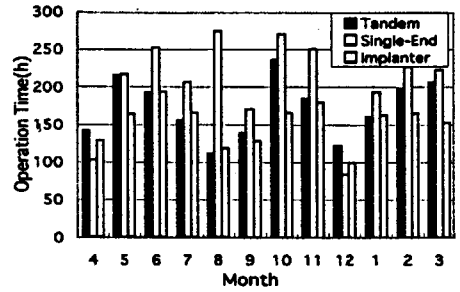

Fig. 1 Monthly operation time for each accelerator in FY 2002.

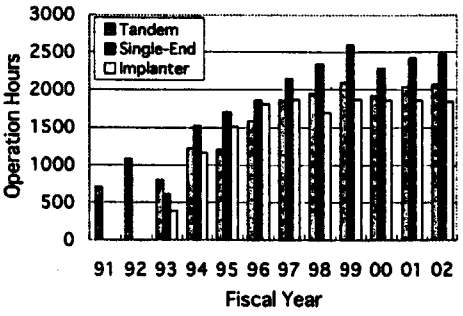

Fig. 2 Yearly operation time for each accelerator since 1991

2. Maintenance

The maintenance for the accelerators was carried out in April, August and December. During these terms several improvement and renewals were performed as follows;

For the tandem accelerator; 1) a inverter -based pellet-chain speed controller was installed on the chain-motor circuit for suppressing the occurrence of dust from sheaves and pulleys. 2) a examination and adjustment of high-voltage generating system which consists of Generating-volt meter (GVM), Capacitive pick off(CPO), Terminal-potential stabilizer(TPS), Corona-Probe and the chain were carried out in August. The voltage stability of accelerator was improved from 5×10^{-4}p-p to1.5×10^{-4}p-p.

For the single-ended accelerator; 3) a steerer of SA-line was moved from the front of SA-1Mg to the back of the MD-2 chamber. 4)The maintenance of the 10kV constant- voltage power supply which was not repaired for the past about eight years was carried out in August.

For the 400kV ion implanter ; 5) a chamber for measurement of accurate beam current of the fullerene ion was installed at the back of BMI-1. 6)the control method for the sifter and prism on IX-line was improved so that it could adjust the parameter of the devices at the control room.

3. Development

we succeeded in the generation and acceleration of MeV cluster ions Ag with the tandem accelerator. We made generating test of the multiple-charged metallic ions by a MINI-ECR ion source with the SF_6 plasma method, and succeeded in the generation of Ta^{+5} beam of 1.2μeA and Nb^{+3} beam of 1.2μeA. We succeeded in the generation up to Ar^{+11} ions with a NEW MINI-ECR from 10MHz to 13MHz. Beam current of $Ar^{+11}$was 0.087μeA.

In order to prevent the damages by spark for the high-voltage measuring resistors of the single-ended accelerator, we continued the endurance test about an improved non-inductive type resistor , and we confirmed a good durability for the high-voltage sparks. In order to develop the stabilization technique of the beam current, we accumulated the attenuation characteristic data about an improved wire system in this years.

10.4 Radiation Control & Radioactive Waste Management in TIARA

Safety Division & Utilities and Maintenance Division
Department of Administrative Services, JAERI

1. Radiation Control

1.1 Individual monitoring

(1) Individual monitoring for the radiation workers

Table 1 shows a distribution on effective dose of the radiation workers in FY 2002. The effective dose values of almost workers were less than 0.1 mSv (minimum detectable dose).

Maximum dose was 0.8 mSv/y due to the overhauling of the cyclotron.

(2) Individual monitoring for the visitors and others

Table 2 shows number of persons who have been temporally entered the radiation controlled areas. The effective dose of all persons was less than 0.1 mSv.

Table1. Distributions on the effective dose in FY 2002.

Items \ Periods	Persons	Number of persons: 1st quarter	2nd quarter	3rd quarter	4th quarter
Distribution range on effective dose HE:Effective dose *1 (mSv)	HE < 0.1	535	563	560	585
	0.1 ≦ HE ≦ 1.0	8	19	3	11
	1.0 < HE ≦ 5.0	0	0	0	0
	5.0 < HE ≦ 50.0	0	0	0	0
	50.0 < HE	0	0	0	0
Persons for radiation control(A)		543	582	563	596
Exposure above 1mSv	Persons(B)	0	0	0	0
	(B)/(A) ×100(%)	0	0	0	0
Mass effective dose (Persons·mSv)		0.9	4.3	0.4	1.5
Mean dose (mSv)		0.00	0.01	0.00	0.00
Maximum dose (mSv)		0.2	0.7	0.2	0.2

*1 Not detected according to internal exposure.

Table 2. Number of temporary entrance persons to radiation controlled areas in FY 2002.

Persons / Periods / Temporary entrance persons	Number of persons				
	1st quarter	2nd quarter	3rd quarter	4th quarter	Total
	342	487	454	536	1819

1.2 Monitoring of radioactive gases

Table 3 shows the maximum radioactive concentrations and total activities for radioactive gases released from TIARA's stack, during each quarter of FY 2002.

The least amount of ^{41}Ar, ^{11}C, ^{13}N, ^{18}F and ^{133}Xe were detected for some time during operation of the cyclotron, but the pulverized substance (^{65}Zn, etc) were not detected.

Table 3. Monitoring results of released gaseous radioactivity in FY 2002.

Nuclide	Items / Periods	1st quarter	2nd quarter	3rd quarter	4th quarter	Total
^{41}Ar	Maximum concentration (Bq/cm^3)	$<5.4 \times 10^{-5}$	$<1.4 \times 10^{-4}$	$<1.4 \times 10^{-4}$	$<1.4 \times 10^{-4}$	$<1.4 \times 10^{-4}$
	Activity (Bq)	2.3×10^{7}	9.6×10^{5}	3.9×10^{8}	3.1×10^{8}	7.2×10^{8}
^{11}C	Maximum concentration (Bq/cm^3)	$<5.4 \times 10^{-5}$	$<1.4 \times 10^{-4}$	$<1.4 \times 10^{-4}$	$<1.4 \times 10^{-4}$	$<1.4 \times 10^{-4}$
	Activity (Bq)	7.5×10^{7}	1.4×10^{8}	8.9×10^{6}	1.3×10^{8}	3.5×10^{8}
^{13}N	Maximum concentration (Bq/cm^3)	$<5.4 \times 10^{-5}$	———	$<1.4 \times 10^{-4}$	———	$<1.4 \times 10^{-4}$
	Activity (Bq)	5.0×10^{8}	———	1.0×10^{8}	———	6.0×10^{8}
^{18}F	Maximum concentration (Bq/cm^3)	$<5.4 \times 10^{-5}$	———	———	———	$<5.4 \times 10^{-5}$
	Activity (Bq)	8.7×10^{6}	———	———	———	8.7×10^{6}
^{133}Xe	Maximum concentration (Bq/cm^3)	———	$<5.4 \times 10^{-5}$	———	$<1.4 \times 10^{-4}$	$<1.4 \times 10^{-4}$
	Activity (Bq)	———	1.1×10^{7}	———	1.9×10^{6}	1.3×10^{7}
^{65}Zn	Maximum concentration (Bq/cm^3)	$<6.6 \times 10^{-10}$	$<4.7 \times 10^{-10}$	$<4.2 \times 10^{-10}$	$<4.1 \times 10^{-10}$	$<6.6 \times 10^{-10}$
	Activity (Bq)	0	0	0	0	0

1.3 Monitoring for external radiation and surface contamination

External radiation monitoring was routinely carried out in/around the radiation controlled areas and surface contamination monitoring was also carried out. Neither unusual value of dose equivalent rate nor surface contamination were detected.

Figure 1 displays a typical example of distribution of the dose equivalent rate at the radiation controlled area in the cyclotron building.

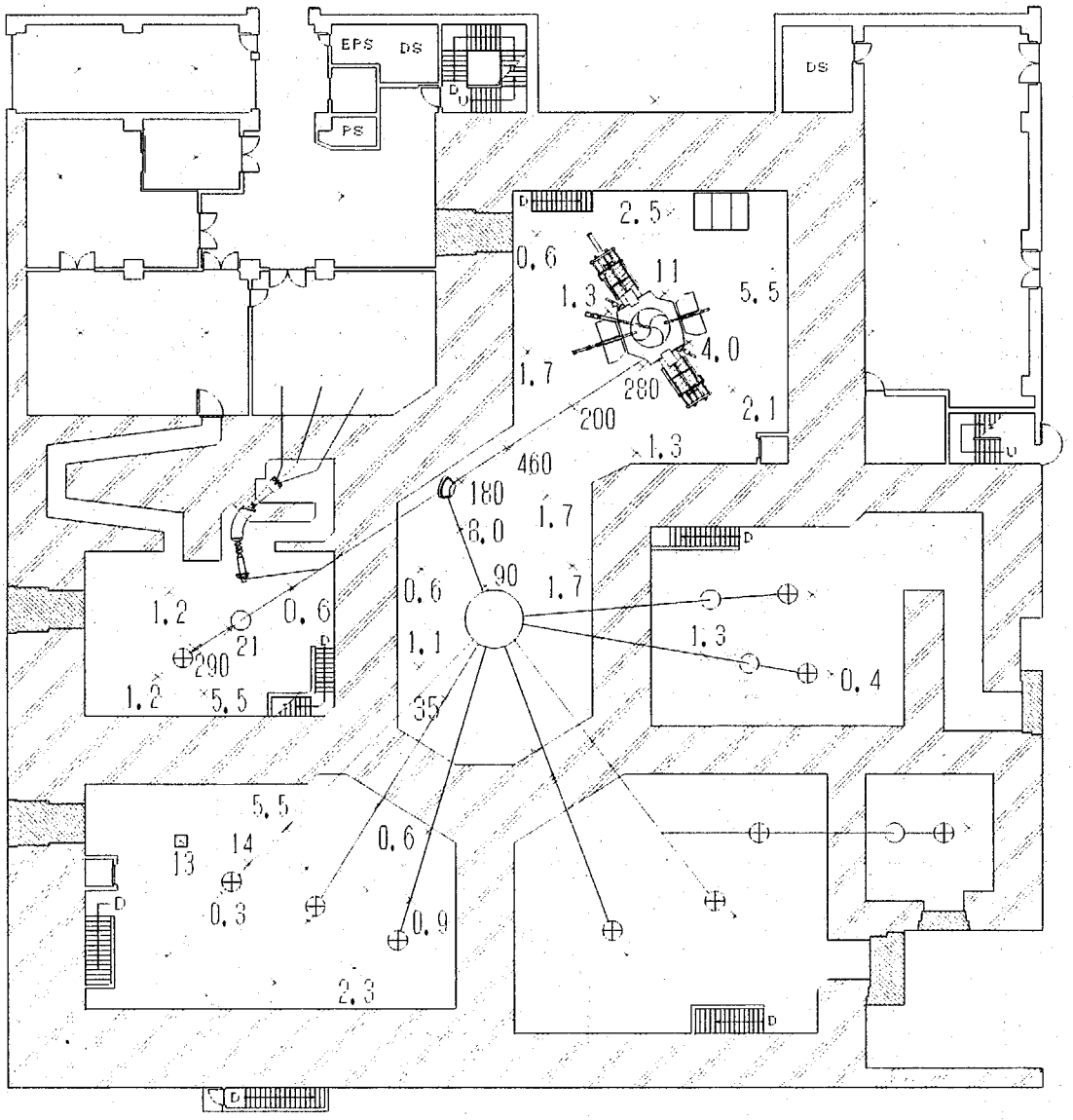

Fig.1 Dose rate distribution at the radiation controlled area in the cyclotron building.
Date measured : March 26, 2003
Measuring position : Indicated with × above 1m from floor
Unit : μSv/h(the dose rates less than 0.2μSv/h are not indicated)

2. Radioactive Waste Management

2.1 Solid wastes

Table 4 shows the amounts of solid wastes at various properties and kinds generated in each quarter of FY 2002. All wastes were combustible matter such as rubber gloves, compressible matter such as thin metals, and incompressible matter such as contaminated components. Compressible wastes were generated mainly by the cyclotron maintenance.

2.2 Liquid wastes

Liquid waste was almost waste water ("inorganic" in Table 5) generated with chemical experiments and operation of air conditioning units installed in each room of the first class radiation controlled area. Larger quantities of the wastewater in summer season (2nd quarter) are mainly due to condensed water, which is treated by evaporation, and condensed water is reused in the controlled area. Only small amounts of residue are generated by the evaporation because the waste quality is very pure.

The evaporation residue and sludge are solidified by cement in a stainless steel drum. The residue and sludge of ca.100 liter makes cement solidify of 200-liter drum.

Table 4. Radioactive solid wastes generated in FY 2002.

Amounts / Items	Amounts of generation in each periods (m^3)					Number of package /drum
	1st quarter	2nd quarter	3rd quarter	4th quarter	Total	
Category A*	0.32	0.32	0.44	2.75	3.83	
1)Combustible	0.24	0.28	0.40	0.48	1.40	9**
2)Incombustible	0.08	0.04	0.04	2.27	2.43	0
Compressible	0.08	0.04	0.04	0.16	0.32	2**
Filters	0	0	0	1.91	1.91	0
Incompressible	0	0	0	0.20	0.20	1**
Ion exchange resin	0	0	0	0	0	0
(Cement solidify)	0	0	0	0	0	0
Category B*	0	0	0	0	0	
1)Incombustible	0	0	0	0	0	0

* defined by dose at the outer surface of container : (A) $<$ 2 mSv/h $\leqq$ (B)

** 200-liter drum

Table 5. Radioactive liquid waste generated in FY 2002.

Amounts / Items	Amounts of generation in each periods (m^3)					Number of package /drum
	1st quarter	2nd quarter	3rd quarter	4th quarter	Total	
Category A*	13.31	15.94	5.33	6.84	41.42	
1)Inorganic	13.31	15.94	5.03	6.84	41.12	treatment
2)Organic	0	0	0	0	0	0
Organic	0	0	0	0	0	0
Oil	0	0	0	0	0	0
3)Sludge	0	0	0	0.10	0.10	1
Category B*	0	0	0	0	0	0
1)Inorganic	0	0	0	0	0	0
2)Organic	0	0	0	0	0	0
Organic	0	0	0	0	0	0
Oil	0	0	0	0	0	0
3)Sludge	0	0	0	0	0	0
Evaporation residue	0	0	0.20	0	0.20	2

* defined by concentrations in $Bq/cm^3(\beta,\gamma)$: (A) $<$ 3.7×10 $\leqq$ (B) $<$ 3.7×10^4

This is a blank page.

Appendix

This is a blank page.

Appendix 1. List of Publication

A. 1.1 Publications in Journal

12J01
S. Kawakita, M. Imaizumi, S. Matsuda,
M. Yamaguchi, K. Kushiya, T. Ohshima,
H. Itoh
Annealing Enhancement Effect by Light Illumination on Proton Irradiated $Cu(In,Ga)Se_2$ Thin-film Solar Cells
Jpn. J. Appl. Phys., 41 (2002), p.797
C T I SCS 21003

12J02
T. Sumita, M. Imaizumi, S. Matsuda,
T. Ohshima, A. Ohi, H. Itoh
Proton radiation analysis of multi-junction space solar cells
Nucl. Instrum. Methods Phys. Res. B, 206(2003) 448
C T I SCS 21003

12J03
K. K. Lee, T. Ohshima, H. Itoh,
Performance of Gamma Irradiated p-Channel 6H-SiC MOSFETs: High Total Dose ,
IEEE Trans. Nucl. Sci. 50 (2003) pp.194-200.
I SCS 22004

12J04
T. Ohshima, K. K. Lee, S. Onoda, T. Kamiya,
M. Oikawa, J. S. Laird, T. Hirao
and H. Itoh,
Observation of Transient Current Induced in Silicon Carbide Diodes by Ion Irradiation
Nucl. Instrum. Methord Phs. Res. B 206 (2003) pp.979-983.
T I SCS 22004

12J05
T. Ohshima, K. K. Lee, S. Onoda, T. Kamiya,
M. Oikawa, J. S. Laird, T. Hirao and H. Itoh,
Evaluation of the Characteristics of Silicon Carbide Diodes Using Transient-IBIC Technique
Nucl. Instrum. Methods Phys. Res. B, in press.
T I SCS 22004

12J06
T. Ohshima, A. Uedono, O. Eryu, K. K. Lee,
K. Abe, H. Itoh, and K. Nakashima,
Annealing of Vacancy-Type Defect and Diffusion of Implanted Boron in 6H-SiC ,
Matrial Sci. Forum *in press*
I SCS 22004

12J07
H. Mori, T. Hirao, J. S. Laird, S. Onoda,
T. Wakasa, T. Yamakawa, H. Itoh,
T. Okamoto, Y. Koizumi
Modering of transient charge collection induced by an angled single ion strike
Nucl. Instrum. Methods Phys. Res. B, 206 (2003) 31-35
T SCS 2200 1

12J08
J. S. Laird, T. Hirao, S. Onoda, H. Mori and H. Itoh,
Temperature dependence of heavy ion-induced current transients in Si epilayer devices,
IEEE Trans. Nucl. Sci. Vol. 49, No. 3, 1389-1395 (2002)
T SCS 22002

12J09
T. Hirao, H. Mori, J. S. Laird, S. Onoda,
H. Abe, T. Wakasa, H. Ito
Study of single-event current pulses induced in SOI diodes by collimated swift heavy -ions micro-beam,
Nucl. Instrum. Methods Phys. Res. B,206 (2003) 457
C SCS 21001

12J10
H.-S. Lee, H. Okada, A. Wakahara,
A. Yoshida, T. Ohshima, H. Itoh, S. Kawakita, M. Imaizumi and S. Matsuda,
Effect of Proton Irradiation on Electrical Properties of CuInSe2 Thin Films,
Solar Energy Materials and Solar Cells 75 (2003) pp.57-63.
I SCS 22005

12J11
Y. Nakanishi, A. Wakahara, H. Okada,
A. Yoshida, T. Ohshima and H. Itoh,
Effect of alloy composition on photoluminescence properties of europium implanted AlGaInN ,
Phys. Stat. Sol. (c) 0, No. 1, 461-464 (2002).
I SCS 22005

12J12
Y. Nakanishi, A. Wakahara, H. Okada,
A. Yoshida, T. Ohshima, H. Itoh, S. Nakao,
K. Saito and Y. T. Kim,
Effects of implantation conditions on the luminescence properties of Eu-doped GaN ,
Nucl. Instrum. Methods Phys. Res. B, 203C, (2003).1033-1036
I SCS 22005

12J13
Y. Nakanishi, A. Wakahara, H. Okada,
A. Yoshida, T. Ohshima and H.Itoh,
Effect of 3MeV electron irradiation on photoluminescence properties of Eu-doped GaN,
Appl. Phys. Lett. 81, 1943-1945 (2002)
I SCS 22005

12J14
Y. Yokota, Y. Hase, N. Shikazono, A. Tanaka and M. Inoue,
LET dependence of lethality of carbon ion irradiation to single tobacco cells,
Int. J. Radiat. Biol. in press.
C BIT 21007

12J15
Y. Nomura, M. Hatashita and M. Inoue
(2002) Production of self-compatible common buckwheat by ion exposure,
FAGOPYRUM, 19, 43-48

C BIT 21007

12J16
Y. Hase, M. Yamaguchi, M. Inoue and A. Tanaka
(2002) Reduction of survival and induction of chromosome aberrations in tobacco irradiated by carbon ions with different linear energy transfers,
Int. J. Radiat. Biol. 78, 799-806.
C BIT 21007

12J17
S. Kitamura, M. Inoue, N. Ohmido, K. Fukui and A. Tanaka
Chromosomal rearrangements in interspecific hybrids between Nicotiana gossei Domin and N. tabacum L., obtained by crossing with pollen exposed to helium ion beams or gamma-rays,
Nucl. Instrum. Methods Phys. Res. B,206, (2003) 548-552.
C BIT 21007

12J18
T. Morishita, H. Yamaguchi, K. Degi,
N. Shikazono, Y. Hase, A. Tanaka and T. Abe
Dose response and mutation induction by ion beam irradiation in buckwheat
Nucl. Instrum. Methods Phys. Res. B, (2003) 206:565-569
C BIT 21011

12J19
M. Okamura et al.:
Wide variety of flower-color and -shape mutants regenerated from leaf cultures irradiated with ion beams,
Nucl. Instrum. Methods Phys. Res. B, 206: 561-564 (2003)
C BIT 21012

12J20
M. Okamura :
Commercialization of 'Ion-beam Breeding' in carnation,
Radiation and Industries, 95 : 57-63 (2002)
C BIT 21012

12J21
S. Nagayoshi,
Irradiation Breeding in KAGOSHIMA; Breeding of 'few axillary bud lines' using ion beam in Chrysanthemum.
Radiation & Industries (2003) 98: 10-16.
C BIT 21013

12J22
K. Ishii, Y. Yamada, Y.Hase, N.Shikazono and A.Tanaka,
RAPD Analysis of Xanta and Waxy Mutants Induced by Ion Beam Irradiation to Hinoki Cypress (Chamaecyparis obtusa),
TIARA Annual Report 2001, November 2002, 47-48
C BIT 21014

12J23
H. Morikawa, M.Takahashi and G. Arimura.
Manipulation of genes for nitrogen metabolism in plants.
In Air Pollution and Biotechnology in

Plants .Ed. by K. Oomasa et al., Springer-Verlag, pp. 383-401 (2002)
C BIT 21018

12J24
T. Yoneyama, H.Y. Kim, H.Morikawa and H. S. Srivastava.
Metabolism and detoxification of nitrogen dioxide and ammonia in plants.
In Air Pollution and Biotechnology in Plants Ed. by K. Oomasa et al., Springer-Verlag, pp. 221-234 (2002)
C BIT 21018

12J25
Y. Kawamura, K. Fukunaga, A. Umehara, M. Takahashi and H. Morikawa.
Selection of Rhododendron mucronatum plants that have a high capacity for nitrogen dioxide uptake.
Acta Biotechnologica, 22:113-120 (2002).
C BIT 21018

12J26
H. Morikawa, M. Takahashi and Y. Kawamura.
Metabolism of nitrogen dioxide in plants-Assimilation, dissimilation and novel metabolites.
Physiology and Molecular Biology of Plants. 8(1) 19-29 (2002)
C BIT 21018

12J27
A. Sakamoto, , M. Ueda, & H. Morikawa,
Arabidopsis glutathione-dependent formaldehyde dehydrogenase is an S-nitrosoglutathione reductase.
FEBS Lett. 515: 20-24 (2002)
C BIT 21018

12J28
K. Kondo, M. Takahashi and H. Morikawa.
Regeneration and transformation of a roadside tree *Pittosporum tobira* A.
Plant Biotechnol., 19 135-139 (2002)
C BIT 21018

12J29
H. Morikawa, A. Sakamoto, M. Takahashi and H. Hokazono.
Mechanism of the integration of transgenes into the host genome introduced by particle bombardment.
Plant Biotechnol., 19: 219-228 (2002)
C BIT 21018

12J30
H. Morikawa, M. Takahashi and Y. Kawamura
Air Pollution Clean Up Using Pollutant-Philic Plants- Metabolism of nitrogen dioxide and genetic manipulation of related genes.
In Phytoremediation: Transformation and Control of Contaminants , ed by S. C. McCutcheon and J.L. Schnoor, John Wiley and Sons, Inc. (2003, in press)
C BIT 21018

12J31
M. Takahashi, K. Kondo, H. Morikawa.

Assimilation of Nitrogen Dioxide in Selected Plant Taxa. Acta Biotechnol., (2003, in press)
C BIT 21018

12J32
M. Hakata, M. Takahashi, W. Zumft, A. Sakamoto, H. Morikawa.
Conversion of the Nitrogen of Nitrate and Nitrogen Dioxide to Nitrous Oxide in Plants.
Acta Biotechnol., (2003, in press)
C BIT 21018

12J33
O. C. Erkin, M. Takahashi, A. Sakamoto and H. Morikawa
Development of a regeneration and transformation system for *Raphiolepis umbellata* L., "Sharinbai" plants by using particle bombardment.
Plant Biotecchnology, 20: 145-152 (2003)
C BIT 21018

12J34
A. Sakamoto, S. Tsukamoto, H. Yamamoto, M. Ueda–Hashimoto, M. Takahashi, H. Suzuki and H. Morikawa.
Functional complementation in yeast reveals a protective role of chloroplast 2-Cys peroxiredoxin against reactive nitrogen species.
Plant Journal, 33: 841-851 (2003)
C BIT 21018

12J35
M. Takahashi, S. Kohama, K. Kondo, M. Hakata, Y. Hase, N. Shikazono, A. Tanaka, and H. Morikawa.
Regeneration of variegated plants from ion-beam irradiated explants of *Ficus stipulata* Thunb..
TIARA Annual Report 2002
C BIT 21018

12J36
M. Maekawa, Y. Hase, N. Shikazono and A. Tanaka,
Induction of somatic instability in stable yellow leaf mutant of rice by ion beam irradiation.
Nucl. Instrum. Methods Phys. Res. B,206: 579-585. 2003.
C BIT 21021

12J37
T.Sato,
Breeding of Chrysanthemum.
Annual of Akita prefecture Agricultural experiment station (2002) in press.
C BIT 21022

12J38
Y. Kobayashi, T. Funayama, S. Wada, M. Taguchi, H. Watanabe,
Irradiation of single mammalian cells with a precise number of energetic heavy ions - Applications of microbeams for studying cellular radiation response -,
Nucl. Instr. Meth. B, (in press)
C BIT 21027

12J39
S. Wada, Y. Kobayashi, T. Funayama,

M. Natsuhori, N. Ito and K. Yamamoto,
Detection of DNA damage in individual cells induced by heavy ion irradiation with an non-denaturing comet assay,
J. Radiat. Res. 43 (2002) S153-S156.
C BIT 21027

12J40
Y. Furusawa, C. Shao, Y. Kobayashi,
T. Funayama, S. Wada,
Bystander effect induced by counted high-LET particles in confluent human fibroblasts: a mechanistic study,
FASEB J. (in press)
C BIT 21027

12J41
T. Funayama, S. Wada, Y. Kobayashi,
Analysis of Radiation Response of Individual Cell Using Heavy Ion Microbeam in JAERI-Takasaki,
J. Radiat. Res. 43 (2002) 420.
C BIT 21027

12J42
Y. Kobayashi, T. Funayama, S. Wada,
M. Taguchi,
Improving of Irradiation Efficiency of JAERI-Takasaki Heavy Ion Microbeam Cell Irradiation System,
J. Radiat. Res. 43 (2002) 430.
C BIT 21027

12J43
T. Funayama, S. Wada, Y. Kobayashi,
The Effect of Heavy Ion Microbeam Irradiation on Cellular Response of Mammalian Cultured Cells,
J. Radiat. Res. 43 (2002) 430.
C BIT 21027

12J44
S. Wada, T. Funayama, Y. Kobayashi,
M. Natsuhori, N. Ito,
The Effect of Track Structure on the Irradiation of DNA Damage and cell Killing,
J. Radiat. Res. 43 (2002) 454.
C BIT 21027

12J45
Y. Furusawa, C. Shao, M. Aoki, Y. Kobayashi,
T. Funayama, S. Wada,
Radiation Induced Bystander Effect by Gap Junction Channels in Human Fibroblast Cells,
J. Radiat. Res. 43 (2002) 473
C BIT 21027

12J46
E. Ling, K. Fukamoto, S. Xu, K. Shirai,
R. Kanekatsu, Y. Kobayashi, Z.-L. Tu,
T. Funayama, H. Watanabe and K. Kiguchi
(2003) Regeneration of hemopoietic organs in the silkworm, Bombyx mori, after locally targeted irradiation with heavy ion beams,
J. Insect Biotechnol. Sericol., 72(2), 95-100
C BIT 21028

12J47
E. Ling, K. Shirai, R.Kanekatsu,
Y. Kobayashi, Z.-L. Tu, T. Funayama,
H. Watanabe and K. Kiguchi

(2003) Why dose hemocyte density rise during the wandering stage of the silkworm, Bombyx mori,
J. Insect Biotechnol. Sericol., 72(2), 101-109
C BIT 21028

12J48
Y. Furusawa, M. Aoki, M. Durante,
Simultaneous exposure of mammalian cells to heavy ions and X-rays,
Adv. Space Res. 30, 877-884, 2002
O BIT 21029

12J49
S. Suzuki, Y. Miura, S. Mizuno, Y. Furusawa,
Models for mixed irradiation with a 'Reciprocal-Time' pattern of the repair function,
J. Radiat. Res. 43, 257-267, 2002.
O BIT 21029

12J50
C. Shao, Y. Furusawa, M. Aoki,
H. Matsumoto, K. Ando,
Nitric oxide-mediated bifunctional bystander effect induced by heavy-Ion Radiation in human salivary grand neoplastic cells,
J. Radiat. Res. 43s, s107-s111, 2002.
C BIT 21029

12J51
C. Shao, Y. Furusawa, M. Aoki,
Sper/NO-induced reversible proliferation inhibition and cycle arrests associated with a micronucleus induction in HSG cells,
Nitric Oxide 8, 83-88, 2003
O BIT 21029

12J52
Y. Furusawa, C. Shao, Y. Kobayashi,
T. Funayama, S. Wada,
Bystander effect induced by counted high-LET particles in confluent human fibroblasts: a mechanistic study,
FASEB J. (in press)
C BIT 21029

12J53
S. Wada, Y. Kobayashi, T. Funayama,
M. Natsuhori, N. Ito and K. Yamamoto.
Detection of DNA Damage in the Individual Cells induced by Heavy Ion Irradiation with Comet assay.
2002. Journal Radiation Research.43 Suppl. S153-156.
C BIT 21030

12J54
S. Matsuhashi, H. Uchida and T. Kume,
Positron Imaging for Plant Study Using Positron Emitting Tracer Imaging System (PETIS) and Imaging Plate (IP),
Radioisotopes, 49, 558-570 (2000).
C BIT 2103 4

12J55
S. Matsuhashi and T. Kume,
Development of Positron Imaging Method for Plant Study,
Radiat. Chemi, 70, 20-25 (2000).
C BIT 2103 4

12J56
H. Fujikake, A. Yamazaki, N. Ohtake,
K. Sueyoshi, S. Matsuhashi, T. Ito,
C. Mizuniwa, T. Kume, S. Hashimoto,
N. S. Ishioka, S. Watanabe, A. Osa, T. Sekine,
H. Uchida, A. Tsuji and T. Ohyama,
Quick and reversible inhibition of soybean root nodule growth by nitrate involves a decrease in sucrose supply to nodules.,
J. Exp. Bot., 54,1399～1388, 2003
C BIT 21035

12J57
H. Nakanishi, S. Kiyomiya, T. Tsukamoto,
H. Tsukada, H. Uchida, S. Mori,
Water ($H_2{}^{15}O$) flow in rice is regulated by the concentration of nutrient as monitored by positron multi-probe system (PMPS).
Soil Sci. Plant Nutr., 48: 759-762 (2002)
C BIT 21036

12J58
S. Takahashi, T. Nakagawa , M. Yoshida and M. Asano,
Role of a bulky hydrophobic pendant in a hydrophilic copolymer and the effect of heavy ion irradiation on this copolymer
J. Membr. Sci., 206, 165-177(2002)
C RCO 21041

12J59
J. Li, Y. Maekaw, T. Yamaki and M. Yoshida
Chemical Modification of a Poly(ethylene terephthalate) Surface by Selective Alkylation of Acid Salts.
Macromol. Chem Phys., 203 , 2470-2474 (2002)
C RCO 21042

12J60
Y. Suzuki, Y. Maekaw, M. Yoshida,
K. Maeyama and N. Yonezawa
Ion Beam Induced Dual Tone Imaging of Polyimide via Two Step Imidization
Chem. Moten., 4186-4191 (2002)
C RCO 21042

12J61
Y. Maekawa, Y. Suzuki, M. Yoshida,
K. Maeyama and N. Yonezawa
Ion Beam-Induced Positive Imaging of Polyimide via Two Step Imidization
Polymer., 44, 2307-23 12 (2003)
C RCO 21042

12J62
H. Koizumi, T. Ichikawa, M. Taguchi,
Y. Kobayashi, H. Namba,
Chemical effects of heavy ion beams on organic materials
Nucl. Instrum. Methods Phys. Res. B, 206, (2003).1124-1127
C RCO 21044

12J63
H. Koizumi, M. Taguchi, Y. Kobayashi,
T. Ichikawa,
Crosslinking of polymers in heavy ion tracks
Nucl. Instrum. Methods Phys. Res. B, 208 (2003) 161-165.
C RCO 21044

12J64
S. Seki, Y. Matsui, S. Tagawa, H. Tsuji,
A. Toshimitsu, K. Tamao
Transient absorption spectroscopy of radical ions of rigid anti- and syn-tetrasilane
Chem. Phys. Lett., in press.
C RCO 21046

12J65
M. Tashiro, C. Y. Tseng, S. Seki, Y. Honda,
S. Tagawa
Influence of Radiation-induced Species on Positronium Formation in Poly(methylmethacrylate) at Low Temperature
Radiat. Phys. Chem., in press.
C RCO 21046

12J66
S. Seki, Y. Terashima, K. Kunimi,
T. Kawamori, M. Tashiro, Y. Honda,
S. Tagawa
The Effects of Free Volumes on Charge Carrier Transport in Polysilanes Probed by Positron Anihilation
Radiat. Phys. Chem., in press.
C RCO 21046

12J67
S. Tsukuda, S. Seki, S. Tagawa, M. Sugimoto,
A. Idesaki, S. Tanaka
Cross-linked Polymer Nanowires with Controlled Shape and Orientation by High Energy Single Ion Hitting
J. Photopolym. Sci. Technol., 16 (2003) 433-434..
C RCO 21046

12J68
T. Kawaguchi, S. Seki, K. Okamoto, A. Saeki,
Y. Yoshida, S. Tagawa
Pulse Radiolysis Study of Radical Cations of Polysilanes
Chem. Phys. Lett., 374 (2003) 353-357.
C RCO 21046

12J69
Y. Terashima, S. Seki, M. Tashiro, Y. Honda,
S. Tagawa
Study of Nano-Space in Au-Polysilane Interfaces by Slow Positron Beam
J. Photopolym. Sci. Technol., 16 (2003) 445-446.
C RCO 21046

12J70
S. Seki, S. Tsukuda, Y. Yoshida, T. Kozawa,
S. Tagawa, M. Sugimoto, S. Tanaka
Nano-wire Formation and Selective Adhesion on Substrates by Single Ion Track Reaction in Polysilanes
Jpn. J. Appl. Phys., 43 (2003) 4159-4161.
C RCO 21046

12J71
Y. Matsui, K. Nishida, S. Seki, Y. Yoshida,
S. Tagawa, K. Yamada, H. Imahori, A. Sakata
A Direct Observation of Intra-molecular Electron Transfer from Excess Electrons in σ-conjugated Main Chain to Porphyrin Side Chain in Polysilanes Having Tetraphenylporphyrin Side Chain by Pulse

Radiolysis Technique
Organometallics, 21 (2002) 5144-5147.
C RCO 21046

12J72
S. Seki, Y. Matsui, Y. Yoshida, S. Tagawa, J. R. Koe, M. Fujiki
Dynamics of Charge Carriers on Poly[bis(p-alkylphenyl)silane]s by Electron Beam Pulse Radiolysis
J. Phys. Chem. B 106 (2002) 6849-6852
C RCO 21046

12J73
Y. Matsui S. Seki, and S. Tagawa
Direct Observation of Intra-molecular Energy Migration in s-conjugated Polymer by Femto-second Laser Flash Photolysis
Chem. Phys. Lett. 357 (2002) 346-350.
C RCO 21046

12J74
F. C. Grozema, L. D. A. Siebbeles, J. M. Warman, S. Seki, S. Tagawa, and U. Scherf
Hole Conduction along Molecular Wires: s-Bonded Silicon versus p-Bond-Conjugated Carbon
Adv. Mater. 14 (2002) 228-231.
C RCO 21046

12J75
S. Seki, S. Tsuji, Y. Matui, and S. Tagawa
Dynamics of Silylenes in Polysilylenes with Structural Defects by Excimer Laser Flash Photolysis
Chem. Lett. (2001) 1208-1209.
C RCO 21046

12J76
S. Seki, K. Maeda, S. Tagawa, H. Kudoh, M. Sugimoto, Y. Morita, and H. Shibata
Formation of Quantum Wires along Ion Projectiles in Si Backbone Polymers
Adv. Mater. 13 (2001) 1663-1665.
C RCO 21046

12J77
Y. Yoshida, Y. Mizutani, T. Kozawa, A. Saeki, S. Seki, S. Tagawa, and K. Ushida
Development of Laser-synchronized Picosecond Pulse Radiolysis System
Radiat. Phys. Chem. 60 (2001) 313-318.
C RCO 21046

12J78
K. Maeda, S. Seki, S. Tagawa, and H. Shibata
Radiation Effects on Branching Polysilanes
Radiat. Phys. Chem. 60 (2001) 461-466.
C RCO 21046

12J79
S. Seki, Y. Kunimi, K. Nishida, Y. Yoshida, and S. Tagawa
Electronic State of Radical Anions on Poly(methyl-n-propylsilane) Studied by Low Temperature Pulse Radiolysis
J. Phys. Chem. B 105 (2001) 900-904.
C RCO 21046

12J80
S. Seki, Y. Yoshida, and S. Tagawa

Charged Radicals of Polysilane Derivatives Studied by Pulse Radiolysis
Radiat. Phys. Chem. 60 (2001) 411-415.
C RCO 21046

12J81
S. Seki, Y. Kunimi, K. Nishida, K. Aramaki, and S. Tagawa
Optical Properties of Pyrrolyl-substituted Polysilanes
J. Organomet. Chem. 611 (2000) 62-68.
C RCO 21046

12J82
Y. Kunimi, S. Seki, M. Tashiro, and S. Tagawa
Free Volume in Poly(n-alkylphenylsilane) Probed by Positron Annihilation
J. Photopolym. Sci. Technol. 13 (2000) 723-726.
C RCO 21046

12J83
S. Seki, Y. Sakurai, K. Maeda, Y. Kunimi, and S. Tagawa
Studies on the Negative Resist Material Based on Polysilanes for EB and X-ray Lithography
Jpn. J. Appl. Phys. 39 (2000) 4225-4230.
C RCO 21046

12J84
S. Takahashi, M. Yoshida, M. Asano, M. Notomi and T. Nakagawa,
Characterizations of Heavy Ion Irradiated PET Membranes,
Nucl. Instrum. Methord Phys. Res. B, submitting.
C RCO 21053

12J85
S. Takahashi, M. Yoshida, M. Asano and T. Nakagawa,
Gas-Permeation Control by PET Membranes with Nanosized Pore,
Polymer J., submitting.
C RCO 21053

12J86
K. Hirata, Y. Saitoh, K. Narumi, and Y. Kobayashi,
Prevention of electric breakdown during ion bombardment of organic insulators using a cluster ion beam
Appl. Phys. Lett., 81, (2002).3669
T ACT 22019

12J87
H. Tanigawa, T. Hirose, M. Ando, E. Wakai, S. Jitsukawa, Y. Katoh, A. Kohyama,
Microstructural analysis of mechanically tested reduced-activation ferritic/martensitic steels,
J. Nucl. Mater., 307-311(2002)293-298.
C IOM 21006

12J88
T. Hirose, H. Tanigawa, M. Ando, S. Jitsukawa, A. Kohyama, Y. Katoh and M. Narui
Radiation Effects on Low Cycle Fatigue Properties of Reduced Activation

Ferritic/Martenisitc Steels,
J. Nucl. Mater., 307-311(2002)304.
C IOM 21006

12J89
E. Wakai, K. Furuya, M. Sato, K. Oka,
T. Tanaka, F. Takada, K. Kato, S. Ohnuki and S. Jistukawa
Shift of ductile-brittle transition temperature of F82H steel by helium and hydrogen-implantation,
J. Nucl. Mater., in press.
C IOM 21006

12J90
A.Hasegawa, S. Nogami, S. Miwa, K. Abe,
T. Taguchi, N. Igawa,
Study of Synergistic Effects of Displacement Damage, H and He on Mechanical Properties of Advanced SiC/SiC Composites Using Triple Ion-Beam Irradiation,
Fusion and Science Technology, in press
T I S IOM 22008

12J91
T. Taguchi, E. Wakai, N. Igawa, S. Nogami,
L. L. Snead, A. Hasegawa, S. Jitsukawa,
Effect of simultaneous ion irradiation on microstructural change of SiC/SiC composites at high temperature,
J. Nucl. Mater., 307-311 (2002) 1135-1140
T I S IOM 22008

12J92
S. Nogami, A. Hasegawa, T. Taguchi, K. Abe,
R. Yamada,
Surface morphology changes in a SiC/SiC composite as caused by simultaneous triple-ion-beam irradiation,
Mater. Trans., Vol.42 No.1 (2001) 171-175

T I S IOM 22008

12J93
I. Mukouda, Y. Shimomura, D. Yamaki,
T. Nakazawa, T. Aruga and S. Jitsukawa
Microstructure in vanadium irradiated by simultaneous multi-ion beam of hydrogen, helium and nickel ions
J. Nucl. Mater., 307-311 (2002) 412-415
T I S IOM 22009

12J94
Y. Nemoto, Y. Miwa, H. Tsuji and T. Tsukada
Evaluation of corrosion behavior of ion irradiated stainless steel using atomic force microscope
Journal of JSAEM (now printing)
T I IOM 22010

12J95
M. Ando, H. Tanigawa, S. Jitsukawa,
T. Sawai, Y. Katoh, A. Koyama,
K. Nakamura and H. Takeuchi,
Evaluation of hardening behavior of ion irradiated reduced activation ferritic/martensitic steels by an ultra-micro-indentation technique,
J. Nucl. Mater., 307-311(2002)260.
T S IOM 22011

12J96

T. Sawai, E. Wakai, S. T. Tomita, A. Naito and S. Jitsukawa,
Swelling behavior of TIG-welded F82H IEA heat,
J. Nucl. Mater., 307-311(2002)312.
T S IOM 22011

12J97
E. Wakai, T. Sawai, K. Furuya, A. Naito,
T. Aruga, K. Kikuchi,, S. Yamashita,
S. Ohnuki, S. Yamamoto, H. Naramoto and
S. Jistukawa,
Effect of triple ion beams in ferritic/martensitic steel on swelling behavior,
J. Nucl. Mater., 307-311(2002)278.
T S IOM 22011

12J98
E. Wakai, K. Kikuchi, S. Yamamoto,
T. Aruga, M. Ando, H. Tanigawa, T. Taguchi,
T. Sawai, K. Oka, S. Ohnuki,
Swelling behavior of F82H steel irradiated by triple/dual ion beams,
J. Nucl. Mater., 318(2003)267.
T S I IOM 22011

12J99
V. Lavrentiev, H. Abe, S. Yamamoto,
H. Naramoto, K. Narumi
Formation of promising Co-C nanocompositions.
Sur. Interface Anal. 35 (2003) 36-39
I IOM 22020

12J100
Y. Kasukabe, Z.L. Dizard, Y. Fujino, H. Tani,
M. Osaka, Y. Yamada, H. Abe
In-situ observation of formation process of titanium compound thin films due to ion implantation in a transmission electron microscope.
Nucl. Instrum. Methods Phys. Res. B, (2003) to be published
I IOM 22020

12J101
K. Niwase, H. Abe
Generation of nano-sized structure on Ni and Fe surfaces by electron irradiation.
Mater. Trans. 43 (2002) 646-649
I IOM 22020

12J102
V. Lavrentiev, H. Abe, S. Yamamoto,
H. Naramoto, K. Narumi
Formation of carbon nanotubes under conditions of Co+C60 film.
Physica B 323 (2002) 303-305
I IOM 22020

12J103
V. Lavrentiev, H. Abe, S. Yamamoto,
H. Naramoto, K. Narumi
Co and C60 interaction under conditions of mixture.
Mol. Cryst. Liq. Cryst. 386 (2002) 139-143
I IOM 22020

12J104
M. Ishino, O. Yoda, Y. Haishi, F. Arimoto,
M. Takeda, S. Watanabe, S. Ohnuki, H. Abe

Boundary structure of Mo/Si multilayers for soft X-ray mirrors
Jpn. J. Appl. Phys. 41 (2002) 3052-3056
I IOM 22020

12J105
H. Abe, S. Yamamoto, A. Miyashita
In-situ TEM observation of nucleation and growth of spherical graphitic clusters under ion implantation
J. Electron Micros. 51 (2002) s183
I IOM 22020

12J106
D. Huličová, K. Hosoi, S. Kuroda, H. Abe, A. Oya
Carbon nanotubes prepared from polymer microshperes by spinning and carbonizing
Mol. Cryst. Liq. Cryst. 387 (2002) 331-336
I IOM 22020

12J107
Y. Choi, S. Yamamoto, H. Abe, H. Itoh
Effect of annealing and quenching treatments on reconstruction of rutile thin films on sapphire substrates
Surf. Sci., 499 (2002) 203-209
I IOM 22020

12J108
D. Huličová, K. Hosoi, S. Kuroda, H. Abe, A. Oya
Carbon nanotubes prepared by spinning and carbonizing fine core/shell polymer microspheres
Advanced Materials 14 (2002) 452-455
I IOM 22020

12J109
H. Abe, S. Yamamoto, A. Miyashita, K. E. Sickafus
Formation mechanisms of carbon onions and nanocapsules in C+- ion implanted copper
J. Appl. Phys 90 (2001) 3353-3358
I IOM 22020

12J110
H. Abe
Nucleation of carbon onions and nanocapsules under ion implantation at high temperature
Diam. Relat. Mater. 10 (2001)1201-1204

I IOM 22020

12J111
Y. Kasukabe, Z. L. Dizard, Y. Fujino, H. Tani, M. Osaka, Y. Yamada and H. Abe
In-situ Observation of Formation Processes of Titanium Compound Thin Films due to Ion Implantation in A Transmission Electron Microscope
Nucl. Instrum. Methods Phys. Res. B, 206 (2003) 390-394.
I IOM 22023

12J112
S. Yamamoto, T. Yamaki, H. Naramoto and S. Tanaka
Characterization of metal-doped TiO2films by RBS/channeling
Nucl. Instrum. Methods Phys. Res. B, 206

(2003) 268-271.
S IOM 22024

12J113
Y. Choi, S. Yamamoto, H. Saitoh, T. Sumita and H. Itoh
Influence of carbon-ion irradiation and hydrogen-plasma treatment on photocatalytic properties of titanium dioxide films
Nucl. Instrum. Methods Phys. Res. B, 206 (2003) 241-244.
S IOM 22024

12J114
T. Sumita, T. Yamaki, S. Yamamoto and A. Miyashita
Ion beam modification of photo-induced charge separation in TiO2 films
Nucl. Instrum. Methods Phys. Res. B, 206 (2003) 245-248.
S IOM 22024

12J115
T. Yamaki, T. Umebayashi, T. Sumita, S. Yamamoto, M. Maekawa, A. Kawasuso and H. Itoh
Fluorine-doping in titanium dioxide by ion implantation technique
Nucl. Instrum. Methods Phys. Res. B, 206 (2003) 254-258.
S IOM 22024

12J116
T. Sumita, T. Yamaki, S. Yamamoto and A. Miyashita
Photo-induced surface charge separation in Cr-implanted TiO2 thin film
Thin Solid Films 416 (2002) 80-84.
S IOM 22024

12J117
T. Ohnuki, F. Sakamoto, N. Kozai, M. Samadfam, T. Kamiya, T. Sakai, T. Satoh, M. Oikawa :
Application of the micro-PIXE technique for analyzing Arsenic in Biomat and Lower Plants of Lichen and Mosses Around An Arsenic Mine Site, Gunma, Japan,
Nucl. Instrum. Methods Phys. Res. B, 190, 477-481(2002).
T C IOM 22027

12J118
H. Kudo, K. Takeda, T. Suguri, W. Iwazaki, C. Sakurai, I. Arano, S. Numazawa, S. Seki,
Electron loss from fast partially-stripped C and O ions incident on crystal targets,
Nucl. Instrum. Methods Phys. Res. B,207 (2003) 283-290.
O MAN 22028

12J119
R. Ookawa, K. Takahiro, K. Kawatsura, F. Nishiyama, S. Yamamoto and H. Naramoto
Structure of amorphized C60 films studied by Raman spectroscopy and X-ray photoelectron spectroscopy
Nucl. Instrum. Methods Phys. Res. B, 206 (2003) 175.
I IOM 22029

12J120

K. Takahiro, R. Ookawa, K. Kawatsura,
F. Nishiyama, S. Nagata, S. Yamamoto,
K. Narumi, H. Naramoto and M. Iwaki
Surface morphology of glassy carbon irradiated with nitrogen ions
Nucl. Instrum. Methods Phys. Res. B, 206 (2003) 206.
I IOM 22029

12J121
K. Takahiro, K. Kawatsura, S. Nagata,
S. Yamamoto, H. Naramoto, M. Sasase and
Y. Ito
Formation of CuCl and AgCl nanoclusters by sequential implantation
Nucl. Instrum. Methods Phys. Res. B, 206 (2003) 206.
I IOM 22029

12J122
K. Takahiro, R. Ookawa, K. Kawatsura,
S. Nagata, F. Nishiyama, S. Yamamoto,
K. Narumi, H. Naramoto and M. Iwaki
Improvement in surface roughness of nitrogen-implanted glassy carbon by hydrogen doping
Diam. Relat. Mater. in press.
I IOM 22029

12J123
H. Abe, A. Uedono, H. Uchida, A. Komatsu,
S. Okada and H. Itoh,
Positron annihilation studies of defects in ion implanted Palladium,
Mater. Sci. Forum, 363-365 (2001), p.156.
I IOM 22039

12J124
H. Abe, A. Uedono, H. Uchida, A. Komatsu,
S. Okada and H. Itoh,
Positron annihilation studies of defects in ion implanted Palladium,
Mater. Sci. Forum, 363-365 (2001), p.156.

I IOM 22039

12J125
Z.Q. Chen, S. Yamamoto, M. Maekawa,
A.Kawasuso, T.Sekiguchi,
Postgrowth Annealing of Defects in ZnO Studied by Positron Annihilation, X-ray Diffraction, Rutherford backscattering, Cathodoluminescence and Hall Measurement
J. Appl. Phys., revised manuscript submitted on May 28.
O MAN 22040

12J126
Z. Q. Chen, T. Sekiguchi, M. Maekawa,
A. Kawasuso,
N+ ion-implantation induced defects in ZnO studied by slow positron beam
J. Phys. Condens. Matter, submitted on May 25
I MAN 22040

12J127
N. Kozai, T. Ohnuki, S. Komarneni,
T. Kamiya, T. Sakai, M. Oikawa, T. Sato,
Uptake of Cadmium by Synthetic Mica and Apatite: Observation by micro-PIXE,
Nucl. Instrum. Methods Phys. Res. B, in

press
S IOM 22043

12J128
M.Ishino, O.Yoda, Y.Haishi, F.Arimoto, M.Takeda, S.Watanabe, S.Ohnuki, H.Abe,
Boundary Structure of Mo/Si Multilayers for Soft X-Ray Mirrors,
Jpn. J. Appl. Phys. Vol. 41 (2002) pp. 3052-3056
T IOM 22022

12J129
T. Suda, M. Ohkawa, S. Sawada,
S. Watanabe, S. Ohnuki, S. Nagata,
Effect of surface modification by ion-implantation on hydrogenation property of TiFe alloy,
Mater. Trans., Vol.43, No.11 (2002) pp.2703-2705
T IOM 22022

12J130
T. Umebayashi, T. Yamaki, H. Itoh and
K. Asai,
Band-Gap Narrowing of Titanium Dioxide by Sulfur Doping,
Appl. Phys. Lett. 81 (2002) 454-456.
I IOM 22026

12J131
T. Umebayashi, T. Yamaki, H. Itoh and
K. Asai,
Analysis of Electronic Structures of 3D Transition Metal-Doped TiO2 Based on Band Calculation,
J. Phys. Chem. Solids 63 (2002) 1909-1920.
I IOM 22026

12J132
T. Umebayashi, T. Yamaki, S. Yamamoto,
A. Miyashita, S. Tanaka, T. Sumita, K. Asai,
Sulfur-doping of rutile-titanium dioxide by ion implantation: Photocurrent spectroscopy and first-principles band calculation studies,
J. Appl. Phys. 93 (2003) 5156-5160.
I IOM 22026

12J133
T. Umebayashi, T. Yamaki, S. Tanaka and
K. Asai,
Sulfur Doped Titanium Dioxide as a Novel Visible-Light Photocatalyst,
Chem. Lett. 32 (2003) 330-331.
I IOM 22026

12J134
T. Umebayashi, T. Yamaki, T. Sumita,
S. Yamamoto, S. Tanaka, K. Asai,
UV-ray photoelectron and ab initio band calculation studies on electronic structures of Cr- or Nb-ion implanted titanium dioxide,
Nucl. Instrum. Methods Phys. Res. B, 206 (2003) 264-267.
I IOM 22026

12J135
T. Umebayashi, T. Yamaki, S. Yamamoto,
S. Tanaka, K. Asai,
Synthesis of sulfur-doped TiO2 by ion implantation,
Trans. Mater. Res. Soc. Jap. 27 (2003)

461-464.
I IOM 22026

12J136
T. Umebayashi, T. Yamaki, M. Yoshikawa, K. Asai,
Visible-light photocatalyst : Sulfur-doped TiO2,
Kogyo Zairyo (2003) 34-36.
I IOM 22026

12J137
T. Yamaki, T. Umebayashi, T. Sumita, S. Yamamoto, M. Maekawa, A. Kawasuso, H. Itoh,
Fluorine-doping in titanium dioxide by ion implantation technique,
Nucl. Instrum. Methods Phys. Res. B, 206 (2003) 254-258.
I IOM 22026

12J138
T. Sumita, T. Yamaki, S. Yamamoto, A. Miyashita,
Ion beam modification of photo-induced charge separation in TiO2 films,
Nucl. Instrum. Methods Phys. Res. B, 206 (2003) 245-248.
I IOM 22026

12J139
T. Sumita, T. Yamaki, S. Yamamoto, A. Miyashita,
Photo-induced surface charge separation in Cr-implanted TiO2 thin film,
Thin Solid Films 416 (2003) 80-84
I IOM 22026

12J140
J. Vacik, H. Naramoto, K. Narumi, S. Yamamoto and K. Miyashita,
Pattern Formation Induced by Co-deposition of Ni and C60 on MgO(100)
J. Chem. Phys., 114 (2001) 9115-9119.
O IOM none

12J141
H. Naramoto, X. D. Zhu, J. Vacik, Y. H. Xu, K. Narumi, S. Yamamoto, K. Miyashita,
Allotropic Conversion of Carbon-related Films by Using Energy Beams
Physics of the Solid State 44 (2002) 668-673.
T S IOM 22030

12J142
H. Naramoto, Y. Xu, K. Narumi, X. Zhu, J. Vacik, S. Yamamoto and K. Miyashita,
Modification of Carbon Related Films with Energy Beams
Mat. Res. Soc. Proc. 647 (2001) O5.18.1-O5.18.6.
T S IOM 22030

12J143
X. D. Zhu, Y. H. Xu, H. Naramoto, K. Narumi and K. Miyashita,
Role of simultaneous Ne+ ion bombardments in preparing carbon films from C60 fullerene
J. Phys.: Condensed Matter 14 (2002) 5083-5090.

O IOM none

12J144
X. D. Zhu, H. Naramoto, Y. H. Xu,
K. Narumi, and K. Miyashita,
Tuning Surface Morphologies of Ion-Assisted Diamond-like Carbon Film on Nanometer Scale
J. Chem. Phys. 116 (2002) 10458-10461.
O IOM none

12J145
X. D. Zhu, H. Naramoto, Y. H. Xu,
K. Narumi and K. Miyashita,
Coarsening Dynamics and Surface Stability of during Ion-beam-assisted Growth of Amorphous Diamond-like Carbon,
Phys. Rev. B 66 (2002) 165426.
O IOM none

12J146
V. Lavrentiev, H. Abe, S. Yamamoto,
H. Naramoto, and K. Narumi,
Formation of carbon nanotubes under conditions of Co+C60 film
Physica B: Condensed Matter 323 (2002) 303-305.
O IOM none

12J147
V. Lavrentiev, H. Abe, S. Yamamoto,
H. Naramoto, K. Narumi,
Co and C60 Interaction under Conditions of Mixture
Mol. Cryst. liquid Cryst. B 323 (2002) 303-305.

O IOM none

12J148
V. Lavrentiev, H. Abe, S. Yamamoto,
H. Naramoto, and K. Narumi,
Formation of Promising Co-C nano-compositions,
Surf. Interface Anal. 35 (2003) 36-39.

O IOM none

12J149
V. Lavrentiev, H. Abe, S. Yamamoto,
H. Naramoto and K. Narumi,
Isolation of Co nanoparticles by C60 molecules in co-deposited film
Materials Letters (2003), accepted for publication.
O IOM none

12J150
V. Lavrentiev, H. Abe, S. Yamamoto,
H. Naramoto, and K. Narumi,
Formation of carbon nanotubes under conditions of Co+C60 film
Physica B: Condensed Matter 323 (2002) 303-305.
O IOM none

12J151
V. Lavrentiev, H. Abe, S. Yamamoto,
H. Naramoto, and K. Narumi,
Formation of promising Co-C nano-compositions,
Surface and Interface Analysis 35 (2003) 36-39.

O IOM none

12J152
V. Lavrentiev, H. Abe, S. Yamamoto,
H. Naramoto, K. Narumi,
Co and C60 Interaction under Conditions of Mixture
Mol. Cryst. Liq. Cryst. B 323 (2002) 303-305.
O IOM none

12J153
V. Lavrentiev, H. Abe, S. Yamamoto,
H. Naramoto and K. Narumi,
Isolation of Co nanoparticles by C60 molecules in co-deposited film
Materials Letters (2003), accepted for publication.
O IOM none

12J154
S. Sakai, Y. Xu, Tri Hardi PRIYANTO,
V. Lavrentiev, K. Narumi and H. Naramoto,
Structure Evolution and Corresponding Electrical Properties in Weakly Bound Co-C60 Mixture
Proc. of Materials Research Society (Boston, 2003) (to be published)
O IOM none

12J155
K. Narumi, Y. Xu, K. Miyashita and
H. Naramoto,
Effect of Ion Irradiation on C_60 Thin Films
European Physical Journal D, in press.
T IOM 22031

12J156
S. Ishino, Y. Chimi, Bagiyono, T. Tobita,
N. Ishikawa, M. Suzuki, A. Iwase,
Radiation enhanced copper clustering processes in Fe-Cu alloys during electron and ion irradiations as measured by electrical resistivity,
J. Nucl. Mater. (2003), in press.
S IOM 22035

12J157
S. C. Jeong, I. Katayama, H. Kawakami.
H. Ishiyama, H. Miyatake, M. Sataka,
A. Iwase, S. Okayasu. H. Sugai, S. Ichikawa,
K. Nishio, Y. Sugiyama. M. Yahagi,
K. Takada , M. Watanabe
Simulation of radiotracer method for diffusion studies using short-lived radioactive nuclear beams
Jpn. J. Appl. Phys. Vol. 42 (2003) in press.
S IOM 22036

12J158
S. Sakai, H. Tanimoto, E. Kita and
H. Mizubayashi,
Characteristic Creep Behavior of Nanocrystalline (n-) Metals Found for High Density n-Gold,
Phys. Rev. B, 66(2002), 214106 (9 pages).
S IOM 22037

12J159
H. Tanimoto, S. Sakai and H. Mizubayashi ,
Anelasticity Study on Motions of Atoms in the Grain Boundary Regions

in Nanocrystalline Gold,
Mater. Trans., 44(2003), 53-58.
S IOM 22037

12J160
J. Isoya, T. Ohshima, A. Ohi, N. Morishita, and H. Itoh,
ESR Characterization of Activation of Implanted Phosphorus Ions in Silicon Carbide
Nucl. Instrum. Methods Phys. Res. B, 206C, (2003) 965-968
T IOM 22038

12J161
N. Mizuochi, S. Yamasaki, H. Takizawa,
N. Morishita, T. Ohshima, H. Itoh, and
J. Isoya,
Continuous-wave and pulsed EPR study of negatively charged silicon vacancy with S=3/2 and C3v symmetry in n-type 4H-SiC
Phys. Rev. B, 66, 235202, 1-12 (2002)
T IOM 22038

12J162
T. Yamaguchi, E. Watanabe, T. Souno,
H. Nishikawa, M. Hattori, Y. Ohki,
T. Kamiya, K. Arakawa,
Evaluation of silica glasses implanted by high-energy ions using a uv-excited microscopy,
Nucl. Instrum. Methods Phys. Res. B, 191, May (2002), pp.371-374.
O IOM 22042

12J163
H. Nishikawa, T. Souno, M. Hattori,
Y. Nishihara, Y. Ohki, E. Watanabe,
M. Oikawa, T. Kamiya, K. Arakawa,
Radiation effects and surface deformation of silica by ion microbeam,
Nucl. Instrum. Methods Phys. Res. B, 191, May (2002), pp.342-345.
O IOM 22042

12J164
M. Hattori, Y. Nishihara, Y. Ohki,
M.Fujimaki, T. Yamaguchi, E. Watanabe,
T. Souno, H. Nishikawa, M. Oikawa,
T. Kamiya,K. Arakawa,
Characterization of ion-implanted silica glass by vacuum ultraviolet absorption spectroscopy,
Nucl. Instrum. Methods Phys. Res. B, 191, May (2002), pp.362-365.
O IOM 22042

12J165
S. Watanabe, N. S. Ishioka, T. Sekine, A. Osa,
M. Koizumi, H. Shimomura, K. Yoshikawa,
H. Muramatsu,
Production of Endohedral 133Xe-Fullerene by Ion Implantation.
J. Radioanal. Nucl. Chem., 255, 495-498 (2003).
O NRI none

12J166
S. Watanabe, N. S. Ishioka, H. Shimomura, H. Muramatsu, T. Sekine,
Dose dependence of the production yield of endohedral 133Xe-fullerene by ion

implantation.
Nucl. Instrum. Methods Phys. Res. B, 206, (2003)399-402
O NRI none

12J167
T. Kamiya, W. Yokota, Y. Kobayashi, M. Cholewa, M. S. Krochmal, G. Laken, I. D. Larsen, L. Fiddes, G. Parkhill, K. Dowsey,
Development of an automated single cell irradiation system combined with a high-energy heavy ion microbeam system
Nucl. Instrum. Methods Phys. Res. B, 181 (2001) 27-31.
C ACT 21047

12J168
M. Oikawa, T. Kamiya, M. Fukuda, S. Okumura, H. Inoue, S. Masuno, S. Umemiya, Y. Oshiyama and Y. Tira,
Design of a focusing high-energy heavy ion microbeam system at the JAERI AVF-cyclotron,
Nucl. Instrum. Methods Phys. Res. B, 210 (2003) 54-58.
C ACT 21047

12J169
M. Kasahara, R. Höller, S. Tohno, Y. Ohnishi and C.-J. Ma,
2002. Application of PIXE technique to studies on global warming/cooling effect of atmospheric aerosols,
Nucl. Instrum. Methods Phys. Res. B, 189, 204-208.
S ACT 22044

12J170
M. Kasahara, S. Akashi, Ma C.-J. and S. Tohno,
2003. Fixation and chemical analysis of individual fog droplet and raindrop.
Atmos. Res., 65, 251-259
S ACT 22044

12J171
C.-J. Ma, M. Kasahara, S. Tohno, and T. Sakai,
2003. A replication technique for the collection of individual fog droplets and their chemical analysis using micro-PIXE
Atmos. Environ. accepted.
S ACT 22044

12J172
Ma C.-J., M. Kasahara, S. Tohno, and T. Sakai,
2003. A new attempt to study the particle scavenging properties of individual snow crystals using a replication technique.
Journal of Japan Society Atmospheric Environment, 38, 89-99.
S ACT 22044

12J173
T. Kamiya, T. Sakai, M. Oikawa, and T. Hirao,
Observation of individual radiation damage using an automated single ion hit technique at the JAERI heavy ion microbeam system.
Nucl. Instrum. Methods Phys. Res. B,181

(2001) 280
T ACT 22045

12J174
S. Harada, Y. Tamakawa, K. Ishii, A. Tanaka, T. Satoh, S. Matsuyama, H. Yamazaki, T. Kamiya, T. Sakai, K. Arakawa, M. Saitoh, S. Oikawa, K. Sera,
The kinetics of Fe and Ca for the development of radiation-induced apoptosis by micro-PIXE imaging,
Nucl. Instrum. Methods Phys. Res. B, 189, (2002).437-442
S ACT 22047

12J175
T. Sakai, T. Kamiya, M. Oikawa, T. Satoh, A. Tanaka, K. Ishii,
JAERI Takasaki in-air micro-PIXE system for various applications,
Nucl. Instrum. Methods Phys. Res. B, 190, (2002), 271-275
S ACT 22047

12J176
M. Rodriguez, T. Yonezawa, K. Ishii, S. Matsuyama, H. Yamazaki, T. Sato, Ts. Amartaivan, S. Sugihara, A. Tanaka, K. Kato, and Y. Komori,
Preliminary measurements of the low energy detection efficiency of a Si(Li) detector for PIXE applications,
International Journal of PIXE, in press
S ACT 22047

12J177
A. Tanaka, K. Ishii, S. Matsuyama, H. Yamazaki, Y. Oishi, M. Rodriguez, Ts. Amartaivan, K. Kubota, H. Fukuda, T. Kamiya, T. Satoh, T. Sakai, M. Oikawa, K. Arakawa and M. Saidoh,
In-air micro-PIXE analysis of tissue samples,
International Journal of PIXE, in press.
S ACT 22047

12J178
H. Yamazaki, K. Ishii, Y. Takahashi, Ts. Amartaivan, S. Matsuyama, T. Satoh, S. Sugihara, K. Sera and G. C. Jon,
PIXE elemental analysis of drinking water supplies,
International Journal of PIXE, in presss.
S ACT 22047

12J179
Ts. Amartaivan, K. Ishii, H. Yamazaki, Y. Takahashi, S. Matsuyama, T. Satoh, S. Sugihara, K. Katoh, Y. Komori and H. Orihara,
PIXE analysis of trace heavy metals in river and tap water using an ion-exchabge cellulose phosphate filter,
International Journal of PIXE, in press.
S ACT 22047

12J180
H. Yamazaki, K. Ishii, Y. Takahashi, S. Matsuyama, T. Satoh and H. Orihara,
Analysis of Trace Level thorium and Uranium in Drainage from a Radioisotope Laboratory by Particle-Induced X-ray

Emission,
J. Nucl. Sci. Techno., in press.
S ACT 22047

12J181
S. Matsuyama, K. Ishii, H. Yamazaki,
R. Sakamoto, M. Fujisawa, Ts. Amartaivan,
Y. Oishi, M. Rodriguez, A. Suzuki,
T. Kamiya, M. Oikawa, K. Arakawa and
N. Matsumoto,
Preliminary Results ob microbeam at Tohoku University,
Nucl. Instrum. Methods Phys. Res. B, in press.
S ACT 22047

12J182
Y. Oishi, K. Hotta, K. Ishii, Y. Komori,
S. Matsuyama, H. Yamazaki, T. Amartivan,
M. Rodriguez, K. Katoh, D. Izukawa,
K. Mizuma, T. Satoh, T. Kamiya, T. Sakai,
K. Arakawa, M. Saidoh, M. Oikawa,
3D imaging of elemental distributions using multi-angle RBS 2D-data,
Nucl. Instrum. Methods Phys. Res. B, in press.
S ACT 22047

12J183
T. Satoh, K. Ishii, T. Kamiya, T. Sakai,
M. Oikawa, K. Arakawa, S. Matsuyama,
H. Yamazaki,
Development of a large-solid-angle and multi-device detection system for elemental analysis,
Nucl. Instrum. Methods Phys. Res. B, in press.
S ACT 22047

12J184
A. Endo, K. Sato, H. Noguchi, Su. Tanaka,
T. Iida, S. Furuichi, Y. Kanda, Y. Oki
Study of particle size distribution and formation mechanism of radioactive aerosols generated in high-energy neutron fields
J. Radioanal. Nucl. Chem., 256(2), (2003)231-237
C RSH 21049

12J185
M. Hagiwara, M. Hosokawa, M. Baba,
T. Sanami, M. Takada,
Development of Bragg curve spectrometer (BCS) for fragment spectroscopy from neutron and proton induced reactions,
Proc of the 16th workshop on radiation detectors and their uses, February 6-8 2002 (KEK,Tsukuba,Japan) p.70.
C RSH 21050

12J186
E. Kim, A. Endo, Y. Yamaguchi,
M. Yoshizawa, T. Nakamura and T. Shiomi
Measurement of Neutron Dose with an Organic Liquid Scintillator Coupled with a Spectrum Weight Function,
Radiat. Prot. Dosim., 102(1), p31-40 (2002).
C RSH 21051

12J187
S. Ishiyama and M.Asano,
The effect of Proton Doping on Ion

conductivity of sol-gel phosphosilicate glasses,
J. of Ceramic Society of Japan(Submitted)
I T RCO 22051

12J188
Y. Ishii, A. Isoya and T. Kojima,
Progress in submicron width ion beam system using double acceleration lenses
Nucl. Instrum. Methods Phys. Res. B, To be printed.
O ACT none

12J189
M. Fukuda, S. Kurashima, S. Okumura,
N. Miyawaki, T. Agematsu, Y. Nakamura,
T. Nara, I. Ishibori, K. Yoshida, W. Yokota and K. Arakawa
Flat-top Acceleration System for the Variable-Energy Multi particle AVF Cyclotron
Rev. Sci. Instrum. 74, 2293 (2002).
C ACT none

This is a blank page.

A.1.2 Publications in Proceeding

12C01

M. Imaizumi, T. Takamoto, T. Ohshima,
M. Yamaguchi, H. Itoh, S. Matsuda
Radiation Effects on High-Efficiency InGaP/InGaAs/Ge Triple-Junction Solar Cells Developed for Terrestrial Use
Proc. of 29th IEEE Photovoltaic Specialists Conference, May 2002 (USA) p.990,
CTI SCS 21003

12C02

S. Kawakita, M. Imaizumi, M. Yamaguchi,
K. Kushiya, T. Ohshima H. Ito S. Matsuda
In-Situ Measurement of Degradation of $Cu(In,Ga)Se_2$ Thin Film Solar Cells During Electron and Proton Irradiations
Proc. of 29th IEEE Photovoltaic Specialist Conference, May 2002 (USA) p.978
CTI SCS 21003

12C03

S. Matsuda, H. Shindou, S. Kawakita, Y. Iide,
N. Yamada, Y. Deguchi, N. Ikeda, K. Aoyama,
M. Imaizumi, S. Kuboyama, T. Ohshima,
T. Hirao, M. Yoshikawa, H. Itoh
Evaluation Results of COTS on MDTS-1(Tsubasa) "Verification Ground Test Validity by Flight Test",
Proc. of The 5th International Workshop on Radiation Effects on Semiconductor Device for Space Application, October 2002(Takasaki) p.27
CTI SCS 21003

12C04

M. Imaizumi, O. Anzawa, S. Kawakita,
T. Sumita, K. Aoyama, S. Matsuda,
N. Tanioka
Radiation Effects in Space on Solar Cells Developed for Terrestrial Use Demonstrated by MDS-1
Proc. of The 5th International Workshop on Radiation Effects on Semiconductor Device for Space Application, October 2002(Takasaki) p.35
CTI SCS 21003

12C05

T. Sumita, M. Imaizumi, S. Matsuda,
S. Kuwajima, A. Ohi, T. Ohshima, T. Kamiya
Radiation Tolerance of Triple Junction Space Solar Cells
Extended Abstracts (The 50th Spring Meeting 2003): The Japan Society of Applied Physics and Related Societies, March (Yokohama) p.1525
CTI SCS 21003

12C06

M. Imaizumi, S. Kawakita, T. Sumita,
S. Matsuda, S. Kuwajima, N. Tanioka
Performance of Terrestrial Solar Cells in Space Demonstrated by "Tsubasa" (MDS-1)
Extended Abstracts (The 50th Spring Meeting 2003): The Japan Society of Applied Physics and Related Societies, March

(Yokohama) p.1525
CTI SCS 21003

12C07
S. Kawakita, M. Imaizumi, T. Sumita,
S. Matsuda, S. Kuwajima, T. Ohshima,
T. Kamiya
Radiation Tolerance of Cu(In, Ga)Se_2 thin-film solar cells
Extended Abstracts (The 50th Spring Meeting 2003): The Japan Society of Applied Physics and Related Societies, March (Yokohama) p.1527
CTI SCS 21003

12C08
M. Imaizumi, T. Sumita, S. Matsuda,
T. Takamoto, T. Ohshima, A. Ohi, T. Kamiya,
M. Yamaguchi
Study of Radiation Response on Single-Junction Component Sub-Cells in Triple-Junction Solar Cells
Proc. of 3rd World Conference on Photovoltaic Energy Conversion, May 2003 (Osaka) p.40
CTI SCS 21003

12C09
T. Sumita, M. Imaizumi, S. Matsuda,
T. Ohshima, A. Ohi, T. Kamiya
Analysis of End-of-Life Performance for Proton Irradiated Triple-Junction Space Solar Cell
Proc. of 3rd World Conference on Photovoltaic Energy Conversion, May 2003 (Osaka) p.45
CTI SCS 21003

12C10
S. Kawakita, M. Imaizumi, S. Matsuda,
K. Kushiya, T. Negami, T. Ohshima,
T. Kamiya, M. Yamaguchi
Super Radiation Tolerance of CIGS Solar Cells Demonstrated in Space by MDS-1 Satellite
Proc. of 3rd World Conference on Photovoltaic Energy Conversion, May 2003 (Osaka) p.45
CTI SCS 21003

12C11
A. Makihara, S. Kuboyama, S. Matsuda,
N. Nemoto, H. Ohtomo, K. Furuse, S. Baba and T. Hirose.
Non-Damaging Beam Blanking SEM Test Method and its Application to Highly Integrated Devices
The IEEE Nuclear and Space Radiation Effects Conference(NSREC 2001).
C SCS 21002

12C12
A. Makihara, H. Shindou, N. Nemoto,
S. Kuboyama, S. Matsuda , T. Ohshima,
T. Hirao, H. Itoh , S. Buchner,
A. B. Campbell
Analysis of Single-Ion Multiple-Bit Upset in High-Density DRAMs
The IEEE Nuclear and Space Radiation Effects Conference(NSREC 2000)..
C SCS 21002

12C13
N. Nemoto, H. Shindou, S. Kuboyama,
S. Matsuda, H. Itoh, S. Okada, I. Nashiyama
Relationship between Single-Event Upset Immunity and Fablication Processes of Recent Memories,
5th Europian conference radiation and its Effects on Components and system (RADECS99)
C SCS 21002

12C14
N. Nemoto, H. Shindou, S. Kuboyama,
S. Matsuda , K. Sugimoto, I. Nashiyama,
H. Itoh
Development of 1M Gate CMOS Gate Array,
Europian Space Components Conference (ESCCON 2000)
C SCS 21002

12C15
T. Hirao, J. S. Laird, H. Mori, S. Onoda,
T. Wakasa, T. Yamakawa, H. Abe, H. Itoh,
Single Event Research at JAERI,
Proc. of 5th international workshop on radiation effects on semiconductor devices for space application, 2002 (Japan)
T SCS 22001

12C16
S. Onoda, T. Hirao, J. S. Laird, H. Mori,
H. Itoh, T. Okamoto, Y. Koizumi,
Displacement damage degradation of single event transient current in Si pin photodiode,
13th international conference on ion beam modification of materials, 2002 (Japan) published in NIMB.
T SCS 22001

12C17
H. Mori, T. Hirao, J. S. Laird, S. Onoda,
T. Wakasa, T. Yamakawa, H. Abe, H. Itoh,
T. Okamoto, Y. Koizumi,
Modeling of the transient charge collection induced by an angled single ion strike,
13th international conference on ion beam modification of materials, 2002 (Japan) published in NIMB.
T SCS 22001

12C18
T. Hirao, H. Mori, J. S. Laird, S. Onoda,
H. Abe, H. Itoh,
Study of single event current pulses induced in SOI diodes by collimated swift heavy-ion micorbeams,
13th international conference on ion beam modification of materials, 2002 (Japan) published in NIMB.
T SCS 22001

12C19
H. Mori, T. Hirao, J. S. Laird, S. Onoda,
H. Abe, H. Itoh,
Study of collection processes of charge induced in multi junction schottky diodes -dependence of ion irradiation position and angle-,
TIARA annual report 2001, 2002 (Japan).
T SCS 22001

12C20

T. Hirao, J. S. Laird, H. Mori, S. Onoda,
H. Abe, H. Itoh,
Studies on single-event phenomena using the heavy-ion microbeam at JAERI,
8th international conference on nuclear microprobe technology & applications, 2002 (Japan) published in NIMB.
T SCS 22001

12C21
H. Mori, T. Hirao, S. Onoda, J. S. Laird,
H. Itoh, T. Okamoto, Y. Koizumi,
Relationship between the angle of an induced MeV ion and its induced transient current,
8th international conference on nuclear microprobe technology & applications, 2002 (Japan) published in NIMB.
T SCS 22001

12C22
T. Hirao, J. S. Laird, H. Mori, S. Onoda,
H. Abe, H. Itoh,
Comparison of the ion induced charge collection in Si epilayer and SOI devices,
8th international conference on nuclear microprobe technology & applications, 2002 (Japan) published in NIMB.
T SCS 22001

12C23
S. Onoda, T. Hirao, J. S. Laird, H. Mori,
H. Itoh, T. Okamoto, Y. Koizumi,
Total dose dependence of transient current induced by heavy ion microbeam in pin photodiode,
8th international conference on nuclear microprobe technology & applications, 2002 (Japan) published in NIMB.
T SCS 22001

12C24
T.Hirao, J. S. Laird, H. Mori, S. Onoda,
H. Abe, S.Itoh,
Analysis of single-event transient current induced in junction diodes by single-ion hit.
Proceedings of the 15th meeting for tandem accelerators and related techniques
T SCS 22001

12C25
J. S. Laird, T. Hirao, S. Onoda, H. Mori,
H. Abe, H. Itoh,
A comparison of heavy ion and laser microbems for investigation into single event related charge collection processes,
8th international conference on nuclear microprobe technology & applications, 2002 (Japan) published in NIMB.
T SCS 22002

12C26
J. S. Laird, T. Hirao, S. Onoda, H. Mori,
H. Itoh,
High energy radiation degradation of high speed p-i-n diodes for space applications,
Asia-pasific workshop on fundamental and application of advanced semiconductor devices, 2002, (Japan).
T SCS 22002

12C27
J. S. Laird, T. Hirao, S. Onoda, H. Mori,

H. Itoh,
TCAD modeling of single MeV ion induced charge collection processes in Si devices,
8th international conference on nuclear microprobe technology & applications, 2002 (Japan) published in NIMB.
T SCS 22002

12C28
Y. Nakanishi, A. Wakahara, H. Okada,
A. Yoshida, T. Ohshima and H. Itoh,
Effect of alloy composition on photoluminescence properties of europium implanted AlGaInN,
International Workshop on Nitride Semiconductors (IWN2002), (Aachen, Germany), July 2002.
I SCS 22005

12C29
Y. Nakanishi, A. Wakahara, H. Okada,
A. Yoshida, T. Ohshima, H. Itoh, S. Nakao,
K. Saito and Y. T. Kim,
Effects of implantation conditions on the luminescence properties of Eu-doped GaN,
The 13th International Conference on Ion Beam Modification of Materials (IBMM2002), (Kobe, Japan), November 2002
I SCS 22005

12C30
S. Kitamura, N. Shikazono, A. Tanaka,
Molecular and physiological characterization of tt19 mutant in Arabidopsis.
Plant Cell Physiol. 44 (Suppl.) s120, 2003.
C BIT 21010

12C31
M. Okamura et al.
Mutation Generation in Pot & Garden Carnations Regenerated from Tissue Cultures Irradiated with Ion Beams,
The Twelfth TIARA Research Review Meeting, 128-129 (2003)
C BIT 21012

12C32
M. Okamura et al
Mutation generation in chrysanthemum plants regenerated from floral organ cultures irradiated with ion beams,
TIARA Annual Report 2001:42-43 (2002)
C BIT 21012

12C33
K. Ishii, Y. Yamada, Y. Hase, N. Shikazono and A. Tanaka,
RAPD Analysis of Mutants Obtained by Ion Beam Irradiation to Hinoki Cypress Shoot Primordia,
Abstracts of IBMM 2002, p.99
C BIT 21014

12C34
Y. Yamamoto, A. Tanaka, Y. Hase and
T. Tashiro
Mutation induction with ion beam irradiation in garlic (*Allium Sativum* L.)
10th Annual Meeting of the Chubu Branch of Japanese Society of Breeding, Aichi, January

25, 2003
C BIT 21015

12C35
Y. Yamamoto, A. Tanaka,, Y. Hase, and
T. Tashiro
Mutation induction with ion beam irradiation in garlic(Allium Sativum L.)
10th Annual Meeting of the Chubu Branch of Japanese Society of Breeding, Aichi, January 25, 2003
C BIT 21015

12C36
M. Mizobuchi and A. Iwasaki
The Use of the Ion Beam to the Rice Breeding
Shikoku J. Crop Sci. 2001 38: p.50-51.
C BIT 21017

12C37
H. Katai, M. Taneishi, A. Tanaka,
N. Shikazono, H. Hase and H.Otsuka
Effect of ion beam irradiation on the growth of netted melon (*Cucumis melo* L.)
Breeding Research 2001(1) p243
C BIT 21019

12C38
Y. Kobayashi, T. Funayama, S. Wada,
M. Taguchi, H. Watanabe,
System of Cell Irradiation with a Precise Number of Heavy Ions,
Proc. of The Third National Conference of Ion Beam Bioengineering and The First International Symposium on Ion Beams: Biological Effects and Molecular Mechanisms, July 2002 (Wulumuqi, China) p. 22.
C BIT 21027

12C39
C. Shao, Y. Furusawa, M. Aoki, K. Ando,
H. Matsumoto, K. Kobayashi, T. Funayama,
S. Wada,
Gap Junction Channels Play an Essential Role in Irradiation-Induced Bystander Effect on Human Fibroblast Cell,
Proc. of The Third National Conference of Ion Beam Bioengineering and The First International Symposium on Ion Beams: Biological Effects and Molecular Mechanisms, July 2002 (Wulumuqi, China) p. 9.
C BIT 21027

12C40
S. Wada, Y. Kobayashi, T. Funayama,
M. Natsuhori, N. Ito, K. Yamamoto,
Detection of DNA damage in the individual cells induced by charged particles with comet assay,
The 13th International Conference on Ion Beam Modification of Materials, Sept. 2002, (Kobe, Japan)
C BIT 21027

12C41
Y. Kobayashi, T. Funayama, S. Wada,
M. Taguchi, H. Watanabe,
The effect of irradiation with a precise number of heavy ions on mammalian cells -

Applications of microbeams for studying cellular radiation response,
The 8th International Conference on Nuclear Microprobe Technology and Applications, Sept. 2002, (Takasaki, Japan) p. 136.
C BIT 21027

12C42
T. Funayama, S. Wada, Y. Kobayashi,
Analysis of Mammalian Cellular Response Using Heavy Ion Microbeam,
International Symposium on Innovative Technology for Radiation Risk Study, March 2003 (Tokyo, Japan) 32-33.
C BIT 21027

12C43
Y. Kobayashi, T. Funayama, S. Wada,
M. Taguchi,
Irradiation of single mammalian cells with a precise number of energetic heavy ions,
International Symposium on Innovative Technology for Radiation Risk Study, March 2003 (Tokyo, Japan) 76-77.
C BIT 21027

12C44
S. Wada, T. Funayama, Y. Kobayashi,
Detection of DNA Damage Induced by Ion Irradiation in Individual Cells,
International Symposium on Innovative Technology for Radiation Risk Study, March 2003 (Tokyo, Japan) 78-79.
C BIT 21027

12C45
Y. Kobayashi, T. Funayama, S. Wada, M. Taguchi, H. Watanabe,
System of cell irradiation with a precise number of heavy ions,
6th International Workshop: Microbeam Probes of Cellular Radiation Response, March 2003 (Oxford, UK), 19-23.
C BIT 21027

12C46
T. Funayama, S. Wada, Y. Kobayashi,
Effect of Single Argon Ion Hit on Mammalian Cultured Cells,
6th International Workshop: Microbeam Probes of Cellular Radiation Response, March 2003 (Oxford, UK), 106-109.
C BIT 21027

12C47
M. Matsumoto, S. Hayashi, Z. Jin,
M. Hatashita, E. Kano, C. Shao, Y. Furusawa,
NItric oxide is an initiator of The Bystander Effect Induced by heavy-ion beams,
Proc. of The Third National Conference of Ion Beam Bioengneering and The First International Symposium on Ion Beams: Biological Effects and Molecular Mechanisms, July 2002 (Wulumuqui) p. 8.
O BIT 21029

12C48
C. Shao, Y. Furusawa, M. Aoki, K. Ando,
H. Matsumoto, K. Kobayashi, T. Funayama,
S. Wada,
Gap Junction Channels Play an Essential Role in Irradiation-Induced Bystander Effect

on Human Fibroblast Cell.
Ivid, p.9.
C BIT 21029

12C49
C. Shao, K.M. Prise, V. Stewart, M. Folkard, B.D. Michael,
Involvenent of Nitric Oide in the Bystander Response Induced by Microbeam Targetted Cells,
Microbeam Probes od Cellular Response, March 2003 (Oxford) Vol.6, 127-129.
C BIT 21029

12C50
K. Akeo, R. Inoue, T. Funayama,
Y. Kobayashi, T. Nakagami, T. Hiramitsu
Effects of radiation on expression of glutathione peroxidase in retinal pigment epithelial cells in vitro.
13th Annual Meeting of Ocular Oxidative Stress Research Society 11. 15. 2002. Osaka
O BIT 21032

12C51
K. Akeo, T. Funayama, A. Ogawa, R. Inoue, Y. Kobayashi
The preservation of the organ-cultured ciliary body by gamma ray irradiation.
107th Annual Meeting of Japanese Ophthalmological Society 4. 18 2003. Fukuoka
O BIT 21032

12C52
Y. Yoshida, S. Seki, A. Saeki, S. Tagawa,
M. Taguchi, T. Kojima, H. Namba
Primary Process of Radiation Chemistry Studied by Ion Pulse Radiolysis
TIARA 11th Research Review Meeting, 2002
C RCO 21045

12C53
S. Tagawa, T. Kozawa, and S. Seki
Sub-picosecond Pulse Radiolysis and Ion Beam Induced Nanowire Formation for Nanolithography and Nanotechnology,
Proc. INC'02, 4 (2002) 159-168.
C RCO 21046

12C54
S. Seki, Y. Sakurai, K. Maeda, Y. Kunimi,
S. Nagahara, and Seiichi Tagawa
Reaction Mechanisms in Silicon-based Resist Materials: Polysilanes for Deep-UV, EUV, and X-ray Lithography,
Proc. SPIE 3999 (2000) 423-431
C RCO 21046

12C55
S. Nogami, N. Igawa, T. Taguchi,
A. Hasegawa, K. Abe,
Study on mechanical property changes of SiC/SiC composites and β-SiC after triple-ion beam irradiation,
Proceeding of CREST International Symposium (2002) 418-424
T S I IOM 22008

12C56
Y. Nemoto, Y. Miwa, T. Tsukada and H. Tsuji

AFM Evaluation for Grain Boundary Corrosion Behavior of Ion Irradiated Stainless Steel,
JAERI-Conf 2003-001 / Proceedings of International Symposium on Material Chemistry in Nuclear Environment (Material Chemistry '02), (2003) 397-404.
T I IOM 22010

12C57
Y. Nemoto, Y. Miwa, T. Tsukada and H. Tsuji
AFM Evaluation for Corrosion Behavior of Ion Irradiated Stainless Steel,
Proceedings of 11th International Conference On Nuclear Engineering (ICONE11), JSME/ASME, (2003) 36093 [CD-ROM].
T I IOM 22010

12C58
E. Wakai, T. Sawai, H. Tanigwa, A. Naito,
T. Taguchi and S. Jistukawa,
Snergistic effect of gas atoms and displacement damage on hardness of F82H steel irradiated by dual/triple beams,
International symposium on materials chemistry in nuclear environment, 2002(tsukuba), in press.
T S I IOM 22011

12C59
I. Ioka, M. Futakawa, Y. Nanjyo, K. Kiuchi, Y. Kuroda and T. Anegawa,
Effect of Triple Ion Beam Irradiation on Mechanical Properties of High Chromium Austenitic Stainless Steel,
JAERI-Conf 2003-001(2003).
T I S MAN 01012

12C60
S. Yamada, J. Ohta, K. Sonoda, M. Kinoshita, T. Sawai and S. Jitsukawa,
Irradiation-formed defect structures in Zircaloy-2-Simulation by accelerator to form lattice defects of Zircaloy cladding irradiated in commercial fuel-
Abstracts of The Twelfth TIARA Research Review Meeting (Takasaki, June 19-20, 2003).
T IOM 22015

12C61
F. Kano, Y. Tsuchiya, N. Saito, S. Shiga ,
S. Kasahara , H. Takahashi,
Irradiation and SCC Properties of Metals under Supercritical-water Cooled Power Reactor Conditions,
ICAPP2003, Cordoba, Spain.
T IOM 22016

12C62
Y. Tsuchiya, F. Kano, N. Saito, A. Shioiri,
S. Kasahara, K. Moriya, H. Takahashi.
SCC and Irradiation Properties of Metals under Supercritical-water Cooled Power Reactor Conditions,
GENES/ANP 2003, Kyoto, Japan.
T IOM 22016

12C63
E. Shioya, T. Suda, S. Watanabe, S. Ohnuki,
M. Ishino, O. Yoda, H. Abe
Electron-irradiation-induced amorphization

in Mo/Si nano multilayer material
4th Pacific Rim International Conference on Advanced Materials and Processing, 2001.12.11-15, Hawaii
I IOM 22020

12C64
T. Ohshima, A. Uedono, H. Abe, Z. Q. Chen, H. Itoh, and M. Yoshikawa,
Positron annihilation study of vacancy-type defects in silicon carbide co-implanted with aluminum and carbon ions,
21st Internat. Conf. on Defects in Semiconductors (ICDS21): Giessen, German, July 16-20, 2001.
I IOM 22039

12C65
Y. Azuma, T. Ohkubo, M. Ohtsuka,
H. Uchida and H. Abe,
Effect of ion irradiation on electrochemical hydryding rate of Pd and MmNi3.48Co0.73Mn0.45Al0.34 (Mm=La0.35Ce0.65),
International Symposium on Metal Hydrogen Systems 2002(MH2002): Annecy, France, September 1-6, 2002.
I IOM 22039

12C66
H. Abe, H. Uchida, Y. Azuma, A. Uedono,
Z. Q. Chen and H. Itoh.
Improvement of Hydrogen Absorption Rate of Pd by Ion Irradiation,
13th International Conference on Ion Beam Modification of Materials (IBMM2002): Kobe, Japan, September 1-6, 2002.
I IOM 22039

12C67
Z.Q.Chen, A.Kawasuso, M.Maekawa, T.Ishimoto, S.Yamamoto, H.Itoh,
Positron Annihilation Study of Defects in ZnO Single Crystals
PSSD-2002, Setp.29-Oct.4, Sendai
O MAN 22040

12C68
Z. Q. Chen, S. Yamamoto, M. Maekawa,
T. Ishimoto, A. Kawasuso,
Radiation Induced defects in ZnO Studied by Positron Annihilation
Kyoto University Nuclear Reactor Institute Workshop, Nov. 15-16, 2002, Kyoto
O MAN 22040

12C69
Z.Q. Chen, S. Yamamoto, T. Sekiguchi,
A. Kawasuso,
Effect of Heat Treatment on the Crystal Quality of ZnO Studied by Positron Annihilation,
XRD, CL, RBS and Hall measurement
50th Annual meeting of JSAP, March 27-30, 2003, Yokohama.
O MAN 22040

12C70
Z.Q.Chen, T.Sekiguchi, M.Maekawa, A.Kawasuso,
N+ ion-implantation induced defects in ZnO studied by slow positron beam

7th International Workshop on BIAMS, May 25-29,2003, Villeneuve d'Ascq, France.
I MAN 22040

12C71
S. Sakai, Y. Xu, T. H. Priyanto,
V. I. Lavrentiev, H. Naramoto,
The Structure Evolution and Corresponding Electrical Properties in Softly Bound Co-C60 Mixture,
Proc. of Materials Research Society (2003, Boston).
O IOM none

12C72
V. Lavrentiev, H. Abe, S. Yamamoto,
H. Naramoto, and K. Narumi,
Formation of carbon nanotubes under condition of Co+C60 film,
Tsukuba Symposium on Carbon Nanotube in Commemoration of the 10th Anniversary of its Discovery, October 3-5, 2001 (Tsukuba, Japan) p.142.
O IOM none

12C73
V. Lavrentiev, H. Abe, S. Yamamoto,
H. Naramoto and K. Narumi,
Formation of promising Co-C nano-compositions,
3rd International Symposium on Atomic Level Characterizations for New Materials and Devices '01, ALC '01, November 11-14, 2001 (Nara-Ken New Public Hall, Japan). Program & Abstracts, p. 113.
O IOM none

12C74
V. Lavrentiev, H. Abe, S. Yamamoto,
H. Naramoto and K. Narumi,
Co and C60 interaction under conditions of mixture,
International Symposium on NanoCarbons, ISNC 2001, November 14-16, 2001 (Nagano, Japan). Program & Abstracts, p. 259.
O IOM none

12C75
V. Lavrentiev, H. Abe, S. Yamamoto,
H. Naramoto, K. Narumi and K. Miyashita,
Evolution of Co+C60 Structures during Co-deposition and Subsequent Annealing,
TIARA Annual Report 2000, November 2001 (Advanced Radiation Technology Center, Japan Atomic Energy Research Institute) JAERI-Review 2001-039, p.181
O IOM none

12C76
V. Lavrentiev, H. Abe, S. Yamamoto,
H. Naramoto, K. Narumi and K. Miyashita,
Evolution of Co+C60 Structures during Co-deposition and Subsequent Annealing,
Abstracts of The Tenth TIARA Research Review Meeting, June 18-19, 2001 (Japan Atomic Energy Research Institute, Takasaki Radiation Chemistry Research Establishment) p. 93-94.
O IOM none

12C77
V. Lavrentiev, S. Yamamoto, H. Naramoto

and K. Narumi,
Structural Features of Epitaxial Cobalt Films,
Abstracts of the Thirteenth International Conference on Crystal Growth, ICCG-13/IGVGE-11, 30 July - 4 August 2001 (Doshisha University, Kyoto, Japan) p. 136.
O IOM none

12C78
V. Lavrentiev, H. Abe, S. Yamamoto,
H. Naramoto and K. Narumi,
Formation of intriguing carbon-related structures in Co+C60 mixed films,
Abstract of the 21th Fullerene General Symposium, July 25-27, 2001 (Tsukuba, Japan) p. 34.
O IOM none

12C79
V. Lavrentiev, H. Abe, S. Yamamoto,
H. Naramoto, and K. Narumi,
Formation of carbon nanotubes under condition of Co+C60 film,
Tsukuba Symposium on Carbon Nanotube in Commemoration of the 10th Anniversary of its Discovery, October 3-5, 2001 (Tsukuba, Japan) p.142.
O IOM none

12C80
V. Lavrentiev, H. Abe, S. Yamamoto,
H. Naramoto and K. Narumi,
Formation of promising Co-C nano-compositions,
3rd International Symposium on Atomic Level Characterizations for New Materials and Devices '01, ALC '01, November 11-14, 2001 (Nara-Ken New Public Hall, Japan). Program & Abstracts, p. 113.
O IOM none

12C81
V. Lavrentiev, H. Abe, S. Yamamoto,
H. Naramoto and K. Narumi,
Co and C60 interaction under conditions of mixture,
International Symposium on NanoCarbons, ISNC 2001, November 14-16, 2001 (Nagano, Japan). Program & Abstracts, p. 259.
O IOM none

12C82
V. Lavrentiev, H. Abe, S. Yamamoto,
H. Naramoto, K. Narumi and K. Miyashita,
Evolution of Co+C60 Structures during Co-deposition and Subsequent Annealing,
TIARA Annual Report 2000, November 2001 (Advanced Radiation Technology Center, Japan Atomic Energy Research Institute) JAERI-Review 2001-039, p.181
O IOM none

12C83
V. Lavrentiev, H. Abe, S. Yamamoto,
H. Naramoto, K. Narumi and K. Miyashita,
Evolution of Co+C60 Structures during Co-deposition and Subsequent Annealing,
Abstracts of The Tenth TIARA Research Review Meeting, June 18-19, 2001 (Japan Atomic Energy Research Institute, Takasaki Radiation Chemistry Research

Establishment) p. 93-94.
O IOM none

12C84
V. Lavrentiev, S. Yamamoto, H. Naramoto and K. Narumi,
Structural Features of Epitaxial Cobalt Films,
Abstracts of the Thirteenth International Conference on Crystal Growth, ICCG-13/IGVGE-11, 30 July – 4 August 2001 (Doshisha University, Kyoto, Japan) p. 136.
O IOM none

12C85
V. Lavrentiev, H. Abe, S. Yamamoto,
H. Naramoto and K. Narumi,
Formation of intriguing carbon-related structures in Co+C60 mixed films,
Abstract of the 21th Fullerene General Symposium, July 25-27, 2001 (Tsukuba, Japan) p. 34.
O IOM none

12C86
Y. Xu, H. Naramoto, K. Miyashita,
T. Kamiya, T. Sakai, T. Hamano, and T. Suda
Micro-Raman Analysis of Diamond Crystal Irradiated with H+ Micro-Beam
8th International Conference on Nuclear Microprobe Technology & Applications, September 2002 (Takasaki) p. 60.
O IOM none

12C87
N. Mizuochi, J. Isoya, S. Yamasaki,
H. Takizawa, N. Morishita, T. Ohshima, and H. Itoh,
EPR Study of Single Silicon Vacancy-Related Defects in 4H- and 6H-SiC
Proceedings of the Materials Science Forum, vol. 389-393, p. 497-500 (2002).
T IOM 22038

12C88
M. Hattori, Y. Ohki, M. Fujimaki, T. Souno,
H. Nishikawa, E. Watanabe, M. Oikawa,
T. Kamiya, K. Arakawa,
Characterization of refractive index changes of silica glass induced by ion microbeam,
8th International Conference on Nuclear Microprobe Technology and Applications, Paper No.P1-29, September 2002, p.57.
T S IOM 22042

12C89
T. Souno, H. Nishikawa , T. Yamaguchi,
E. Watanabe, M. Hattori, M. Fujimaki, Y. Ohki, M. Oikawa, T. Kamiya, K. Arakawa,
Characterization of Ion-Implanted Silica Glass by Micro-Photoluminescence and Raman Spectroscopy,
8th International Conference on Nuclear Microprobe Technology and Applications, Paper No.P2-19, September 2002, p.101.
TS IOM 22042

12C90
M. Hattori, M. Fujimaki, Y. Ohki, T. Souno,
H. Nishikawa, E. Watanabe, M. Oikawa,
T. Kamiya, K. Arakawa,
Evaluation of Three Dimensional

Microstructures on Silica Glass Fabricated by Ion Microbeam,
Abstracts of The Eleventh TIARA Research Review Meeting, July 2002, pp.101-102.
TS IOM 22042

12C91
T. Souno, H. Nishikawa, E. Watanabe,
M. Hattori, Y. Ohki, M. Oikawa, T. Kamiya, K. Arakawa ,
Distribution of Defects and Refractive Index Change in Silica Glass Implanted by Ion Microbeam (II),
Extended Abstracts (The 63rd Autumn Meeting, 2002); The Japan Society of Applied Physics, No.2, 25p-YB-14, September 2002, p.817.
S IOM 22042

12C92
T. Souno, H. Nishikawa, E. Watanabe,
M. Hattori, Y. Ohki, M. Oikawa, T. Kamiya, K. Arakawa,
Evaluation of Silica Implanted by Ion Microbeam Using Microspectroscopy Measurement,
Extended Abstracts (The 63rd Autumn Meeting, 2002); The Japan Society of Applied Physics, No.2, 25a-B-8, September 2002, p.648.
T IOM 22042

12C93
M. Hattori, M. Fujimaki, Y. Ohki, T. Souno,
H. Nishikawa, E. Watanabe, M. Oikawa,
T. Kamiya, K. Arakawa,
Depth profile of the densification in silica glass irradiated by ion microbeam,
Extended Abstracts (The 63rd Autumn Meeting, 2002); The Japan Society of Applied Physics, No.2, 25a-YB-16, September 2002, p.818.
S IOM 22042

12C94
T. Souno, H. Nishikawa, E. Watanabe,
M. Hattori, Y. Ohki, M. Oikawa, T. Kamiya,
K. Arakawa,
Radiation effects on silica glass by ion microbeam,
Proceedings of The 34th Symposium on Electrical and Electronic Insulating Materials and Applications in Systems, Nov. 2002, pp.89-92.
S IOM 22042

12C95
K. Fukagawa, T. Souno, H. Nishikawa,
E. Watanabe, T. Yanagi, M. Hattori, Y. Ohki,
M. Oikawa, T. Kamiya, K. Arakawa,
Effects of Irradiation of Heavy Ion Microbeam on Silica Glass,
Extended Abstracts (The 50th Spring Meeting, 2003); The Japan Society of Applied Physics and Related Societies, No.2, 28a-M-1, March 2003, p.979.
T IOM 22042

12C96
M. Hattori, T. Yanagi, Y. Ohki, T. Souno,
K. Fukagawa, H. Nishikawa, E. Watanabe,
M. Oikawa, T. Kamiya, K. Arakawa,

Distribution of a refractive index change induced by ion microbeam into silica glass, Extended Abstracts (The 50th Spring Meeting, 2003); The Japan Society of Applied Physics and Related Societies, No.2, 28a-M-5, March 2003, p.981.
S IOM 22042

12C97
M. Kasahara, C.-J. Ma, Y. Inokuchi, T. Kamiya,
2002. Preliminary study on quantitative elemental analysis for environmental sample using micro-PIXE.
8th International Conference on Nuclear Microprobe Technology and Applications, Sep. 8-13, Takasaki, Gunma, Japan. pp. 118.
S ACT 22044

12C98
K. Sato, A. Endo, H. Noguchi, Su. Tanaka, T. Iida, S. Furuichi, Y. Kanda, Y. Oki,
Effect of added aerosol on formation of radioactive aerosol due to neutron irradiation
Proc. of AESJ fall meeting (Autumn), (I), September 2002 (Iwaki) p.177
C RSH 21049

12C99
T. Sato, A. Endo, Y. Yamaguchi and F. Takahashi
Development of Neutron-Monitor Detector using Liquid Organic Scintillator Coupled with 6Li+ZnS(Ag) Sheet,
Proc. of Ninth Neutron Dosimetry Symposium, September 2003 (Delft), will be published.
C RSH 21051

12C100
M. Fukuda, S. Kurashima, N. Miyawaki, S. Okumura, T. Kamiya, M. Oikawa, Y. Nakamura, T. Nara, T. Agematsu, I. Ishibori, W. Yokota, K. Arakawa, M. Saidoh, Y. Kumata, Y. Fukumoto and K. Saito ,
An Energy Spread Minimization System for Microbeam Generation in the JAERI AVF Cyclotron,
Proc. 8th Int. Conf. on Nuclear Microprobe Technology and Applications, Takasaki, Japan (2002) in press
C ACT none

12C101
T. Agematsu, K. Arakawa, S. Okumura, Y. Nakamura and S. Tajima
An Operator Assistance System for Beam Adjustment of JAERI AVF Cyclotron,
Proc. on Workshop on Accelerator Operation 2003, http://conference.kek.jp/wao2003/
C ACT none

12C102
Y. Nakamura, T. Nara, T. Agematsu, I. Ishibori, S. Kurashima, M. Fukuda, S. Okumura, W. Yokota, K. Arakawa, N. Miyawaki, K. Yoshida and S. Tajima
Operation and maintenance for JAERI AVF Cyclotron system,
Proc. of International Workshop on Accelerator Operation, Hayama and Tsukuba,

Kanagawa and Ibaraki, Japan, March (2003)
C ACT none

12C103
T. Sakai, S. Uno, K. Mizuhasi
Development of PC-based Real-time Signal Analysis System
Proceedings of the 16th meeting for tandem accelerators and related techniques (in press)
S ACT none

Appendix 2. Type of Research Collaboration

Section of this Report	Reseach Program Number	Type of Research Collaborations*	Section of this Report	Reseach Program Number	Type of Research Collaborations*
1.1	21003/22003	Joint.Res.			
1.2	21002	Joint.Res.	3.1	21041	JAERI
1.3	22004	JAERI	3.2	21042	Coop.Res.Univ.
1.4	22001	JAERI	3.3	21043	JAERI
1.5	22002	JAERI	3.4	21044	Coop.Res.Univ.
1.6	21001	JAERI	3.5	21045	Coop.Res.Univ.
1.7	21004	Coop.Res.Univ.	3.6	21046	Coop.Res.Univ.
1.8	21005/22006	Joint.Res.	3.7	21053	JAERI
1.9	22005	Coop.Res.Univ.	3.8	22019	Joint.Res.
2.1	21007	Coop.Res.Univ.	4.1	21006	Proj.Res.Univ.
2.2	22017	Coop.Res.Univ.	4.2	22007	Proj.Res.Univ.
2.3	21008	Joint.Res.	4.3	22008	Proj.Res.Univ.
2.4	21009	Joint.Res.	4.4	22009	Proj.Res.Univ.
2.5	21010	JAERI	4.5	22010	Proj.Res.Univ.
2.6	21011	Joint.Res.	4.6	22011	Proj.Res.Univ.
2.7	21012	Joint.Res.	4.7	22012	JAERI
2.8	21013	Joint.Res.	4.8	22013	JAERI
2.9	21013	Joint.Res.	4.9	22014	JAERI
2.10	21014	Joint.Res.	4.10	22015	Joint.Res.
2.11	21015	Coop.Res.Univ.	4.11	22016	Joint.Res.
2.12	21016	Coop.Res.Univ.	4.12	22020	JAERI
2.13	21017	Joint.Res.	4.13	22023	Coop.Res.Univ.
2.14	21018	Coop.Res.Univ.	4.14	22024	JAERI
2.15	21019	Joint.Res.	4.15	22027	JAERI
2.16	21020	Coop.Res.Univ.	4.16	22028	Coop.Res.Univ.
2.17	21021	Coop.Res.Univ.	4.17	22029	Coop.Res.Univ.
2.18	21052	JAERI	4.18	22039	JAERI
2.19	21022	Joint.Res.	4.19	22040	JAERI
2.20	21024	Joint.Res.	4.20	22043	JAERI
2.21	21025	Coop.Res.Univ.			
2.22	21026	Joint.Res.	5.1	22022	Coop.Res.Univ.
2.23	21027	JAERI	5.2	22025	Coop.Res.Univ.
2.24	21028	Coop.Res.Univ.	5.3	22026	JAERI
2.25	21029	Joint.Res.	5.4	22030	JAERI
2.26	21030	Coop.Res.Univ.	5.5	off line	JAERI
2.27	22018	JAERI	5.6	off line	JAERI
2.28	21031	Coop.Res.Univ.	5.7	22031	JAERI
2.29	21032	Joint.Res.	5.8	22033	JAERI
2.30	21033	Coop.Res.Univ.	5.9	22034	JAERI
2.31	21034	JAERI	5.10	22035	JAERI
2.32	21035	Proj.Res.Univ.	5.11	22036	Coop.Res.Univ.
2.33	21036	Proj.Res.Univ.	5.12	22037	Coop.Res.Univ.
2.34	21037	Proj.Res.Univ.	5.13	22038	Coop.Res.Univ.
2.35	21038	Proj.Res.Univ.	5.14	22041	Coop.Res.Univ.
2.36	21039	Proj.Res.Univ.	5.15	22042	Coop.Res.Univ.
2.37	21054	JAERI			

Section of this Report	Reseach Program Number	Type of Research Collaborations*
6.1	21040	JAERI
6.2	off line	JAERI
7.1	21047	JAERI
7.2	22044	Coop.Res.Univ.
7.3	22045	JAERI
7.4	22046	Coop.Res.Univ.
7.5	22047	Coop.Res.Univ.
8.1	21049	Proj.Res.Univ.
8.2	21050	Proj.Res.Univ.
8.3	21051	Proj.Res.Univ.
9.1	21048	JAERI
9.2	22049	JAERI
9.3	22050	Coop.Res.Univ.
9.4	22051	JAERI
9.5	off line	JAERI
9.6	Machine Study	JAERI
9.7	Machine Study	JAERI
9.8	Machine Study	JAERI
9.9	Machine Study	JAERI
9.10	Machine Study	JAERI
9.11	Machine Study	JAERI
9.12	Machine Study	JAERI
9.13	Machine Study	JAERI
9.14	off line	JAERI

*Joint Res.: Joint research with private company or governmental institution
Coop. Res. Univ.: Cooperative research with a university or universities #
Proj. Res.Univ.: The JAERI-Universities Joint Research Project #
#For administration of these programs, we appreciate the cooperation of:
Research Center for Nuclear Science and Technology, The University of Tokyo.

Appendix 3. Organization and Personnel of TIARA (FY 2002)

1) Organization for the Research and Development of Advanced Radiation Technology

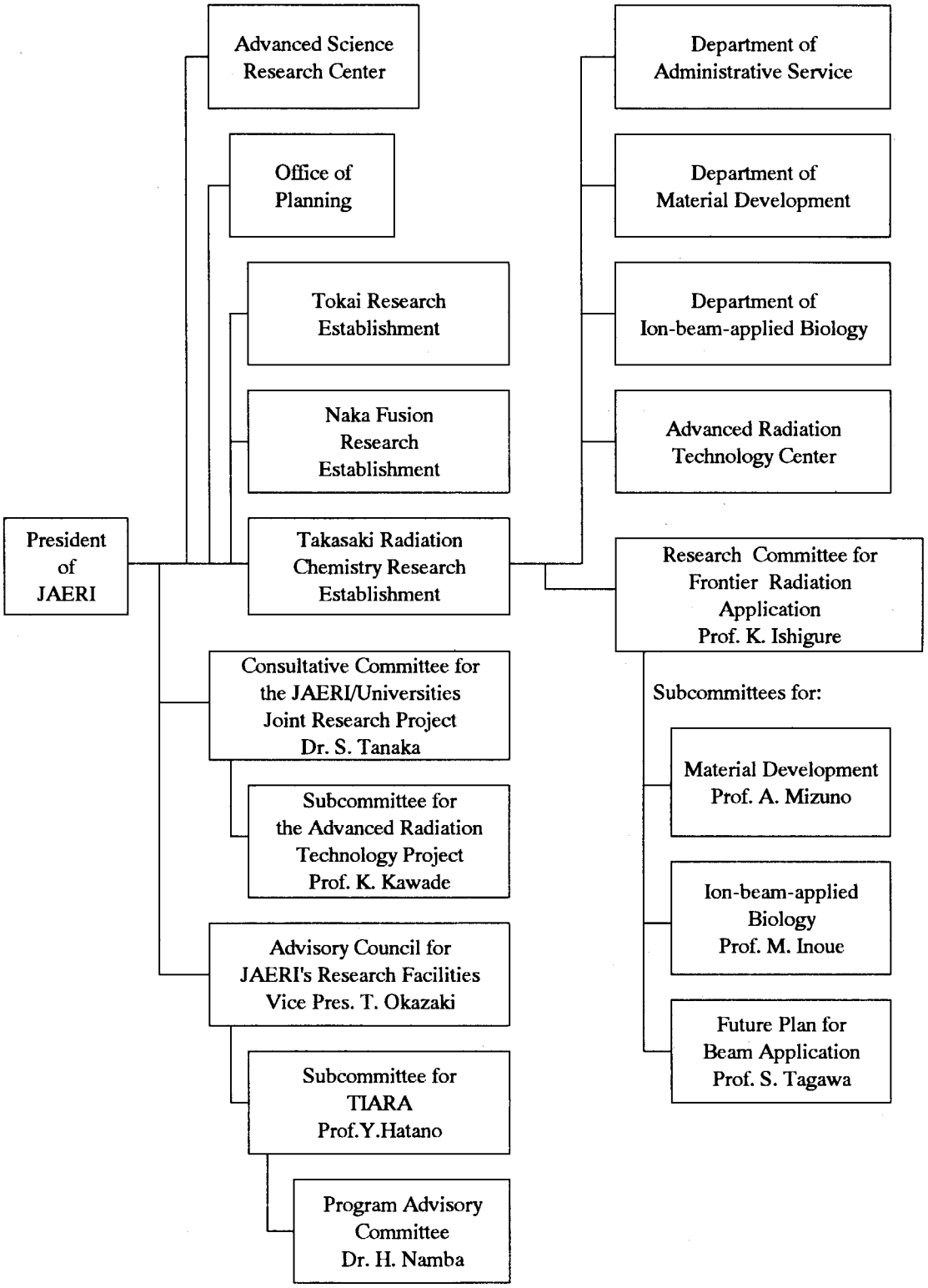

2) Personnel for the Administration, Operation and Control of TIARA

Advanced Radiation Technology Center

Director	M. Saidoh
Deputy Director	Y. Ohara

Administration Division

General Manager	M. Ottsubo
Staff Member	K. Morishita, A. Habuto

Utilization and Coordination Division

General Manager	Su. Tanaka
Staff Member	K. Nishimura, H. Takizawa, M. Hosono

Ion Accelerator Operation Division

General Manager	S. Taiima

Group of Cyclotron Operation

Staff Member	Y. Nakamura, T. Nara, T. Agematsu, I. Ishibori, S. Kurashima, K. Yoshida

Guoup of Electrostatic Accelerators Operation

Staff Member	I.Takada, K.Mizuhashi, S. Uno, K. Ohkoshi, Y. Nakajima, A. Chiba

Beam Engineering Division

Head	K. Arakawa
Staff Member	M. Fukuda, T. Kamiya, S. Okumura, Y. Saito, Y. Ishii, T. Sakai, M. Oikawa, T. Satoh, N. Miyawaki

Irradiation Service Division

General Manager	H. Sunaga
Staff Member	T. Kanazawa, Y. Haruyama, T.Ohkubo, N. Haneda, H. Hanaya

Department of Administrative Services

Safety Division

Staff Member	Y. Ohi, H. Miyauchi

(Radiation Monitoring and Control in TIARA)

Utilities and Maintenance Division

Staff Member	S. Kaneko, Y. Takayama

(Radioactive Waste Management and Utility Control in TIARA)

国際単位系（SI）と換算表

表1　SI基本単位および補助単位

量	名称	記号
長さ	メートル	m
質量	キログラム	kg
時間	秒	s
電流	アンペア	A
熱力学温度	ケルビン	K
物質量	モル	mol
光度	カンデラ	cd
平面角	ラジアン	rad
立体角	ステラジアン	sr

表2　SIと併用される単位

名称	記号
分，時，日	min，h，d
度，分，秒	°，′，″
リットル	l，L
トン	t
電子ボルト	eV
原子質量単位	u

1 eV=1.60218×10^{-19}J

1 u=1.66054×10^{-27}kg

表5　SI接頭語

倍数	接頭語	記号
10^{18}	エクサ	E
10^{15}	ペタ	P
10^{12}	テラ	T
10^{9}	ギガ	G
10^{6}	メガ	M
10^{3}	キロ	k
10^{2}	ヘクト	h
10^{1}	デカ	da
10^{-1}	デシ	d
10^{-2}	センチ	c
10^{-3}	ミリ	m
10^{-6}	マイクロ	μ
10^{-9}	ナノ	n
10^{-12}	ピコ	p
10^{-15}	フェムト	f
10^{-18}	アト	a

表3　固有の名称をもつSI組立単位

量	名称	記号	他のSI単位による表現
周波数	ヘルツ	Hz	s^{-1}
力	ニュートン	N	$m\cdot kg/s^2$
圧力，応力	パスカル	Pa	N/m^2
エネルギー,仕事,熱量	ジュール	J	N·m
工率，放射束	ワット	W	J/s
電気量，電荷	クーロン	C	A·s
電位，電圧，起電力	ボルト	V	W/A
静電容量	ファラド	F	C/V
電気抵抗	オーム	Ω	V/A
コンダクタンス	ジーメンス	S	A/V
磁束	ウェーバ	Wb	V·s
磁束密度	テスラ	T	Wb/m^2
インダクタンス	ヘンリー	H	Wb/A
セルシウス温度	セルシウス度	℃	
光束	ルーメン	lm	cd·sr
照度	ルクス	lx	lm/m^2
放射能	ベクレル	Bq	s^{-1}
吸収線量	グレイ	Gy	J/kg
線量等量	シーベルト	Sv	J/kg

表4　SIと共に暫定的に維持される単位

名称	記号
オングストローム	Å
バーン	b
バール	bar
ガル	Gal
キュリー	Ci
レントゲン	R
ラド	rad
レム	rem

1 Å=0.1nm=10^{-10}m

1 b=100fm^2=10^{-28}m^2

1 bar=0.1MPa=10^5Pa

1 Gal=1cm/s^2=10^{-2}m/s^2

1 Ci=3.7×10^{10}Bq

1 R=2.58×10^{-4}C/kg

1 rad=1cGy=10^{-2}Gy

1 rem=1cSv=10^{-2}Sv

（注）

1．表1－5は「国際単位系」第5版，国際度量衡局 1985年刊行による。ただし，1 eVおよび1 uの値はCODATAの1986年推奨値によった。

2．表4には海里，ノット，アール，ヘクタールも含まれているが日常の単位なのでここでは省略した。

3．barは，JISでは流体の圧力を表わす場合に限り表2のカテゴリーに分類されている。

4．EC閣僚理事会指令ではbar，barnおよび「血圧の単位」mmHgを表2のカテゴリーに入れている。

換算表

力	N(=10^5dyn)	kgf	lbf
	1	0.101972	0.224809
	9.80665	1	2.20462
	4.44822	0.453592	1

粘度　1 Pa·s(N·s/m^2)=10 P(ポアズ)(g/(cm·s))

動粘度　1m^2/s=10^4St(ストークス)(cm^2/s)

圧力	MPa(=10bar)	kgf/cm^2	atm	mmHg(Torr)	lbf/in^2(psi)
	1	10.1972	9.86923	7.50062×10^3	145.038
	0.0980665	1	0.967841	735.559	14.2233
	0.101325	1.03323	1	760	14.6959
	1.33322×10^{-4}	1.35951×10^{-3}	1.31579×10^{-3}	1	1.93368×10^{-2}
	6.89476×10^{-1}	7.03070×10^{-2}	6.80460×10^{-2}	51.7149	1

エネルギー・仕事・熱量	J(=10^7 erg)	kgf·m	kW·h	cal(計量法)	Btu	ft·lbf	eV
	1	0.101972	2.77778×10^{-7}	0.238889	9.47813×10^{-4}	0.737562	6.24150×10^{18}
	9.80665	1	2.72407×10^{-6}	2.34270	9.29487×10^{-3}	7.23301	6.12082×10^{19}
	3.6×10^6	3.67098×10^5	1	8.59999×10^5	3412.13	2.65522×10^6	2.24694×10^{25}
	4.18605	0.426858	1.16279×10^{-6}	1	3.96759×10^{-3}	3.08747	2.61272×10^{19}
	1055.06	107.586	2.93072×10^{-4}	252.042	1	778.172	6.58515×10^{21}
	1.35582	0.138255	3.76616×10^{-7}	0.323890	1.28506×10^{-3}	1	8.46233×10^{18}
	1.60218×10^{-19}	1.63377×10^{-20}	4.45050×10^{-26}	3.82743×10^{-20}	1.51857×10^{-22}	1.18171×10^{-19}	1

1 cal= 4.18605J（計量法）

= 4.184J（熱化学）

= 4.1855J（15℃）

= 4.1868J（国際蒸気表）

仕事率　1 PS(仏馬力)

= 75 kgf·m/s

= 735.499W

放射能	Bq	Ci
	1	2.70270×10^{-11}
	3.7×10^{10}	1

吸収線量	Gy	rad
	1	100
	0.01	1

照射線量	C/kg	R
	1	3876
	2.58×10^{-4}	1

線量当量	Sv	rem
	1	100
	0.01	1

（86年12月26日現在）